Phase Transitions and Doping in Semiconductor Nanocrystals

A DISSERTATION
SUBMITTED TO THE FACULTY OF THE GRADUATE SCHOOL
UNIVERSITY OF MINNESOTA
BY

Ayaskanta Sahu

IN PARTIAL FULFILLMENT OF THE REQUIREMENTS
FOR THE DEGREE OF
DOCTOR OF PHILOSOPHY

David J. Norris, Adviser

November 2012

ACKNOWLEDGEMENTS

First of all, I would like my express my sincere thanks to my adviser, Prof. David Norris, for his constant support and guidance during the last five years. His untiring encouragement, stimulating suggestions and regular feedback on my work, are major factors in the progress of my research project and the writing of this thesis. David, I have enjoyed greatly working with you. You have always been there when I needed you, backed me up (with confidence and funds) and supported all my ideas (albeit some of them were crazy). One could not have wished for a more enthusiastic, passionate and amicable adviser. I still am amazed that I am graduating with all the work we managed to get done in these five years even after moving across continents, and most certainly, the credit goes to you.

I owe a large debt of gratitude to you, Moon, for your invaluable and always forthcoming help and assistance. Not only have you been a perennial source of ideas and insightful suggestions, you have always inspired me to look forward to my research with enthusiasm. I shall cherish our regular 2 a.m. visits to McDonalds and our pseudointellectual discussions over beer and chicken wings forever. I would also like to express my appreciation to Andrew Wills, for guiding me through the initial phase of my work. Regular brainstorming sessions and stimulating discussions with Moon and Andy, have contributed substantially to this thesis. Be it research, camping or canoeing, you both have always been there for me through thick and thin during my time at UMN. I would also like to express my heartfelt appreciation to my smart undergraduate researchers – Donna and Clara. You both have been wonderful students and contributed immensely in this dissertation. Thanks for your help and pleasant company.

I am grateful to my talented lab-mates at ETH, Kevin and Daniele, for teaching me everything related to plasmonics and devices. I hope we get to get to work together in

the future. My sincere gratitude goes to Kurtis Leschkies, Prashant Nagpal, and Lejun Qi, for their insightful perspectives, suggestions and help along the way. I am thankful to Ankur, Lisa, Vince, Jong Hyuk, Sriharsha, Boris, Florian, and all my current and ex-lab-mates, office-mates and colleagues both at UMN and ETH for maintaining a lively environment both in the lab and the office, which made my life at Minneapolis and Zurich much more fun and enjoyable. Special mention must go to Shameek and Mike for patiently answering my incessant queries and helping me out whenever the need arose. Shameek, it was already great to talk to someone who understood what I was doing in the office, but it was way nicer to have someone to talk to about everything – work related or completely unrelated - at home or over a coffee at Starbucks.

I must also thank Professors Wayne Gladfelter, Eray Aydil, and Daniel Frisbie for agreeing to serve on my thesis defense committee as well as letting me use their labs and resources regularly. Andre, thanks for always taking out time to answer my questions. Over the course of a PhD, collaborations with other research groups are often necessary and have been very fruitful for me, in particular. Even though I have not included a lot of the EXAFS, DFT and EPR work, I have had a pleasant experience working with you – Alex, Christian and Professor Winterer. Many thanks for introducing me to the world of EXAFS and showing me around Hamburg and Duisburg. I would like to express my thanks to Florian for his DFT calculations. It was a pleasure learning all the details from you. I would also like to thank Rui, Toze and Martin for their help with the EPR experiments. Oli and Johannes - without your help, the phase transition work would never have been complete. Many thanks to Stefan for your technical assistance. I am also grateful to IPrime and ETH Zurich for extending their financial support to me.

Julie, Teresa and Pascale, my deepest thanks go to you all, for making me feel at home from day one and for rendering my transition across continents so smooth. Jason, Raghu, Richa, Katie, Ammu, Akshay, Amit, Shreya, Pandey “ji”, Anudha, Reetam and Parthiv – thanks for making life outside the lab fun. I would also like to extend my thanks to all my friends in the United States, Europe and India.

Last, but not the least, I am deeply obliged to my parents, my sister and Guneet, for their unconditional and constant love and support. It is their encouragement which has always kept me motivated, and given me the strength to get through tough times.

Finally, I would like to thank Subir Sabharwal and Prof. Ajay Ray. Neither this PhD, nor this thesis would have ever materialized if it was not for the faith and confidence that you both had in me and my abilities. If it was not for your motivation, I would probably be grinding my life away at some oil-rig in some god forsaken place. This thesis is dedicated to you both.

To Subir Sabharwal and Ajay K. Ray

ABSTRACT

Colloidal semiconductor nanocrystals are a promising technological material because their size-dependent optical and electronic properties can be exploited for a diverse range of applications such as light-emitting diodes, bio-labels, transistors, and solar cells. For many of these applications, electrical current needs to be transported through the devices. However, while their solution processability makes these colloidal nanocrystals attractive candidates for device applications, the bulky surfactants that render these nanocrystals dispersible in common solvents block electrical current. Thus, in order to realize the full potential of colloidal semiconductor nanocrystals in the next-generation of solid-state devices, methods must be devised to make conductive films from these nanocrystals. One way to achieve this would be to add minute amounts of foreign impurity atoms (dopants) to increase their conductivity. Electronic doping in nanocrystals is still very much in its infancy with limited understanding of the underlying mechanisms that govern the doping process. This thesis introduces an innovative synthesis of doped nanocrystals and aims at expanding the fundamental understanding of charge transport in these doped nanocrystal films. The list of semiconductor nanocrystals that can be doped is large, and if one combines that with available dopants, an even larger set of materials with interesting properties and applications can be generated. In addition to doping, another promising route to increase conductivity in nanocrystal films is to use nanocrystals with high ionic conductivities. This thesis also examines this possibility by studying new phases of mixed ionic and electronic conductors at the nanoscale. Such a versatile approach may open new pathways for interesting fundamental research, and also lay the foundation for the creation of novel materials with important applications.

In addition to their size-dependence, the intentional incorporation of impurities (or doping) allows further control over the electrical and optical properties of nanocrystals. However, while impurity doping in bulk semiconductors is now routine, doping of nanocrystals remains challenging. In particular, evidence for electronic doping,

in which additional electrical carriers are introduced into the nanocrystals, has been very limited. Here, we adopt a new approach to electronic doping of nanocrystals. We utilize a partial cation exchange to introduce silver impurities into cadmium selenide (CdSe) and lead selenide (PbSe) nanocrystals. Results indicate that the silver-doped CdSe nanocrystals show a significant increase in fluorescence intensity, as compared to pure CdSe nanocrystals. We also observe a switching from *n*- to *p*-type doping in the silver-doped CdSe nanocrystals with increased silver amounts. Moreover, the silver-doping results in a change in the conductance of both PbSe and CdSe nanocrystals and the magnitude of this change depends on the amount of silver incorporated into the nanocrystals.

In the bulk, silver chalcogenides (Ag_2E, E=S, Se, and Te) possess a wide array of intriguing properties, including superionic conductivity. In addition, they undergo a reversible temperature-dependent phase transition which induces significant changes in their electronic and ionic properties. While most of these properties have been examined extensively in bulk, very few studies have been conducted at the nanoscale. We have recently developed a versatile synthesis that yields colloidal silver chalcogenide nanocrystals. Here, we study the size dependence of their phase-transition temperatures. We utilize differential scanning calorimetry and *in-situ* X-ray diffraction analyses to observe the phase transition in nanocrystal assemblies. We observe a significant deviation from the bulk α (low-temperature) to β (high-temperature) phase-transition temperature when we reduce their size to a few nanometers. Hence, these nanocrystals provide great potential for devices to utilize the properties of both phases at a significantly lower temperature than that of the corresponding bulk material. Moreover, a wide range of properties of both phases that meet specific requirements can be obtained simply by tuning the crystal size.

TABLE OF CONTENTS

LIST OF TABLES

LIST OF FIGURES

CHAPTER 1

INTRODUCTION

1.1 SEMICONDUCTOR NANOCRYSTALS

The nano-scale ranges from about 1 nanometer (nm) to 100 nanometers corresponding to roughly 100 atoms to 10 million atoms. The upper and lower boundaries of this scale are not sharply defined, but are chosen such that one excludes individual atoms on the bottom end and micrometer-scale objects on the top end. This intermediate state of matter lies somewhere between the bulk phase and the atomic or molecular regime. Material properties in nano-sized systems can be controlled appreciably by tuning their size and give rise to potentially new phenomena. Electronic and optical properties of metals and semiconductors depend strongly on the crystallite size once one starts to venture into the nano-scale regime. The evolution of these size dependent fundamental properties can be attributed to the increased surface area in addition to quantum effects that become increasingly important with decreasing size. This change is quite impressive especially in the case of semiconductors.[1-3] For instance, simply altering the size of CdSe nanocrystals can tune its band gap between 1.7 and 3 eV and hence, the material can absorb and emit across the entire visible spectrum.[3] It is fascinating that the properties in a material of a single chemical composition can be varied so significantly, simply by tailoring bulk material parameters such as size.

A semiconducting crystallite, which is a few nanometers in scale, with size-specific optical and electronic behavior, is referred to as a semiconductor nanocrystal (NC) or a quantum dot (QD). Semiconductor (SC) NCs are a promising technological material because the ability to control their optical and electronic properties can be

exploited for a diverse range of applications, such as light-emitting diodes,[4,5] bio-labels,[6,7] single molecule transistors[8] and solar cells.[9]

1.2 DOPING SEMICONDUCTOR NANOCRYSTALS

The introduction of trace intentional impurities (or doping) is central to controlling the behavior of SC materials. Dopants possess the ability to modify strongly the optical, magnetic, and electronic properties of bulk SCs. A dopant, with one more valence electron than the host atom it substitutes for, can donate its extra electron to the SC for electronic charge transport. Similarly, an impurity atom with one less electron can donate a hole to the SC. Modern SC-based technology owes its existence, in large part, to the fact that these materials can be doped. It is the ability to control precisely the number of carriers available in the SC by doping, which has expedited the advance in SC-based electronic and optoelectronic technology. The advantage of doped SCs is that they provide the device engineer with a wide range of mobilities, so that materials are available with properties that meet specific requirements. Hence, it is natural to extend the versatility of nanocrystals by adding dopants. Doping can expand the range of properties in SC NCs substantially; thus opening up a plethora of applications ranging from solar cells[9] and bio-imaging[10] to wavelength tuned lasers.[11]

However, while the field of bulk-doping can be traced back many decades, the first breakthrough in nanocrystal doping came in 1994 when Bhargava *et al.* observed interesting luminescent properties in manganese-doped zinc selenide NCs.[12] Since then, several II-VI SC NCs have been doped by transition metals and rare earth elements.[13,14] However, until now, no group has managed to dope SC NCs with electronic dopants that have proved as useful as their analogues in bulk SCs.

1.3 CHALLENGES AND ISSUES IN DOPING NANOCRYSTALS

NCs represent one of the most promising classes of nanotechnology. Over the last two decades, most of their intrinsic properties have been mapped out. Adding dopants to NCs further extends their properties and possible applications. However, the ability to incorporate dopants successfully and efficiently into NCs faces several challenges. One of the major bottlenecks is the non-existence of any specific or reliable synthetic technique which can ensure controlled dopant incorporation. Due to the high surface-to-volume ratios of NCs, a large percentage of the total dopant population is at the NC surfaces. Dopants at the surface sites may differ considerably from those in the NC cores. Dopant atoms inside the NC also do not distribute uniformly throughout the NC. Moreover, any ensemble of doped NCs will always have a statistical distribution of dopants per NC.[13] This inhomogeneity may lead to an adverse effect on the targeted properties of the doped material.

Furthermore, how does one know for sure that the NCs have been successfully doped? NC doping suffers from the intrinsic problem that only an extremely small fraction of the product is the impurity, and hence, the doped NC is virtually indistinguishable from its pure analogue if one uses X-ray crystallographic techniques and microscopy (Scanning Electron Microscopy and Transmission Electron Microscopy). Hence, these materials are considerably more challenging to probe experimentally.

Due to these challenges, attempts at doping SC NCs have been largely unsuccessful. However, even if one manages to incorporate dopants inside a NC and introduces extra charge carriers by some technique, there is a high probability that one might run into additional problems. NCs with an extra electron (hole) can behave as a strong reducing (oxidizing) agent. This leads to a redox reaction at the surface, which can consume the extra charge carrier and render it unavailable for conduction.[15,16] Also, it has been observed that wide band gap II–VI SCs (ZnTe, ZnSe, CdSe, CdS) exhibit a strong proclivity for only one type of doping - either p-type (extra holes) or n-type (extra electrons) - which restricts their use in practical applications such as light-emitting diodes

and lasers.[17] An intricate understanding of the doping mechanism is required to circumvent the above mentioned problems and achieve successful doping in SC NCs.

This study aims at trying to understand the fundamental science behind doping mechanisms, developing new techniques for incorporating dopant molecules into NCs, using appropriate spectroscopic techniques to verify the presence of dopants and finally characterizing the location of the dopants. The thesis focuses largely, but not exclusively, on doping of II-VI (CdSe) and IV-VI (PbSe) colloidal SC NCs because these are the mostly widely and thoroughly studied NC-systems to date. Moreover, these NCs hold enormous potential for applications in light-emitting diodes, field effect transistors and solar cells. The use of dopants for enhancing the luminescence and magnetic properties of SC NCs has already been demonstrated. To date, however, no one has presented evidence of electronically doped NCs. By electronically doping NCs, we hope to fill this gap and complete the entire set of optical, magnetic and electronic properties for SC NCs. This exciting opportunity to research and further advance the understanding of doping SC NCs has motivated the submission of this thesis. Electronic doping of NCs might also provide a niche for opening new pathways for interesting fundamental research, and lay the foundation for the creation of novel materials with important applications.

1.4 PHASE TRANSITIONS IN NANOCRYSTALS

While the main focus of this thesis is to study the effect of a few dopant atoms (especially silver) on the properties of cadmium and the lead chalcogenide NCs, we were also interested in looking at the effects of these impurity atoms at the other end of the spectrum *i.e.*, in the high doping limit, where one would have the silver chalcogenides mostly, with minute amounts of lead and cadmium atoms as the impurities. While cadmium and lead chalcogenide NCs have been extremely well studied, very few reports exist that study silver chalcogenide NCs. Hence, this lack of information about the silver chalcogenide NCs motivated us to pursue a detailed study of their properties.

Apart from tuning the material properties of NCs by changing their size and adding impurities, another way is to vary their temperature and tap into new crystal phases of the same material that exhibit different properties. One such material system, which shows rich phase behavior, is the silver chalcogenides. As a bulk material, silver chalcogenides are a class of semiconductor with many intriguing properties. They are mixed conductors with high electronic and ionic mobility, *i.e.*, both electrons and silver ions can travel rapidly within the semiconductor. They undergo a reversible phase transition [*e.g.*, water undergoes phase transitions from solid (ice) to liquid (water) to gas (water vapor)] from a low-temperature phase (α-phase) to a high-temperature phase (β-phase) at temperatures varying from 135 – 180 °C (depending on whether it is silver sulfide, silver selenide or silver telluride) with a strong change in electronic properties.[18] Whilst all these materials have been very well studied in the bulk, very few studies have been conducted at the nano-scale. By shrinking the size of the material into the nano-scale, new metastable crystal phases can be observed which are not seen in bulk crystals.[18,19] By varying the size of the material and the temperature of the same, one might expand the possible range of structures further and hence derive novel properties.

1.5 THESIS OVERVIEW

The main motivation of this thesis lies in expanding the possible range of material properties. We aim at doing so by doping NCs and synthesizing NCs of a new class of materials – the silver chalcogenides. The next chapter (Chapter 2) gives a very basic, but extensive overview of properties of SC NCs. It reviews the various methods of synthesis for NCs, followed by an introduction to the various doping challenges, successes and failures, theories and techniques. Chapter 3 focuses on silver doping of CdSe NCs and a detailed study of the resulting optical properties. Chapter 4 describes the theory of charge transport in SC NC assemblies. With this knowledge in mind, charge transport in undoped CdSe NC assemblies is studied followed by silver-doped samples. The changes in the electrical transport induced by doping can be observed easily once a systematic study of electrical transport in undoped NCs has been conducted. We extend our doping

scheme described in Chapter 3 for silver doping of CdSe NCs to PbSe NCs. We utilize these samples to study charge transport in both doped and undoped PbSe NC systems. This is described in detail in Chapter 5. In Chapter 6, we demonstrate a simple, one-pot, single-step synthesis of nearly monodisperse silver chalcogenide NCs with a focus on silver selenide NCs. Chapter 7 details the optical properties of these silver selenide NCs while Chapter 8 focuses on the rich phase behavior of these material. It describes both the size- and temperature-dependence of the phase transitions in these NC systems and the resulting effect of the phase transitions on their electronic properties.

1.6 REFERENCES

(1) Brus, L. *Applied Physics A-Materials Science & Processing* **1991**, *53*, 465.

(2) Brus, L. *Journal of Physics and Chemistry of Solids* **1998**, *59*, 459.

(3) Alivisatos, A. P. *Science* **1996**, *271*, 933.

(4) Colvin, V. L.; Schlamp, M. C.; Alivisatos, A. P. *Nature* **1994**, *370*, 354.

(5) Tessler, N.; Medvedev, V.; Kazes, M.; Kan, S. H.; Banin, U. *Science* **2002**, *295*, 1506.

(6) Chan, W. C. W.; Nie, S. M. *Science* **1998**, *281*, 2016.

(7) Bruchez, M., Jr.; Moronne, M.; Gin, P.; Weiss, S.; Alivisatos, A. P. *Science* **1998**, *281*, 2013.

(8) Klein, D. L.; Roth, R.; Lim, A. K. L.; Alivisatos, A. P.; McEuen, P. L. *Nature* **1997**, *389*, 699.

(9) Gur, I.; Fromer, N. A.; Geier, M. L.; Alivisatos, A. P. *Science* **2005**, *310*, 462.

(10) Michalet, X.; Pinaud, F. F.; Bentolila, L. A.; Tsay, J. M.; Doose, S.; Li, J. J.; Sundaresan, G.; Wu, A. M.; Gambhir, S. S.; Weiss, S. *Science* **2005**, *307*, 538.

(11) Klimov, V. I.; Ivanov, S. A.; Nanda, J.; Achermann, M.; Bezel, I.; McGuire, J. A.; Piryatinski, A. *Nature* **2007**, *447*, 441.

(12) Bhargava, R. N.; Gallagher, D.; Hong, X.; Nurmikko, A. *Physical Review Letters* **1994**, *72*, 416.

(13) Bryan, J. D.; Gamelin, D. R. Doped Semiconductor Nanocrystals: Synthesis, Characterization, Physical Properties, and Applications. In *Progress in Inorganic Chemistry, Vol 54*, 2005; Vol. 54; pp 47.

(14) Nalwa, H. S. *Encyclopedia of Nanoscience and Nanotechnology*; American Scientific Publishers: Stevenson Ranch, Calif., 2004.

(15) Brus, L. E. *Journal of Chemical Physics* **1983**, *79*, 5566.

(16) Henglein, A. *Berichte Der Bunsen-Gesellschaft-Physical Chemistry Chemical Physics* **1982**, *86*, 301.

(17) Chadi, D. J. *Annual Review of Materials Science* **1994**, *24*, 45.

(18) Sahu, A.; Qi, L.; Kang, M. S.; Deng, D.; Norris, D. J. *Journal of the American Chemical Society* **2011**, *133*, 6509.

(19) Chen, C. C.; Herhold, A. B.; Johnson, C. S.; Alivisatos, A. P. *Science* **1997**, *276*, 398.

CHAPTER 2

SEMICONDUCTOR NANOCRYSTALS – AN OVERVIEW

2.1 INTRODUCTION

Despite the recent excitement surrounding nanotechnology, nanostructures are not really new. Nanometer-sized devices and structures have existed since the Roman era. The Purple of Cassius consisting of a mixture of tin oxide and Au nanocrystals (NCs)[1] and the Lycurgus cup, with Au and Ag NCs in its walls, are two classic examples. Maya blue, with metal and oxide NCs,[2] and metal nanoparticles in the glass windows of medieval cathedrals demonstrate that nanoparticles have been used for ages without any clear knowledge of nanoscale phenomena.

Despite some early work in the 17th century, systematic studies on nano-sized materials did not really begin until the 1800s. Finally in 1857, Michael Faraday[3] realized the role of metal particles in the color of church windows followed by Einstein, Gustav Mie and Gans,[4-7] who proposed several theories for the properties of nanoparticles. However, colloidal nanoparticle science was fairly neglected until the early 20th century. This prompted Ostwald[8] to title his 1915 book on colloids as "*The World of Neglected Dimensions*." Feynman's lecture[9] at the American Physical Society in 1960, entitled "*There is Plenty of Room at the Bottom,*" led to a revived interest in generating nanoparticles of various materials. Despite the identification of unique properties in metal nanoparticles, similar exciting properties were not observed in semiconductor (SC) nanoparticles until early 1980's when Ekimov and Brus *et al.* observed a size dependent shift in energy of the HOMO (Highest Occupied Molecular Orbital) – LUMO (Lowest Unoccupied Molecular Orbital) transition in SC NCs.[10,11] This breakthrough generated a renewed interest and led to rapid advancements in the field of SC NCs. The progress has

been aided by advances in instrumentation, which help in characterizing these nanomaterials. Today, it is possible to prepare and study NCs of metals, SCs and other substances by various means. Rapid advances in both experimental and theoretical methods have led to a much better understanding of the properties of NCs than ever before.

2.2 PHYSICS OF SEMICONDUCTOR NANOCRYSTALS

Nanoparticles can either be amorphous or crystalline. Crystalline nanoparticles can again exist as single crystalline or polycrystalline particles. The term "*nanocrystals*" is used for those nanoparticles which have a single crystalline domain.[12] The focus of my work, and hence, this chapter will be on semiconductor (SC) NCs.

2.2.1. Surface

The dimensions of NCs are so small that a substantially high fraction of the total atoms is present on their surfaces as compared to the bulk. The surface of the NCs plays an essential role in determining the properties exhibited by the nanocrystal. Typically, the surface is passivated by attaching long-chained molecules. However, more often than not, there exist lots of dangling bonds due to incomplete passivation. Hence, the surface is dynamic and chemically accessible, with the surface atoms sufficiently mobile. The poor knowledge of the surface has typically impeded the study of these NCs. Many important properties of the NCs, such as the fluorescence quantum yields,[12] carrier trapping,[13] and energy relaxation[14] are affected by the surface. Therefore, it is essential to achieve surface control for these colloidal NCs, since it is this surface that governs many of their versatile properties.

2.2.2. Strong Quantum Confinement Effect

The gap that separates the conduction and the valence energy bands is characteristic of any semiconductor (SC) material. In bulk SCs, it is fixed. Additionally, it can either be direct or indirect. Direct-gap SCs can absorb a photon, when an electron is

promoted directly from the valence band into the conduction band; thus creating an electron–hole pair (or exciton). Indirect-gap SCs require the assistance of a phonon to absorb or emit light. However, when the size of the SC material decreases to a level where the electrons, the holes and the excitons start to feel the physical boundary of the particle, the material starts to adjust its energy levels in response to this change in size and thus exhibits a phenomenon known as quantum confinement.

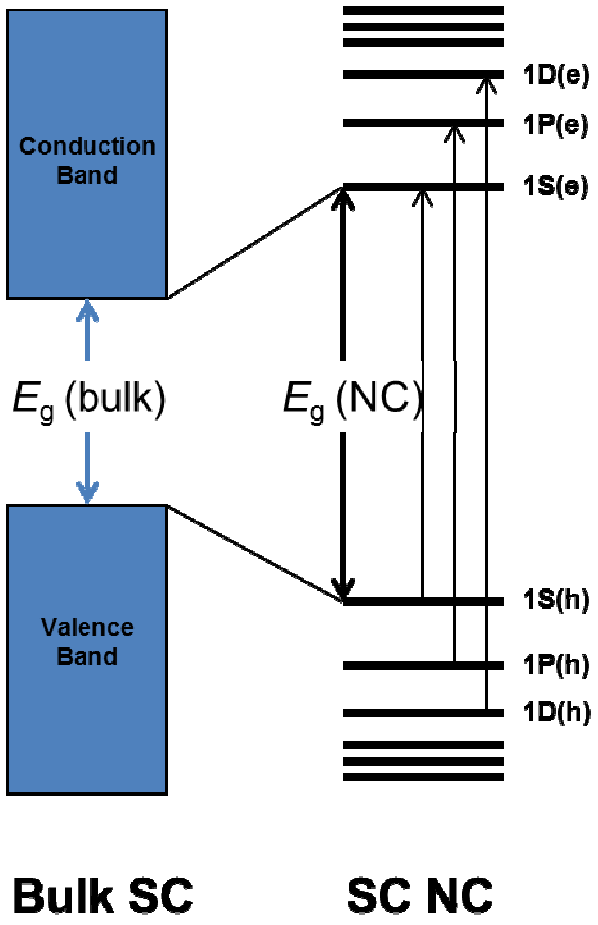

Figure 2.1: Comparison of bulk SC electronic states with NC electronic states. *E*g (bulk) is the band gap in the bulk and *E*g (NC) is the effective band gap in the NC. The conduction and valence bands in bulk SC collapse to discrete atomic-like states in SC NCs (1S, 1P, 1D etc.). The "e" and "h" in brackets refer to electron and hole states respectively.

Any particles that exhibit quantum confinement are named quantum dots (QDs). Typical features of quantum confinement include an increase in band gap and a collapse of the continuous valence and conduction bands of the bulk material into discrete energy

levels. This leads to sharp features in the absorption spectra of QDs instead of a continuous absorption spectrum observed in bulk SCs (Figure 2.1).[15] It can also lead to an indirect-gap material in bulk converting to a direct band-gap material at the nano-scale. By varying the size of the QD, one can have only the electron confined or the hole or the electron-hole pair (exciton). The regime where the exciton, the hole and the electron are all confined is referred to as the strong confinement regime. Correspondingly, when only the exciton is confined, but not the hole and the electron, it is referred to as the weak confinement regime.

In the strong confinement regime, the electron and hole can be treated as independent carriers. To model this system using the effective mass approximation, one assumes parabolic conduction and valence bands with bulk effective masses for the electron and hole.[11] Using a simple particle in a sphere model, the electron and hole in the NC can then be described by hydrogenic wave functions. By solving the Schrödinger equation while including the electron-hole Coulomb interaction, the band gap of the SC NC ($E_{\text{bandgap}}^{\text{NC}}$) as a function of its size can be approximated as:

$$E_{\text{bandgap}}^{\text{NC}}(R) = E_{\text{bandgap}}^{\text{bulk}} + \frac{\hbar^2 \pi^2}{2R^2}\left[\frac{1}{m_{\text{e}}} + \frac{1}{m_{\text{h}}}\right] - \frac{1.8e^2}{4\pi\varepsilon\varepsilon_0 R} \qquad (2.1)$$

where R denotes the radius of the NC, $E_{\text{bandgap}}^{\text{bulk}}$ the band gap in bulk, $\hbar$ the Planck's constant, ε the dielectric constant of the material, ε_0 the vacuum permittivity, and m_{e} and m_{h} are the effective masses of the electron and hole, respectively.

2.3 SYNTHESIS OF NANOCRYSTALS

Nano-science is characterized by a close interplay between physics, chemistry, biology and materials science. This is demonstrated vividly by a wide range of synthetic techniques that have been developed and used extensively for nano-scale materials. All these various techniques can be grouped into two broad schemes – the top-down and the bottom-up approaches. The top-down methods involve starting with bulk materials and

breaking them down to smaller and smaller particles. Conversely, the bottom-up methods start from the respective atoms and progressively build up the nanoparticle. The top-down and bottom-up approaches are also at times broadly categorized into physical and chemical methods, respectively. While physical methods produce large quantities of nanoparticles, chemical synthesis techniques offer much better reaction control, provide higher quality nanocrystals and can be easily tailored to produce different materials. Consequently, my work focuses on the chemical methods.

2.3.1 Physical Methods

A characteristic feature of any physical method is a high input of energy which is used to evaporate the bulk solid material forming a supersaturated vapor. Owing to the supersaturation, nucleation of nanoparticles takes place. It is extremely hard to control the particle size and distribution as the growth is extremely fast (on the order of milliseconds). Some popular examples of physical processes include molecular-beam-epitaxy (MBE), metal organic-chemical-vapor-deposition (MOCVD)[15-19] and vapor–liquid solid (VLS) approaches.[20,21] However, our emphasis is on low-energy input colloidal chemical syntheses of SC NCs.

2.3.2 Chemical methods

Chemical methods are generally carried out under much milder conditions than the physical methods. The focus of these methods lies on the development of different means of producing NCs, which are then dispersible in solvents. These are better known as colloidal NCs. My entire work on NCs revolves around these colloidal NCs. Any chemical reaction that leads to formation of colloidal NCs consists of three basic steps - *nucleation, growth*, and *termination*. One usually starts with a mixture of the NC constituents (precursors containing the elements forming the NC), capping agents (for colloidal stability), and the solvent (to control the growth temperature and manipulate precursor concentrations). NCs of different dimensions can be obtained from the same reaction mixture by manipulating relative rates of the various steps, which, in turn, are altered by changing precursor concentrations and temperature.

An important process that one needs to consider during the growth of a colloidal NC is *Ostwald ripening*.[15] It is a growth mechanism wherein smaller particles with higher surface energy dissolve, and thus release monomers or ions which are consumed by larger particles. This, however, leads to defocusing of the size distribution of synthesized NCs during early periods of growth and hence, severely limits the ultimate size distribution. One way to avoid this scenario is to keep adding reaction precursors during growth to ensure that monomer concentrations are never depleted.

The important factors that determine the quality and success of any NC synthetic procedure are the crystallinity, surface passivation, dispersity in various polar or nonpolar solvents, and the size distribution of the NCs obtained. Since the properties of nanoparticles are strongly size-dependent, it is highly desirable to have nanoparticles of nearly the same size, in order to be able to distinguish and study the properties that arise due to quantum size effects. Although the definition of monodispersity in its strictest sense requires identical or indistinguishable particles, colloidal NC samples, with a standard deviation, $\sigma \leq 5\%$ in diameter, are nominally termed as fairly monodisperse.[2]

NCs produced by chemical means can either be dispersed in aqueous media (sterically or electrostatically stabilized) or in organic solvents (sterically stabilized). Sterically stabilized NCs are redispersible, *i.e.* the NCs in the solvents can be precipitated, filtered, and dispersed again in a solvent. Furthermore, NCs in a sterically stabilized solvent can be dispersed in a wide range of concentrations. Most of the NCs used in this thesis are sterically stabilized.

Following La Mer and Dinegar's studies,[12,22] Murray *et al.* pioneered a high temperature NC synthesis method in the early 1990s which yielded fairly monodisperse NCs with high crystallinity. This technique involved a rapid injection of organometallic precursors of the target NCs into a coordinating solvent maintained at a high temperature. Hence, it is popularly known as the hot-injection method. This rapid injection was essential to achieve a discrete nucleation event and separate it from the growth process. Immediately after the injection, the precursor concentration is forced above the solubility

limit which leads to a nucleation burst. The nucleation event decreases the precursor concentration below the threshold following which nucleation is suppressed. Subsequently, the leftover precursors add to the existing nuclei and growth proceeds.[23] In this growth regime where the monomer concentration is relatively high, small particles grow faster than larger particles resulting in focusing of the size distribution. Once the monomer concentration is sufficiently depleted, growth proceeds by Ostwald ripening.

If nucleation is fast, *i.e.* the concentration of the precursors falls below the threshold concentration quickly, then nucleation can be separated from growth. The separation of nucleation and growth is imperative for monodispersity since particles that nucleate simultaneously will grow at similar rates and will eventually end up the same size.

To produce high quality colloidal NCs, the size and size dispersion of these NCs needs to be controlled precisely. Growth time, temperature, and precursor concentrations are the key variables. Longer reaction times, in general, imply a larger average particle size. Injection and growth temperatures have a huge impact on the final size of the NCs. Lower injection temperatures lead to a smaller number of nuclei and thus yield larger-sized particles with similar precursor concentrations. When one has sufficiently high precursor concentrations in the reaction solution, higher growth temperatures generate larger particles after the same period of growth compared to lower growth temperatures due to enhanced reaction rates.

Precursor and surfactant concentrations play a pivotal role in both nucleation and growth. Analogous to higher injection temperatures, a high precursor concentration leads to a large number of nuclei while lower precursor concentrations imply fewer nuclei. The final particle size would depend on the interplay between the precursors consumed during nucleation and the amount left for growth. Surfactants can have an adverse effect on the growth of the NCs. A higher concentration of surfactants implies lower growth rates and hence smaller NCs with similar growth times. On one hand, if the surfactant binds too strongly to the NC, it will hinder NC growth while a very weakly coordinating surfactant

can lead to uncontrolled growth resulting in agglomerates which cannot be dispersed in solvents.[23]

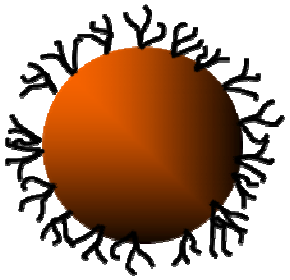

Figure 2.2: Cartoon showing the ligands surrounding a colloidal nanocrystal.

Alkylphosphines (tri-octylphosphine, diphenylphosphine, tri-butylphosphine), alkylphosphine oxides (tri-octylphosphine oxide), alkylamines (hexadecylamine, octadecylyamine, oleyl amine), alkylthiols (dodecanethiol), alkylphosphonic acids (dodecylphosphonic acid) and fatty acids (oleic acid) are typical examples of surfactants or coordinating solvents used during high temperature NC syntheses. They contain a lyophilic polar head group which is attached to the surface atoms of the nanocrystal, and a lyophobic tail which is exposed. These surfactant molecules, thus, act as *ligands* and form an organic capping shell around the NC core (Figure 2.2). The lyophobic tail renders the NCs soluble in common nonpolar solvents like hexane, octane, chloroform, toluene, carbon tetrachloride. The ligands also help to prevent aggregation of individual NCs by keeping them apart. Finally, the ligands can reversibly attach or detach from the NC surface which explains the fact that the NC nuclei can grow even when ligands are present in solution during growth. Also this permits ligand exchanges post synthesis by exposure of the NC to an excess of a different desired surfactant.[12] Moreover, these ligands serve to passivate the surface trap sites which result due to uncoordinated or dangling bonds from the surface atoms.[24] Hence, NCs with well passivated surfaces and high crystallinity exhibit high photoluminescence (PL) yields, *i.e.* higher quantum efficiencies.[25,26] Crystallinity is important because defects in the crystal can scatter phonons and/or photons. However, the ligand shell lends an insulating potential barrier to charge transport between NCs, and thus, has an adverse effect on electrical properties.[27]

Reduction, reverse-micelle, and high-temperature injection are the three most prominent chemical methods employed for NC syntheses. The first two techniques are simpler and use less toxic reagents. The advantages of high temperature injection are that it produces nearly monodisperse particles with fewer trap states, and they form stable dispersions. Even though the high temperature route is more difficult, the higher-quality material which it yields is better for fundamental studies. Since many nanoparticle properties are size dependent, polydisperse samples make characterization difficult. Polydisperse samples usually show broadened peaks in their spectra, so it is hard to pinpoint the energy of a particular transition. Therefore, it is desirable to study nearly monodisperse samples. The high-temperature synthesis method pioneered by Murray *et al.* produces a low polydispersity by separating nucleation from growth. In general, the low temperature methods suffer from relatively poor size dispersions ($\sigma > 20\%$) and often exhibit significant, if not exclusively, trap-state PL. The latter is inherently weak and broad compared to band-edge PL, and it is less sensitive to quantum-size effects and particle-size control. The high-temperature technique relies on surfactant ligands to transport atoms to the correct location in the crystal, so that the NC surface is coated with a layer of stabilizing ligands. In reduction-based syntheses, since ligands are added after the crystal is grown, it becomes much harder to attach these ligands; hence resulting in more trap states.[28] Moreover, high-temperature injection provides the atoms plenty of thermal energy to move around and find the best location in the crystal, thus resulting in fewer defects. NCs prepared by the low-temperature routes do not have the energy to find the most thermodynamically favorable bonding, resulting in poor crystallinity.

Any potential application or study involving NCs calls for stable NC dispersions. If NCs continue to grow and/or ripen after synthesis, all measurements must be taken immediately after synthesis to have a consistent set of data. Any industrial application such as printing or ink-jetting requires stable dispersions. This is another area where the high-temperature injection methods are preferable to the incomplete surface ligand coverage (which leads to unstable dispersions) of alcohol-based syntheses (reduction-based).

Further, low-temperature aqueous preparations (reverse-micelle) are limited in their applicability to mostly ionic NCs. In general, higher temperatures are required to synthesize covalent NCs and have them crystalline as well. Thus, II–VI compounds, which are more ionic compared to III–V compounds, have been successfully prepared at relatively low temperatures, whereas III–V compound SCs have not.[29] For all the reasons mentioned, the high-temperature synthetic method provides the best route to small quantities of high quality material for study.

2.4 SEMICONDUCTORS AND DOPING

The ability to introduce precise amounts of impurity atoms (dopants), to control the behavior of SC materials, is central to the SC industry. Without these impurities, negligible charge transport occurs through the SC crystals. To enhance this transport and render the materials benign for applications in devices, the concept of "doping" was developed. It involves controlled addition of impurity atoms to obtain desired conductivity in a given device.

While conductors will always show high electrical conductivities, insulators will always possess low conductivities. The ability to manipulate the conductivity of the material by tuning the level of doping with additional donor or acceptor atoms distinguishes SCs from both conductors and insulators. Modern SC technology thrives due to the ability to exert precise control over the number of carriers (electrons and holes) available in the SC crystal. By controlling the carriers, the electrical properties of the SC can be precisely tailored for a particular application. However, this adaptability of doped SCs to various applications comes at a price. Since minute concentration of dopants have a huge effect on their electronic properties, inevitably, one runs into the risk of unintentional doping of these SCs. Thus, these SC materials need to handled with utmost care to prevent any contamination. Apart from their electrical properties, since SCs possess a finite band gap, they can also be used to absorb and emit light efficiently. However, the band gap is fixed and depends on the identity of the material. Thus,

applications that require light at certain fixed wavelengths demand materials with matching optical properties. Thus, new materials need to be synthesized to exploit the potential of SCs for optical applications. This is where SC NCs can aid with their unique size tunable properties.

2.5 DOPING SEMICONDUCTOR NANOCRYSTALS

In light of the importance of doping in bulk SCs, it is interesting to consider their potential impact on SC NCs. NCs differ significantly from their bulk counterparts, since they possess a different band structure. Also, their carriers behave differently due to quantum confinement. Recently, concentrated efforts have started to explore the possibility of combining quantum confinement with the introduction of extra carriers by doping, to obtain a completely novel set of properties in these materials. Intrinsic SCs need to be doped to modify their charge transport characteristics. Doping of nanocrystals (NCs) can be used for entirely different reasons as well. SC NCs can be doped with a low percent of foreign atoms to create impurity centers that interact with the electrons and holes. A valuable effect of this interaction is that the mid gap states arising from surface species can be shifted outside the gap region. Dopants (when added in trace amounts) do not affect the absorption spectra; however, the intensity of emission is vastly increased. Doping enhances the properties of NCs by providing another means to control and subsequently tailor their remarkable electronic, optical, transport, and magnetic properties. In this sense, the development of doped nanocrystalline materials is progressing along the same lines as bulk SCs did half a century ago.

In general, dopants have been incorporated into nanocrystals for three main applications: to act as luminescence activators, to create improved dilute magnetic semiconductors, and to alter the electronic properties of NCs. Electronic dopants are those that introduce carriers by acting as either shallow donors or acceptors within the SC band structure. Typically, donor atoms are substitutional impurities with one more valence electron than the host atoms they replace. They can be ionized by thermal energy

and provide additional electrons in the conduction band, which help in charge transport ("n-type" doping since we have extra electrons). In the same way, acceptor atoms incorporated into a SC crystal create holes (missing electrons) in the valence band which aid charge transport by acting as positively charged particles (thus "p-type doping). The promise of NCs, as a technological material for applications which often require thin conducting films, depends in many cases on the ability to introduce these carriers. Although electronic doping of NCs has not yet been widely explored, it is clear that this area will play a major role in the future of nanotechnology as self-assembled device structures become more accessible.

High absorption coefficients, high quantum yields and narrow line widths make NCs exciting candidates for optical applications like bio-imaging applications.[30] Manipulation of the luminescent properties of NCs, by doping with impurities, has the potential to broaden the range of spectroscopic properties that can be achieved currently from these materials. Lasers based on NC emission are intrinsically inefficient.[14] Introducing dopants, which provide carriers, might help to achieve higher mobility in colloidal quantum dot films and higher injection currents. A threefold reduction in the lasing threshold in CdSe nanocrystals is observed by eliminating induced absorption through addition of extra electrons.[31] In solar cells, unwanted reactions and photooxidation might occur on the nanocrystal surface due to protracted exposure. This can be avoided by adding dopants which can absorb the energy from adsorbed photons thus localizing the excitation.[30]

Giant Zeeman effects observed in SCs containing magnetic impurities or ''diluted magnetic semiconductors'' (DMSs)[32,33] sparked a huge interest in these materials. DMSs hold the potential to pave the way for applications in optical gating[34] and future spintronic and spin-based electronic devices.[32,33]

2.6 CHALLENGES IN DOPING

Difficulties in doping wide band gap II–VI SCs (ZnTe, ZnSe) were encountered as early as the 1950's. These SCs, unlike group IV SCs (Si, Ge) exhibited a strong proclivity for only one type of doping - either p-type or n-type - which restricted their use in practical applications such as light-emitting diodes and lasers. CdSe, CdS, ZnSe and ZnS were resistant to p-type doping, whereas ZnTe could be doped p- but not n-type. Although dopants would not be expected to behave exactly the same way in SC NCs as they do in bulk SCs, basic complexities (like deep defect levels scavenging the charge carriers provided by dopants, donor-acceptor compensation *etc.*) encountered while doping bulk SCs are inherent to doping at the nanoscale too. In addition to these issues, challenges which are specific to nanoparticles are discussed below.

2.6.1 Host Material

New challenges arise when nanoscale materials are doped with small quantities of impurities. The high surface/volume ratios of NCs and the inherent statistical inhomogeneities of any ensemble of doped NCs play a key role in determining the dopant behavior. A 5-nm diameter CdSe NC would consist of around 2400 atoms, ~30% of which are on the surface, where they are exposed to surface ligands and/or solvent.[35] Assuming a Poissonian distribution, a mean concentration of 1 dopant per 1000 atoms is necessary to ensure almost every NC is doped. Comparing this doping level to heavily doped bulk SCs, which might have 1 dopant atom per 10,000 atoms; one concludes that dopant concentrations must be inherently much higher in NCs than in the bulk.

The number of dopants at the NC surfaces comprises a large percentage of the total dopant population. Dopants, substituting for host ions at the surface sites, may differ considerably from those in the NC cores in terms of their geometries, electronic structures, redox potentials, and interactions with the SC.[35] Since surface-exposed dopants and those within the NC core (Figure 2.3a) can show starkly different behavior, this may obscure the origin of the physical properties of doped NCs, and even compromise some of the target physical properties of the doped material. Two diverse

approaches have been employed to remove dopants from the NC surface. The first technique uses coordinating solvents or ligands, such as pyridine or tri-octylphosphine oxide, as surface cleaning agents.[36-38] The second method, demonstrated to eliminate surface-exposed dopants successfully, is the isocrystalline core–shell (ICS) procedure.[36,38] This procedure involves purifying the as-synthesized NCs to remove excess dopants from the growth solution, followed by epitaxial growth of additional layers of the pure host material to coat the surface-exposed dopants and encapsulate them.

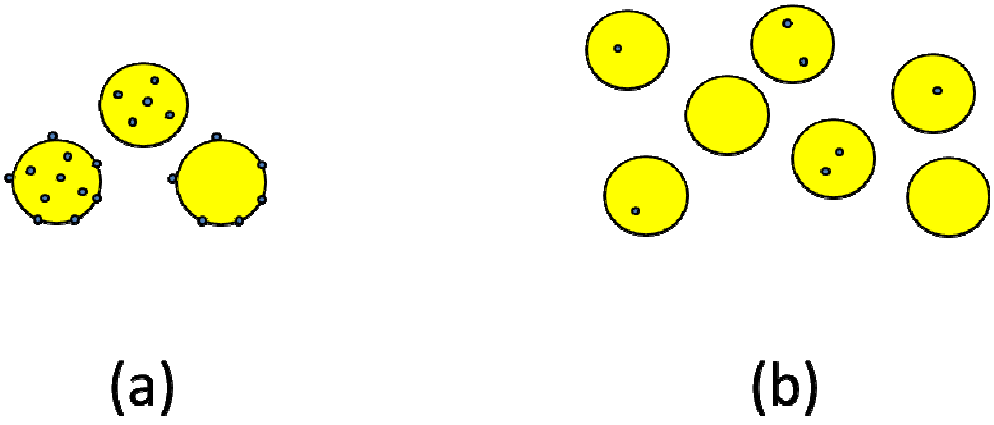

Figure 2.3: (a) Cartoon showing the inhomogeneity in location of dopants in a sample of doped NCs. (b) Cartoon depicting the stochastic fluctuations in dopant distributions within a sample of doped NCs.

In addition to inhomogeneities introduced in doped NCs due to surface-exposed dopants and those inside the NC core, any sample of doped NCs will also exhibit a statistical distribution of dopant populations per NC (Figure 2.3b). While the dopant concentration may be well defined on average, the number of dopants in any individual NC cannot be controlled or determined. A NC with a single dopant might show significantly different behavior than one with two or more dopants. Due to this heterogeneous distribution of dopants in any NC sample, it becomes complicated to draw conclusions from subsequent physical measurements. This feature could significantly impact single quantum dot electronics or photonics measurements that rely on doped NCs. While purification to ensure size uniformity is possible (size-selective

precipitation), no purification method has yet been developed for ensuring uniform dopant concentrations in an ensemble of NCs.

2.6.2 Impurity Atom and Characterization of Doped Nanocrystals

Another category of challenges concerns the impurities themselves and how one knows when the NCs have been doped successfully. X-ray diffraction studies of doped crystals yield predominantly the characteristic diffraction features of the host, and provide little reliable indication of the success or failure of doping (except at extremely high doping). NC doping suffers from the intrinsic problem that only an extremely small fraction of the product is the impurity, and consequently a doped NC is virtually indistinguishable from its pure analogue by microscopy techniques, such as scanning electron microscopy (SEM) and transmission electron microscopy (TEM). Hence these systems are more challenging to probe experimentally.

Solving this problem requires using other analytical techniques. Spectroscopic methods that are sensitive to some physical property inherent to the dopants themselves can prove to be extremely successful. For instance, if they absorb light within the forbidden gap of the SC, then absorption spectroscopy may be applied to probe the dopants selectively. The existence of a manganese (Mn) luminescence peak has been reported in Mn-doped ZnS[39] and ZnSe.[40] Optical absorption spectroscopy has been used to verify cobalt (Co) doping in CdS and ZnS NCs.[32,41] If the dopant is magnetic, then magnetic spectroscopic techniques may be applied to probe them selectively within the diamagnetic hosts. Unusual phenomena, such as giant Zeeman splittings, observed in the case of Mn-doped NCs by magnetic circular dichroism (MCD) studies, can be used as an effective tool to verify Mn doping (*e.g.* CdS).[42]

Another challenge in the synthesis of doped NCs is to ensure that the impurity is in the NC core, rather than at the surface or the interface. Impurities on the surface are always plausible, since the NC is only a few lattice constants in size. Very few analytical techniques possess the ability to distinguish impurities on the surface from those inside the core of the NC. Spectrum changes, in an electron paramagnetic resonance (EPR)

study, can reveal whether Mn is incorporated or surface-bound. EPR spectroscopy has been the primary tool to confirm Mn doping in ZnS,[43] CdS[44] and ZnSe.[33,42] Mikulec *et al*. studied the distribution of dopants in NCs.[36] They synthesized Mn-doped CdSe NCs. EPR spectroscopy revealed a four-fold decrease in Mn concentration, when the NC surface was cleaned with pyridine, which implies that most of the Mn was on the surface, rather than in the core. After the ligand exchange with pyridine and trioctylphosphine oxide, they gradually etched away the NCs with tripyrrolidinophosphine oxide. They observed a decrease from 2.9 Mn / NC on an average to 0.5 Mn / NC, when the NC was etched from 4.0 nm to 3.3 nm in diameter. This proves that dopant molecules do not always distribute uniformly throughout the NC.

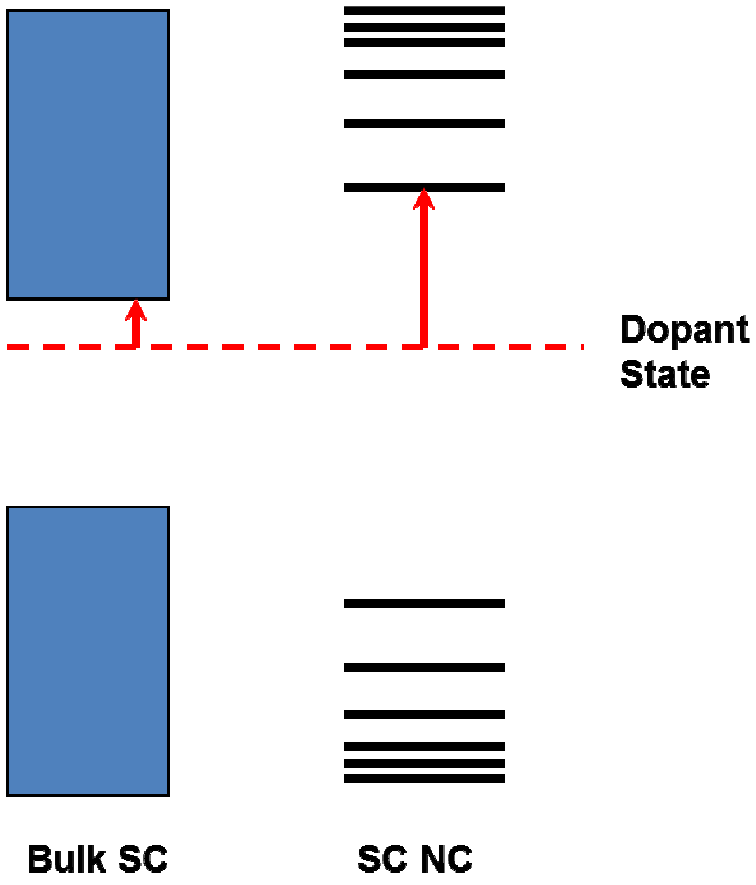

Figure 2.4: Schematic describing how a shallow dopant level in a bulk SC could potentially turn into a deep defect level in the corresponding SC NC.

2.6.3 Quantum Confinement

Addition of extra charge carriers in bulk SCs is generally achieved by substitution of a host atom with a dopant atom. In bulk, this electronic impurity atom introduces a shallow dopant state which lies within a few tens of meVs of the corresponding band edge (valence band for p-type and conduction band for n-type doping) thus facilitating thermalization into the band even at room temperature. Now the incorporation of this dopant atom in the corresponding NC of the same material does not necessarily guarantee stable electronic doping. Due to quantum confinement, this favorable alignment of the dopant state and the bulk band edge can be entirely distorted for the doped NC case (Figure 2.4).

Two situations can potentially arise in such a situation. Firstly, the depth of the dopant state can increase due to increase in band gap of the NC as a direct result of quantum confinement. Hence the probability to thermalize a free charge carrier drops down drastically. Secondly, when the hydrogenic Bohr radius of the charge carrier in the NC becomes comparable to the size of the NC, the dopant starts to feel the effect of the confinement and shifts to higher energies. These two effects compete against one another. If the dopant state shifts into the band states of the NC, the dopant would undergo auto ionization and provide charge carriers to the NC. The interplay of all these effects complicates electronic doping in SC NCs.

2.6.4 Instability of Electronically Doped Nanocrystals

The stability of excited state carriers also needs to be taken into account when doping NCs. These carriers have relatively high energies and NCs have much more surface area as compared to bulk crystals, at which reactions may occur. These reactions might scavenge the carriers, which would make them unavailable for conduction.

It has been shown that CdSe and CdS NCs produce free radicals from the surrounding solution when they are exposed to UV light.[45] Ipe *et al.* noted that CdS NCs produced both superoxide (O^{2-}) and hydroxide (OH•) radicals, while CdSe NCs only produced the lower energy hydroxide radicals. Shim and Guyot-Sionnest observed that

chemically reduced CdSe and ZnO NCs showed peaks correlated with conduction band electrons which disappeared in the presence of oxygen.[46,47] These results imply that n-type NCs, with an extra electron, behave like reducing agents. Extending this idea to p-type NCs, they would behave as strong oxidizing agents with an excess of holes. To avoid surface redox reactions and confine the carriers within the NC, one might coat the doped NC core with a shell of a wide band gap SC material. However, this would lead to a huge potential barrier which would hinder the transport of the carriers and ultimately result in low conductivity.

2.7 NANOCRYSTAL DOPING MODELS

A number of models, which try to explain the mechanism of doping in SC NCs, have been proposed. Some of them are discussed in this section.

2.7.1 Turnbull Model

Turnbull argued that, for uniform constant defect density, small crystals are statistically less likely to contain defects than large crystals and hence they tend to be pure.[48] This model assumes that dopant solubility in the NC is the same as in bulk. Therefore if an impurity is highly soluble in the bulk, it should still exist in fairly small NCs. This is contrary to what is actually observed; particularly in the case of Mn doping in II-VI SCs. Mn concentrations in II-VI SC NCs such as ZnSe are 1-2 orders of magnitude lower than in their bulk counterparts.

2.7.2 Self-Purification Model

This model, proposed by Dalpian and Chelikowsky, takes into account the thermodynamics of the system to understand the incorporation of dopants in NCs.[49] They consider the case of thermodynamic equilibrium and examine the formation energies of impurities as the NC gets smaller. They observe that, as the NC size decreases, the formation energy increases. This suggests that it will cost more energy to insert impurities into small NCs than the larger ones, *i.e.* the impurity will be less stable in the

small NCs. Hence, the impurities can be easily annealed out owing to the material's limited size since the distance the impurity must move, to be ejected from the NC, is much smaller than in bulk materials. In the limit of large NCs, the formation energy will approach, asymptotically, the value for bulk. According to Dalpian *et al.*, this provides clear evidence that doping NCs should be more difficult than doping bulk materials. However, a significant assumption in this model is thermodynamic equilibrium, which implies that impurity atoms can readily diffuse in and out of the NC. But in the case of Mn, the bulk diffusion coefficient at typical colloidal growth temperatures of around 300 ^{o}C is negligible.[50] Therefore, the assumption of thermodynamic equilibrium, on which the model is based, is difficult to justify. Furthermore, Du e*t al.* showed that the increase in impurity formation energy with decreasing size of CdSe NCs is fairly small (~0.03 eV) and hence, almost independent of size.[51]

2.7.3 Trapped Dopant Model

Du *et al.*[52] suggested that non-equilibrium kinetic effects, such as activation barriers for substitutional impurities, will control doping at the low temperatures commonly used in liquid-phase colloidal syntheses. They argue that, since diffusion of the impurity through the NC is strongly inhibited, doping depends on the surface adsorption of the impurity during growth. If the dopant atom binds strongly to the surface, it can be subsequently "trapped" when overgrown by additional material. If a dopant molecule adheres to the crystal long enough to be overgrown, it will be incorporated into the NC. Impurity adsorption, in turn, depends strongly on the surface morphology, the shape of the NC, and surfactants in the growth solution. In a previous paper, Erwin *et al.*[50] explained Mn doping in II-VI SC NCs, based on these factors, which earlier were not considered significant to the doping mechanism. They argued that successful doping in NCs depends on the "stickiness" of the crystal facets. They noted that all SC NCs that had been successfully doped with Mn adopt the zinc-blende crystal structure. Density-functional theory (DFT) computations suggest that the (001) facets of zinc-blende structure crystals provide stable binding sites for Mn. These facets consist solely of anions and therefore strongly attract cationic dopants. They, then, proceeded to grow Mn-doped CdSe around ZnSe cores. The ZnSe core (which commonly exists in the

zinc blende structure) topotaxially forced the CdSe [which commonly exists in the wurtzite structure and hence lacks (001) facets] into a zinc-blende crystal structure, and Mn was successfully incorporated throughout the shell. Previous attempts to dope wurtzite CdSe nanoparticles with Mn had failed. Their model establishes the importance of kinetics in NC doping.

2.8 DOPING SUCCESSES

The most studied systems have been Mn-doped colloidal QDs of ZnS,[39,53,54] CdS,[55-57] and ZnSe.[40,58] Early efforts to dope Mn into CdSe, the most-studied NC system, failed to incorporate any impurities[36] but Erwin *et al.* were successful in doping this system with Mn.[50] Gamelin and co-workers have been successful in doping CdSe with Co and ZnO with Mn and Co.[35,37]

The problem with Mn and Co doping in all of these II-VI SCs is that they are isovalent with the cation. Thus, no extra carriers are obtained and no net electronic effect can be observed. Recent efforts aim at achieving electronic doping of NCs. Knox *et al.* tried to dope CdSe NCs with indium (In^{3+}) but succeeded only in coating the surface with indium that could easily be removed by pyridine exchange.[59] Colloidal Mn-doped InAs[60] and Li-doped ZnO[61] have also been synthesized. By co-doping aluminium (Al) and copper (Cu) into ZnS NCs, Manzoor *et al.* reported a new luminescence peak, which they ascribe to an Al^{3+} - Cu^{+} transition.[62,63] However, the resulting NCs would show unaltered electronic properties since their method is based on stoichiometric inclusion of n-type and p-type dopants.

More recently, Cd-doped InAs NCs showed changes in their electronic behavior. However, these dopants were most likely coating the surface.[63] Viswanatha and co-workers managed to incorporate Cu dopants into ZnSe/CdSe core-shell NCs but the Cu dopant existed primarily as Cu^{2+} as proven by optical spectroscopy studies and hence was isovalent with the host atom replaced.[64,65] Using a "*core-shell doping*" approach, Wills *et*

al. were able to dope In and Al into CdSe NCs, with the Al-doped NCs showing n-type doping.[66] Recent progress has been made by incorporating rapidly diffusing electronically active dopant atoms [Cu, silver (Ag) and gold (Au)] in InAs,[67] CdSe[68] and PbSe NCs (Chapter 5 of this thesis). Ag-doping in CdSe and PbSe NCs will be discussed further in Chapters 3-5.

An alternative approach to control the number of carriers (electrons and holes) in SC NCs is through *charging* which involves the use of applied electric fields to manipulate carrier densities near an interface or junction.[69]

2.9 CHARGING NANOCRYSTALS

The conventional approach of obtaining n- and p-type NCs, by doping with a heterovalent impurity, such as In in bulk CdSe, has not been successful in colloidal quantum dots (QDs) to date, possibly because of difficulties in introducing the impurity, or in eliminating surface traps that can capture the extra carrier. An alternative approach involves obtaining n- and p-type NCs, by direct injection of charge carriers into undoped NCs. For example, oxidizing or reducing agents, gates, or electrochemical processes can be used.[70] This method is also referred to as *remote doping*.[71]

Colloidal QDs can be charged n-type by electron-transfer from a strongly reducing species (e.g., sodium and sodium biphenyl).[46] However, for such charge transfer to occur, the lowest unoccupied electronic state of the NC, the $1S_e$ state, should be below the reduction potential of the reducing species. Optical measurements confirm the *n*-type character of such NCs. Upon reduction, if the extra electron occupies the $1S_e$ state, then the exciton transitions that involve this state should be bleached. Shim *et al.* observe this bleach in the absorption spectra of CdSe/ZnS core-shell colloidal QDs after charge-transfer doping.[72] However, trap states or other phenomena could produce a similar bleach. Conclusive evidence of the n-type character is obtained from the appearance of a

new intraband peak in the IR spectrum of the NCs, which can be ascribed to a transition from the $1S_e$ to the $1P_e$ state.

These n-type NCs are stable indefinitely at low temperatures, but they lose their n-type character under ambient conditions due to oxidation. Close-packed films of NCs were more permanently doped n-type, by the evaporation of potassium, in a high vacuum chamber.[73] However, a more practical approach involves electrochemical doping of colloidal QDs, in which a thin film of NCs is put in contact with a metal electrode in an electrochemical cell.[74] By controlling the potential to the cell, electrons could be reversibly injected into the colloidal QD, as confirmed by changes in visible and IR spectra.

However, in the remote doping experiments, many traps need to be filled by the injected electrons, before the $1S_e$ level can be occupied. The number of these unknown traps could not be quantified. This has a serious implication for n-type impurity doping, since these traps might consume all the electrons donated by the dopants. Therefore, even if successful n-type doping is achieved, one might still not have any free carriers in the doped NCs.

2.10 STABILITY TRENDS IN DOPED/CHARGED NANOCRYSALS

In the remote doping experiments conducted by Shim and Guyot-Sionnest, they observed that the lifetime of injected electrons decreased from ZnO to CdSe to ZnSe.[46] N-type doping of ZnO with Li impurities has also been achieved.[61] This suggests that ZnO is somehow amenable to n-type doping while ZnSe is not. A simple approach to determine which systems can be doped n-type was proposed by Guyot-Sionnest *et al*. They explained this behavior by looking at the reduction potential of the NCs and of their constituent elements.[73,75,76] An extra electron in the bulk crystal sits at the bottom of the conduction band. They noted that the conduction band electron stability in the NCs was inversely proportional to the energy of the conduction band minimum. This energy

increases from ZnO to CdSe to ZnSe; and from larger to smaller NCs. Accordingly, smaller n-type NCs, with a larger degree of confinement, were also observed to be less stable. Since they carried out their experiments in oxidant-free conditions, they hypothesized that redox reactions might be occurring within the NC. N-type ZnSe NCs may be less stable, because the reduction potential of Zn^{2+}/Zn [-0.762 V versus Standard Hydrogen Electrode (SHE)] is below the conduction band minimum of ZnSe (-1.5 V versus SHE).[71] Therefore, it is energetically favorable for conduction band electrons to undergo the electrochemical reaction and reduce Zn^{2+} to form Zn atoms, which can then break apart from the crystal by corrosion, if other factors such as lattice binding energies are ignored. On the other hand, ZnO, with a conduction band minimum far below the reduction potential of Zn, is expected to be more stable, if auto-corrosion were the cause of instability. Similarly, in the bulk, an extra hole will sit at the top of the valence band. In a NC, the hole will be pushed lower in energy by confinement. The lower the hole, the more likely that the hole might become less stable compared to the competing electrochemical reactions.

Despite the simplistic nature, the predictions from this theory correlate roughly with results to date in bulk as well as NC doping of II-VI SCs. However, this data excludes many factors such as crystal binding energies. The reduction potentials are for aqueous conditions, while colloidal NCs are generally dispersed in organic solvents. Details such as the surroundings of NCs and kinetic barriers to reactions have not been taken into account. Bulk band gap values are used,[77] except for PbSe, which is estimated from NC results[76] and includes some confinement. This theory thus represents a lower bound for stability. It seems that the limited amount of data on band offsets in NCs matches this theory, but the theory fails for several cases in the bulk. In the bulk, all II-VI SCs except ZnTe can be doped n-type.[78] The theory predicts that ZnTe should be very unstable when doped n-type, but so should ZnS, which, however, can be doped n-type. Similarly, ZnTe and CdTe can be doped p-type in the bulk, which agrees with the theory, but so can ZnSe, which should be unstable following this hypothesis.[78,79] This theory may, however, give a qualitative explanation, and a general guide to select appropriate SCs for obtaining stable carriers.

2.11 REFERENCES

(1) Barber, D. J.; Freestone, I. C. *Archaeometry* **1990**, *32*, 33.

(2) JoseYacaman, M.; Rendon, L.; Arenas, J.; Puche, M. C. S. *Science* **1996**, *273*, 223.

(3) Faraday, M. *Philosophical Transactions of the Royal Society of London* **1857**, *147*, 145.

(4) Einstein, A. *Annalen Der Physik* **1905**, *17*, 549.

(5) Gans, R. *Annalen Der Physik* **1912**, *37*, 881.

(6) Gans, R. *Annalen Der Physik* **1915**, *47*, 270.

(7) Mie, G. *Annalen Der Physik* **1908**, *25*, 377.

(8) Ostwald, W. *Die Welt Der Vernachlässigten Dimensionen*; Steinkopff: Dresden & Leipzig, 1915.

(9) Drexler, K. E. *Nanosystems: Molecular Machinery, Manufacturing, and Computation*; Wiley: New York, 1992.

(10) Ekimov, A. I.; Efros, A. L.; Onushchenko, A. A. *Solid State Communications* **1985**, *56*, 921.

(11) Brus, L. E. *Journal of Chemical Physics* **1984**, *80*, 4403.

(12) Murray, C. B.; Kagan, C. R.; Bawendi, M. G. *Annual Review of Materials Science* **2000**, *30*, 545.

(13) Guyot-Sionnest, P.; Wehrenberg, B.; Yu, D. *Journal of Chemical Physics* **2005**, *123*, 074709.

(14) Klimov, V. I.; Ivanov, S. A.; Nanda, J.; Achermann, M.; Bezel, I.; McGuire, J. A.; Piryatinski, A. *Nature* **2007**, *447*, 441.

(15) Klimov, V. I. *Semiconductor and Metal Nanocrystals: Synthesis and Electronic and Optical Properties*; Marcel Dekker, Inc.: New York, 2004.

(16) Swihart, M. T. *Current Opinion in Colloid & Interface Science* **2003**, *8*, 127.

(17) Yoffe, A. D. *Advances in Physics* **2001**, *50*, 1.

(18) Bimberg, D.; Grundmann, M.; Ledentsov, N. N. *MRS Bulletin* **1998**, *23*, 31.

(19) Petroff, P. M.; MedeirosRibeiro, G. *MRS Bulletin* **1996**, *21*, 50.

(20) Hu, J. T.; Odom, T. W.; Lieber, C. M. *Accounts of Chemical Research* **1999**, *32*, 435.

(21) Lauhon, L. J.; Gudiksen, M. S.; Wang, C. L.; Lieber, C. M. *Nature* **2002**, *420*, 57.

(22) Lamer, V. K.; Dinegar, R. H. *Journal of the American Chemical Society* **1950**, *72*, 4847.

(23) Murray, C. B.; Sun, S. H.; Gaschler, W.; Doyle, H.; Betley, T. A.; Kagan, C. R. *IBM Journal of Research and Development* **2001**, *45*, 47.

(24) Huang, X. Y.; Lindgren, E.; Chelikowsky, J. R. *Physical Review B* **2005**, *71*.

(25) Munro, A. M.; Jen-La Plante, I.; Ng, M. S.; Ginger, D. S. *Journal of Physical Chemistry C* **2007**, *111*, 6220.

(26) Zeng, J.; Lu, W.; Wang, X.; Wang, B.; Wang, G.; Hou, J. G. *Journal of Colloid and Interface Science* **2006**, *298*, 685.

(27) Morgan, N. Y.; Leatherdale, C. A.; Drndic, M.; Jarosz, M. V.; Kastner, M. A.; Bawendi, M. *Physical Review B* **2002**, *66*.

(28) Wang, Y. S.; Thomas, P. J.; O'Brien, P. *Journal of Physical Chemistry B* **2006**, *110*, 4099.

(29) Kershaw, S. V.; Harrison, M.; Rogach, A. L.; Kornowski, A. *IEEE Journal of Selected Topics in Quantum Electronics* **2000**, *6*, 534.

(30) Pradhan, N.; Goorskey, D.; Thessing, J.; Peng, X. G. *Journal of the American Chemical Society* **2005**, *127*, 17586.

(31) Wang, C. J.; Wehrenberg, B. L.; Woo, C. Y.; Guyot-Sionnest, P. *Journal of Physical Chemistry B* **2004**, *108*, 9027.

(32) Furdyna, J. K. *Journal of Applied Physics* **1988**, *64*, R29.

(33) Furdyna, J. K.; Kossut, J. *Semiconductors and semimetals. Volume 25, Diluted magnetic semiconductors*; Academic Press: Boston, 1988.

(34) Sugano, S.; Kojima, N. *Magneto-Optics*; Springer: Berlin; New York, 2000.

(35) Bryan, J. D.; Gamelin, D. R. Doped Semiconductor Nanocrystals: Synthesis, Characterization, Physical Properties, and Applications. In *Progress in Inorganic Chemistry, Vol 54*, 2005; Vol. 54; pp 47.

(36) Mikulec, F. V.; Kuno, M.; Bennati, M.; Hall, D. A.; Griffin, R. G.; Bawendi, M. G. *Journal of the American Chemical Society* **2000**, *122*, 2532.

(37) Radovanovic, P. V.; Gamelin, D. R. *Journal of the American Chemical Society* **2001**, *123*, 12207.

(38) Radovanovic, P. V.; Gamelin, D. R. Isocrystalline Core/Shell Synthesis of High Quality II-VI Diluted Magnetic Semiconductor Quantum Dots: Ligand-Field Spectroscopic Studies. In *Physical Chemistry of Interfaces and Nanomaterials*, 2002; Vol. 4807; pp 223.

(39) Bhargava, R. N.; Gallagher, D.; Hong, X.; Nurmikko, A. *Physical Review Letters* **1994**, *72*, 416.

(40) Norris, D. J.; Yao, N.; Charnock, F. T.; Kennedy, T. A. *Nano Letters* **2001**, *1*, 3.

(41) Chan, W. C. W.; Nie, S. M. *Science* **1998**, *281*, 2016.

(42) Coe, S.; Woo, W. K.; Bawendi, M.; Bulovic, V. *Nature* **2002**, *420*, 800.

(43) Colvin, V. L.; Schlamp, M. C.; Alivisatos, A. P. *Nature* **1994**, *370*, 354.

(44) Dabbousi, B. O.; Bawendi, M. G.; Onitsuka, O.; Rubner, M. F. *Applied Physics Letters* **1995**, *66*, 1316.

(45) Ipe, B. I.; Lehnig, M.; Niemeyer, C. M. *Small* **2005**, *1*, 706.

(46) Shim, M.; Guyot-Sionnest, P. *Nature* **2000**, *407*, 981.

(47) Shim, M.; Guyot-Sionnest, P. *Journal of the American Chemical Society* **2001**, *123*, 11651.

(48) Turnbull, D. *Journal of Applied Physics* **1950**, *21*, 1022.

(49) Dalpian, G. M.; Chelikowsky, J. R. *Physical Review Letters* **2006**, *96*.

(50) Erwin, S. C.; Zu, L. J.; Haftel, M. I.; Efros, A. L.; Kennedy, T. A.; Norris, D. J. *Nature* **2005**, *436*, 91.

(51) Du, M. H.; Erwin, S. C.; Efros, A. L.; Norris, D. J. *Physical Review Letters* **2008**, *100*, 179702.

(52) Du, M.-H.; Erwin, S. C.; Efros, A. L. *Nano Letters* **2008**, *8*, 2878.

(53) Sooklal, K.; Cullum, B. S.; Angel, S. M.; Murphy, C. J. *Journal of Physical Chemistry* **1996**, *100*, 4551.

(54) Wang, Y.; Herron, N.; Moller, K.; Bein, T. *Solid State Communications* **1991**, *77*, 33.

(55) Counio, G.; Esnouf, S.; Gacoin, T.; Boilot, J. P. *Journal of Physical Chemistry* **1996**, *100*, 20021.

(56) Hoffman, D. M.; Meyer, B. K.; Ekimov, A. I.; Merkulov, I. A.; Efros, A. L.; Rosen, M.; Couino, G.; Gacoin, T.; Boilot, J. P. *Solid State Communications* **2000**, *114*, 547.

(57) Levy, L.; Hochepied, J. F.; Pileni, M. P. *Journal of Physical Chemistry* **1996**, *100*, 18322.

(58) Suyver, J. F.; Wuister, S. F.; Kelly, J. J.; Meijerink, A. *Physical Chemistry Chemical Physics* **2000**, *2*, 5445.

(59) Knox, C. K.; Fillmore, S. D.; Call, D. M.; Allen, D. G.; Hess, B. C.; Davis, R. C.; Evenson, W. E.; Harrison, R. G. *Journal of Colloid and Interface Science* **2006**, *300*, 591.

(60) Stowell, C. A.; Wiacek, R. J.; Saunders, A. E.; Korgel, B. A. *Nano Letters* **2003**, *3*, 1441.

(61) Orlinskii, S. B.; Schmidt, J.; Baranov, P. G.; Hofmann, D. M.; Donega, C. D.; Meijerink, A. *Physical Review Letters* **2004**, *92*.

(62) Manzoor, K.; Vadera, S. R.; Kumar, N.; Kutty, T. R. N. *Materials Chemistry and Physics* **2003**, *82*, 718.

(63) Geyer, S. M.; Allen, P. M.; Chang, L. Y.; Wong, C. R.; Osedach, T. P.; Zhao, N.; Bulovic, V.; Bawendi, M. G. *ACS Nano*, *4*, 7373.

(64) Brovelli, S.; Galland, C.; Viswanatha, R.; Klimov, V. I. *Nano Letters* **2012**, *12*, 4372.

(65) Viswanatha, R.; Brovelli, S.; Pandey, A.; Crooker, S. A.; Klimov, V. I. *Nano Letters* **2012**, *11*, 4753.

(66) Wills, A. W.; Kang, M. S.; Wentz, K. M.; Hayes, S. E.; Sahu, A.; Gladfelter, W. L.; Norris, D. J. *Journal of Materials Chemistry* **2012**, *22*, 6335.

(67) Mocatta, D.; Cohen, G.; Schattner, J.; Millo, O.; Rabani, E.; Banin, U. *Science* **2011**, *332*, 77.

(68) Sahu, A.; Kang, M. S.; Kompch, A.; Notthoff, C.; Wills, A. W.; Deng, D.; Winterer, M.; Frisbie, C. D.; Norris, D. J. *Nano Letters* **2012**, *12*, 2587.

(69) Shim, M.; Wang, C. J.; Norris, D. J.; Guyot-Sionnest, P. *MRS Bulletin* **2001**, *26*, 1005.

(70) Chiang, C. K.; Druy, M. A.; Gau, S. C.; Heeger, A. J.; Louis, E. J.; Macdiarmid, A. G.; Park, Y. W.; Shirakawa, H. *Journal of the American Chemical Society* **1978**, *100*, 1013.

(71) Norris, D. J.; Efros, A. L.; Erwin, S. C. *Science* **2008**, *319*, 1776.

(72) Shim, M.; Wang, C. J.; Guyot-Sionnest, P. *Journal of Physical Chemistry B* **2001**, *105*, 2369.

(73) Yu, D.; Wang, C. J.; Guyot-Sionnest, P. *Science* **2003**, *300*, 1277.

(74) Yang, Y.; Chen, O.; Angerhofer, A.; Cao, Y. C. *Journal of the American Chemical Society* **2006**, *128*, 12428.

(75) Wang, C. J.; Shim, M.; Guyot-Sionnest, P. *Science* **2001**, *291*, 2390.

(76) Wehrenberg, B. L.; Guyot-Sionnest, P. *Journal of the American Chemical Society* **2003**, *125*, 7806.

(77) Van de Walle, C. G.; Neugebauer, J. *Nature* **2003**, *423*, 626.

(78) Dow, J. D.; Hong, R. D.; Klemm, S.; Ren, S. Y.; Tsai, M. H.; Sankey, O. F.; Kasowski, R. V. *Physical Review B* **1991**, *43*, 4396.

(79) Chadi, D. J. *Annual Review of Materials Science* **1994**, *24*, 45.

CHAPTER 3

SILVER DOPING IN CdSe NANOCRYSTALS*

3.1 OVERVIEW

We dope CdSe nanocrystals with Ag impurities and investigate their optical and electrical properties. Doping leads not only to dramatic changes but surprising complexity. The addition of just a few Ag atoms per nanocrystal causes a large enhancement in the fluorescence, reaching efficiencies comparable to core-shell nanocrystals. While Ag was expected to be a substitutional acceptor, non-monotonic trends in the fluorescence and Fermi level suggest that Ag changes from an interstitial (*n*-type) to a substitutional (*p*-type) impurity with increased doping. In this chapter, we focus on the optical properties while the next chapter discusses the electrical properties of these Ag-doped CdSe nanocrystals.

3.2 INTRODUCTION

Electronic impurity doping is the process in which impurity atoms are intentionally added to bulk semiconductors to provide either extra electrons (*n*-type doping) or extra holes (*p*-type doping). The carriers then enable electrical transport through an otherwise poorly conducting material. Surprisingly, even after decades of research, little progress has been made on this process in colloidal quantum dots, also known as semiconductor nanocrystals.[1,2] These materials exhibit size-dependent optical spectra, which can be useful in solar cells[3] and solid-state-lighting.[4] For these applications, electrical current must be collected or injected from films of nanocrystals.

* This chapter is reproduced with permission from Ayaskanta Sahu, Moon Sung Kang, Alexander Kompch, Christian Notthoff, Andrew W. Wills, Donna Deng, Markus Winterer, C. Daniel Frisbie, and David J. Norris, "Electronic Impurity Doping in CdSe Nanocrystals," Nano Letters **2012**, 12 (5), 2587 (DOI: 10.1021/nl300880g).

Because the films are inherently insulating, the introduction of extra carriers is beneficial for enhancing conduction. For CdSe, the most studied nanocrystal system, several methods have provided the carriers, including placement of electron-donating molecules in the vicinity of the nanocrystal surface (remote doping)[5-7] and application of external electric fields (electrochemical doping).[6-9] When carriers were added, conductivity was dramatically increased.[6] In principle, it should also be possible to provide extra carriers to CdSe nanocrystals via impurity doping.

However, studies of electronic impurity doping in colloidal nanocrystals have been fairly limited.[10-24] Development has been impeded by the broader synthetic challenge of incorporating an impurity into a nanoscale particle.[25] While progress has been made with magnetic substitutional impurities in II-VI semiconductor nanocrystals,[2] these dopants (*e.g.*, Mn and Co) are isovalent with the cations that they replace, and no additional carriers are introduced. Recently, efforts have attempted to incorporate heterovalent impurities that can provide these carriers, most notably in InAs. In Cd-doped InAs, conductivity through films was clearly affected, but the impurities were likely coating the nanocrystal surfaces.[12] In Cu-, Ag-, and Au-doped samples, shifts in the valence and conduction bands were observed through scanning tunneling microscopy on individual nanocrystals, and a simple model assuming interstitial Cu and substitutional Ag and Au was proposed.[16] However, both InAs studies[12,16] focused on the heavily doped limit (tens to hundreds of dopants per nanocrystal). "Solotronic" behavior[26] arising from a solitary or a few electronic dopants has not been fully explored in colloidal nanocrystals. Furthermore, little work has addressed electronic impurity doping in the prototypical system, CdSe.[15,19,24]

Here, we analyze CdSe nanocrystals that are lightly doped with Ag. Herein, we use the phrase "light doping" to indicate that only a few impurities are added to each nanocrystal. We note that in the language of bulk semiconductors, where the number of impurities is quoted per unit volume, the concentration of the dopants is still high.[22] Of course, studying this limit where a small number of impurities are confined in a small volume provides an additional motivation to study their physical properties. In analyzing

the behavior of our materials, the results not only confirm electronic impurity doping in CdSe, but they also reveal unexpected complexity. The addition of even one impurity per nanocrystal causes a dramatic enhancement in the fluorescence efficiency. At slightly higher concentrations, a dopant-related fluorescence peak appears that dominates at cryogenic temperatures. In electrical measurements on films of Ag-doped CdSe nanocrystals (shown in Chapter 4), we observe non-monotonic shifts in the Fermi energy as a function of dopant concentration. We argue that all of these findings can be explained by an unexpected transition from *n*- to *p*-type doping for Ag with increasing impurity concentration.

A priori, one would expect Ag^{+} to be a substitutional impurity, replacing Cd^{2+} in the CdSe lattice. In that case, the dopant could provide an extra hole due to its deficiency in valence electrons. In other words, Ag should be an acceptor (*p*-type impurity). Indeed, in the previous report on Ag-doped InAs nanocrystals, all of the observed trends in the high-doping limit were rationalized by *p*-type doping due to the substitution of Ag^{+} for In^{3+} in the lattice.[16] Of course, as discussed further below, bulk studies have shown that impurity centers in semiconductors can be quite complex and it is difficult to predict whether Ag will be *p*- or *n*-type in either InAs or CdSe nanocrystals. Thus, experiments must be performed, particularly in nanocrystals where quantum confinement and surface effects can lead to new physics for the dopant.

3.3 CATION EXCHANGE AS A NOVEL APPROACH FOR DOPING

Ion exchange, via diffusion or exchange of atoms, has been demonstrated to be a facile and proficient way to create a variety of inorganic nanostructures starting from a parent nanostructure. Son *et al*.[27] have shown that the process, by which one type of cation (positively charged atoms) is exchanged for another, takes place at a much faster rate in NCs than in bulk crystals, and is fully reversible. This is virtually forbidden in micro-sized or bulk crystals under the same environmental conditions and such modifications, if they can be accomplished at all, are typically very slow and require very

high temperatures or pressures. However, fast kinetics and reversibility of the reaction in NCs are considered to be mainly due to the lower activation barrier for the diffusion of atoms in nanocrystalline solids compared to the bulk phase.

Son *et al.* studied these reactions by mixing colloidal CdSe NCs, dispersed in toluene, with a small amount of methanol (1% by volume) and a slight excess of silver nitrate (by moles) at room temperature. In less than one second, the silver cations reacted with the CdSe NCs to produce NCs of silver-selenide (Ag_2Se). This can be explained by the strongly favorable thermodynamic driving force for the forward reaction from CdSe to Ag_2Se. When these Ag_2Se NCs were mixed with a solution containing an excess amount (50-100 fold excess by moles) of cadmium cations, the reaction was reversed. Though the reverse reaction took somewhat longer - about a minute - to complete, the final product was CdSe NCs which were nearly identical in size and shape to the starting material. The reversibility exists over multiple cycles of exchanges and the number of anions per NC was invariant over these cycles.

Similar tests to transform hollow NCs of cadmium sulfide into hollow NCs of silver sulfide, and crystals of cadmium telluride in the shape of tetrapods into tetrapod crystals of silver telluride, were performed. Again, the transformation reactions were fast, complete, and fully reversible. The reaction could easily be extended to exchanges with other cations, *e.g.* Cu^{2+} and Pb^{2+}. To date, however, attempts to induce exchanges of anions (negatively charged ions) have not been successful under similar experimental conditions, presumably because the much larger size of the anions, relative to the cations, makes diffusion more difficult. Thus, the reaction can be viewed as the diffusion of cations through the anion sublattice that has a limited flexibility.

Robinson *et al.*[28] suggested that, because of the high mobility of cations in the CdS (Se,Te) lattice, a partial cation exchange may lead to interesting patterns of segregated domains of Ag chalcogenide within a Cd-chalcogenide nanorod. They proceeded to convert a previously formed nanorod of a single chemical composition (CdS) into a striped pattern (CdS-Ag_2S), by a single-step partial chemical transformation.

A linear arrangement of regularly spaced Ag_2S dots, contained within a CdS rod, formed spontaneously at -66 ^oC, with ~36% cation exchange.

Based on the above results, one could postulate that these cation exchange reactions could be used to dope NCs. If a partial cation exchange with a very low percentage (~1 %) of Ag^+ ions could be carried out successfully, it might possibly dope the CdSe NCs. Silver is a good choice as the dopant because it is one of the fastest diffusers, and hence, it is easy to incorporate into the host material at ambient conditions. It has much more rapid diffusion rates than other common choices such as I_2 or K^{+}[29] and possesses excellent ionic mobility. Moreover, Ag^+ is known to be an effective p-type dopant in bulk PbTe, CdS, CdTe and HgTe.[30-32] In addition to being stable in air, CdSe NCs have been studied extensively and a high degree of control over their size and shape has been achieved. Hence, our efforts below are aimed at p-type doping of CdSe NCs with silver as the dopant.

3.4 RESULTS AND DISCUSSION

To begin, we prepared lightly doped nanocrystals by adapting a standard cation-exchange procedure for nanocrystals.[27,28,33] As discussed above, it was shown that CdSe nanocrystals that were exposed to Ag cations in solution could be completely or partially converted to Ag_2Se. However, due to the high efficiency of this exchange, it proved difficult to apply to doping at lower concentrations because the nanocrystals can quickly become heavily doped or even multi-phase. To avoid this, we included trioctylphosphine as a surfactant during the exchange to mediate the incorporation. Ethanolic $AgNO_3$ was mixed with trioctylphosphine and added to a dispersion of pre-prepared CdSe nanocrystals[34] with mild heating. The resulting nanocrystals were then isolated and dispersed in toluene. Nanocrystals with less than ~20 Ag per nanocrystal (<4% Ag to Cd) were stable for months under ambient. At higher concentrations, Ag films appeared on glass storage vials after several weeks, which has also been seen in Ag_2Se nanocrystals.[35]

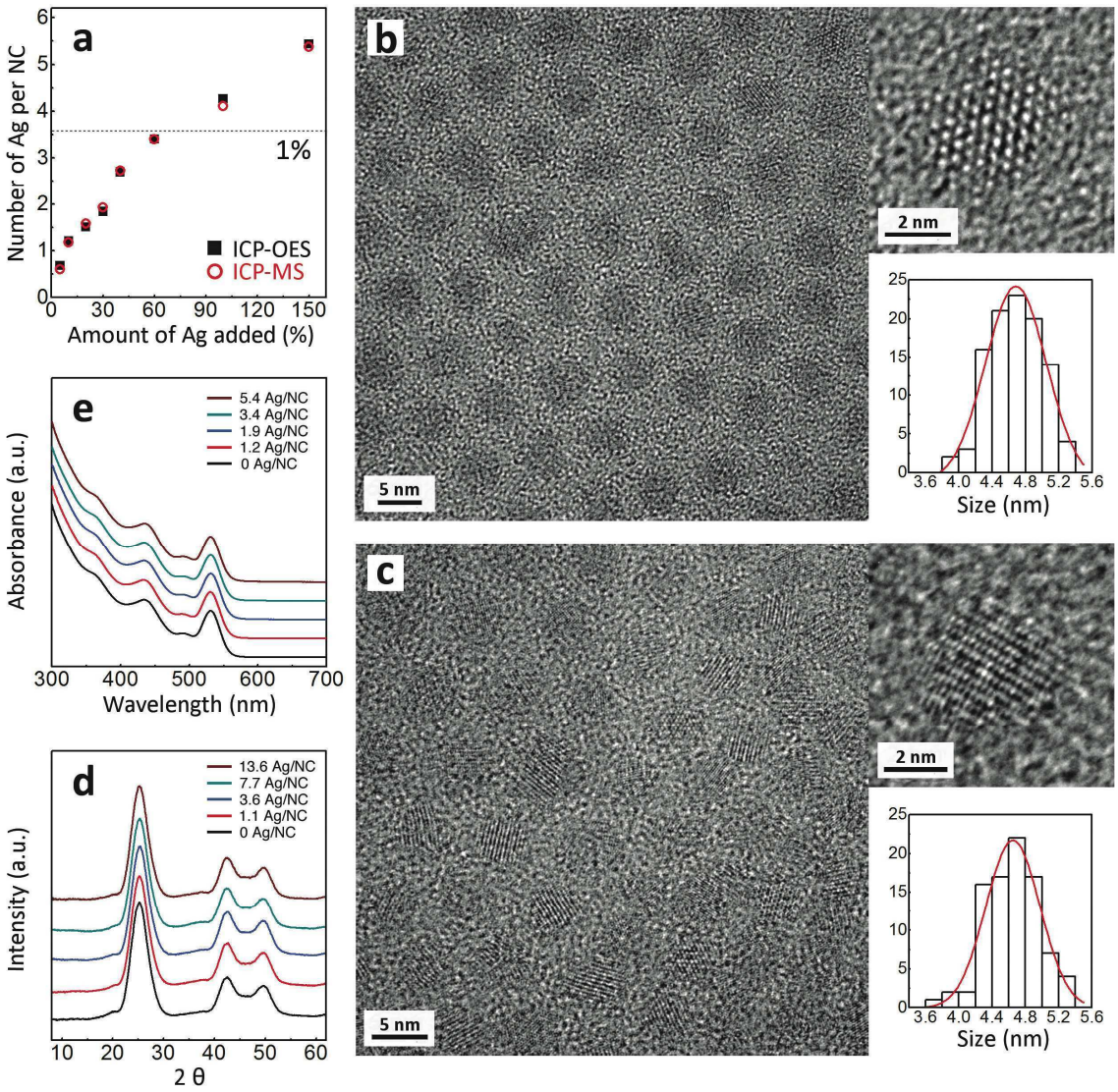

Figure 3.1: (a) The number of Ag atoms incorporated per 2.7-nm-diameter CdSe nanocrystal (NC), determined via ICP-OES and ICP-MS, versus the amount of Ag added to the exchange solution, as a percent of the total Cd present. (b) Electron micrograph of undoped 4.7-nm-diameter CdSe nanocrystals. (c) Electron micrograph of the same nanocrystals as in (b) but doped with ~12 Ag/NC (0.60% Ag). The insets in (b) and (c) show single-crystalline particles with size histograms that are unaltered by doping. (d) X-ray diffraction patterns for 3.0-nm-diameter CdSe nanocrystals with no Ag (black), 1.1 Ag/NC (0.20% Ag, red), 3.6 Ag/NC (0.67% Ag, blue), 7.7 Ag/NC (1.4% Ag, green), and 13.6 Ag/NC (2.5% Ag, brown). (e) Room-temperature absorption spectra of 2.7-nm-diameter CdSe nanocrystals dispersed in hexanes with no Ag (black), 1.2 Ag/NC (0.32% Ag, red), 1.9 Ag/NC (0.53% Ag, blue), 3.4 Ag/NC (0.93% Ag, green), and 5.4 Ag/NC (1.5% Ag, brown).

One key advantage of the cation-exchange approach is that it automatically provides a control sample for determining changes due to doping. In other syntheses, where the impurities are added during the nanocrystal growth, it is challenging to prepare an undoped sample of the same size, shape, and quality. Furthermore, with cation

exchange, an entire series of samples that only differ by the amount of Ag that is incorporated can be easily prepared. In Figure 3.1a, we plot the average number of Ag atoms in 2.7-nm-diameter CdSe nanocrystals versus the amount of $AgNO_3$ in the exchange solution. To quantify Ag incorporation, we used both inductively coupled plasma optical emission spectroscopy (ICP-OES) and mass spectroscopy (ICP-MS). We observed a consistent monotonic increase in the incorporated dopant with increasing $AgNO_3$. Thus, dopant concentration could be easily controlled in the lightly doped limit.

Figure 3.1b,c show transmission electron micrographs of 4.7-nm-diameter CdSe nanocrystals before and after the exchange process. This doped sample has a large number (~12) of Ag per nanocrystal. This was chosen to confirm that the particles are still highly crystalline (with no noticeable increase in stacking faults or twins) and have a size distribution that is unaltered even at this high concentration. X-ray diffraction patterns (Figure 3.1d) and room-temperature absorption spectra (Figure 3.1e) also show no significant changes as a function of dopant concentration.

However, dramatic changes were observed when the nanocrystal fluorescence was analyzed. Figure 3.2 shows a set of undoped sample and doped sample under UV illumination. One can clearly observe that the doped NCs are much more fluorescent than the undoped NCs.

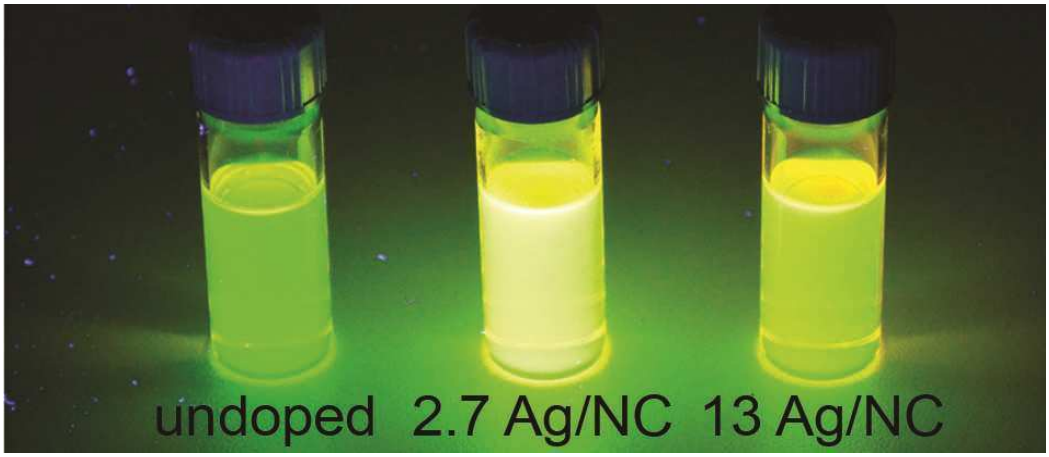

Figure 3.2: Room-temperature (RT) image of 2.6-nm-diameter CdSe nanocrystals (NCs) dispersed in hexanes with no Ag (left sample), 2.7 Ag/NC (middle sample), and 13.7 Ag/NC (right sample) under UV illumination.

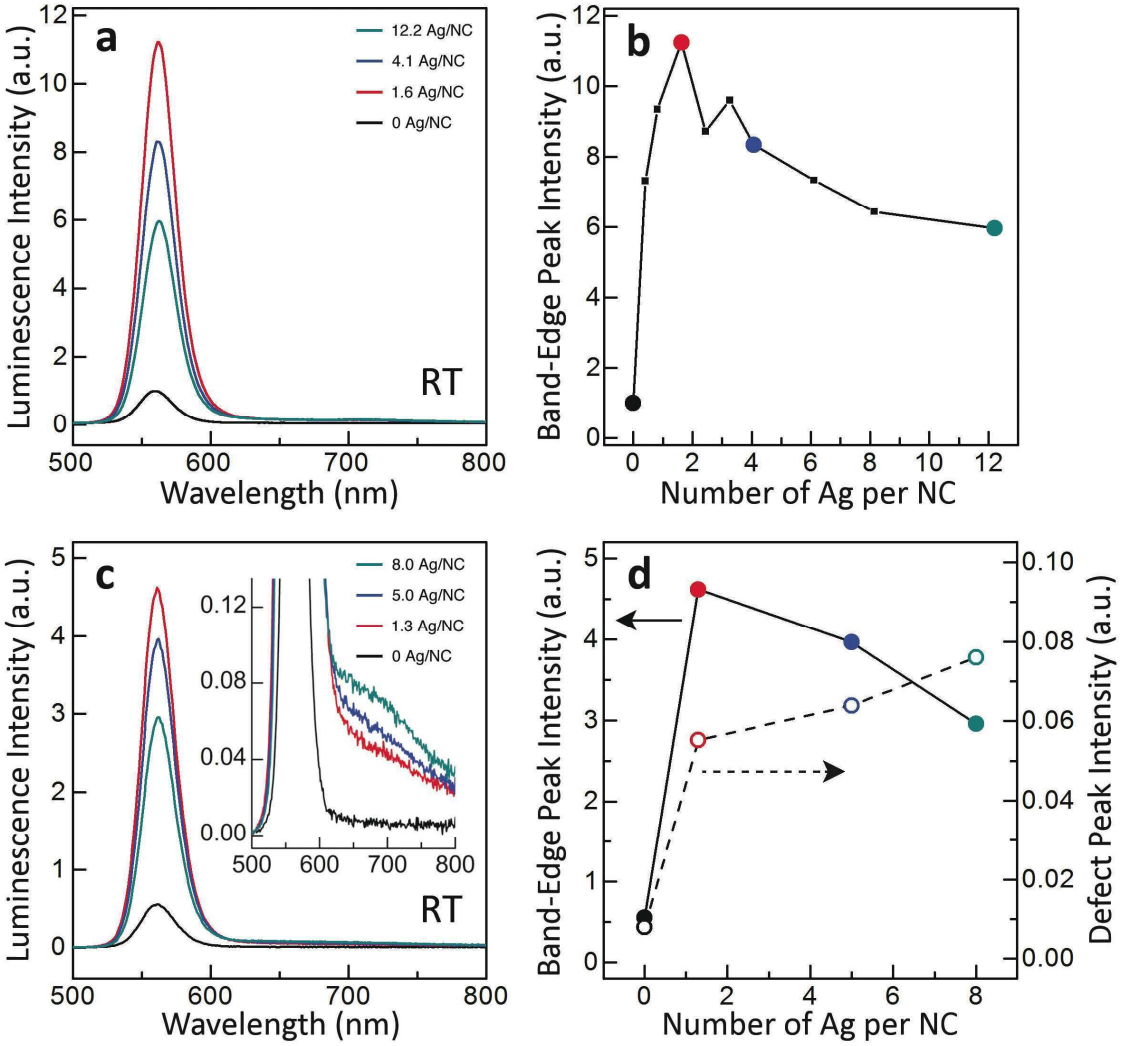

Figure 3.3: (a) Room-temperature (RT) fluorescence spectra of 3.1-nm-diameter CdSe nanocrystals (NCs) dispersed in hexanes with no Ag (black), 1.6 Ag/NC (0.3% Ag, red), 4.1 Ag/NC (0.74% Ag, blue), and 12.2 Ag/NC (2.22% Ag, green). The excitation wavelength was 350 nm. (b) The intensity of the band-edge fluorescence peak near 560 nm plotted as a function of the number of Ag per nanocrystal. The colored data points correspond to the spectra in (a). (c) RT data for 3.0-nm-diameter CdSe nanocrystals dispersed in hexanes, plotted as in (a), with no Ag (black), 1.3 Ag/NC (0.26% Ag, red), 5.0 Ag/NC (1.0% Ag, blue), and 8.0 Ag/NC (1.5% Ag, green). The inset magnifies the weak fluorescence feature near 700 nm. (d) The intensity of the band-edge fluorescence peak near 560 nm (solid line) and the defect-related peak near 700 nm (dashed line), plotted as in (b). The colored data points correspond to the spectra in (c).

Figure 3.3a shows room-temperature emission spectra for 3.1-nm-diameter CdSe nanocrystals dispersed in hexanes as a function of the average number of Ag per nanocrystal. To compare the data, we first matched the absorbance for all samples at the lowest-energy electronic transition by controlling the nanocrystal concentration in the

dispersion. The addition of the Ag clearly enhances the fluorescence, with the maximum intensity (Figure 3.3b) peaking around 2 Ag per nanocrystal. Additional Ag then decreases the intensity from this maximum.

This same trend, an enhancement of the fluorescence with the addition of a few Ag per nanocrystal and then a slow decrease at higher concentrations, was observed consistently across different samples and sizes (Figure 3.3d and Figures 3.4 – 3.11). The magnitude of the initial increase depended on how much the nanocrystals had been cleaned, but we verified that the addition of trioctylphosphine alone (*i.e.*, the replenishment of the surface ligand) could not explain the increase (Figure 3.11). Furthermore, we quantified the fluorescence quantum yield for the 3.5-nm-diameter sample shown in Figure 3.9 and observed a jump from 14% to 27% with the addition of 1.2 Ag per nanocrystal. Note that the quantum yield of CdSe nanocrystals with ~2 Ag atoms is comparable to that of CdSe/ZnS core/shell nanocrystals.[36,37]

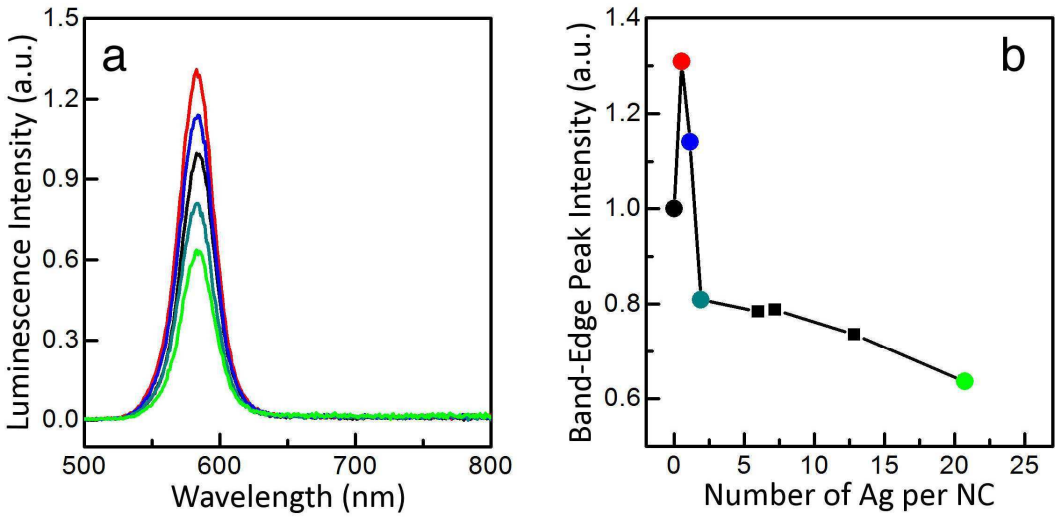

Figure 3.4: Optical characterization of 3.6-nm-diameter Ag-doped CdSe nanocrystals (NCs) dispersed in hexanes. (a) Room-temperature photoluminescence spectra of an undoped sample (black) and a series of doped samples with 0.6 Ag/NC (red), 1.1 Ag/NC (blue), 1.9 Ag/NC (dark cyan), and 20.7 Ag/NC (green). (b) Variation in the band-edge peak intensity with Ag doping. The black, red, blue, dark cyan, and green circles show the maximum fluorescence intensity for the spectra in (a). The addition of a few Ag atoms enhances the fluorescence by a factor of 1.3 and then the fluorescence slowly drops down with further doping.

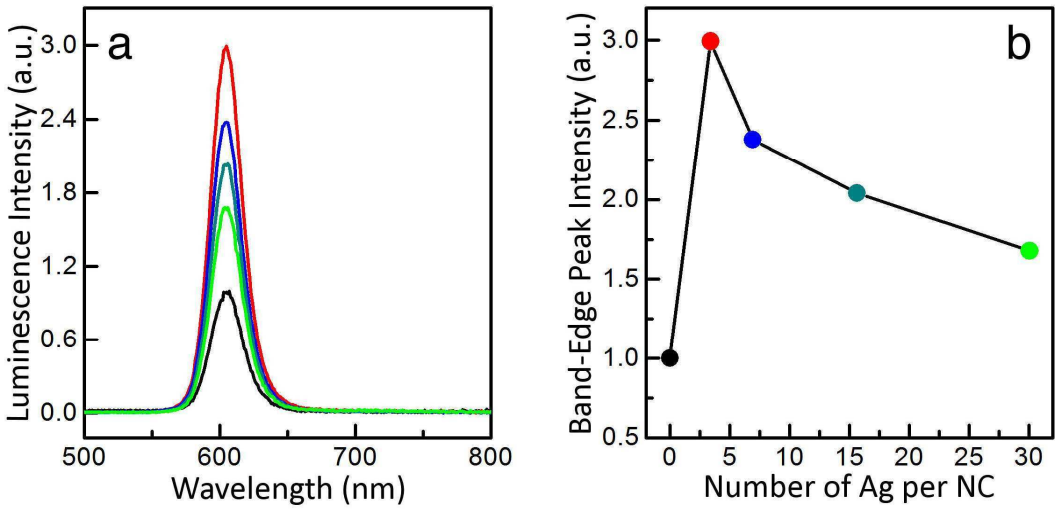

Figure 3.5: Optical characterization of 4.3-nm-diameter Ag-doped CdSe nanocrystals (NCs) dispersed in hexanes. (a) Room-temperature photoluminescence spectra of an undoped sample (black) and a series of doped samples with 3.4 Ag/NC (red), 6.9 Ag/NC (blue), 15.6 Ag/NC (dark cyan), and 30.1 Ag/NC (green). (b) Variation in the band-edge peak intensity with Ag doping for the samples in (a). The black, red, blue, dark cyan, and green circles show the maximum fluorescence intensity for the spectra in (a). The addition of a few Ag atoms enhances the fluorescence by a factor of 3 and then the fluorescence slowly drops down with further doping.

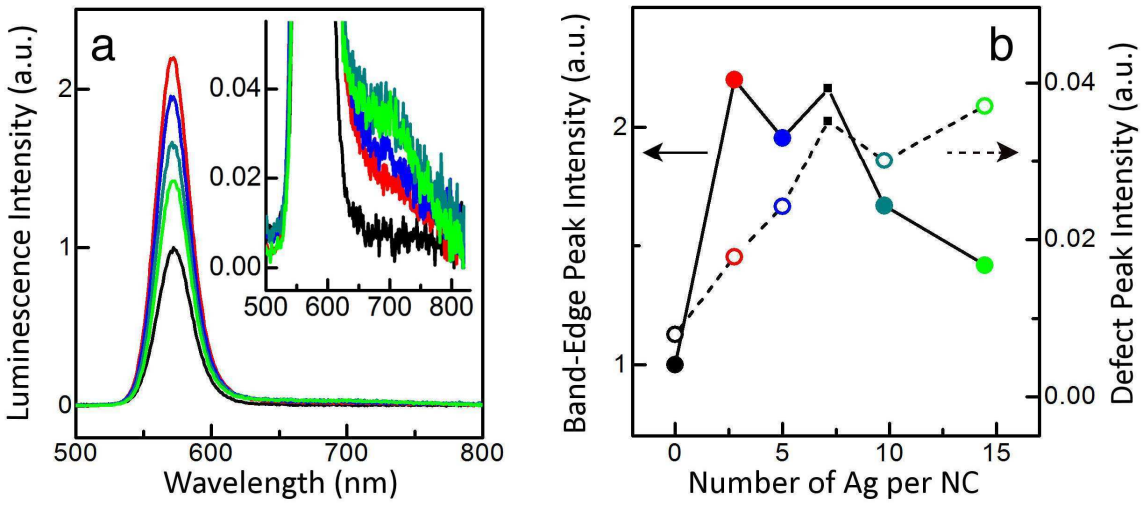

Figure 3.6: Optical characterization of 3.27-nm-diameter Ag-doped CdSe nanocrystals (NCs) dispersed in hexanes. (a) Room-temperature photoluminescence spectra of an undoped sample (black) and a series of doped samples with 2.8 Ag/NC (red), 5.0 Ag/NC (blue), 9.8 Ag/NC (dark cyan), and 14.5 Ag/NC (green). The inset shows the magnified image of a weak defect-state peak on the long-wavelength side of the band-edge peak present only in the doped samples. (b) Variation in the band-edge (solid lines and filled circles) and defect-state (dashed lines and open circles) peak intensity with Ag doping. The black, red, blue, dark cyan, and green circles show the maximum fluorescence intensity and defect-state peak intensity for the spectra in (a). The addition of a few Ag atoms enhances the band-edge fluorescence and then the fluorescence slowly drops down with further doping while the defect peak grows uniformly with doping.

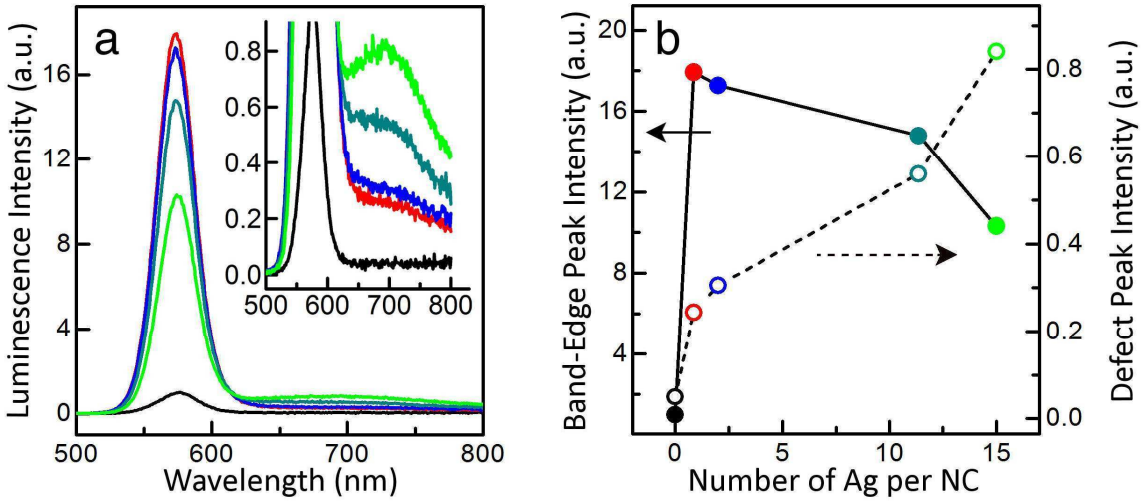

Figure 3.7: Optical characterization of 3.33-nm-diameter Ag-doped CdSe nanocrystals (NCs) dispersed in hexanes. (a) Room-temperature photoluminescence spectra of an undoped sample (black) and a series of doped samples with 0.9 Ag/NC (red), 2.0 Ag/NC (blue), 11.4 Ag/NC (dark cyan), and 15.0 Ag/NC (green). The inset shows the magnified image of a weak defect-state peak on the long-wavelength side of the band-edge peak present only in the doped samples. (b) Variation in the band-edge (solid lines and filled circles) and defect-state (dashed lines and open circles) peak intensity with Ag doping for the samples in (a). The black, red, blue, dark cyan, and green circles show the maximum fluorescence intensity and defect-state peak intensity for the spectra in (a). The addition of a few Ag atoms enhances the band-edge fluorescence and then the fluorescence slowly drops down with further doping while the defect peak grows uniformly with doping.

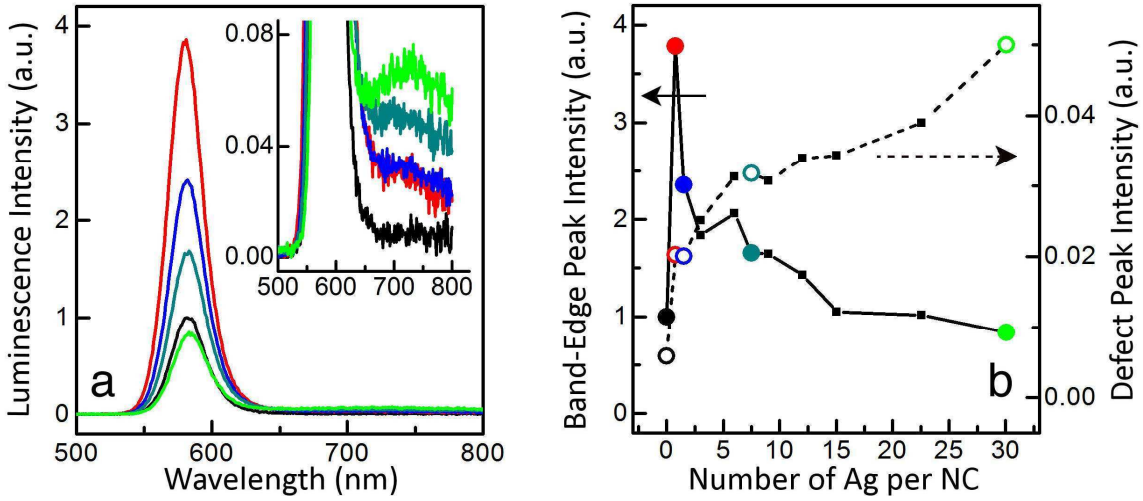

Figure 3.8: Optical characterization of 3.4-nm-diameter Ag-doped CdSe nanocrystals (NCs) dispersed in hexanes. (a) Room-temperature photoluminescence spectra of an undoped sample (black) and a series of doped samples with 0.8 Ag/NC (red), 1.5 Ag/NC (blue), 7.5 Ag/NC (dark cyan), and 30.1 Ag/NC (green). The inset shows the magnified image of a weak defect-state peak on the long-wavelength side of the band-edge peak present only in the doped samples. (b) Variation in the band-edge (solid lines and filled circles) and defect-state (dashed lines and open circles) peak intensity with Ag doping. The black, red, blue, dark cyan, and green circles show the maximum fluorescence intensity and defect-state peak intensity for the spectra in (a.) The addition of a few Ag atoms enhances the band-edge fluorescence and then the fluorescence slowly drops down with further doping while the defect peak grows uniformly with doping.

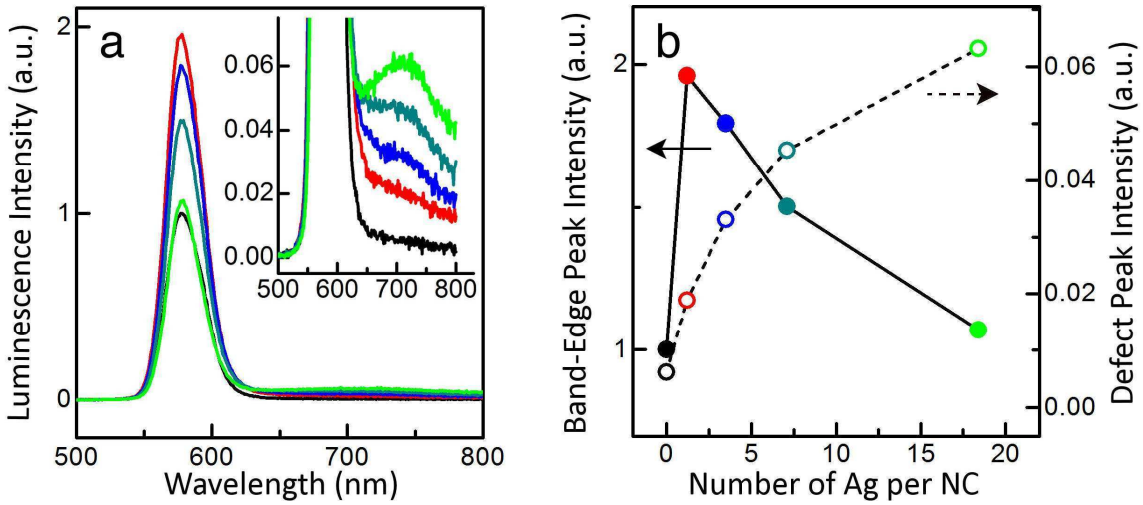

Figure 3.9: Optical characterization of 3.5-nm-diameter Ag-doped CdSe nanocrystals (NCs) dispersed in hexanes. (a) Room-temperature photoluminescence spectra of an undoped sample (black) and a series of doped samples with 1.2 Ag/NC (red), 3.5 Ag/NC (blue), 7.1 Ag/NC (dark cyan), and 18.4 Ag/NC (green). The inset shows the magnified image of a weak defect-state peak on the long-wavelength side of the band-edge peak present only in the doped samples. (b) Variation in the band-edge (solid lines and filled circles) and defect-state (dashed lines and open circles) peak intensity with Ag doping for the samples in (a). The black, red, blue, dark cyan, and green circles show the maximum fluorescence intensity and defect-state peak intensity for the spectra in (a). The addition of a few Ag atoms enhances the band-edge fluorescence and then the fluorescence slowly drops down with further doping while the defect peak grows uniformly with doping. The fluorescence quantum yield was estimated for the undoped and 1.2 Ag/NC samples. An increase from 14 to 27% was measured.

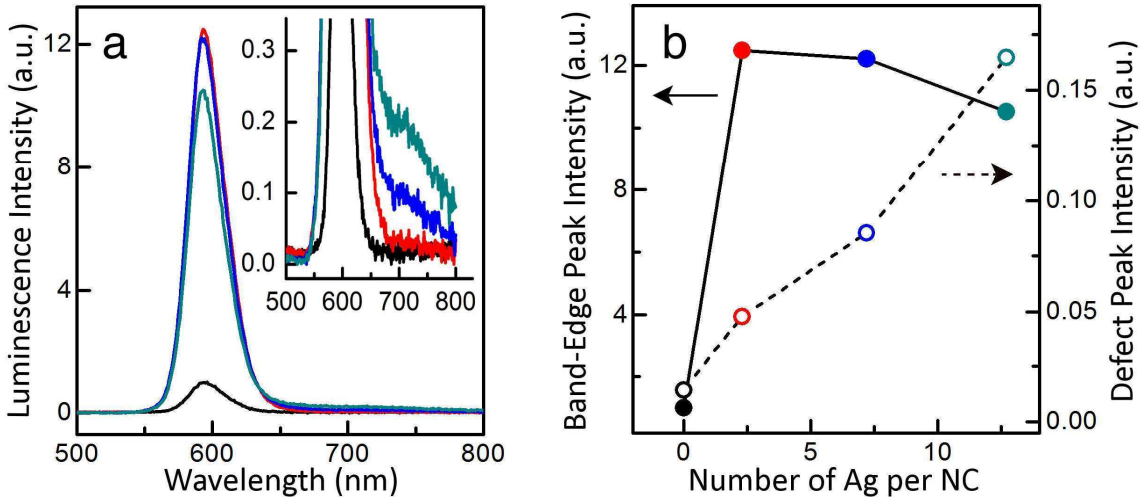

Figure 3.10: Optical characterization of 3.9-nm-diameter Ag-doped CdSe nanocrystals (NCs) dispersed in hexanes. (a) Room-temperature photoluminescence spectra of an undoped sample (black) and a series of doped samples with 2.3 Ag/NC (red), 7.2 Ag/NC (blue), and 12.7 Ag/NC (dark cyan). The inset shows the magnified image of a weak defect-state peak on the long-wavelength side of the band-edge peak present only in the doped samples. (b) Variation in the band-edge (solid lines and filled circles) and defect-state (dashed lines and open circles) peak intensity with Ag doping for the samples in (a). The black, red, blue, and dark cyan circles show the maximum fluorescence intensity and defect-state peak intensity for the spectra in (a). The addition of a few Ag atoms enhances the band-edge fluorescence and then the fluorescence slowly drops down with further doping while the defect peak grows uniformly with doping.

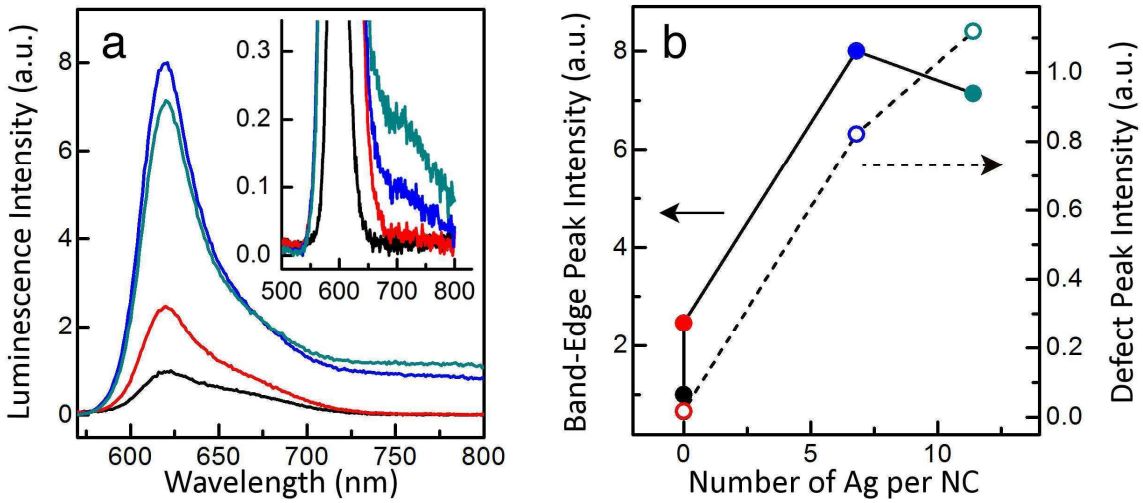

Figure 3.11: Optical characterization of 4.8-nm-diameter Ag-doped CdSe nanocrystals dispersed in hexanes with a tri-*n*-octylphosphine control experiment. (a) Room-temperature photoluminescence spectra of an undoped oleic-acid-capped CdSe nanocrystal (NC) sample (black), an undoped CdSe sample mixed with tri-*n*-octylphosphine to replicate the doping conditions (red), and two doped samples with 6.8 Ag/NC (blue) and 11.4 Ag/NC (dark cyan). The inset shows the magnified image of a weak defect-state peak on the long-wavelength side of the band-edge peak present only in the doped samples. (b) Variation in the band-edge (solid lines and filled circles) and defect-state (dashed lines and open circles) peak intensity for the samples in (a). The black, red, blue, and dark cyan circles show the maximum fluorescence intensity and defect-state peak intensity for the spectra in (a). While the addition of tri-*n*-octylphosphine enhances the band-edge fluorescence of the undoped sample, the addition of a few Ag atoms has a much greater impact on the band-edge fluorescence. Addition of tri-*n*-octylphosphine has no effect on the defect peak intensity in the undoped sample, which supports the conclusion that this feature is due to the presence of the dopants.

The rise in the fluorescence intensity with the addition of a few dopants is quite unexpected. For example, it was recently reported that the fluorescence of CdSe/CdS quantum dot/rods is quenched 100-fold with the introduction of Cu impurities.[38] To explain our enhancement, several possible mechanisms can be considered. First, each Ag atom could provide an extra carrier (either electron or hole) to one of the quantum-confined levels of the nanocrystal and enhance the radiative rate. This would be surprising because the presence of the extra carrier should cause rapid nonradiative Auger recombination,[39] which should decrease the fluorescence intensity. Nevertheless, an increase in fluorescence intensity has been observed in CdSe nanocrystals in which an extra electron was injected via electrochemical doping.[9] In that case, the increase was explained by the presence of a negatively charged exciton (or negative trion, X^-), which should have a faster radiative rate than a neutral exciton. Further, it has recently been argued that Auger recombination is much less efficient for the negative trion compared to

the positive trion,[40] which in principle could rationalize why the fluorescence is not quenched with the addition of an extra carrier. This picture would then suggest that the Ag acts as a donor and provides an extra electron. However, this explanation suffers from several inconsistencies with the data. The presence of an extra electron in a quantum-confined level would induce a bleach in the lowest energy absorption feature,[7] which we do not observe (Figure 3.1e). An increase of the fluorescence by a factor of ~10 is also difficult to explain quantitatively based on the negative trion model.[41]

A second explanation is that the Ag atoms passivate nonradiative traps, either by binding to the nanocrystal surface directly or by incorporating into the nanocrystal and providing extra carriers that then fill these traps. However, the data would then suggest that in all samples only ~2 traps must be filled to have a dramatic effect. While possible, we believe this explanation is unlikely.

Rather, we propose that a third mechanism is more plausible. We must recognize that a fundamental difference exists between impurity doping and electrochemical doping. In impurity doping, one does not just add an extra carrier, but also the impurity center as well. If the extra carrier fills a trap (or otherwise escapes from the nanocrystal, for example by reducing some chemical species on the nanocrystal surface or in the surrounding matrix[25]), this will leave behind an ionized impurity center in the nanocrystal. Even at one or two impurities, the electrostatic field of such centers can presumably influence the fluorescence. For example, positively charged CdSe nanocrystals have recently been invoked to explain nanocrystals with unusual brightness.[42,43] If the Ag atoms provide extra electrons, which then leave to traps outside the nanocrystals, this would induce a positively charged impurity center, which could enhance the brightness. This would suggest that Ag is acting as an *n*-type donor.

In addition to the initial rise, the fluorescence spectra also reveal a weak feature on the long-wavelength side of the main "band-edge" emission peak (Figure 3.3c). This weak feature appears only in the doped samples, increases in intensity with dopant

concentration (Figure 3.3d), and was present in all sizes of Ag-doped CdSe nanocrystals (Figures 3.6-3.11).

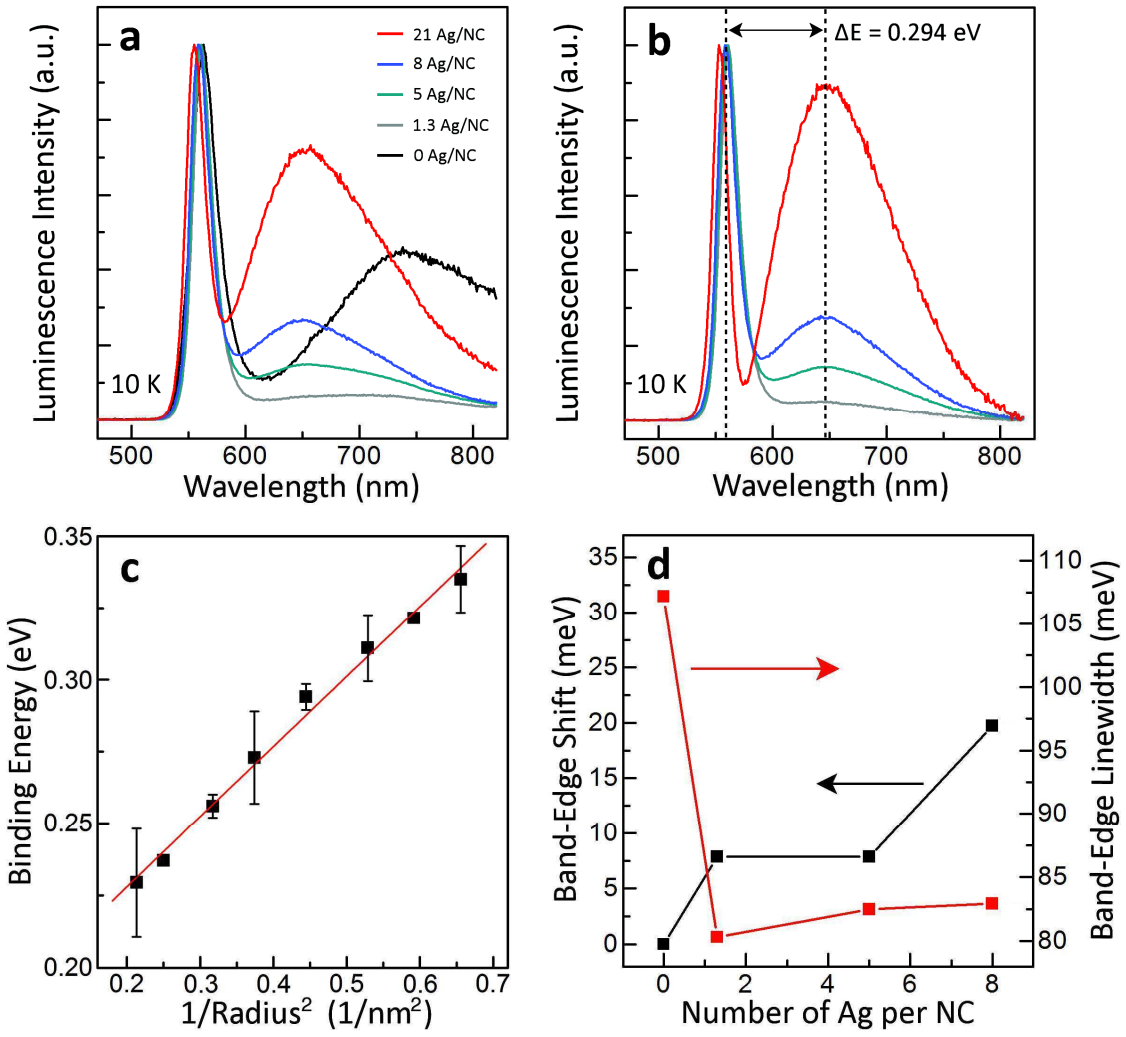

Figure 3.12: (a) Fluorescence spectra of the 3.0-nm-diameter CdSe nanocrystals (NCs) from Figure 2c cast as neat films and cooled to 10 K. The samples have no Ag (black), 1.3 Ag/NC (0.26% Ag, gray), 5.0 Ag/NC (1.0% Ag, green), 8.0 Ag/NC (1.5% Ag, blue), and 21 Ag/NC (4.0% Ag, red). The spectra were normalized to the peak of the band-edge feature. The excitation wavelength was 430 nm. (b) Normalized spectra from (a) after subtracting the deep-trap fluorescence that is present in all CdSe nanocrystals at low temperatures [see black curve in (a)]. The energy separation between the band-edge peak and the defect-related feature is marked with vertical lines. (c) This energy separation, which is assigned to the defect binding energy, versus the inverse nanocrystal radius squared. The values were extracted from data as in (b) for a range of nanocrystal sizes. A linear regression fit (red line) yields a coefficient of determination of 0.992. The error bars represent the standard deviation from averaging 2 to 5 samples for each size. Data points without error bars are for one sample. (d) The extracted linewidth (red) and energy shift (black) of the band-edge fluorescence peak versus the number of Ag per nanocrystal.

However, because its intensity is 30-100 times less than the main peak, an analysis is challenging from room-temperature data. Therefore, we cast neat films of the nanocrystals on sapphire discs and acquired fluorescence spectra at 10 K. The results, shown in Figure 3.12a, are normalized to the intensity of the band-edge peak. The weak feature is more intense at low temperature and becomes prominent at higher doping. To resolve this feature further, we subtracted the "deep-trap" fluorescence that is present in all CdSe nanocrystals at 10 K (see the black curve for the undoped sample in Figure 3.12a). The resulting spectra (Figure 3.12b) show a dopant-related peak separated from the band-edge emission by a constant 294 meV.

One possible origin for this dopant-related peak is the recombination of carriers that are bound to the impurity with those that are optically excited into the lowest quantum-confined level. The separation would then be related to the binding energy of the impurity. To explore this, we measured the low-temperature fluorescence spectra for different sizes of Ag-doped CdSe nanocrystals and extracted the separation between the dopant-related peak and the band-edge emission. If the separation is due to the binding energy, its size dependence should depend on the confinement regime of the dopant.[44] If the dopant is weakly confined, its binding energy should scale as $1/R^2$, where R is the nanocrystal radius. If the dopant is strongly confined, it should go as $1/R$. Assuming hydrogenic impurities, an acceptor in CdSe would have a Bohr radius of ~0.7 nm. Thus, in our size regime it should be weakly confined and yield a $1/R^2$ size dependence. In contrast, a donor in CdSe would have a Bohr radius of ~5.0 nm, would be strongly confined, and lead to a $1/R$ dependence. Figure 3.12c and Figure 3.13 plot the data versus $1/R^2$ and $1/R$, respectively. Unfortunately, the data fit well to either dependence (with coefficients of determination of 0.992 and 0.997). Consequently, it is difficult to distinguish the two cases from the size dependence. However, if we extrapolate each fit to infinite size, we can estimate what each scaling would predict for the binding energy of Ag in bulk CdSe. We extract values of 180 and 83 meV, respectively. These values are much closer to what is expected[45,46] for a hydrogenic acceptor (84 meV) than for a hydrogenic donor (13 meV) in CdSe. Thus, keeping in mind all of the assumptions in the above analysis, this defect-related peak appears to be more consistent with Ag as an

acceptor. The dopant-related peak would then be explained by the recombination of photoexcited electrons with Ag-bound holes. In this case, at higher concentrations, where the dopant-related peak becomes significant, Ag is acting as a *p*-type dopant.

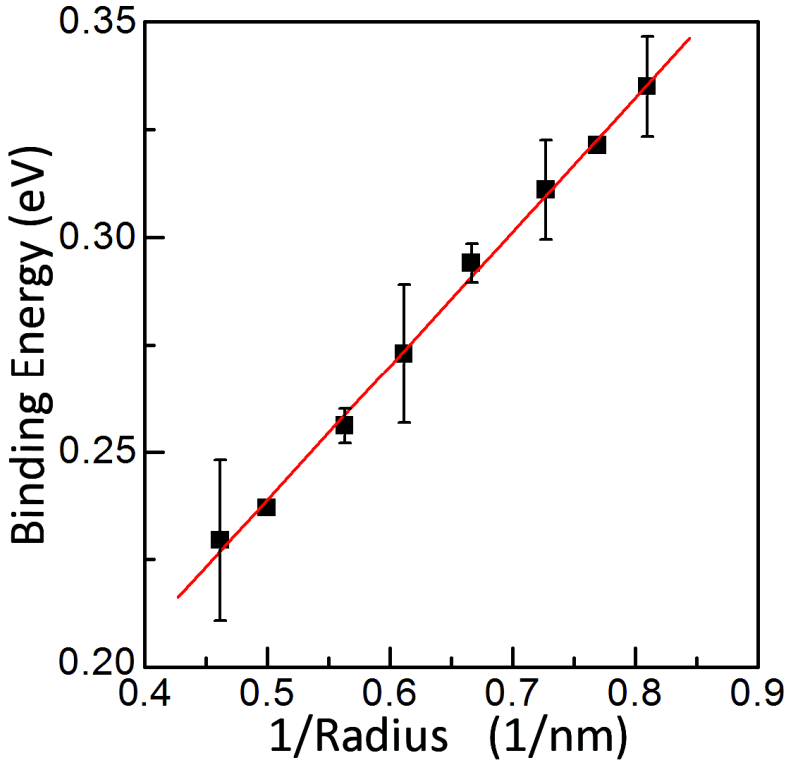

Figure 3.13: The energy separation between the band-edge emission feature and the dopant-related peak, assigned to the defect binding energy, plotted versus the inverse nanocrystal radius. The values were extracted from data as in Figure 3.12b for a range of nanocrystal sizes. A linear regression fit (red line) yields a coefficient of determination of 0.997. The error bars represent the standard deviation from averaging 2 to 5 samples for each size. Data points without error bars are for one sample.

At this point, it may be helpful to summarize our interpretation of the optical data. At low doping of Ag, we argue that the impurity is an *n*-type dopant. Because the donor electrons are quickly trapped outside the nanocrystals, the particles become positively charged due to the ionized impurity. The absence of an extra electron in the conduction band states of the nanocrystals can explain the absence of changes in the absorption spectra (Figure 3.1e) and Auger quenching.[39] At the same time, the positive impurity center can explain the enhanced photoluminescence. At higher doping, the Ag begins to behave as a *p*-type dopant. Because of the strong binding energy and localized character of a hydrogenic acceptor in CdSe, a small population of the extra holes remain bound to

the impurity center even at room temperature. This gives rise to the weak dopant-related shoulder in Figure 3.3c. At 10K where thermal activation is diminished, a much larger percent of the holes remain bound, leading to the more pronounced dopant-related peak in Figure 3.12b.

Before discussing this further, we note that other subtle changes were observed in the fluorescence with doping (Figure 3.12d). At 10 K, the band-edge peak shifts to higher energy; its linewidth decreases by ~25% with the incorporation of just 1.3 Ag per nanocrystal (0.26% Ag). While the exact origin of these effects is not yet clear, both the blue shift and line narrowing in our lightly-doped samples are in contrast to observations in the heavily-doped InAs nanocrystals.[16] There, room-temperature red shifts and peak broadening were explained by band tailing due to high doping. At room temperature, our samples exhibit essentially no change in peak position or linewidth in the low-doping limit (<10 Ag per nanocrystal).

While the optical results clearly show that the addition of a few Ag per nanocrystal can cause large changes, our interpretation, in which Ag acts as a *n*-type dopant (donor) at very low concentrations and then transitions to a *p*-type donor (acceptor) as the number of Ag per nanocrystal is increased, is fairly speculative. If such a doping trend occurs, however, it should also affect electrical transport. To study the effect of silver on the transport properties of CdSe nanocrystals, we fabricate thin film transistors of both undoped and Ag-doped CdSe nanocrystals. We discuss the electrical transport in these nanocrystal samples in the next chapter.

3.5 EXPERIMENTAL SECTION

3.5.1 Chemicals and Substrates

Carbon tetrachloride (reagent grade, 99.9%), chloroform (HPLC grade, ≥99.8%), hexadecylamine (HDA, technical grade, 90%), methanol (HPLC grade, ≥99.9%),

anhydrous methanol (99.8%), anhydrous ethanol (≥99.5%), octane (reagent grade, 98%), anhydrous octane (≥99%), selenium pellets (Se, 99.999%), tetrachloroethylene (TCE, spectrophotometric grade, ≥99.9%), toluene (HPLC grade, 99.9%), diphenylphosphine (DPP, 98%), tri-*n*-octylphosphine (TOP, technical grade, 90%), tri-*n*-octylphosphine oxide (TOPO, technical grade, 90%), hydrochloric acid (TraceSELECT®, for trace analysis, fuming, ≥37%), and nitric acid [TraceSELECT®, for trace analysis, ≥69.0% (T)] were purchased from Sigma Aldrich. Hexanes (ACS grade) was purchased from VWR International. Reagent alcohol (histological grade, 90% ethanol, 5% methanol, and 5% butanol) and butanol were obtained from Fisher Scientific. *n*-dodecylphosphonic acid (DDPA) was purchased from PCI Synthesis. Cadmium (II) oxide (CdO, 99.999%) and silver nitrate (AgNO3, 99.9995%) were purchased from Strem Chemicals. All chemicals were used as delivered without further purification.

Circular sapphire windows, 12.7 mm (0.5") in diameter and 1.0 mm (0.040") thick, were purchased from Esco Products Inc.

3.5.2 Synthesis of CdSe Nanocrystals

CdSe nanocrystals were prepared by modifying a known procedure.[34] For 3-nm-diameter CdSe nanocrystals, CdO (410.0 mg, 3.2 mmol), hexadecylamine (HDA, 18.54 g, 76.8 mmol), *n*-dodecylphosphonic acid (DDPA, 1.608 g, 6.4 mmol), and tri-*n*-octylphosphine oxide (TOPO, 8.096 g, 20.9 mmol) were heated to 90 °C in a 100-ml four-neck round-bottom flask with continuous stirring. The flask was degassed under vacuum (<20 millitorr) and purged with dry N_2. The degassing process was repeated at least three times to remove water and O_2. The mixture was then heated to 315 °C under N_2, and held at that temperature for nearly 30 minutes until the precursor solution turned clear. After stabilizing the colorless mixture at 280 °C, a mixture of 20 ml of a 0.2 M solution of Se in tri-n-octylphosphine (TOP, 4 mmol) and 0.3 ml of diphenylphosphine (DPP) prepared in a N_2-filled glove box was rapidly injected into the reaction vessel with continuous stirring, resulting in a temperature drop to ~225 °C. The temperature was then quickly elevated to ~270 °C using a heat gun, and kept at that temperature for ~10 minutes to facilitate nanocrystal growth. The reaction vessel was cooled to ~90 °C and 40

ml of 1-butanol was added to prevent solidification of the reaction mixture. The nanocrystals were isolated by addition of methanol to induce flocculation, followed by centrifugation. The resulting precipitate yielded nanocrystals with surfaces coated by a mixture of HDA, DDPA, and TOP/TOPO.

To remove excess ligands, several additional purification steps were performed. Namely, the precipitate was redispersed in hexanes and centrifuged. The supernatant, which contained the nanocrystals was saved, and the precipitate [mostly unreacted hexadecylamine (HDA)] was redispersed in hexanes and centrifuged again to extract more nanocrystals. This process was repeated multiple times (typically 3) until all the possible nanocrystals were extracted from the precipitate into the supernatant. The dispersion was then stored overnight in a freezer (–20 °C). During this time, excess surfactant precipitated out of the dispersion and was removed by centrifugation. The supernatant was then filtered through a 0.2 μm polytetrafluoroethylene (PTFE) syringe filter, reagent alcohol was added, and the solution was centrifuged. Multiple iterations (in general two more cycles) of redispersion and precipitation using hexanes and reagent alcohol were done to obtain pure CdSe nanocrystals. Finally the nanocrystals, isolated as solid centrifuge pellets, were dried under vacuum, dispersed in toluene, filtered through a 0.2 μm PTFE syringe filter to obtain a stable colloidal dispersion and stored under ambient conditions until needed.

3.5.3 Doping of CdSe Nanocrystals with Ag

To incorporate Ag, a typical exchange reaction heated 6 ml of a 5 mg/ml dispersion of CdSe nanocrystals in toluene to ~60 °C in a glass vial with continuous stirring. 1 ml of 0.1 M ethanolic $AgNO_3$ was combined with 1.5 ml of TOP and then added to the rapidly stirring dispersion. After ~2 minutes the reaction was quenched with ~10 ml of ethanol. The precipitated nanocrystals were isolated by centrifugation and then dispersed and isolated several times with hexanes and ethanol, respectively, to obtain a clean product. This process generates nanocrystals with ~1 Ag per particle on average.

3.5.4 Sample Characterization

X-ray diffraction (XRD), transmission electron microscopy (TEM), inductively coupled plasma optical emission spectroscopy (ICP-OES), inductively coupled plasma mass spectroscopy (ICP-MS), ultraviolet-visible (UV-Vis) absorption spectroscopy, and fluorescence spectroscopy were used to characterize the size, shape, structure, composition, and optical properties of the doped nanocrystals.

For XRD, a Bruker-AXS microdiffractometer was utilized to collect wide-angle powder patterns (Cu-Kα). Samples were prepared from concentrated dispersions of CdSe nanocrystals in hexane. Films of these nanocrystals were deposited onto heavily doped Si wafers covered with a thermally grown 300-nm-thick SiO_2 layer.

For TEM, an FEI Tecnai G2 F30 microscope was used to image the nanocrystals with an acceleration voltage of 300 kV. Each sample was prepared by depositing a drop of a dilute dispersion of nanocrystals in hexanes onto a 400-mesh carbon-coated copper grid and allowing the solvent to evaporate at room temperature.

For optical characterization, nanocrystals were dispersed in hexanes and placed in a 1-cm-path-length quartz cuvette. Absorption spectra were obtained using a Cary 5E UV-Vis-near-infrared spectrophotometer. Photoluminescence spectra were collected with a Spex Fluorolog-2 spectrofluorometer equipped with two double monochromators (0.22 m, SPEX 1680) and a 450 W xenon lamp as the excitation source. For measurements at 10 K, the nanocrystals were deposited on sapphire flats that were mounted in a Janis continuous flow cryostat that was positioned in the sample compartment of the fluorometer.

For ICP-MS, we used a Thermo Scientific XSeries2 instrument with a hexapole collision/reaction cell. For calibration, we compared the intensities of the unknown to data from 4 multi-element standards purchased from SPEX Industries. Elements were analyzed at standard mass resolution using the helium/hydrogen collision reaction mode with kinetic energy discrimination. The mean and standard deviation were calculated

from five measurements on each sample. The unknowns were introduced with an ESI PC3 (Peltier cooler) FAST system with sample loops to reduce oxide formation and carryover between samples. ^{89}Y was used as an internal standard.

For ICP-OES, we used a Thermo Scientific iCAP 6500 duo optical emission spectrometer with a simultaneous charge-induction detector. We measured each sample five times to determine the mean and standard deviation for each elemental wavelength. For calibration, we utilized NIST-traceable single or multi-element standards. To lessen matrix effects, we matched the matrix acid for all blanks, standards, and samples. We diluted each sample such that the elemental concentrations were in the linear range of the standard and detector combination. The probe and all tubing for introduction of the samples were made from Teflon and flushed for at least 45 seconds with clean matrix acid.

For both ICP-MS and ICP-OES, samples were prepared by dissolving ~1-2 mg of vacuum-dried nanocrystals in 5 ml of aqua regia (3:1 HCl:HNO_3). The resulting ions were then diluted to ~100 ppm with 18 MΩ deionized water. To avoid contamination, trace-grade acids (HCl and HNO_3) and HCl-leached plasticware and glassware were used.

3.6 REFERENCES

(1) Alivisatos, A. P. *Science* **1996**, *271*, 933.

(2) Klimov, V. I. *Semiconductor and Metal Nanocrystals: Synthesis and Electronic and Optical Properties*; Marcel Dekker, Inc.: New York, 2004.

(3) Gur, I.; Fromer, N. A.; Geier, M. L.; Alivisatos, A. P. *Science* **2005**, *310*, 462.

(4) Coe, S.; Woo, W. K.; Bawendi, M.; Bulovic, V. *Nature* **2002**, *420*, 800.

(5) Shim, M.; Guyot-Sionnest, P. *Nature* **2000**, *407*, 981.

(6) Talapin, D. V.; Murray, C. B. *Science* **2005**, *310*, 86.

(7) Yu, D.; Wang, C. J.; Guyot-Sionnest, P. *Science* **2003**, *300*, 1277.

(8) Roest, A. L.; Kelly, J. J.; Vanmaekelbergh, D.; Meulenkamp, E. A. *Physical Review Letters* **2002**, *89*, 036801.

(9) Wang, C. J.; Shim, M.; Guyot-Sionnest, P. *Science* **2001**, *291*, 2390.

(10) Buonsanti, R.; Llordes, A.; Aloni, S.; Helms, B. A.; Milliron, D. J. *Nano Letters* **2011**, *11*, 4706.

(11) Fujii, M.; Yamaguchi, Y.; Takase, Y.; Ninomiya, K.; Hayashi, S. *Applied Physics Letters* **2005**, *87*, 211919.

(12) Geyer, S. M.; Allen, P. M.; Chang, L. Y.; Wong, C. R.; Osedach, T. P.; Zhao, N.; Bulovic, V.; Bawendi, M. G. *ACS Nano* **2010**, *4*, 7373.

(13) Ishizumi, A.; Kanemitsu, Y. *Journal of the Physical Society of Japan* **2010**, *79*, 093706.

(14) Luther, J. M.; Jain, P. K.; Ewers, T.; Alivisatos, A. P. *Nature Materials* **2011**, *10*, 361.

(15) Meulenberg, R. W.; van Buuren, T.; Hanif, K. M.; Willey, T. M.; Strouse, G. F.; Terminello, L. J. *Nano Letters* **2004**, *4*, 2277.

(16) Mocatta, D.; Cohen, G.; Schattner, J.; Millo, O.; Rabani, E.; Banin, U. *Science* **2011**, *332*, 77.

(17) Orlinskii, S. B.; Schmidt, J.; Baranov, P. G.; Hofmann, D. M.; Donega, C. D.; Meijerink, A. *Physical Review Letters* **2004**, *92*.

(18) Pi, X. D.; Gresback, R.; Liptak, R. W.; Campbell, S. A.; Kortshagen, U. *Applied Physics Letters* **2008**, *92*, 123102.

(19) Roy, S.; Tuinenga, C.; Fungura, F.; Dagtepe, P.; Chikan, V.; Jasinski, J. *Journal of Physical Chemistry C* **2009**, *113*, 13008.

(20) Srivastava, B. B.; Jana, S.; Pradhan, N. *Journal of the American Chemical Society* **2011**, *133*, 1007.

(21) Stegner, A. R.; Pereira, R. N.; Klein, K.; Lechner, R.; Dietmueller, R.; Brandt, M. S.; Stutzmann, M.; Wiggers, H. *Physical Review Letters* **2008**, *100*, 026803.

(22) Stowell, C. A.; Wiacek, R. J.; Saunders, A. E.; Korgel, B. A. *Nano Letters* **2003**, *3*, 1441.

(23) Viswanatha, R.; Brovelli, S.; Pandey, A.; Crooker, S. A.; Klimov, V. I. *Nano Letters* **2012**, *11*, 4753.

(24) Wills, A. W.; Kang, M. S.; Wentz, K. M.; Hayes, S. E.; Sahu, A.; Gladfelter, W. L.; Norris, D. J. *Journal of Materials Chemistry* **2012**, *22*, 6335.

(25) Norris, D. J.; Efros, A. L.; Erwin, S. C. *Science* **2008**, *319*, 1776.

(26) Koenraad, P. M.; Flatte, M. E. *Nature Materials* **2011**, *10*, 91.

(27) Son, D. H.; Hughes, S. M.; Yin, Y. D.; Alivisatos, A. P. *Science* **2004**, *306*, 1009.

(28) Robinson, R. D.; Sadtler, B.; Demchenko, D. O.; Erdonmez, C. K.; Wang, L.-W.; Alivisatos, A. P. *Science* **2007**, *317*, 355.

(29) Noda, Y.; Orihashi, M.; Nishida, A. I. *Journal of the Japan Institute of Metals* **1997**, *61*, 180.

(30) Dzhafarov, T. D.; Serin, M.; Oren, D.; Sungu, B.; Sadigov, M. S. *Journal of Physics D - Applied Physics* **1999**, *32*, L5.

(31) Lyubomirsky, I.; Lyakhovitskaya, V.; Triboulet, R.; Cahen, D. *Journal of Electronic Materials* **1997**, *26*, 97.

(32) Orihashi, M.; Noda, Y.; Kaibe, T. H.; Nishida, I. A. *Journal of the Japan Institute of Metals* **1997**, *61*, 241.

(33) Mokari, T.; Aharoni, A.; Popov, I.; Banin, U. *Angewandte Chemie - International Edition* **2006**, *45*, 8001.

(34) Reiss, P.; Bleuse, J.; Pron, A. *Nano Letters* **2002**, *2*, 781.

(35) Sahu, A.; Qi, L. J.; Kang, M. S.; Deng, D. N.; Norris, D. J. *Journal of the American Chemical Society* **2011**, *133*, 6509.

(36) Dabbousi, B. O.; RodriguezViejo, J.; Mikulec, F. V.; Heine, J. R.; Mattoussi, H.; Ober, R.; Jensen, K. F.; Bawendi, M. G. *Journal of Physical Chemistry B* **1997**, *101*, 9463.

(37) Hines, M. A.; Guyot-Sionnest, P. *Journal of Physical Chemistry* **1996**, *100*, 468.

(38) Jain, P. K.; Beberwyck, B. J.; Fong, L. K.; Polking, M. J.; Alivisatos, A. P. *Angewandte Chemie - International Edition* **2012**, *51*, 2387.

(39) Klimov, V. I.; Mikhailovsky, A. A.; McBranch, D. W.; Leatherdale, C. A.; Bawendi, M. G. *Science* **2000**, *287*, 1011.

(40) Park, Y. S.; Malko, A. V.; Vela, J.; Chen, Y.; Ghosh, Y.; Garcia-Santamaria, F.; Hollingsworth, J. A.; Klimov, V. I.; Htoon, H. *Physical Review Letters* **2011**, *106*, 187401.

(41) Jha, P. P.; Guyot-Sionnest, P. *ACS Nano* **2009**, *3*, 1011.

(42) Spinicelli, P.; Buil, S.; Quelin, X.; Mahler, B.; Dubertret, B.; Hermier, J. P. *Physical Review Letters* **2009**, *102*, 136801.

(43) Wang, X. Y.; Ren, X. F.; Kahen, K.; Hahn, M. A.; Rajeswaran, M.; Maccagnano-Zacher, S.; Silcox, J.; Cragg, G. E.; Efros, A. L.; Krauss, T. D. *Nature* **2009**, *459*, 686.

(44) Ekimov, A. I.; Kudryavtsev, I. A.; Ivanov, M. G.; Efros, A. L. *Journal of Luminescence* **1990**, *46*, 83.

(45) Gelmont, B. L.; Dyakonov, M. I. *Soviet Physics Semiconductors - USSR* **1972**, *5*, 1905.

(46) Pankove, J. I. *Optical Processes in Semiconductors*; Prentice-Hall: Englewood Cliffs, N.J., 1971.

CHAPTER 4

ELECTRICAL TRANSPORT IN DOPED CdSe NANOCRYSTAL ASSEMBLIES*

4.1 OVERVIEW

As discussed in the previous chapter, we have successfully doped CdSe nanocrystals with Ag impurities and investigated their optical properties. While Ag is expected to be a substitutional acceptor, we observe non-monotonic trends in the fluorescence which suggests that Ag changes from an interstitial (*n*-type) to a substitutional (*p*-type) impurity with increased doping. In this chapter, we study electrical transport in Ag-doped CdSe nanocrystal assemblies with the aid of thin film transistors and use the results to explain the trends observed from our optical data. Furthermore, we investigate the influence of another dopant – aluminium – on the charge transport in CdSe nanocrystal films.

4.2 INTRODUCTION

The ability of colloidal nanocrystals (NCs) to be cast as films, with very high degree of order, presents an opportunity to engineer their band structure. These NC solids rely on interactions facilitated by the long surfactants and the drying solvent. Colloidal

* This chapter is reproduced with permission from Moon Sung Kang, Ayaskanta Sahu, David J. Norris, and C. Daniel Frisbie, "Size-Dependent Electrical Transport in CdSe Nanocrystal Thin Films," Nano Letters **2010**, 10 (9), 3727 (DOI: 10.1021/nl102356x) Copyright © 2010 American Chemical Society, Ayaskanta Sahu, Moon Sung Kang, Alexander Kompch, Christian Notthoff, Andrew W. Wills, Donna Deng, Markus Winterer, C. Daniel Frisbie, and David J. Norris, "Electronic Impurity Doping in CdSe Nanocrystals," Nano Letters **2012**, 12 (5), 2587 (DOI: 10.1021/nl300880g) Copyright © 2012 American Chemical Society and Andrew W. Wills , Moon Sung Kang , Katherine M. Wentz , Sophia E. Hayes , Ayaskanta Sahu , Wayne L. Gladfelter and David J. Norris, "Synthesis and characterization of Al- and In-doped CdSe nanocrystals," Journal of Materials Chemistry **2012**, 22, 6335 (DOI: 10.1039/C2JM00068G) Copyright © The Royal Society of Chemistry 2012.

semiconductor (SC) NCs are typically capped with bulky organic molecules such as dodecanethiol, hexadecylamine, oleylamine, dodecylphosphonic acid, oleic acid, tri-*n*-octyphosphine and tri-*n*-ctylphosphine oxide. While these surfactants are essential to prevent aggregation and keep the NCs dispersed in various solvents thus providing immense chemical flexibility, this shell of organic ligands surrounding the inorganic crystalline NC core acts as an electrically insulating barrier and seriously hinders charge transport in NC films. Charge transport in NC films is inherently different from that in bulk inorganic semiconductors due to the potential barrier that exists at the boundary of each NC, and an even higher potential barrier due to the organic capping layer, which inhibits charge transport. Thus strategies need to be devised to improve the conduction in NC films for potential use in electronic and optoelectronic devices. However, prior to that, one needs to understand the mechanism of charge transport in these films which is discussed in the following section.

4.3 CHARGE TRANSPORT IN NANOCRYSTAL SOLIDS

4.3.1 Transport between Resonant Sites

Interparticle charge transport, which can be described as transport between sets of localized states separated by potential walls, is the key rate limiting step in conduction in NC films. When two resonant energy-levels (say two NCs of the same size and thus at the same energy level) are separated by a barrier of higher energy (ligands which lend a finite potential barrier), charge transport between them is classically forbidden. Quantum mechanically, however, the wave-functions on the two sites decay exponentially in the barrier, and the overlap between them results in a finite probability of *tunneling*.[1] According to the Wentzel-Kramers-Brillouin (WKB) approximation, the resonant tunneling rate (Γ) between two sites is given by [2-4]

$$\Gamma = \Gamma_0 \exp\left[-\frac{1}{\hbar}\sqrt{2m^* E_a}\,R\right] \tag{4.1}$$

where, m^* is the effective mass of the charge carrier, R is the width of the barrier (spatial edge-to-edge distance between the NCs due to ligands) and E_a corresponds to its height. Γ_0 is the rate at vanishing barrier height or width. For simplicity the exponent is often written as $-2R/a$, where a represents the decay of the squared wave-function in the barrier and is called the localization length. One can immediately observe that the tunneling rate varies exponentially with the separation between the NCs. Thus, decreasing the separation *i.e.* reducing the length of the ligands would be one viable strategy to increasing the tunneling rate of charge carriers between NCs. The height of the barrier can be reduced effectively by introducing cross linking agents as well.[5,6]

4.3.2 Transport between Disordered Non-Resonant Sites

The above expression (4.1) assumes tunneling between resonant sites *i.e.* an ideal scenario in which one has a sample of monodisperse NCs with homogeneous electronic states. Charge transfer between two NCs is most efficient when their energies are equal. However, the energetic landscapes of NC films are not usually resonant and are subject to large degrees of disorder, even if not obviously visible in transmission electron microscopy (TEM) images. There exists a finite size and shape dispersion in NCs. As the energy levels of these NCs are strongly size dependent, this size distribution always leads to a finite distribution of orbital energies in a NC film. Disorder can also occur in NC films due to differences in packing which leads to variation in widths of the tunneling barrier.

As a result, charge transport is *non-resonant*: each time a charge carrier moves from one site in the material to another, energy has to be absorbed or emitted during the transition (Figure 4.1). This process of *non-resonant tunnelling* is also called *hopping*. The term *hopping*, previously used to describe a thermally activated conduction mechanism, has also been broadly used in literature to explain charge transport between two localized states.[7] In this terminology, the emphasis lies on whether the transport occurs *between* localized states or not, rather than *how* the transport is occurring. Thus, even charge transport via tunneling can be named *hopping* if the charge transport occurs

between two localized states.[8] For example, although models such as the "*Nearest Neighbor Hopping*" or the "*Variable Range Hopping*" contain the term *hopping*, the physics is based on tunneling. To avoid any confusion, when we refer to just hopping here, we shall be addressing the thermally activated process.

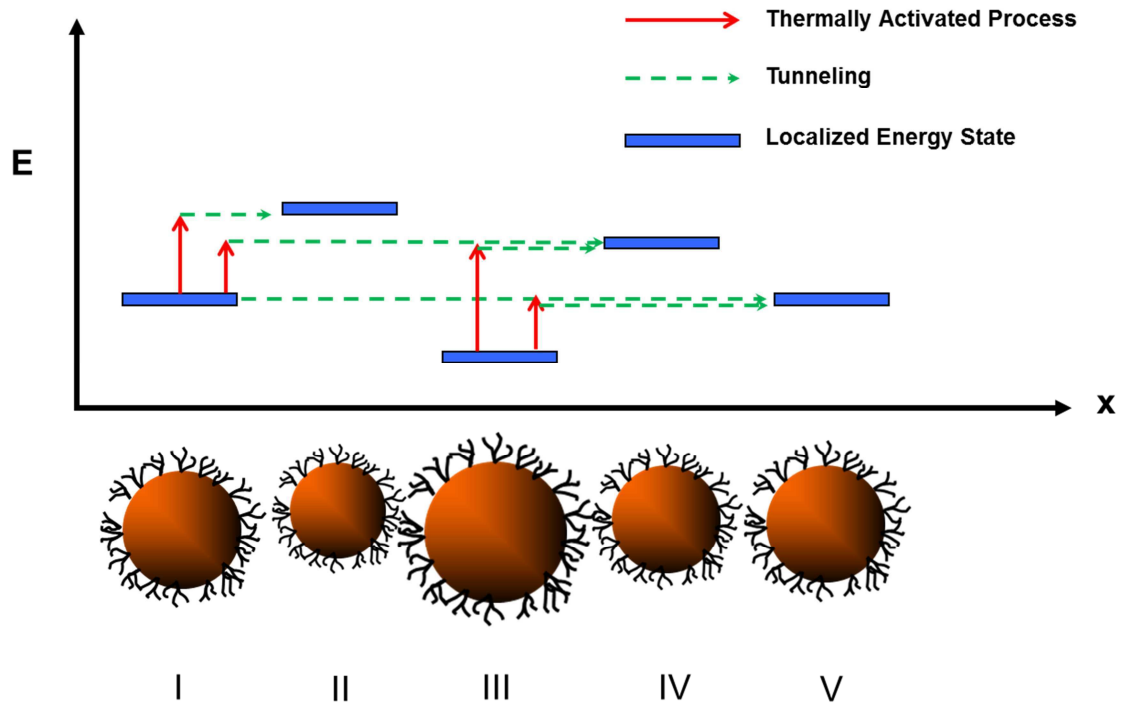

Figure 4.1: Schematic description of hopping following the Miller-Abraham expression.

It is noteworthy, that, at any given temperature, charge transport can proceed through both a hopping and a tunneling mechanism, with varying degrees of dominancy. To describe a hopping rate, an expression that contains the energy mismatch ΔE between initial and final sites is required. In 1960, Miller and Abrahams[9] derived such an expression wherein the hopping probability is given by

$$\Gamma = \Gamma_0 \exp\left[-\frac{2R}{a}\right] \times \exp\left[-\frac{\Delta E}{k_B T}\right] \qquad \text{for } \Delta E > 0 \qquad (4.2)$$

$$\Gamma = \Gamma_0 \exp\left[-\frac{2R}{a}\right] \qquad \text{for } \Delta E \leq 0$$

Since the conductivity is directly proportional to the hopping rate, any expression that describes the conductivity in a sample should also take into account the dependence

of hopping rate on the barrier width and temperature. In general, the temperature dependency of conductivity, σ, can be expressed by[8]

$$\sigma \sim \exp\left[-\left(\frac{T_0}{T}\right)^n\right]$$

where, T_0 is a constant. At very high temperatures, thermally activated hopping is the dominant conduction mechanism (n=1), following Arrhenius-type temperature dependence. As the temperature decreases, the hopping mechanism is suppressed due to lower thermal energies, and the tunneling mechanism starts to dominate. Charge transfer occurs via sequential tunneling between the nearest neighboring localized states called *Nearest Neighbor Hopping* (NNH, n=1). In this temperature regime, the conductivity still follows the Arrhenius-type temperature dependence with lower activation energy than that of the hopping mechanism. As temperature decreases further, the energy disorder in electronic states starts to gain prominence in determining tunneling probability. This leads to origin of *Variable Range Hopping* (VRH).

When the tunneling probability is given by equation 4.2, it depends exponentially on the distance between initial and final site and on the increase in energy. Consider Figure 4.1; when a charge moves from *e.g.* site I to site II it minimizes the tunneling distance, but it has to pay for this because the energy mismatch is large. Tunneling from site I to site V minimizes ΔE, but corresponds to a larger value of R. In general there is an optimum combination of R and ΔE that maximizes the total tunneling probability. As the second term in equation 4.2 decreases with increasing temperature, the first term becomes more important resulting in a smaller optimum R. Thus, the balance between distance and energy dependence determines the temperature dependence of conductivity in disordered systems. This balance depends on (i) the expression for the tunneling rate, and (ii) the energy dependence of the distance between sites $R(\Delta E)$. In this temperature regime, it is possible that the energy cost of tunneling to a distant site is smaller than the tunneling to a neighboring site, and tunneling to a distant site becomes the most efficient tunneling route (Mott-VRH with n=1/4).[10] If the temperature is lowered further, Coulomb

interactions between electrons must be taken into account and leads to Efros and Shklovskii-variable range hopping (ES-VRH with n=1/2).[3,10]

4.3.3 Coulombic Charging Energy

In addition to the above factors, there is another parameter that has an important contribution to charge transport in these disordered systems. When a charge carrier is transferred into a NC, the carrier polarizes the dielectric medium of the NC. Since the dielectric screening length of a NC is in general larger than its radius, the electron induces negative charge density on the surface of NC which leads to a Coulombic interaction between the carrier, the dielectric medium and the neighboring states. Once the electron hops to a neighboring state which is at a different energy level, the charge density is now localized at a different level. The entire system now reacts to this change by adjusting their respective energy states. This interaction demands that a finite amount of energy needs to be paid always for a hopping event to occur. At higher temperatures, thermal energy washes out this effect but at lower temperatures, the Coulomb potential becomes increasingly significant. At very low temperatures, this energy (also known as the Coulomb blockade) sets the minimum penalty that needs to be paid for a hopping event to occur and is given by

$$E_C = \frac{\beta e^2}{4\pi\varepsilon\varepsilon_0 R}$$

where β is a numerical coefficient equal to 0.35, ε is dielectric constant of the medium and R is the radius of the NC.[11]

4.4 STRATEGIES TO IMPROVE CONDUCTIVITY IN NANOCRYSTAL FILMS

As discussed in the previous section, the bulky organic ligands on the surface of the NCs hinder charge transport. One simple way to remove these ligands and reduce interparticle spacing would be through high temperature annealing of the NCs. However, annealing often leads to sintering of NCs (and hence one loses the size-dependent properties of the material) and at times also leaves behind unwanted carbon species.[12,13]

On one hand, while removing these ligands would lead to higher conductivities, more often than not, it generates dangling bonds on the surface and mid-gap states which acts as charge carrier traps.[14] To avoid this, ligand exchanges with short chain ligands, which reduce the interparticle separation as well as passivate the surface, have also been used to good effect.[15] This approach effectively reduces the size of the potential barrier and increases the coupling between the particles. Typical short chain ligands include pyridine[16] and 1-butylamine.[17] With these systems, ligand exchange is accomplished with the particles dispersed in solution and then the NCs are deposited as a thin film. Mild annealing or applying vacuum removes the ligands leading to conductive assemblies. A typical drawback of this approach is that the ligand-exchanged particles are not very stable in solution anymore which often leads to aggregation

To avoid this scenario, ligand exchange is carried out within NC films instead. This approach involves immersing or dipping a NC film capped with bulky ligands into a solution containing a stoichiometric excess of the new short-chain capping ligands such as ethanedithiol,[18] sodium hydroxide[19-21] or hydrazine.[22] The mobilities of these SC NC systems are competitive with the best organic materials. However, they are still orders of magnitude worse than bulk SCs.

Recently, huge advances have been made in obtaining fairly conductive NC assemblies, mobilities of which are comparable to those in bulk. Most notably, replacing the bulky ligands with soluble molecualr metal chalcogenide complexes (MCCs) such as SnS_4^{4-}, $Sn_2Se_6^{4-}$, $In_2Se_4^{2-}$, and $Ge_2S_{10}^{4-}$ resulted in NCs which could be dispersed in polar solvents like water, formamide and dimethylsulfoxide.[23-25] Also, on mild heating after deposition onto thin films, these Zintl ions decompose to form their respective chalcogenides which not only decreases the inter-particle spacing even further but also "sticks" the particles together forming a robust and conductive NC assembly. Other successful approaches include replacing organic capping ligands on chemically synthesized NCs with metal-free inorganic ions[26] such as S^{2-}, HS^-, Se^{2-}, HSe^-, Te^{2-}, HTe^-, TeS_3^{2-}, OH^- and NH^{2-} and thiocyanates[27] (SCN^-).

4.5 CHARGE TRANSPORT IN CdSe NANOCRYSTALS

We need to investigate the charge transport in Ag-doped nanocrystals to probe the influence of the electronically active impurities. However, in order to do so, we must first understand the transport in undoped CdSe nanocrystals. A complete assessment of charge transport in CdSe nanocrystals will, require an examination of both the size- and temperature-dependence of conduction in these semiconductor nanocrystal films.

Thin-film transistors (TFTs) are used as the test structure to probe the fundamental transport metrics, including carrier type, turn-on voltage, and mobility. Electrical conductance is measured from electrical current through an assembly of semiconductor nanocrystals under an electrical field between two electrodes. Coupling a gate electrode with the assembly allows electrostatic control over carrier concentration within the nanocrystal layer.[22] A three terminal electronic device which employs this working principle is known as a field-effect transistor (FET).[28,29] It consists of three electrodes (the source, drain, and gate electrodes), a layer of dielectric material (gate dielectric), and a layer of semiconductor (nanocrystals in our case) (Figure 4.1).

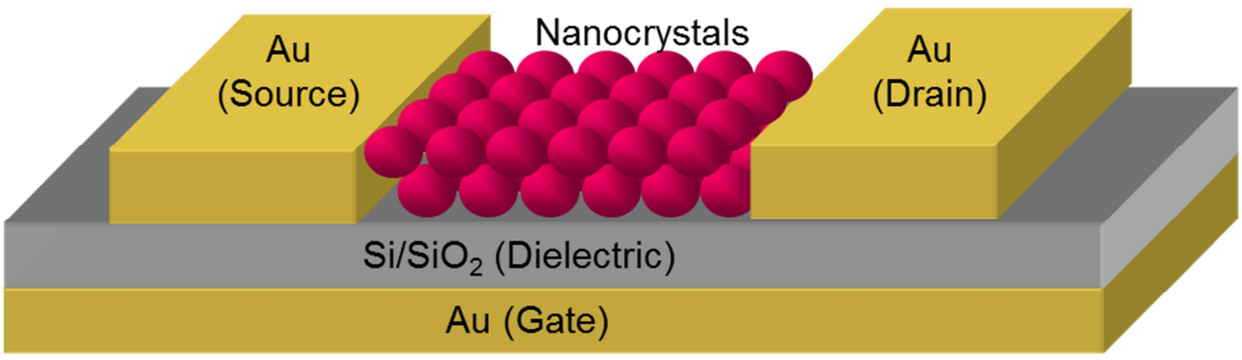

Figure 4.1: Schematic diagram of a field-effect transistor.

The current–voltage (*I–V*) characteristics of TFTs measured as a function of temperature allow us to investigate the mechanism of carrier transport through nanocrystal films. We use six different particle diameters and observed systematic reductions in device turn-on voltage and increases in mobility with increasing nanocrystal

size.[21] The electron conduction is consistent with the nearest-neighbor-hopping mechanism in which particle size impacts both the activation energy and the pre-exponential factor for the carrier mobility. Because these results focus on the role of particle size, which is the most characteristic parameter of nanocrystals, they provide fundamental information for understanding charge transport in CdSe nanocrystal films.

To control the carrier concentration in the films, we employed a high-capacitance gel electrolyte as the gate-dielectric material for the TFTs.[30] The gel is a self-assembled network of tri-block copolymer infused with an ionic liquid, and it has several advantages for charge transport experiments. First, as an electrolyte, it enables extremely large carrier densities to be obtained, on the order of ~1 electron per particle or ~10^{14} electrons/cm^2, through electrochemical charging.[31] At such high carrier densities, charge traps are easily compensated, meaning the measured transport can reflect the inherent properties of the NC film much better. Second, the ion gel is readily compatible with variable temperature measurements because it does not freeze until ~220 K. Finally, the potential drop at the gel/NC-film interface can be monitored by means of a reference electrode which allows very small shifts in the conduction onset voltage (referred to as the turn-on voltage) to be detected.[32]

Specifically, we used ion gels comprising the triblock copolymer poly(styrene-*block*-methylmethacrylate-*block*-styrene) (PS-PMMA-PS) (10 wt%) and the ionic liquid 1-ethyl-3-methylimidazolium bis(trifluoromethylsulfonyl)imide ([EMIM][TFSI]) (90 wt%). The gels were prepared by a procedure described previously (see Section 4.8.3 for details).[31] The polymer network in the ion gel provides solid integrity to the electrolyte, while not appreciably changing the ionic conductivity.

Separately, six different sizes of CdSe NCs, passivated primarily with trioctylphosphine, trioctylphosphine oxide, hexadecylamine, and dodecylphosphonic acid as surface ligands, were prepared by modified literature methods (see Section 3.5.2 for details).[33] The optical absorbance spectra of these CdSe NCs are shown in Figure 4.2a along with diameters determined from a published calibration.[34]

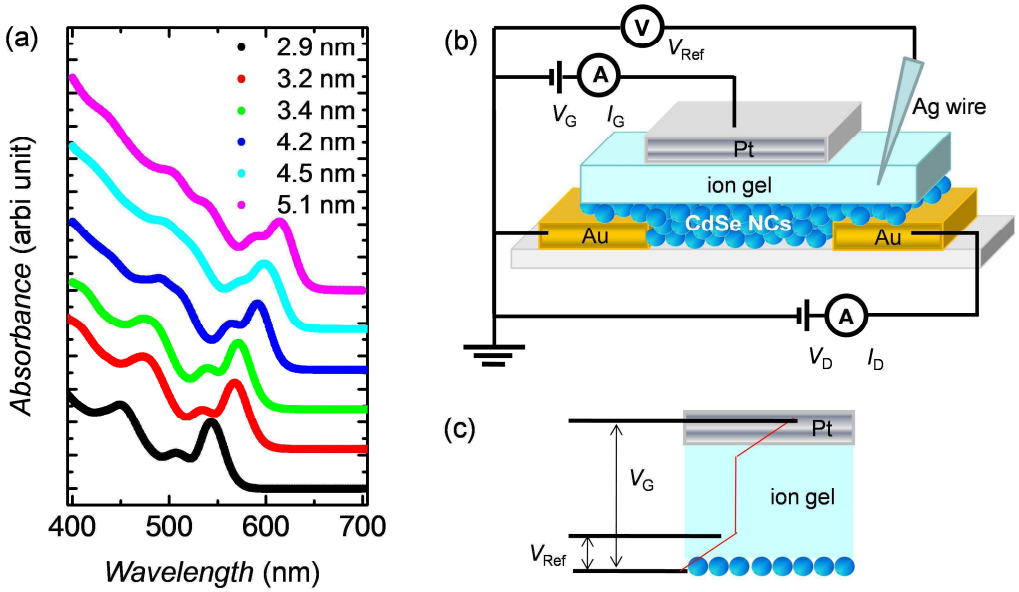

Figure 4.2: (a) Optical absorbance spectra of six different sizes of CdSe NCs dispersed in hexane. (b) Schematic cross-sectional diagram of an ion-gel-gated CdSe NC TFT (not to scale). The length and the width of the channel varied from 100 to 200 μm and 1 to 2 mm, respectively. (c) Schematic diagram of a gate electrode/ion gel/NC film in cross section (not to scale). For a given gate voltage, V_G, the potential drop mostly occurs at the gate-electrode/ion-gel and ion-gel/NC-film interfaces. Therefore, by measuring the reference potential, V_{Ref}, relative to the grounded source electrode, the potential drop at the ion-gel/semiconductor interface can be accurately monitored.

Figure 4.2b shows a schematic cross section of an ion-gel-gated CdSe NC TFT that was fabricated by the following procedure. In a nitrogen glove box, spin-coated films of NCs (~50 nm thick) were prepared from a 20 mg/ml dispersion of CdSe NCs in anhydrous octane on a Si/SiO_2 substrate that was pre-patterned with source and drain Cr/Au (2.5 nm/37.5 nm) electrodes. The length (L) and the width (W) of the channel varied from 100 μm to 200 μm and from 1 mm to 2 mm, respectively. To improve the conduction of the as-deposited insulating films, they were chemically treated with 0.08 M NaOH in anhydrous methanol for 10 min. The role of NaOH was to remove the original bulky ligands and form cadmium hydroxide complexes.[19,20] The treatment resulted in a reduction of the interparticle spacing to ~0.2 nm, which was obtained from X-ray scattering, while retaining the excitonic features in the absorption spectra. Due to the reduced interparticle spacing, micron-wide cracks were formed in the NC films. These were filled with a second round of spin-coating from the same CdSe NC dispersion,

followed by another cycle of NaOH treatment. The resulting films were then continuous without noticeable cracks. On top of the chemically treated film, the ion gel was spread over the channel region (~120 μm thick). Finally, a platinum electrode (area, A = 3–6 × 10^{-3} cm^2) was laminated to the top of the ion gel to serve as the gate electrode. The entire device fabrication was performed inside a nitrogen glove box.

Figure 4.3 displays typical I–V characteristics and the capacitance–voltage (C–V) characteristic obtained from a film of 4.2 nm CdSe NCs measured at room temperature. All electrical characterization was performed in a Desert Cryogenics (Lakeshore) probe station under vacuum (~10^{-6} Torr). An oxidized Ag wire was used as the reference electrode.[32] Figure 4.3a displays the drain current–gate voltage (I_D–V_G) characteristic of the film obtained at a constant drain voltage (V_D) of 0.1 V. V_G was swept from 0 to 2.5 V at a rate of 100 mV/sec. The curve reveals characteristic n-channel conduction in which I_D increases more than three orders of magnitude with positive V_G. Also, a pronounced hysteresis was observed such that I_D for the reverse sweep (R) was higher than for the forward sweep (F). By recording the reference potential (V_{Ref}) relative to the grounded source using the Ag reference wire embedded in the ion gel during the V_G sweep, the potential drop across the ion-gel/NC-film interface was measured [see Figure 4.3c]. Note that the measured reference potential did not depend on the location of the reference wire within the gel. Figure 4.3b displays I_D as a function of V_{Ref} which shows negligible hysteresis compared to that shown in Figure 4.3a. Because the measured reference potential corrects for the potential drop across the ion-gel/NC film interface, the disappearance of the hysteresis in I_D–V_{Ref} plot indicates that the hysteresis of the original I_D–V_G trace is likely the result of sluggish motion of ions at the ion-gel/gate-electrode interface, while the penetration of the electrolyte into the NC films is reversible. Finally, Figure 4.3c shows an I_D–V_D characteristic of the film measured at five different V_Gs, which also demonstrates typical n-channel conduction through the film.

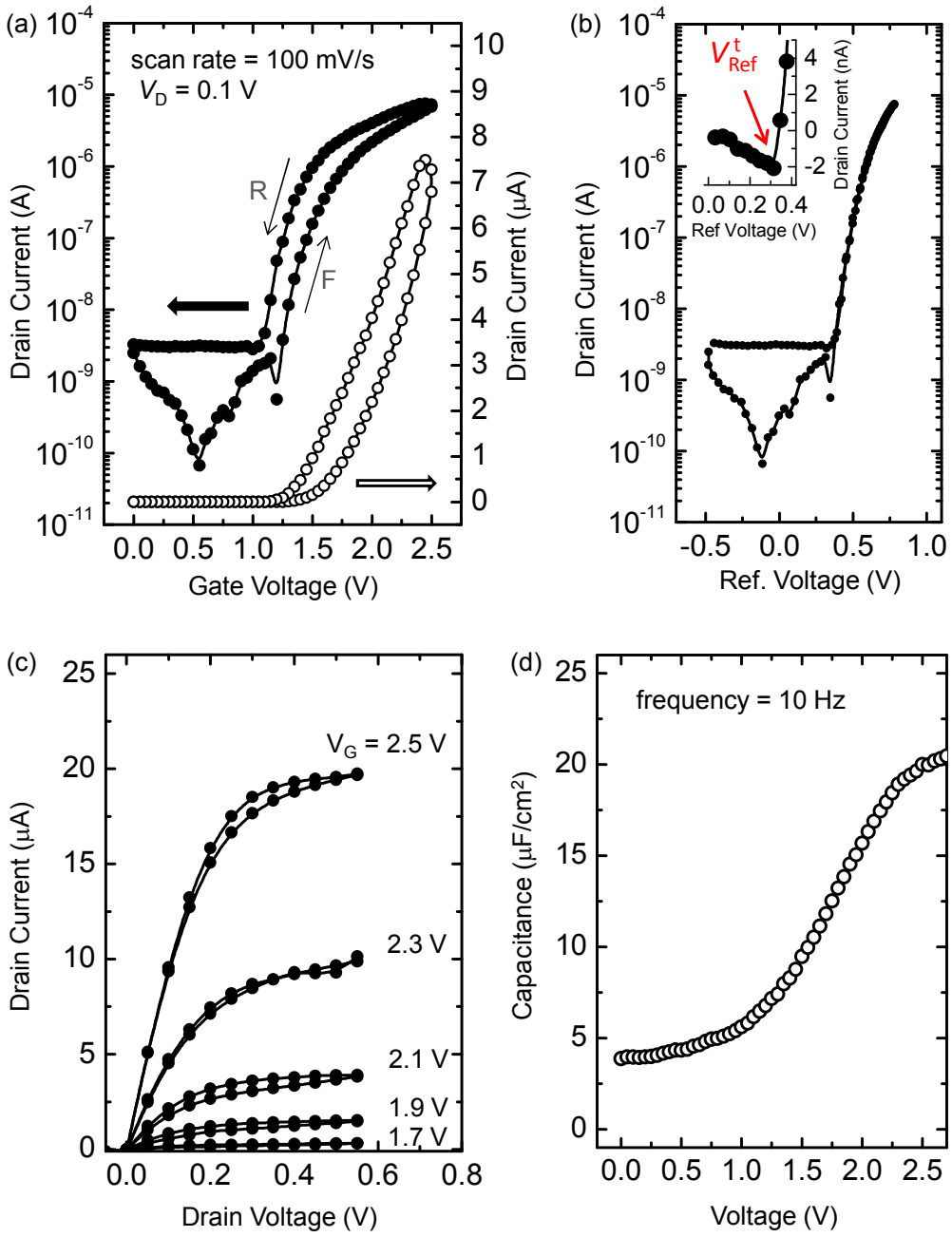

Figure 4.3: (a) I_D–V_G characteristic at V_D of 0.1 V. V_G was swept at 100 mV/sec. F and R represent the forward and the reverse sweep directions. (b) I_D–V_{Ref} characteristic at V_D of 0.1 V. V_{Ref} was measured simultaneously during the V_G sweep. The referenced voltage at the onset of conduction is named V^t_{Ref} and is indicated with a red arrow. (c) I_D–V_D characteristic at different V_Gs. V_D was swept at 100 mV/sec. (d) C–V characteristic of a gate-electrode/ion-gel/CdSe-NC-film test structure embedded in the TFT. The measurement was performed at a frequency of 10 Hz.

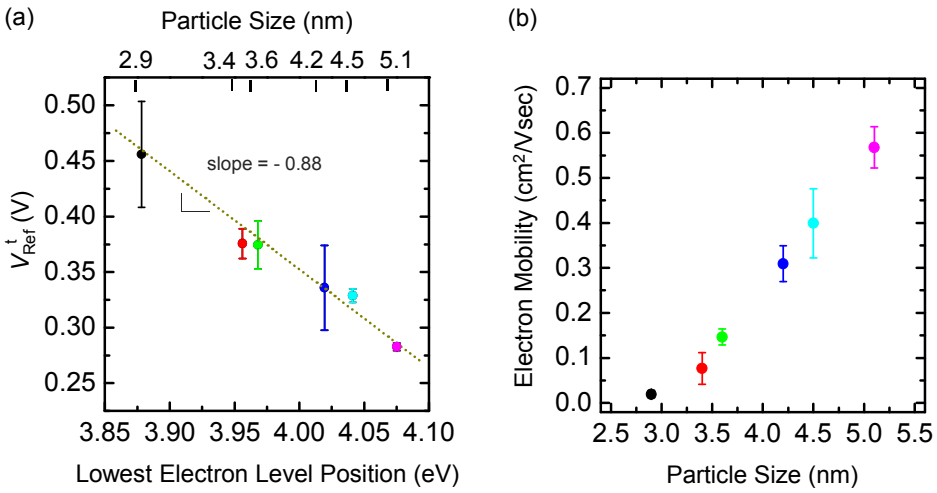

Figure 4.4: (a) Size dependence of V^t_{Ref}. The values were averaged from 3–5 devices and the error bar represents one standard deviation. The position of the lowest unoccupied electronic state for a given sized NC was estimated as described in the text. The slope of the trend line is –0.88 and the R^2 value of the linear regression is 0.933, implying a strong correlation between V^t_{Ref} and the position of the electron level. (b) Size dependence of mobility. Mobilities were computed at a gate voltage of 2.5 V. The values were averaged from 3–5 devices and the error bar represents one standard deviation.

As mentioned above, accurate measurement of the potential drop across the ion-gel/NC-film interface by the reference electrode allows determination of the turn-on voltage, V^t_{Ref}. This parameter denotes the interfacial potential at which free carriers are injected into the NC films. Because the injection of free carriers leads to an onset of conduction, V^t_{Ref} can be determined from the voltage at which I_D sharply rises, as indicated with a red arrow in the inset of Figure 4.3b. Figure 4.4a shows the average values of V^t_{Ref} that were obtained from 3–5 devices for each of our six different sizes of CdSe NCs. These values were plotted *versus* the absolute energies of the lowest conduction-band state in each of the samples. These energies were estimated by proportioning the energy shifts of the first absorption feature into electron and hole levels using the simple effective mass approximation and then combining the electron offsets with the position of the conduction-band edge in CdSe.[35] The data show a clear correlation between the position of the electron levels and V^t_{Ref}. Smaller applied voltages were necessary to inject electrons into films of larger NCs which have lower electron levels.[36] Moreover, the slope of the trend line is close to 1, which demonstrates a nearly

one-to-one correspondence between the turn-on voltage and the lowest electron level. This indicates that the position of this level, rather than trap states, determines the potential required for carrier injection in our devices.

Electron mobilities (μ) in these NC TFTs were computed using the equation $\mu = (L/W)(I_D/enV_D)$ which is derived from Ohm's law. Here e and n are the elemental charge and sheet carrier density, respectively. Two independent methods were employed to obtain n. The first method involved measuring the C–V characteristics of the ion gel in the TFTs using an HP 4192A LF impedance analyzer, and then applying the equation $n = (\int C\mathrm{d}V)/e$ to determine the carrier density (cm^{-2}).[31] For the measurement, the source and drain electrodes were grounded and a bias was applied to the gate electrode. Figure 4.2d displays the C–V characteristic at a frequency of 10 Hz obtained for the same film from which the I–V characteristics were taken. Capacitance increased with larger applied voltage showing the electron accumulation during the voltage sweep. An electron density of 1.3×10^{14} carriers/cm^2 (~1 carrier/particle)[31] was obtained from the integral between 1.15 V (the corresponding V_G value at V_{Ref}^{t}) and 2.5 V. The large carrier densities (greater than 10^{14} carriers/cm^2) are a result of the high capacitance of the gel electrolyte and the penetration of the electrolyte into the NC lattice.[30] Using this n, an electron mobility of 0.3 cm^2/Vsec was obtained. Note that penetration of electrolyte into NC films does not affect the average mobility calculation using the equation above. The calculation of μ is based on Ohm's law and requires only that the sheet carrier density n is known. An effective two dimensional sheet density can be accurately defined even if the transport in the NC film is distributed through the film thickness.

The second method employed to obtain n involved measuring the gate current–gate voltage (I_G–V_G) characteristics at different gate voltage sweep rates (r_v). From this method, an electron density of 1.1×10^{14} carriers/cm^2 and an electron mobility of 0.4 cm^2/Vsec were obtained. These values are reasonably consistent with those obtained from the first method above. To our knowledge, these mobilities are amongst the highest values that have been achieved to date in CdSe NC films. We attribute such high

mobilities to (i) the high induced carrier densities obtained from electrolyte gating,[37,38] which results in substantial trap filling and (ii) the short interparticle distance between NCs resulting from NaOH treatment. (It has been suggested that OH^- groups are the shortest ligands for interparticle coupling.[19,20]) Also, note that by using the ion-gel gate dielectric, high electron mobilities in our CdSe NC films were achieved while retaining the integrity of the solid state device, which is an important practical requirement for applications of CdSe NC devices.

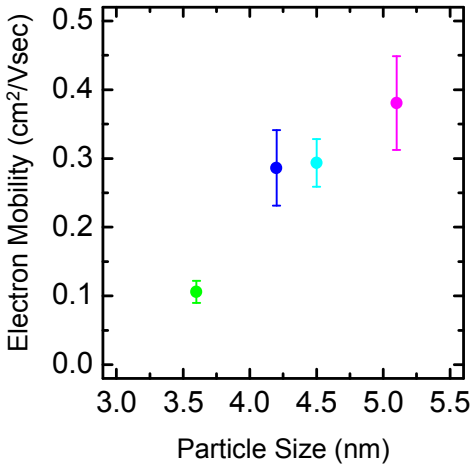

Figure 4.5: Size dependence of mobility. Mobilities were computed at a carrier concentration of 1×10^{14} carriers/cm^2. The values were averaged from 3–5 devices and the error bar represents one standard deviation of the values.

Figure 4.4b depicts the average mobility values that were obtained from 3–5 devices for each of our six different sizes of CdSe NCs at a fixed gate voltage of 2.5 V. Clearly, we observe an increase in electron mobility with increasing particle size, similar to the trend observed for PbSe NC films.[26] A mobility as high as 0.6 cm^2/Vsec was obtained for the largest particles (5.1 nm). In general, the mobility in NC films depends on the carrier concentration and the mobility values above, calculated at a fixed gate voltage, were not necessarily obtained at a constant carrier concentration due to the threshold voltage shift. For a more rigorous comparison, therefore, we computed mobilities for the NC films with different particle sizes calculated at a fixed carrier concentration of 1×10^{14} carriers/cm^2. However, a monotonic increase in mobility was still observed with increasing particle size, as shown in Figure 4.5.

4.6 CHARGE TRANSPORT IN SILVER-DOPED CdSe NANOCRYSTALS

After conducting the electrical studies with undoped CdSe nanocrystals, we proceed to do the same with our Ag-doped nanocrystals. As described in the previous chapter, while the optical results clearly show that the addition of a few Ag atoms per nanocrystal can cause large changes, our interpretation, in which Ag acts as a *n*-type dopant (donor) at very low concentrations and then transitions to a *p*-type donor (acceptor) as the number of Ag per nanocrystal is increased, is fairly speculative. If such a doping trend occurs, however, it should also affect electrical transport. Thus, we fabricated electrolyte-gated thin-film transistors to probe the conductivity of films of Ag-doped CdSe nanocrystals.

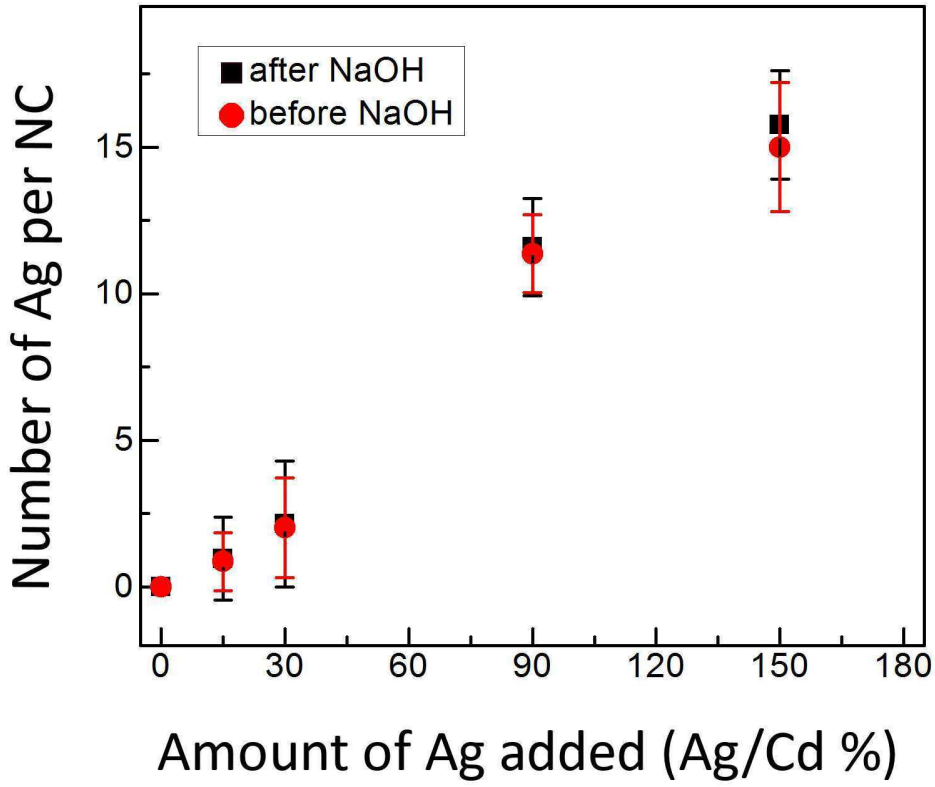

Figure 4.6: Elemental analyses of films of 3.3-nm-diameter CdSe nanocrystals. The average number of Ag atoms in the nanocrystals is plotted versus the amount of $AgNO_3$ added to the exchange solution (as a percentage of the Cd present). Electron-probe micro analysis (EPMA) was used. The analyses were performed on devices used for electrical-transport measurements before (red circles) and after (black circles) treatment with methanolic sodium hydroxide (NaOH). The values plotted were averaged from ten measurements on different points of each sample and the error bar represents one standard deviation. The data shows no significant change in the Ag concentration in the films after the NaOH treatment.

Following the protocol described in the previous sections, films of nanocrystals (~50 nm thick) were spin-coated onto Si/SiO_2 substrates that were pre-patterned with source and drain electrodes (Cr/Au). Since the as-deposited films are insulating due to the bulky ligands on the nanocrystal surfaces, we first treated the films with methanolic sodium hydroxide to remove the ligands and improve conduction.[19,20] The resulting films are *n*-type even without Ag doping. Before testing the influence of Ag, we first verified that the NaOH treatment did not affect the number of Ag per nanocrystal in the films (Figure 4.6).

For the gate dielectric, we employed an ion gel composed of 10 wt% of the triblock copolymer poly(styrene-*block*-methylmethacrylate-*block*-styrene) and 90 wt% of the ionic liquid 1-ethyl-3-methylimidazolium bis(trifluoromethylsulfonyl)imide.[30] The gel was spread over the channel region of the device. On top of the ion-gel layer, a Pt foil was attached as the gate electrode and electrical measurements were performed in an evacuated probe station (~10^{-6} Torr).

Figure 4.7a displays a schematic cross section of the device.[21] Our devices also included an oxidized silver wire as a reference electrode. This can measure the potential drop across the interface between the ion gel and the nanocrystal film under gate bias.[21] Thus, the local potential in each film at which conduction turned on could be accurately determined. Because this turn-on voltage is directly related to the energy offset between the Fermi level in the film and the conducting states in the nanocrystals at zero bias (Figure 4.7b), it can give very useful information about the influence of dopants. For example, Figure 4.7c shows measurements for transistors made from 3.6-nm-diameter CdSe nanocrystals at four different dopant concentrations. The drain current (I_D) is plotted as a function of the voltage at the reference electrode (V_{Ref}). As in previous studies, our film of undoped CdSe nanocrystals started to conduct when the interface potential (V_{Ref}) was biased positively. More specifically, I_D increased sharply with increasing positive voltage, which indicates that the charge carriers in these films are negatively charged electrons. More importantly, for doped films, Figure 4c shows that the turn-on voltage varies with impurity concentration (see inset). Assuming that the energy

of the lowest electronic level ($1S_e$) of the nanocrystals does not change significantly with light doping, the shift in the turn-on voltage for different doping concentrations is then a direct observation of changes in the Fermi level (Figure 4.7b).

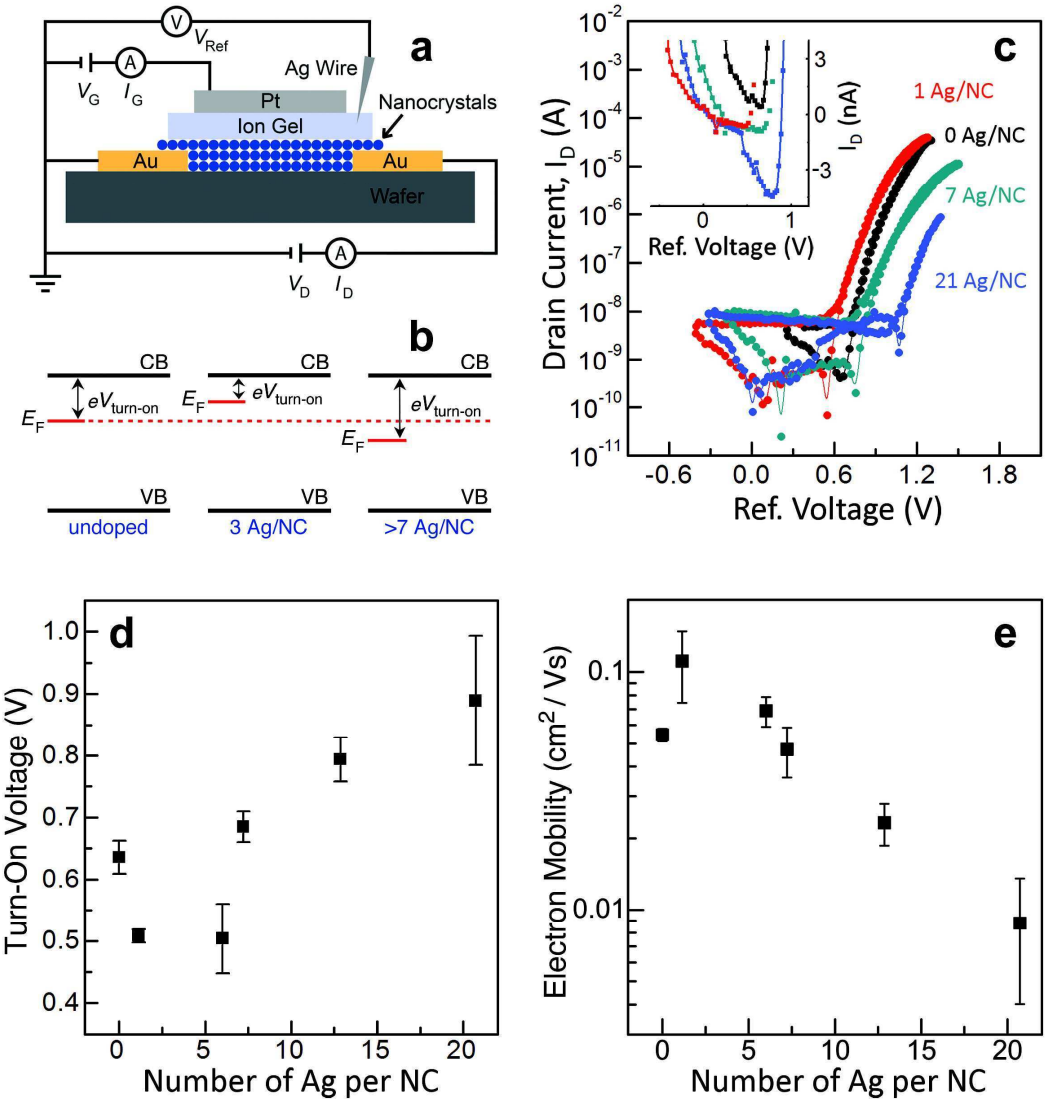

Figure 4.7: (a) Schematic cross-section (not to scale) of the ion-gel-gated thin-film transistors used to characterize the electrical properties of the doped nanocrystals (NCs). The length and width of the channel was 10 μm and 1 mm, respectively. (b) Energy-level diagram depicting the relationship between the Fermi energy, the turn-on voltage, and the conduction band for films of CdSe nanocrystals (undoped, ~3 Ag/NC, and >7 Ag/NC). (c) Absolute value of the drain current, I_D, versus the reference voltage, V_{Ref}, for 3.6-nm-diameter nanocrystals with no Ag (black), 1.0 Ag/NC (0.13% Ag, red), 7.0 Ag/NC (0.85% Ag, green), and 21 Ag/NC (2.4% Ag, blue). V_D was 0.1 V and V_{Ref} was measured from an oxidized silver wire in the ion gel. The inset shows a magnified plot of the drain current near the turn-on voltage. (d) The turn-on voltage versus the number of Ag per nanocrystal, extracted from data as in (c). (e) The electron mobility computed at a gate voltage of 2.5 V (a carrier concentration of $10^{14}/cm^2$) versus the number of Ag per nanocrystal, extracted from data as in (c). The error bars in (d) and (e) represent the standard deviation from averaging 2-5 devices. Data points without error bars are for one device.

Figure 4.7d plots the variation in the turn-on voltage for the same 3.6-nm-diameter CdSe nanocrystals at six Ag concentrations. At low doping, we observe that the turn-on voltage is smaller than that of the undoped CdSe nanocrystals. This indicates that the Fermi level shifts closer to the lowest electronic level of the nanocrystals (Figure 4.7b), which is a signature of *n*-type doping. (We have also recently reported a similar shift in Al-doped CdSe nanocrystals,[39] where Al is expected to be an *n*-type dopant – details in Section 4.7) For Ag, we see this behavior below ~6 Ag per nanocrystal. At higher dopant concentrations, the turn-on voltage reverses direction and increases above the value for undoped nanocrystals. The Fermi level now shifts away from the lowest electronic level of the nanocrystals (Figure 4.7b), which is a signature of *p*-type doping. Therefore, these non-monotonic shifts in the Fermi level support the conclusions from the optical experiments. However, we note that, while the doping clearly influenced the Fermi level, it was not possible to observe any hole conduction even at our highest dopant concentrations. It is unknown whether this is due to the inherent instability of extra holes in CdSe[40] or the large excess of electrons induced by the NaOH treatment. Unfortunately, our transistors were not gateable without the NaOH treatment.

In addition to the possibility of Fermi-level shifts, it is important to consider an alternative origin for the shifts in the turn-on voltage. Namely, it is possible that Ag cations are decorating the nanocrystal surface and inducing positive local electrostatic fields. The positive external voltage that is required to turn on conduction would then be diminished, as observed in Figure 4.7d at low doping. In this case, the measured voltage shifts would have nothing to do with the introduction of extra carriers by the dopants. However, this model has several inconsistencies with the data. First, it is difficult to explain why the turn-on voltage reverses direction at higher dopant concentration with only a surface effect. Second, we observe enhanced conduction even without the gate. As shown in Figure 4.8, the conductivity of films of doped CdSe nanocrystals increased by ~2 orders of magnitude with the addition of ~5 Ag/NC. These conductivity measurements were performed on films that were not treated with NaOH, ruling out any unexpected influence of this treatment. We also confirmed by steady-state current measurements that the enhanced conduction was not due to ionic transport of Ag cations (which would be

inherently limited). Rather, the data support the conclusion that the dopants are electronically active. Indeed, we observed this enhanced conductivity early in this project. However, because these measurements are quite hysteretic (Figure 4.8), a detailed analysis of this effect is challenging. We therefore moved to the transistors, which allow a precise determination of the Fermi level.

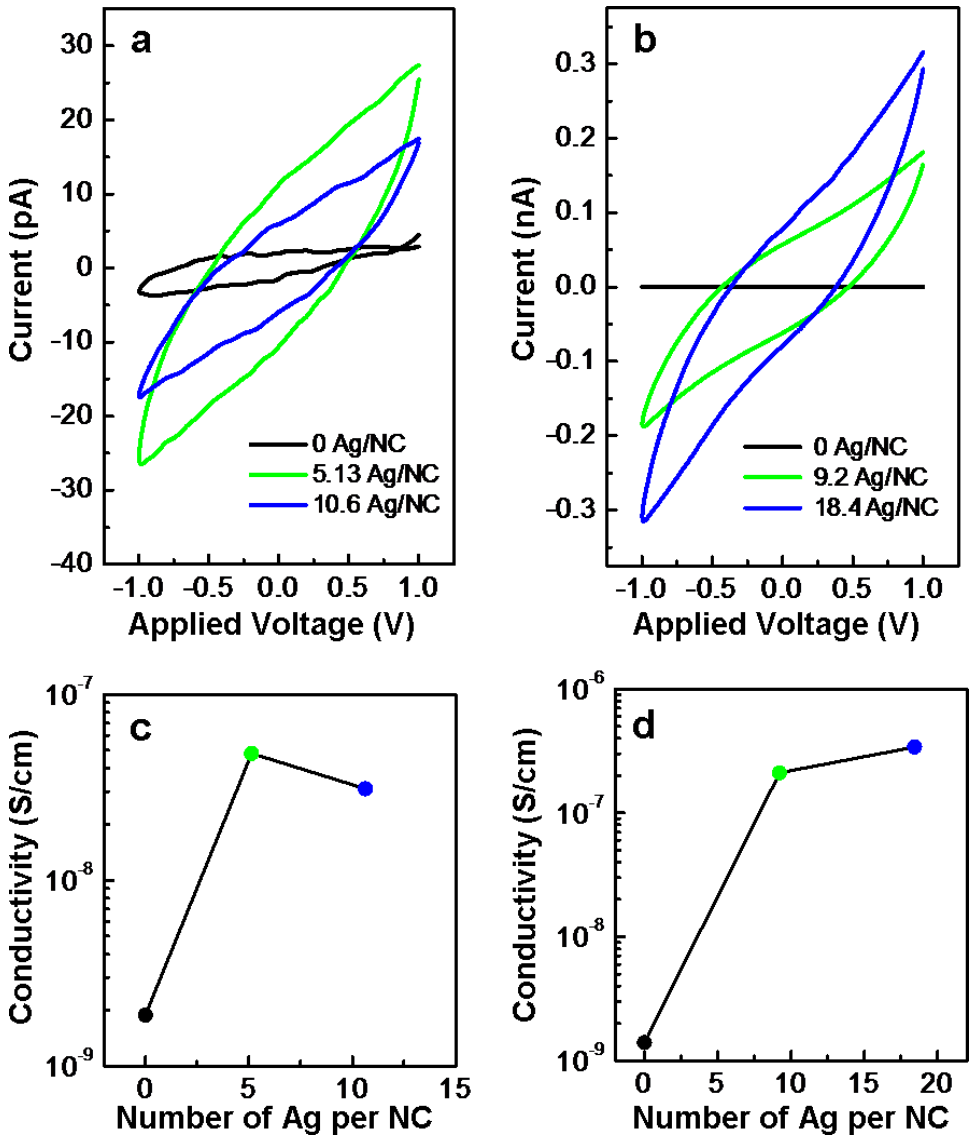

Figure 4.8: Electrical characterization of Ag-doped CdSe nanocrystals (NCs). (a) Drain current, I_D, versus the drain voltage, V_D, for 3.7-nm-diameter CdSe nanocrystals that are undoped (black) and doped with 5.13 Ag/NC (green) and 12.7 Ag/NC (blue). (b) I_D versus V_D for 4.8-nm-diameter CdSe nanocrystals that are undoped (black) and doped with 9.2 Ag/NC (green) and 18.4 Ag/NC (blue). (c) Variation in conductivity of the 3.7-nm-diameter sample in (a) with Ag doping. The black, green, and blue circles correspond to the traces in (a). (d) Variation in conductivity of the 4.8-nm-diameter sample in (b) with Ag doping. The black, green, and blue circles correspond to the traces in (b). The addition of a few Ag atoms enhances the conductivity of the NC film by ~2 orders of magnitude.

Further support for our interpretation can be found in the influence of the dopant concentration on the electron mobility of the film (Figure 4.7e). Mobility (μ) was again estimated from the equation $\mu=(L/W)\times(I_D/enV_D)$, where L and W are the channel length and width, respectively, e is the elemental charge, and n is the electron concentration, determined as previously described.[21] Because electron mobility also varies with carrier concentration, we fixed the gate-induced carrier density (at 10^{14} carriers/cm^2) and then compared electron mobilities for films of CdSe nanocrystals with different dopant concentrations. We observed that the electron mobility first increased at low dopant concentrations and then decreased gradually with further doping, again consistent with a transition from *n*- to *p*-type doping.

In bulk II-VI semiconductors, a silver atom can behave either as a *p*-type dopant[41-47] when it substitutes for the cation or as an *n*-type dopant[45,47-49] when it occupies an interstitial site. In the latter case, the valence electron from the interstitial Ag atom can be directly donated to the lattice. Interestingly, Au atoms can even form interstitial donors at low doping concentrations and substitutional acceptors at higher doping concentrations.[50] A similar mechanism might be occurring for Ag in CdSe nanocrystals. At low doping concentrations Ag atoms could act as interstitial donors. At higher concentrations, these donors could be compensated by donor-acceptor complexes, and then act as substitutional acceptors at even higher concentrations.

This mechanism could be confirmed if the local structure around the Ag dopants could be determined. In general, this is a difficult task in nanocrystals. Indeed, Mn impurities have been heavily studied, at least in part, because their local environment can be measured with electron paramagnetic resonance (EPR).[51] For other dopants, alternative techniques must be applied.[52] To address this in our system, we have begun experiments on extended X-ray absorption fine structure (EXAFS) spectroscopy to locate the Ag atoms within the CdSe lattice. Due to the low concentration of Ag, the experiments are extremely challenging. So far, our preliminary analyses for data from samples with 3.6 Ag per nanocrystal suggest only that the spectra cannot be fit with the following: (i) Ag placed in only substitutional sites of the CdSe lattice or (ii) Ag placed in

a separate tetragonal phase of Ag_2Se. The latter is observed if the cation exchange process leads to multi-phase Ag_2Se-CdSe nanocrystals.[53] In other words, the data suggests that at low concentrations, the Ag atoms are not substitutional dopants only and they do not form a separate Ag_2Se phase. Therefore, these preliminary findings are so far consistent with our model of having both interstitial and substitutional placement of Ag. However, further analyses and EXAFS experiments are required to determine the exact local structure of the Ag.

In combination, our optical and electrical data indicate that Ag is an electronically active impurity in CdSe nanocrystals. More generally, they suggest that if dopants are added to nanocrystals, the creation of *n*- and *p*-type films of semiconductor nanocrystals should be attainable. Our specific observations also lead to several surprising conclusions about doped nanocrystals in the lightly doped limit. First, even the first few dopants can provide electrons that alter the electrical properties of the films. Under what conditions these are available to fill band-edge electronic states, impurity-bound states, or traps is not yet known. Second, even within a small particle, the behavior of the dopant is very complicated and does not follow simple predictions. Perhaps this should have been expected since the dopant-site energetics can be more complicated than in the bulk material due to the proximity of the nanocrystal surface.[54] Certainly, these results show that further theoretical and experimental work is needed to understand specific dopant-semiconductor pairs in nanocrystals, both for fundamental understanding and use in applications.

4.7 CHARGE TRANSPORT IN ALUMINIUM-DOPED CdSe NANOCRYTALS

In addition to silver, the influence of aluminium doping on the electrical transport in films of CdSe NCs was also examined.[39] The Al-doped CdSe NCs were prepared by following a more complicated synthetic route, which separates the three steps of nucleation, dopant binding, and growth. An analysis similar to the one conducted with

Ag-doped CdSe NCs was carried out on a set of Al-doped CdSe NCs with three different dopant concentrations.

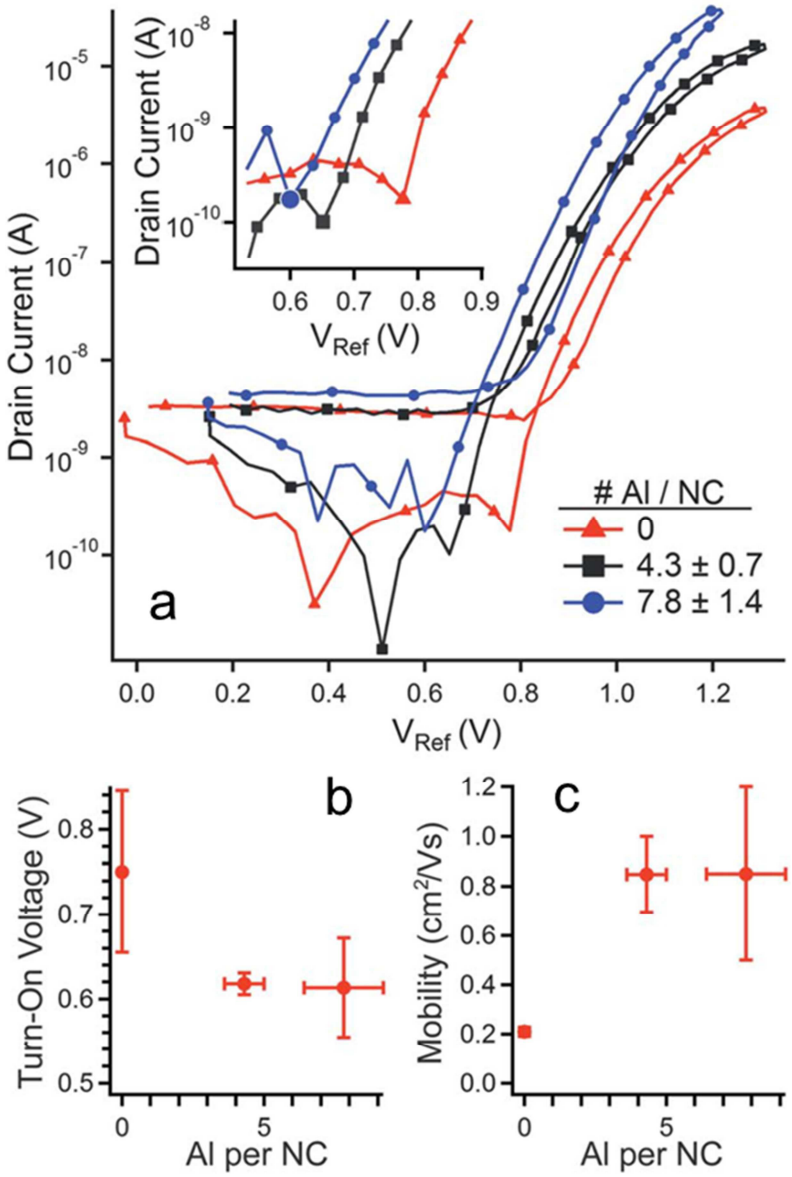

Figure 4.9: Shift in Fermi level with Al-doping. (a) Drain current (I_D) versus reference gate voltage (V_{Ref}) for thin films of CdSe nanocrystals doped with Al 0 to 8 Al / NC. The nanocrystals are 3.4 $\pm$ 0.1 nm in diameter. The drain voltage (V_D) was 0.1 V and V_{Ref} was measured during the gatevoltage (V_G) sweep. The inset shows an enlarged view of the conduction onset, with V_{Ref} at the conduction onset ($V_{Turn-On}$) marked by larger data points. (b) Change in $V_{Turn-On}$ with dopant concentration. (c) Variation of electron mobility with dopant concentration. Mobilities were computed at 10^{14} charge carriers/cm^2. (b) and (c) were derived from 3–5 devices per data point and the error bars represent one standard deviation. Adapted with permission from Wills *et al.*[39]

Figure 4.9a displays I_D as a function of V_{Ref} measured from a Ag wire reference electrode during a gate voltage sweep. The device turn-on voltage of Al-doped CdSe NC devices was reduced by 140 meV from undoped to highest doped samples (Figure 4.9b), which is a signature of *n*-type doping. Al is known to be an *n*-type donor in bulk CdSe.[55] Also, an increase in the electron mobility was observed from 0.2 to 0.9 cm^2/Vs with doping (Figure 4.9c). For comparison, these values were estimated at a fixed gate-induced carrier density (*e.g.*, at 10^{14} carriers/cm^2) following the method described earlier. This also lends further credence to the observation that Al indeed *n*-type dopes the CdSe nanocrystals.

4.8 EXPERIMENTAL SECTION

4.8.1 Chemicals and Substrates

Carbon tetrachloride (reagent grade, 99.9%), chloroform (HPLC grade, ≥99.8%), hexadecylamine (HDA, technical grade, 90%), methanol (HPLC grade, ≥99.9%), anhydrous methanol (99.8%), anhydrous ethanol (≥99.5%), octane (reagent grade, 98%), anhydrous octane (≥99%), selenium pellets (Se, 99.999%), tetrachloroethylene (TCE, spectrophotometric grade, ≥99.9%), toluene (HPLC grade, 99.9%), sodium hydroxide pellets, platinum wire (99.9%), diphenylphosphine (DPP, 98%), tri-*n*-octylphosphine (TOP, technical grade, 90%), tri-*n*-octylphosphine oxide (TOPO, technical grade, 90%), hydrochloric acid (TraceSELECT®, for trace analysis, fuming, ≥37%), and nitric acid [TraceSELECT®, for trace analysis, ≥69.0% (T)] were purchased from Sigma Aldrich. Hexanes (ACS grade) was purchased from VWR International. Reagent alcohol (histological grade, 90% ethanol, 5% methanol, and 5% butanol) and butanol were obtained from Fisher Scientific. *n*-dodecylphosphonic acid (DDPA) was purchased from PCI Synthesis. Cadmium (II) oxide (CdO, 99.999%) and silver nitrate ($AgNO_3$, 99.9995%) were purchased from Strem Chemicals. 1-ethyl-3-methylimidazolium bis(trifluoromethylsulfonyl)imide ([EMIM][TFSI]) was purchased from Solvent Innovation GmbH (Germany). All chemicals were used as delivered without further purification.

<100>-oriented, boron-doped silicon (Si) wafers (resistivity=0.005–0.01 Ωcm, thickness=525±25 μm) coated with 300 nm of thermal oxide (SiO_2) were purchased from Silicon Valley Microelectronics.

4.8.2 Transistor Measurements

For the thin-film transistors (TFTs), source and drain contacts (5 nm Cr / 35 nm Au) were patterned on Si/SiO_2 wafers using standard lift-off techniques. These wafers were then sonicated in acetone, isopropanol, and methanol (10 minutes in each), rinsed with methanol, and then transferred into a N_2 glove box. Films of nanocrystals were spin-coated (10 seconds at 900 rpm followed by 15 seconds at 1200 rpm) from a 20 mg/ml dispersion in anhydrous octane passed through a 0.2 μm PTFE filter, and were dried at room temperature for more than 1 hour. The films were then dipped into a 0.08 M solution of NaOH in anhydrous methanol for 10 minutes, rinsed with fresh anhydrous methanol, and finally annealed at 100 °C for 1 hour. To fill cracks formed during the chemical treatment, a second layer of nanocrystals was spin-coated and treated with NaOH, following the same procedure used for the first layer.

To ensure that the NaOH ligand exchange did not remove any dopants from the nanocrystal films, we performed electron-probe micro analysis (EPMA) to determine the amount of Ag in the films before and after treatment with NaOH. For these EPMA measurements, we utilized a JEOL 8900R electron-probe micro analyzer with an acceleration voltage of 10 kV and a beam current of 50 nA with a 75 μm beam diameter. Each element was analyzed in its own wavelength-dispersive spectrometer and pure metals or binary compounds were used as standards. A JEOL thin-film correction algorithm was used for the quantitative elemental analyses. Films of Ag-doped CdSe nanocrystals were spin-coated from dispersions in anhydrous octane on heavily doped Si wafers covered with a thermally grown 300-nm-thick SiO_2 layer. Data for EPMA was collected from 10 different points on each sample and analyzed. The results are summarized in Figure 4.6.

For the TFT measurements, the ion gel and Pt gate were applied on the top of the NaOH-treated nanocrystal film. The entire device fabrication was carried out in a N_2 glove box. Current–voltage (*I-V*) characteristics were measured in a Desert Cryogenics (Lakeshore) probe station with Keithley 237 and 6517A electrometers. Prior to electrical characterization, one of the probes was attached with a silver wire (25 μm diameter) that was then treated with piranha solution to form an oxidized quasi-reference electrode (Ag/Ag_2O). For capacitance–voltage (C–V) measurements on the working device, the probe station was connected to an HP 4192A LF impedance analyzer, and the voltage sweep was applied to the gate electrode while the source and drain electrodes were grounded. All the measurements were carried out under vacuum (~10^{-6} Torr).

4.8.3 Ion Gels

A symmetric poly(styrene-*block*-(methyl methacrylate)-*block*-styrene) (PS-PMMA-PS) triblock copolymer was synthesized, as previously described,[56] with block molecular weights of M_n(PS)=8.9 kg/mol and M_n(PMMA)=67 kg/mol (overall polydispersity M_w/M_n=1.15). To prepare the ion gels, PS-PMMA-PS and 1-ethyl-3-methylimidazolium bis(trifluoromethylsulfonyl)imide [EMIM][TFSI] (1:9 by weight) were dissolved in dichloromethane (CH_2Cl_2). The solution was stirred overnight, and then poured into a Petri dish. Dichloromethane was slowly evaporated at room temperature for 24 hours, and the ion-gel solution was further dried under vacuum for an additional 24 hours. After complete evaporation of the solvent, transparent ion gels were formed. They were stored in a nitrogen glove box until needed.

4.8.4 Conductivity Measurements

Films of nanocrystals (~50 nm thick) were spin-coated onto a Si/SiO_2 substrate that was pre-patterned with source and drain electrodes (Cr/Au). The films were not treated with NaOH. The I_D - V_D (current – voltage) characteristics for the 10-μm channel were measured under vacuum, and are shown in Figure 4.8. The scan rate was 750 mV/s. The conductivity was determined from the linear *I-V* relationship in the bias voltage range of -1.0 V to 1.0 V. As expected, the films were mostly insulating due to bulky ligands on the nanocrystal surface. The hysteresis observed between the forward and

reverse scans can be explained by charge traps at the surface of the nanocrystals or in the surrounding medium.

4.9 REFERENCES

(1) Cohen-Tannoudji, C.; Diu, B.; Laloë, F. *Quantum Mechanics*; Wiley: New York,NY, 1977.

(2) Fowler, A. B.; Wainer, J. J.; Webb, R. A. *IBM Journal of Research and Development* **1988**, *32*, 372.

(3) Efros, A. L.; Shklovskii, B. I. *Journal of Physics C-Solid State Physics* **1975**, *8*, L49.

(4) Mott, N. F.; Davis, E. A. *Electronic Processes in Non-Crystalline Materials*; Clarendon Press ; Oxford University Press: Oxford; New York, 1979.

(5) Terrill, R. H.; Postlethwaite, T. A.; Chen, C. H.; Poon, C. D.; Terzis, A.; Chen, A. D.; Hutchison, J. E.; Clark, M. R.; Wignall, G.; Londono, J. D.; Superfine, R.; Falvo, M.; Johnson, C. S.; Samulski, E. T.; Murray, R. W. *Journal of the American Chemical Society* **1995**, *117*, 12537.

(6) Wuelfing, W. P.; Green, S. J.; Pietron, J. J.; Cliffel, D. E.; Murray, R. W. *Journal of the American Chemical Society* **2000**, *122*, 11465.

(7) Han, J. P.; Shen, M. R.; Cao, W. W.; Senos, A. M. R.; Mantas, P. Q. *Applied Physics Letters* **2003**, *82*, 67.

(8) Baranovski, S. *Charge Transport in Disordered Solids with Applications in Electronics*; Wiley: Chichester, England; Hoboken, NJ, 2006.

(9) Miller, A.; Abrahams, E. *Physical Review* **1960**, *120*, 745.

(10) Shklovskii, B. I.; Efros, A. L. *Electronic Properties of Doped Semiconductors*; Springer-Verlag: Berlin; New York, 1984.

(11) Yu, D.; Wang, C. J.; Wehrenberg, B. L.; Guyot-Sionnest, P. *Physical Review Letters* **2004**, *92*, 216802.

(12) Ridley, B. A.; Nivi, B.; Jacobson, J. M. *Science* **1999**, *286*, 746.

(13) Drndic, M.; Jarosz, M. V.; Morgan, N. Y.; Kastner, M. A.; Bawendi, M. G. *Journal of Applied Physics* **2002**, *92*, 7498.

(14) Kuno, M.; Lee, J. K.; Dabbousi, B. O.; Mikulec, F. V.; Bawendi, M. G. *Journal of Chemical Physics* **1997**, *106*, 9869.

(15) Guyot-Sionnest, P.; Wang, C. *Journal of Physical Chemistry B* **2003**, *107*, 7355.

(16) Murray, C. B.; Norris, D. J.; Bawendi, M. G. *Journal of the American Chemical Society* **1993**, *115*, 8706.

(17) Konstantatos, G.; Howard, I.; Fischer, A.; Hoogland, S.; Clifford, J.; Klem, E.; Levina, L.; Sargent, E. H. *Nature* **2006**, *442*, 180.

(18) Luther, J. M.; Law, M.; Song, Q.; Perkins, C. L.; Beard, M. C.; Nozik, A. J. *ACS Nano* **2008**, *2*, 271.

(19) Jarosz, M. V.; Porter, V. J.; Fisher, B. R.; Kastner, M. A.; Bawendi, M. G. *Physical Review B* **2004**, *70*, 195327.

(20) Yu, D.; Wehrenberg, B. L.; Jha, P.; Ma, J.; Guyot-Sionnest, P. *Journal of Applied Physics* **2006**, *99*, 104315.

(21) Kang, M. S.; Sahu, A.; Norris, D. J.; Frisbie, C. D. *Nano Letters* **2010**, *10*, 3727.

(22) Talapin, D. V.; Murray, C. B. *Science* **2005**, *310*, 86.

(23) Kovalenko, M. V.; Bodnarchuk, M. I.; Zaumseil, J.; Lee, J. S.; Talapin, D. V. *Journal of the American Chemical Society* **2010**, *132*, 10085.

(24) Kovalenko, M. V.; Scheele, M.; Talapin, D. V. *Science* **2009**, *324*, 1417.

(25) Lee, J. S.; Kovalenko, M. V.; Huang, J.; Chung, D. S.; Talapin, D. V. *Nature Nanotechnology* **2011**, *6*, 348.

(26) Nag, A.; Kovalenko, M. V.; Lee, J. S.; Liu, W. Y.; Spokoyny, B.; Talapin, D. V. *Journal of the American Chemical Society* **2011**, *133*, 10612.

(27) Fafarman, A. T.; Koh, W.-k.; Diroll, B. T.; Kim, D. K.; Ko, D.-K.; Oh, S. J.; Ye, X.; Doan-Nguyen, V.; Crump, M. R.; Reifsnyder, D. C.; Murray, C. B.; Kagan, C. R. *Journal of the American Chemical Society* **2011**, *133*, 15753.

(28) Talapin, D. V.; Lee, J.-S.; Kovalenko, M. V.; Shevchenko, E. V. *Chemical Reviews* **2010**, *110*, 389.

(29) Sze, S. M.; Ng, K. K. *Physics of Semiconductor Devices*; Wiley-Interscience: Hoboken, N.J., 2007.

(30) Cho, J. H.; Lee, J.; Xia, Y.; Kim, B.; He, Y. Y.; Renn, M. J.; Lodge, T. P.; Frisbie, C. D. *Nature Materials* **2008**, *7*, 900.

(31) Kang, M. S.; Lee, J.; Norris, D. J.; Frisbie, C. D. *Nano Letters* **2009**, *9*, 3848.

(32) Xia, Y.; Cho, J.; Paulsen, B.; Frisbie, C. D.; Renn, M. J. *Applied Physics Letters* **2009**, *94*, 013304.

(33) Reiss, P.; Bleuse, J.; Pron, A. *Nano Letters* **2002**, *2*, 781.

(34) Yu, W. W.; Qu, L. H.; Guo, W. Z.; Peng, X. G. *Chemistry of Materials* **2003**, *15*, 2854.

(35) Jasieniak, J.; Pacifico, J.; Signorini, R.; Chiasera, A.; Ferrari, M.; Martucci, A.; Mulvaney, P. *Advanced Functional Materials* **2007**, *17*, 1654.

(36) Wang, C. J.; Shim, M.; Guyot-Sionnest, P. *Science* **2001**, *291*, 2390.

(37) Yu, D.; Wang, C. J.; Guyot-Sionnest, P. *Science* **2003**, *300*, 1277.

(38) Vanmaekelbergh, D.; Liljeroth, P. *Chemical Society Reviews* **2005**, *34*, 299.

(39) Wills, A. W.; Kang, M. S.; Wentz, K. M.; Hayes, S. E.; Sahu, A.; Gladfelter, W. L.; Norris, D. J. *Journal of Materials Chemistry* **2012**, *22*, 6335.

(40) Norris, D. J.; Efros, A. L.; Erwin, S. C. *Science* **2008**, *319*, 1776.

(41) Avinor, M.; Meijer, G. *Journal of Chemical Physics* **1960**, *32*, 1456.

(42) Chamonal, J. P.; Molva, E.; Pautrat, J. L.; Revoil, L. *Journal of Crystal Growth* **1982**, *59*, 297.

(43) Georgobiani, A. N.; Aminov, U. A.; Dravin, V. A.; Lepnev, L. S.; Mullabaev, I. D.; Ursaki, V. V.; Iljukhina, Z. P. *Nuclear Instruments & Methods in Physics Research Section A - Accelerators Spectrometers Detectors and Associated Equipment* **1999**, *426*, 164.

(44) Inoue, M. *Journal of Physics and Chemistry of Solids* **1979**, *40*, 857.

(45) Robinson, A. L.; Bube, R. H. *Journal of Applied Physics* **1971**, *42*, 5280.

(46) Sato, F.; Kagawa, T.; Yodo, Y.; Iida, T. Ion microprobe analysis of acceptor-doped II-VI compounds. In *2003 IEEE Nuclear Science Symposium, Conference Record, Vols 1-5*; IEEE: New York, 2004; pp 3527.

(47) Swaminathan, V.; Greene, L. C. *Journal of Luminescence* **1976**, *14*, 357.

(48) Dzhafarov, T. D.; Serin, M.; Oren, D.; Sungu, B.; Sadigov, M. S. *Journal of Physics D - Applied Physics* **1999**, *32*, L5.

(49) Laiho, R.; Lashkul, A. V.; Lahderanta, E.; Nedeoglo, D. D.; Nedeoglo, N. D.; Shakhov, M. A. *Semiconductor Science and Technology* **2006**, *21*, 654.

(50) Nedeoglo, N. D.; Sirkeli, V. P.; Nedeoglo, D. D.; Laiho, R.; Lahderanta, E. *Journal of Physics - Condensed Matter* **2006**, *18*, 8113.

(51) Kennedy, T. A.; Glaser, E. R.; Klein, P. B.; Bhargava, R. N. *Physical Review B* **1995**, *52*, 14356.

(52) Gunawan, A. A.; Mkhoyan, K. A.; Wills, A. W.; Thomas, M. G.; Norris, D. J. *Nano Letters* **2011**, *11*, 5553.

(53) Sahu, A.; Qi, L. J.; Kang, M. S.; Deng, D. N.; Norris, D. J. *Journal of the American Chemical Society* **2011**, *133*, 6509.

(54) Erwin, S. C.; Petukhov, A. G. *Physical Review Letters* **2002**, *89*, 227201.

(55) Hartmann, H.; Mach, R.; Selle, B. *Wide Gap II-VI Compounds as Electronic Materials*; Akad. d. Wiss. d. DDR, Zentralinst. für Elektronenphysik: Berlin, 1982.

(56) Hadjichristidis, N.; Pispas, S.; Floudas, G. *Block Copolymers: Synthetic Strategies, Physical Properties, and Applications*; Wiley-Interscience: Hoboken, N.J., 2003.

CHAPTER 5

ELECTRICAL TRANSPORT IN SILVER-DOPED PbSe NANOCRYSTAL ASSEMBLIES*

5.1 OVERVIEW

As discussed in the last two chapters, we have developed a facile scheme to electronically dope CdSe nanocrystals with Ag impurities and we have investigated their optical and electronic properties. We observe non-monotonic trends in the fluorescence and shifts in Fermi level which suggest that Ag changes from an interstitial (*n*-type) to a substitutional (*p*-type) impurity with increased doping. In this chapter, we extend this approach of doping to PbSe nanocrystals and study the electrical transport in Ag-doped PbSe nanocrystal assemblies.

5.2 INTRODUCTION

Colloidal semiconductor nanocrystals are nanometer-scale particles that exhibit size-tunable optical properties.[1-3] Their solution processability[4] has made them attractive candidates for many potential applications, such as light-emitting diodes,[5,6] photodetectors,[7] and photovoltaic cells.[8-10] For these applications, the nanocrystals are deposited as densely packed thin films.[11] Because electrical current must be transported in all of these devices, methods have been sought to enhance the conduction through these films. One strategy is to apply the well-established methods of impurity doping from bulk semiconductors, *i.e.* introduce electronic impurities (atomic dopants) into the nanocrystals

to provide extra charge carriers (electrons or holes). However, success with this approach in nanocrystals has been slow.[12] First, the incorporation of atomic impurities into nanocrystals can present synthetic challenges.[13] Second, even when these can be overcome, it can be difficult to verify that the impurities are actually inside the nanocrystals. Consequently, most work to date on electronic impurities in nanocrystals has addressed the synthesis and characterization of these materials.[14-24] The study of electrical transport through films of such nanocrystals has only recently begun.[25-30] Electrically detected magnetic resonance,[28] scanning tunneling microscopy,[26] and thin-film-transistor measurements[25,27,29] have been employed on Si, InAs, and CdSe nanocrystals and the influence of extra carriers is starting to be unraveled.

In particular, thin-film-transistor measurements provide a useful technique that can determine the position of the Fermi level in a film of nanocrystals. Because the Fermi level is related to the number of electrons in the system, such data can reveal the influence of impurities. We have applied this approach to study doped CdSe nanocrystals as discussed in Chapter 4.[27,29] We observed shifts in the Fermi level when Al or Ag atoms were introduced that were consistent with electronically active impurities.

Due to the prominence of CdSe in nanocrystal research, studies on this material are important for exploring both the fundamentals of doping as well as the potential of electronically active impurities to control electrical transport. So much is now known about the intrinsic properties of CdSe nanocrystals[31,32] that the influence of the impurities can be detected easily. Beyond CdSe, another important material system is PbSe. Among many other NC systems, PbSe NCs have attracted great interest because PbSe NCs feature (i) size-tunable interband transitions in the near-infrared,[33] (ii) multiple exciton generation,[34,35] (iii) opportunities for hot-electron transfer,[36] (iv) high thin-film charge carrier mobility,[37] and (v) ambipolar (hole and electron) charge transport.[38,39] To avail these properties and use these NCs for potential applications, significant progress has been made in understanding their optical properties[40] as well as in development of synthetic methods to prepare monodisperse NCs.[11,33,41] Nanocrystals of the lead chalcogenides (PbSe and PbS) have optical properties well suited for photovoltaic

applications. Impurity doping can help improve present devices or allow new architectures to be explored. However to recognize the influence of doping on the electrical transport, electrical transport through films of intrinsic PbSe nanocrystals needs to be investigated.

5.3 CHARGE TRANSPORT IN UNDOPED PbSe NANOCRYSTAL THIN FILMS

To exploit the attractive properties of PbSe NCs in optoelectronic applications, more emphasis on fundamentals of the charge transport in NC assemblies is necessary, since many of these devices rely on electrical conduction between NCs. In particular, a basic understanding of the influence of particle size, which is the most characteristic parameter of nanomaterials, on the charge transport mechanism is essential. For PbSe NC assemblies, Coulomb-blockade transport[42] and variable-range-hopping transport[43] were observed at low temperatures, whereas Arrhenius-type thermally activated transport was observed at high temperatures.[42,44] However, all these studies were performed on a film based on NCs with single particle size and the influence of particle size on charge transport mechanism has not been elucidated yet. Recently, the dependence of electron and hole mobility on particle size was demonstrated for chemically-treated PbSe NC films.[45] However, this study did not include any temperature-dependent transport measurements, which are critical to understand the origin of the size-dependent electrical conduction.

Here we describe the influence of particle size on the charge transport mechanisms, the transitions in the transport mechanisms, the carrier localization length, the conductivity, and the thermal activation energy in chemically-treated PbSe NC thin films. We employed field effect transistors (FETs) based on films of different-sized NCs, which allowed monitoring of electrical transport in these films at different temperatures (200–28 K). We observed that electron transport exhibits nearest-neighbor-hopping (NNH) at higher temperatures and transitions to Efros-Shklovskii variable-range-hopping (ES-VRH) at lower temperatures, consistent with a previous report by Guyot-Sionnest

and coworkers on single-sized CdSe NC films.[46,47] The transition temperature between these charge transport mechanisms was size-dependent, with the transition taking place at higher temperature for films of smaller particles. From the temperature regime that exhibits ES-VRH transport, the electron localization length in the NC films was determined to scale linearly with particle diameter. The activation energy for charge transport from the NNH temperature regime was inversely proportional to the particle diameter. We attribute the origin of the NNH activation energy to the sum of (i) the size-dependent Coulomb penalty necessary for each hopping process between NCs and (ii) the inherent energy disorder due to the inherent finite particle size distribution. These two contributions can be qualitatively estimated, and their sum is in good agreement with the measured activation energy values from experiments. Overall, the size- and temperature-dependent charge transport properties of NC films described here provides more thorough understanding of electrical conduction in NC films.

Various sizes of PbSe NCs (diameters ranging from 3.8 nm to 8.4 nm), passivated primarily with oleic acid, were prepared by injecting a mixture of tri-*n*-octylphosphine selenide and diphenylphosphine into a hot solution of lead oxide, oleic acid, and octadecene following a modified literature procedure.[48,49] Throughout the particle synthesis and the post-synthesis procedure to prepare clean NC dispersions, exposure of the particles to ambient was carefully avoided. The optical absorbance spectra of these NCs dispersed in tetrachloroethylene are displayed in Figure 5.1a. Particle diameters were determined from a published correlation of size with the first absorbance peak.[50]

Figure 5.1b shows a schematic of the cross section of a typical PbSe NC FET that was prepared by the following procedure. Briefly, a layer of Al/Au (10 nm/75 nm) was deposited on the backside of a heavily doped Si wafer to work as a gate electrode. The front side of the wafer was covered with thermally grown 300 nm thick SiO_2 (specific capacitance=11.5 nF/cm^2). On top of the SiO_2 layer, source and drain Cr/Au (2.5 nm/32.5 nm) electrodes were patterned by standard photolithography.[51] The length (L) and the width (W) of the channel varied from 50 to 200 μm and from 1 to 2 mm, respectively. These wafers were treated with octadecyltrimethoxysilane (OTMS)[52] to passivate electron

traps at the SiO_2/NC solid interface and then transferred into a nitrogen glove box. Films of NCs were spin-coated on these wafers from dispersions of different sized PbSe NCs in anhydrous octane. To improve conduction, the films were treated with 0.05 M ethanedithiol (EDT) in acetonitrile.[49,51] Cracks in the films, which resulted from the chemical treatment, were filled by a second round of spin-coating of NC dispersions. The resulting films were continuous and devoid of cracks, as shown in an atomic force microscopy (AFM) image in Figure 5.1c. Without any air exposure, these devices were then transferred into another glove box equipped with a vacuum probe station. The devices were inserted into the vacuum probe station either at room temperature or at 235 K and stored under vacuum (~10^{-6} Torr) for more than two hours before taking electrical measurements.

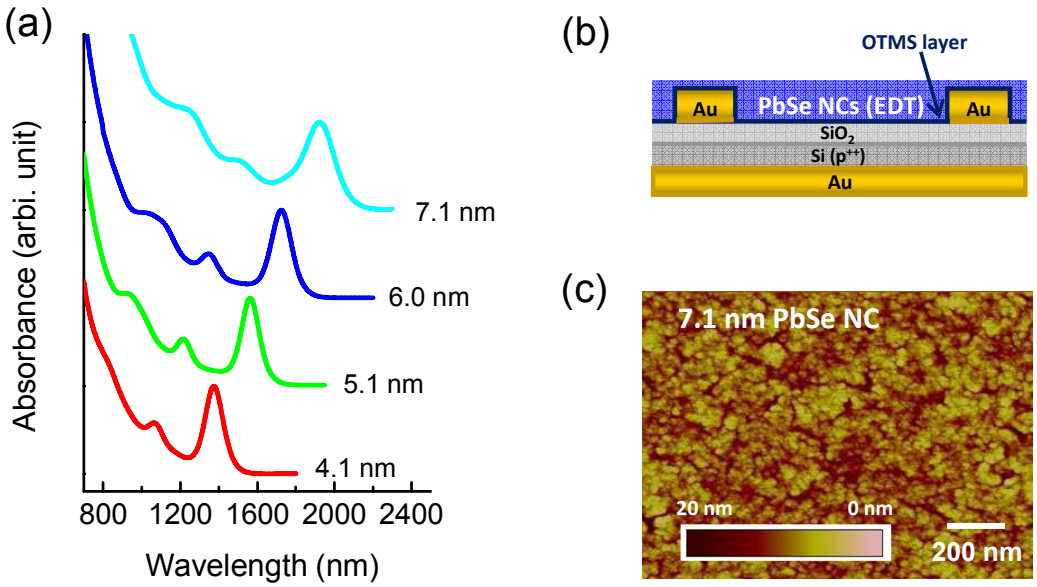

Figure 5.1: (a) Optical absorbance spectra of four different-sized PbSe NCs dispersed in tetrachloroethylene. (b) Schematic of cross section of PbSe NC FET (not to scale). (c) AFM height image of EDT treated 7.1 nm PbSe NC films.

The drain current–gate voltage (I_D–V_G) characteristics of the PbSe NC FETs at a given drain voltage (V_D) showed a typical *V*-shaped ambipolar transport characteristic, where I_D increases with the magnitude of applied V_G ($|V_G|$) (Figure 5.2a). The increase in I_D with positive gate voltage (right wing) indicates electron conduction while increased I_D with negative gate voltage (left wing) results from hole conduction. The I_D–V_G characteristics measured near room temperature showed significant hysteresis such that I_D

upon carrier injection (while $|V_G|$ increases) was higher than that upon carrier extraction (while $|V_G|$ decreases) for both electron and hole conduction. This type of hysteretic behavior is generally observed from a system where injected charge carriers become trapped and screen the gate bias.[49,53] Unfortunately, the prominent hysteresis in the I_D–V_G curve prevented extraction of meaningful electron and hole mobilities or conductivities at room temperature. This is because an I_D–V_G curve with noticeable hysteresis yields two very distinct transconductance (dI_D/dV_G) values (one upon carrier injection and the other upon carrier extraction) and thus two distinct mobility or conductivity values.

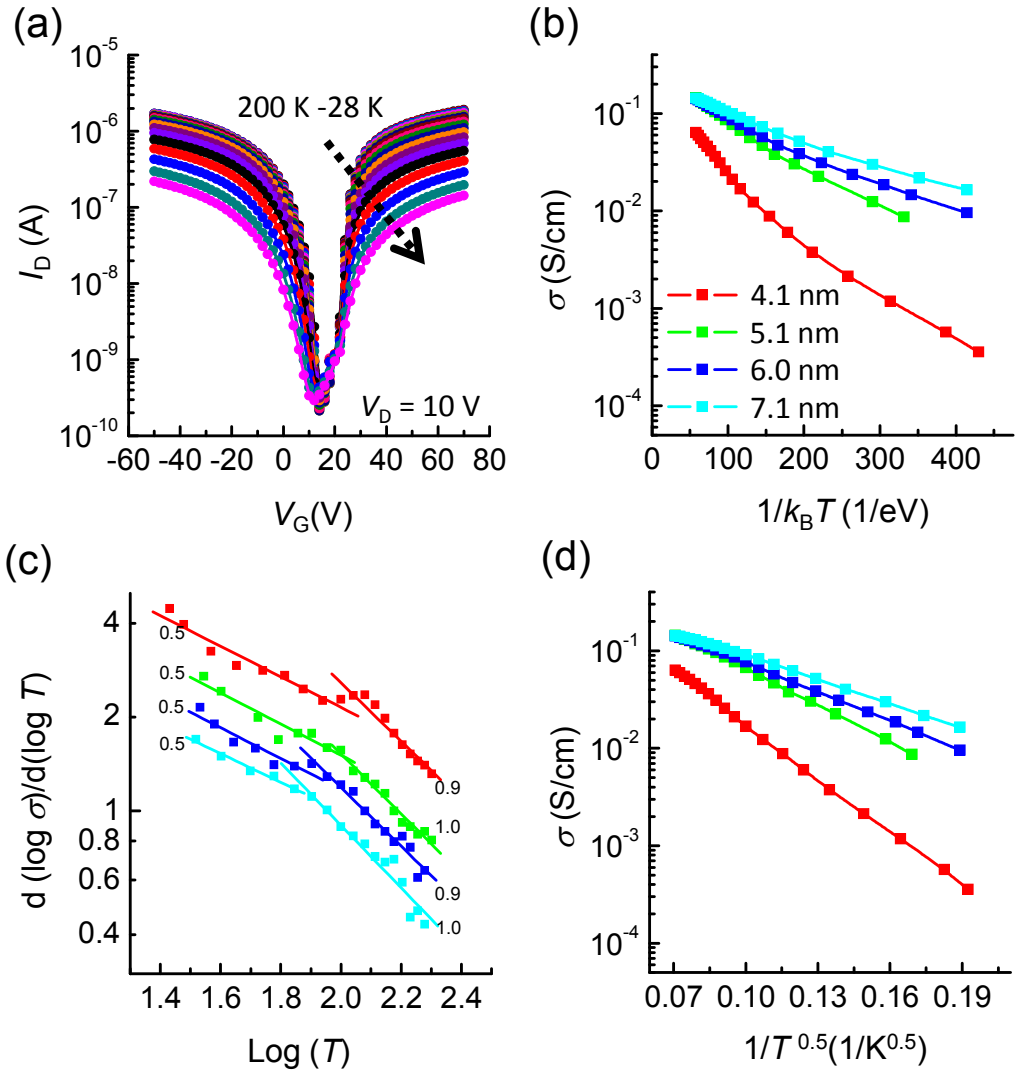

Figure 5.2: (a) I_D–V_G characteristics of an FET based on 7.1 nm PbSe NCs measured at different temperatures from 200 K to 28 K (V_G sweep direction: from –50 V to 70 V). (b) semi-log plot of σ *vs.* $1/k_BT$ for films of four different sized NCs. (c) log-log plot of d(logσ)/d(log$T$) vs.T to determine temperature dependence of conductivity. (d) semi-log plot of σ *vs.* $1/T^{0.5}$ for films of four different sized NCs.

Importantly, the hysteresis was significantly suppressed at lower temperatures, especially for electron conduction. As a consequence, the hysteresis for electron conduction (right wing) became essentially negligible below 200 K, whereas noticeable hysteresis for hole conduction (left wing) persisted even at lower temperatures. Such a suppression of hysteresis upon cooling suggests that carrier trapping is thermally activated. Also, the nearly complete disappearance of hysteresis for electron conduction at low temperatures implies that electron transport is not influenced by traps at these low temperatures. This leads us to believe that electron transport in PbSe NC films below 200 K occurred through the quantum states of each particle, rather than particle surface trap states. More importantly, the disappearance of the hysteresis in I_D–V_G characteristics allowed us to extract meaningful mobility and conductivity values for electron transport. The main discussion in this chapter will, hence, be focused on electron transport, rather than hole transport, in PbSe NC films.

Figure 5.2a displays I_D–V_G characteristics (at V_D=10 V) that were obtained from a film of 7.1 nm PbSe NCs measured from 200–28 K. Conductivity (σ) at a specific temperature was estimated from the equation $\sigma = e \times n \times \mu = (L/W) \times (V_G - V_{th}) \times (dI_D/dV_G)/V_D$, where e is the elemental charge, n is the carrier concentration, μ is the mobility, and V_{th} is the threshold voltage of electron conduction in an I_D–V_G characteristic. The slope of an I_D–V_G curve (dI_D/dV_G) was taken at (V_G–V_{th})=50 V, which corresponds to ~ $4*10^{12}$ charges/cm^2. Because the thermal coefficient of capacitance for the SiO_2 gate dielectric is quite small (<100 ppm/K), the variation of the charge density is negligible over the given temperature range. The condition that (V_G–V_{th})>V_D was satisfied to ensure that only the electrons, but not the holes, contribute to electrical conduction. Note that if (V_G–V_{th}) is comparable to or lower than V_D, both electrons and holes can be involved in charge transport (true ambipolar transport).

Arrhenius plots of conductivity *vs*. temperature (σ *vs*. T) for four different sized PbSe NC films are displayed in Figure 5.2b. As described above, these conductivity values were obtained at a charge density of ~$4*10^{12}$ charges/cm^2, which corresponds to inducing 0.7, 1.0, 1.3, and 1.8 charges per NC for 4.1, 5.1, 6.0, and 7.1 nm NCs,

respectively. A linear relation of σ *vs*. T in the Arrhenius plots suggests that the transport follows the nearest neighbor hopping mechanism within the given temperature range.[42,54] However, as shown in Figure 5.2b, the temperature dependence of conductivity deviated from a simple linear relation over the given temperature range. This implies that the charge transport cannot be simply described as NNH over the range 28–200 K.

As discussed in Chapter 4, it is well known that for hopping conduction, the temperature dependence of the conductivity takes the general form of

$$\sigma=\sigma_0\times\exp[-(T^*/T)^z] \quad (1)$$

where σ_0 is the conductivity pre-exponential factor, T^* is a fitting parameter with units of Kelvin, and z is a parameter that describes the power of the temperature dependence. z can be determined from the slope of a d(logσ)/d(log$T$) vs. T plot.[55] As shown in Figure 5.2c, a clear transition in the slope of d(logσ)/d(log$T$) vs. T plot was observed for all sizes of particles tested over 28–200 K, such that z values close to 0.5 were observed at lower temperatures and close to 1 at higher temperatures.[54] Temperature dependence with z=1, or an Arrhenius relation is consistent with the NNH model, whereas z=0.5 corresponds to the ES-VRH model. In the ES-VRH model, conductivity follows $\sigma=\sigma_0\times\exp[-(T_0/T)^{0.5}]$, where T_0 is a fitting parameter with units of Kelvin, as a consequence of considering the soft Coulomb gap (E_C).[55,56] The Coulomb gap, which arises from electron correlations, can be considered as the minimum energy required for a hopping process to occur between localized states with finite energy and spatial distribution. The change in slope of the d(logσ)/d(log$T$) vs. T plot implies that rather than following a single charge transport mechanism over the entire temperature span, a transition in the charge transport mechanism from ES-VRH to NNH occurs at 70–100 K. Pinpointing an exact transition temperature (T_{tr}) may not be trivial from the plot but one can observe that the transition temperature increases with decreasing particle diameter.

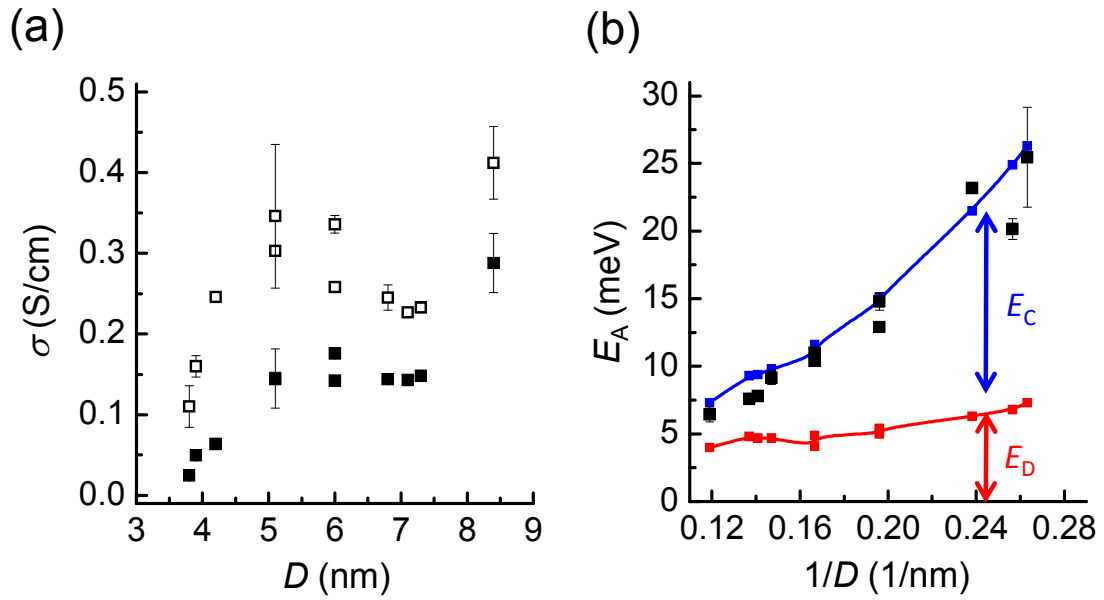

Figure 5.3: (a) Size dependence of σ at 200 K (closed) and σ_0 (open) for electron conduction. (b) Size dependence of E_A (black squares) and its comparison to the sum of E_C (blue) and E_D (red).

The conductivity pre-exponential factor (σ_0) is displayed in open squares in Figure 5.3a. This value describes the hopping rate between NCs, which is determined by (i) the number of hops necessary for charge transport, and (ii) the interparticle coupling between NCs. If the conductivity pre-exponential factor is primarily determined by the number of hops, one would expect a monotonic increase in σ_0 with increasing particle diameter, because the total number of hops should be less for films based on larger particles. Such behavior was observed from films of different sized CdSe NCs.[57] However, the results on our PbSe NC films shows a slight deviation from a monotonic increase. This deviation from monotonicity probably originates from a nonlinear change in interparticle electronic coupling upon the variation of particle diameter. This is reasonable because the electronic coupling can vary with numerous factors including the packing density of the particles, the packing density of the ligands on the particle surface, and the size or the shape of the particles, which may not be controlled precisely for particles with different diameters.[45] In addition to the conductivity pre-exponential factors, conductivities for different sized particles at 200 K are shown in Figure 5.3a with closed squares. The overall size-dependence of conductivity for electron conduction is consistent with the size-

dependence of electron mobility from PbSe NCs measured at room temperature that was reported previously.[45]

The activation energy (E_A) obtained from the Arrhenius plot describes the average energy that is necessary for each hop. As displayed in Figure 5.3b, a monotonic increase in E_A is observed with decreasing particle diameter. A similar trend was also observed in the previous chapter for activation energies of electron transport in films of different sized CdSe NCs.[57] In that chapter, we claimed that the size-dependent activation energy scales with the size-dependent charging energy which scales with $1/d$.

The origin of the size-dependent activation energy can be primarily understood from a description based on the transition in the mechanism for charge transport that takes place upon increasing temperature. We discussed above that electron transport in our PbSe NC films follows the ES-VRH model at lower temperatures, but transitions to NNH above T_{tr} (that follows $\sigma=\sigma_0\times\exp[-E_C/k_BT]$).[58] It is important to emphasize that above T_{tr}, E_C is temperature-independent but is size-dependent ($E_C=0.35e^2/4\pi\varepsilon\varepsilon_0 d$, ε_0 is the vacuum permittivity, and ε is the dielectric constant). This suggests that even in nearest-neighbor-hopping transport, the size-dependent Coulomb penalty or E_C must be paid for each nearest neighbor hop to occur, unless the thermal energy is significantly high enough to ignore E_C completely. Therefore, the Coulomb gap with fixed d contributes to the activation energy for a given size of particles in the NNH temperature regime. Note that this formula of $E_C=0.35e^2/4\pi\varepsilon\varepsilon_0 d$ resembles the formula for the charging energy of a spherical capacitor with a numerical coefficient; previous reports often used the concept of charging energy to describe the size-dependence of transport activation energy.[46,57] As summarized in Table 1, estimated values of E_C and experimentally obtained values of E_A both scale inversely with particle diameter. However, the values of E_C are always smaller than those of E_A for all of the sizes of NCs tested. This implies that an additional component that has not yet been treated contributes to the activation energy.

Table 5.1. Summary of characteristic values describing charge transport in PbSe NC films. Values in bold are from the sets of particles for which the electrical measurements were taken down to 28 K.

D	FWHM	E_D	E_C	$E_D + E_C$	E_A
nm	meV	meV	meV	meV	meV
3.8	80	7.3	19.0	26.3	24.0 ± 2.3
3.9	75	6.8	18.0	24.9	20.1 ± 0.8
4.2	**69**	**6.3**	**15.2**	**21.5**	**23.2**
5.1	**59**	**5.4**	**9.7**	**15.1**	**12.9**
5.1	55	5.0	9.7	14.7	14.6 ± 0.5
6.0	**54**	**4.9**	**6.7**	**11.6**	**10.4**
6.0	45	4.1	6.7	10.8	10.8 ± 0.2
6.8	51	4.7	5.1	9.8	9.2 ± 0.5
7.1	**51**	**4.7**	**4.8**	**9.4**	**7.8**
7.3	53	4.8	4.5	9.3	7.9 ± 0.4
8.4	44	4.0	3.3	7.3	6.5 ± 0.5

Consequently, the influence of disorder in the electronic states was considered, which is inherent for NCs with a finite size-distribution. Assuming that energy states follow a Gaussian distribution, one can estimate the average spacing in energy between the states. Because charge transport occurs through the very first PbSe NC layer on top of a SiO_2 gate dielectric layer, charge transport can be considered as taking place between closed packed spheres in a two-dimensional layer. This yields a 6-fold coordination between adjacent particles. Then, the average energy difference between the adjacent energy states, which is the minimum energy (E_D) necessary for electrons to hop to neighboring states, can be calculated to be $0.43 \times s_{1S}$. Here, a numerical coefficient of 0.43 was obtained from a standard normal distribution table that corresponds to a probability of 1/6 and s_{1S} is the standard deviation in energy of the Gaussian distribution which can be estimated from the full-width-at-half-maximum (FWHM) of the first excitonic peak in the absorbance spectrum according to $s_{1S}=\text{FWHM}/(4\times(2\ln 2)^{0.5})$. As displayed in Figure 5.3b, good agreement between the sum of E_C (blue) and E_D (red) and E_A is observed. This suggests that, although the thermal activation energy results primarily from the size-

dependent Coulomb penalty for each hopping process, the inherent energy disorder in the NC films also contributes and should be considered.

In summary, the size- and temperature-dependent electron transport in EDT-treated PbSe NC films was thoroughly investigated. At low temperatures, electron transport followed the ES-VRH model. The charge transport mechanism transitioned to NNH upon increasing the temperature. The transition temperature was higher for films of smaller particles. The activation energy for charge transport in the NNH model was size-dependent and closely matched to the sum of the size-dependent Coulomb gap and an average energy disorder due to size distribution in NC films. We believe that this study provides fundamental understanding of charge transport in NC films and thus will promote further applications of NCs in optoelectronics.

5.4 SILVER DOPING OF PbSe NANOCRYTALS

To our knowledge, doping of PbSe nanocrystals with electronically active impurities has not yet been reported. Herein, we address this by first preparing PbSe nanocrystals that are doped with Ag atoms. We then examine the influence of these impurities on the charge transport through nanocrystal films. To obtain detailed information, we collect data as a function of temperature. Specifically, we study field-effect transistors (FETs)[37] based on thin films of Ag-doped PbSe nanocrystals (with diameters of 3.8, 5.1, and 7.1 nm) over a temperature (T) range of 78–200 K. We observe shifts in the Fermi level due to doping. In addition, we find that the electron mobilities of the doped PbSe nanocrystals exhibit an Arrhenius-type temperature dependence, implying nearest-neighbor-hopping transport between the nanocrystals. Finally, the charge-transport activation energy decreases with doping, which may result from a reduced Coulomb penalty for hopping.[58]

Before presenting the results, we note that, based on a bulk-semiconductor picture,[59] one would expect that a Ag impurity (having only one valence electron) would

behave as an electron acceptor (or *p*-type dopant) if it substitutes for Pb(II) on the PbSe lattice. A hole would then be provided to the semiconductor, lowering the Fermi level of the film. However, our previous work on CdSe nanocrystals (discussed in Chapters 3 and 4), in which Ag could similarly substitute for Cd(II), suggested that at low concentrations (*i.e.* a few impurities per nanocrystal) the Ag was not a substitutional but an interstitial dopant.[27] In this case, the valence electron of the Ag could be provided to the lattice, and Ag would act as an electron donor (or *n*-type dopant). Only at higher impurity concentrations in CdSe did we observe *p*-type behavior consistent with Ag impurities substituting for Cd.[27] This transition from interstitial to substitutional Ag could explain non-monotonic experimental shifts in the Fermi level as a function of the dopant concentration. The Fermi level first rose and then fell as the amount of incorporated Ag in CdSe was increased. Whether similar behavior will be observed in other nanocrystal systems, such as PbSe, remains an open question.

To prepare Ag-doped PbSe nanocrystals, we first synthesized undoped PbSe nanocrystals with surfaces passivated primarily with oleic acid using methods described in the literature.[48,49,58] The average diameters of the as-prepared nanocrystals were estimated from a published correlation of size with the first optical absorbance peak.[50] To introduce Ag atoms into these PbSe nanocrystals, we then employed a partial cation-exchange reaction.[27,60,61] During our experiments on Ag-doping of CdSe nanocrystals, we found that the addition of trioctylphosphine could mediate the rate of the cation exchange, allowing the amount of incorporated dopant to be controlled.[27] Here, we extended this approach to PbSe. Briefly, a toluene dispersion of the undoped PbSe nanocrystals was mixed with trioctylphosphine and ethanolic $AgNO_3$ with stirring. We allowed the cation exchange reaction to proceed for 1 minute and then the nanocrystals were isolated following standard procedures. The degree of Ag doping could be tuned by adjusting the amount of Ag added to the exchange reaction. This allowed us to obtain a series of nanocrystal samples of the exact same size with different dopant concentrations. The amount of Ag in each sample was measured by inductively coupled plasma mass spectrometry (ICP-MS), as shown in Figure 5.4a. Values for our samples are summarized in Table 5.2.

Table 5.2. Doping concentrations for our three different sizes of Ag-doped PbSe nanocrystals. The average diameter was estimated from optical absorbance spectra. The amount of Ag in the exchange reaction is reported relative to the amount of Pb present. Inductively coupled plasma mass spectroscopy (ICP-MS) was used to estimate the average number of Ag incorporated per nanocrystal and the Ag to Pb ratio in the nanocrystals.

Average Diameter (nm)	Ag/Pb in Reaction (%)	Average Ag per NC (number)	Ag/Pb in NC (%)
3.8	100	5.8	0.77
3.8	200	11	1.4
3.8	300	17	2.3
5.1	50	11	0.62
5.1	100	14	0.76
5.1	175	23	1.3
5.1	250	34	1.9
5.1	350	40	2.2
7.1	50	13	0.27
7.1	100	26	0.55
7.1	175	58	1.2
7.1	250	63	1.3

However, in contrast to CdSe, we could not find conditions to obtain very low Ag doping of PbSe (*e.g.* below ~5–10 Ag atoms per PbSe nanocrystal). Rather, Ag was incorporated only when the $AgNO_3$ in the exchange solution was above a threshold concentration (~50–100% Ag/Pb). At this concentration the average amount of Ag incorporated immediately jumped to 5–10 per nanocrystal, depending on the size. This behavior explains the data for the 5.1 nm sample in Table 2, where reducing the Ag in the exchange reaction from 100 to 50% Ag/Pb, only decreased the Ag incorporated by ~20%. Unfortunately, because we could not achieve low doping concentrations, this impeded our

ability to address whether Ag-doped PbSe nanocrystals also exhibit an interstitial-to-substitutional transition, as observed in CdSe.[27] This issue is discussed further below.

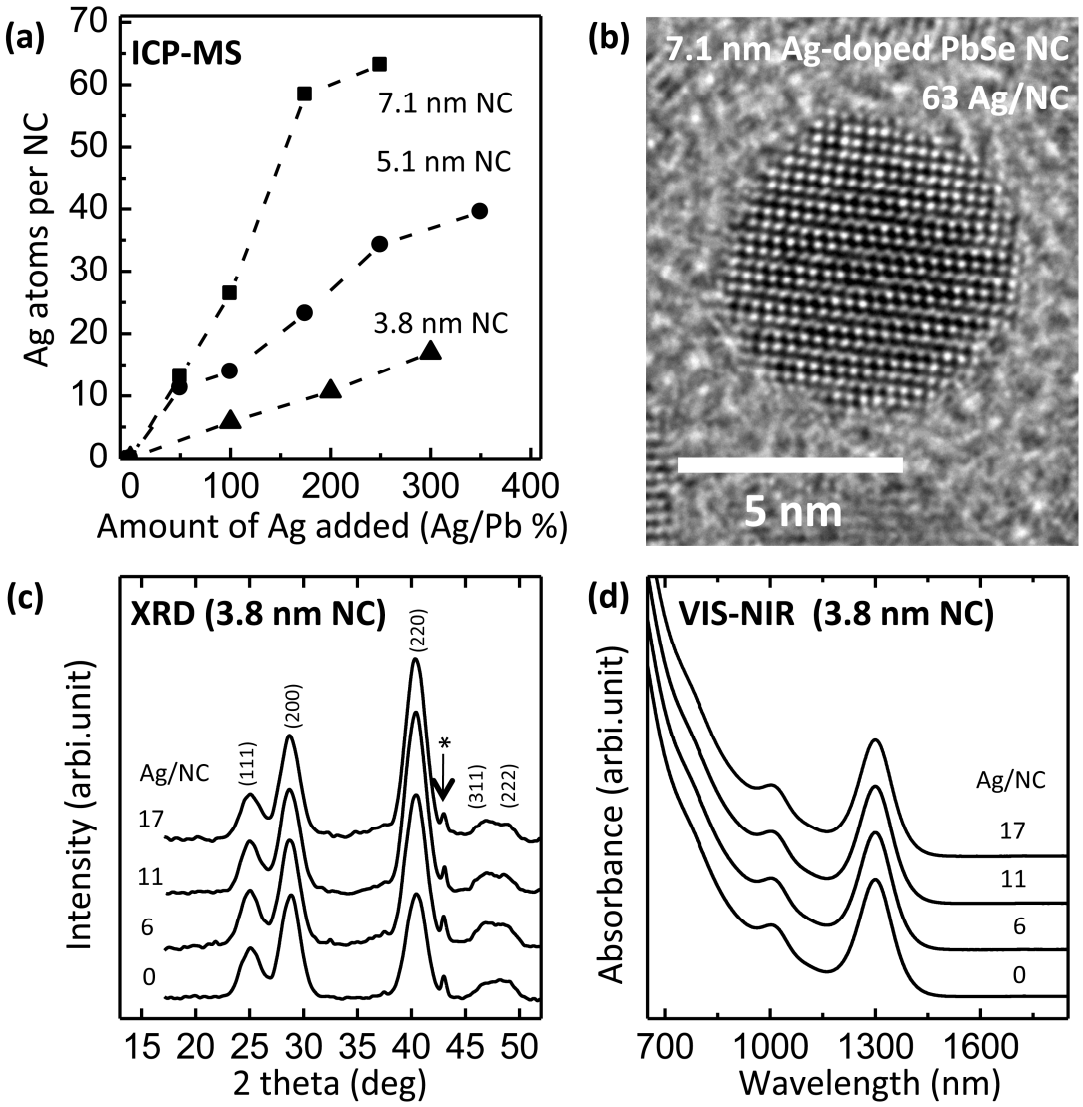

Figure 5.4: (a) The average number of Ag atoms per nanocrystal (NC) determined from inductively coupled plasma mass spectroscopy (ICP-MS) versus the amount of Ag added during the cation-exchange reaction, as a percent of the total Pb present. (b) A transmission electron micrograph of a doped 7.1-nm-diameter PbSe NC (~63 Ag/NC). (c) X-ray diffraction (XRD) patterns indexed to the bulk rock salt crystal structure for 3.8-nm-diameter PbSe NCs with different Ag concentrations. The peak labeled with an asterisk is from the substrate holder made of Al. (d) Visible-near-infrared (VIS-NIR) absorbance spectra for 3.8-nm-diameter PbSe NCs with different Ag concentrations dispersed in tetrachloroethylene.

Transmission electron microscopy (TEM) images of doped PbSe nanocrystals showed that the particles were single crystalline even when they contained tens of Ag

impurities. For example, Figure 5.4b presents a micrograph of a 7.1 nm PbSe nanocrystal. According to ICP-MS, nanocrystals in this sample contained ~63 Ag atoms on average. We also did not observe significant changes in X-ray diffraction (XRD) patterns with doping, as demonstrated in Figure 5.4c for 3.8 nm nanocrystals. In general, we found no evidence of phase separation (*e.g.* to pure Ag or Ag_2Se). Rather, the crystalline structure of the PbSe nanocrystals was maintained. Room-temperature absorbance spectra also showed no significant variations with doping, as displayed in Figure 5.4d. Room-temperature absorbance spectra also showed no significant variations with doping, as displayed in Figure 5.4d. The same result was observed in Ag-doped CdSe nanocrystals.[27] If any impurity-induced carriers occupied quantum-confined electronic states in the nanocrystals, one would expect to see bleached transitions in the absorbance spectra.[43] The absence of this effect implies that if the Ag is providing extra carriers, they are leaving the nanocrystals, *e.g.* to fill traps on the surface or in the surrounding matrix.

To investigate the electrical properties we assembled FETs based on thin films of Ag-doped PbSe nanocrystals. As described previously,[58] the FETs were prepared by spin-coating a 20 mg mL^{-1} dispersion of nanocrystals in anhydrous octane onto a Si/SiO_2 wafer with pre-patterned source/drain electrodes. The film was then treated with an ethanedithiol (EDT) solution (0.05 M EDT in anhydrous acetonitrile)[49] followed by a second round of spin coating using a 5 mg mL^{-1} dispersion of doped PbSe nanocrystals in anhydrous octane. Heavily doped Si and SiO_2 (thickness = 300 nm and specific capacitance C = 11.5 nF cm^{-2}) were used as the gate electrode and the gate dielectric, respectively (Figure 5.5a). Au/Cr (32.5/2.5 nm) was used to form the source and drain electrodes. The length (L) and the width (W) of the channel were 100 μm and 1 mm, respectively. Note that a layer of octadecyltrimethoxysilane (OTMS)[52] was deposited on the SiO_2 prior to the nanocrystal-film deposition to eliminate electron traps at the SiO_2/nanocrystal interface. The entire device fabrication was performed under a N_2 atmosphere. The FETs were then inserted into a vacuum probe station (without exposure to ambient), cooled to 235 K, and stored under vacuum (~10^{-6} Torr) for more than two hours prior to taking electrical measurements,[58] which were carried out between 78 and 200 K.

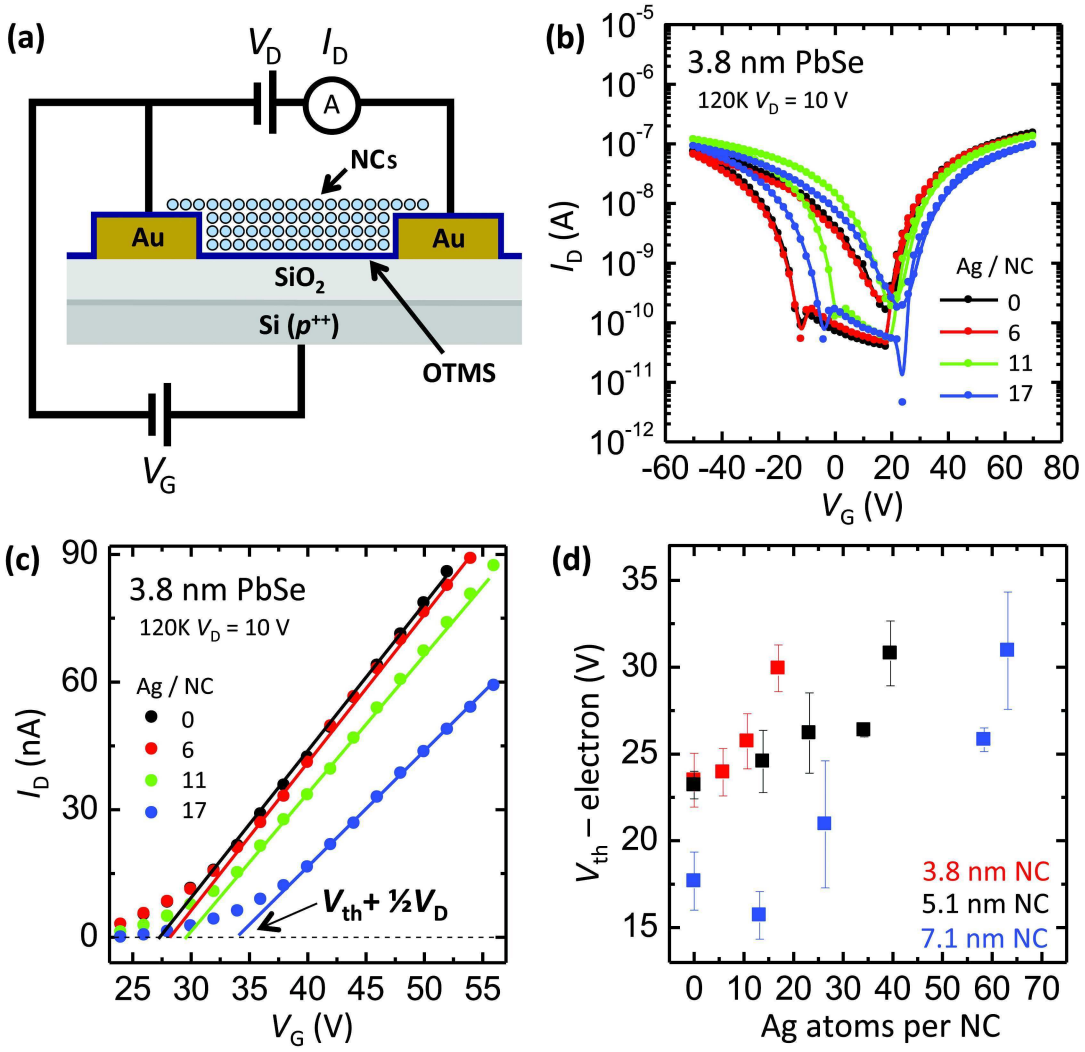

Figure 5.5: (a) Schematic cross section (not to scale) of a field-effect transistor (FET) made from PbSe nanocrystals (NCs). A layer of octadecyltrimethoxysilane (OTMS) was used to eliminate electron traps at the SiO_2/nanocrystal interface. (b) Comparison of I_D–V_G characteristics (V_D = 10 V) of FETs on a semi-log plot for films of Ag-doped 3.8-nm-diameter PbSe NCs with varying Ag concentrations, measured at 120 K. (c) A magnified plot of the same curves in (b) on a linear scale near the threshold voltage. The threshold voltage, V_{th}, of a device can be estimated from the x-intercept of a linear fit to the I_D–V_G characteristic minus half of the drain voltage. (d) The electron V_{th} for three different-sized Ag-doped PbSe NCs with various Ag concentrations. The error bars represent one standard deviation obtained from measurements on 3 devices.

Figure 5.5b displays the drain-current-(I_D)–gate-voltage-(V_G) characteristics of FETs made from 3.8 nm PbSe nanocrystals doped at different Ag concentrations. The measurements were performed at 120 K with a drain voltage (V_D) of 10 V and a sweep rate of ~5V/sec. The curves all show typical V-shaped ambipolar transport behavior. The hysteresis in the I_D–V_G plots for electron transport (right wing of the V-shaped curve) was

negligible, consistent with previous results.[58] In contrast, the hysteresis for hole transport (left wing) was prominent such that I_D was higher upon hole accumulation (while $|V_G|$ increases) than upon hole depletion (while $|V_G|$ decreases). Because such hysteretic behavior is generally associated with charge trapping,[49,54] our results imply that hole transport is significantly influenced by traps. We also note that such hysteretic behavior for hole transport was observed from all samples and at all temperatures. This prevented a direct study of the influence of doping on hole transport. However, a detailed analysis of electron transport was possible due to the lack of hysteresis on the right wing of the characteristics. We note that such an analysis can still provide useful information about the influence of the impurities, regardless of whether they are acting as donors or acceptors (*n* or *p*). Consequently, the discussion below will focus on electron transport.

From the I_D–V_G curves obtained at varying temperatures, four important parameters that describe the electron transport in doped PbSe nanocrystals were extracted and examined: the threshold voltage, the mobility, the mobility pre-exponential factor, and the charge-transport-activation energy. First, the threshold voltage (V_{th}), which represents the gate voltage necessary to shift the Fermi level of the semiconductor for transport, was obtained from the *x*-intercept of a linear fit to the I_D–V_G plot using the relation $I_D = (W/L)\times C\times\mu\times[V_G-(\frac{1}{2}V_D+V_{th})]\times V_D$.[37] As displayed in Figure 5.5c and summarized in Figure 5.5d, V_{th} for electron transport increased with doping for all three particle sizes tested. In other words, it was necessary to apply a larger shift in the Fermi level (a more positive gate voltage) to accumulate mobile electrons into the films as more Ag atoms were introduced into the PbSe nanocrystals. This implies that Ag atoms behave as *p*-type dopants (*i.e.* they lower the Fermi level) when they are incorporated into PbSe nanocrystals. This result is consistent with Ag impurities substituting for Pb and behaving as electron acceptors, as discussed above.

However, we note that for our lowest doping concentration (0.27% Ag/Pb, or 13 Ag per 7.1 nm nanocrystal), a decrease in V_{th} is seen in Figure 5.5d, which implies an increase in the Fermi level. Although we were not able to explore fully this concentration regime, as explained above, this result is consistent with the interstitial-to-substitutional

transition observed in CdSe. The increase in the Fermi level would then be due to interstitial Ag donors (*n*-type dopants) in PbSe nanocrystals at low concentrations.

The second important parameter, the electron field-effect mobility, μ, was estimated from the slope of the I_D–V_G curves based on the relation, $\mu = (L/W)/C \times (dI_D/dV_G)/V_D$. We took the slope at a V_G where $|V_G - V_{th}| > |V_D|$ to ensure that only a single type of carrier, electrons in this case, was involved in the electrical conduction. Otherwise, both electrons and holes could be involved in charge transport and the estimation of the mobility becomes complicated (in the true ambipolar regime). In addition, because the mobility varies with carrier concentration, we kept the gate-induced carrier density approximately constant in our measurements. Interestingly, we do not observe a significant change in the electron mobility with doping. Figure 5.6 displays the electron mobilities estimated at 120 K for our three sizes of PbSe nanocrystals. Within experimental error, we find no variation of the mobility with increasing Ag concentration.

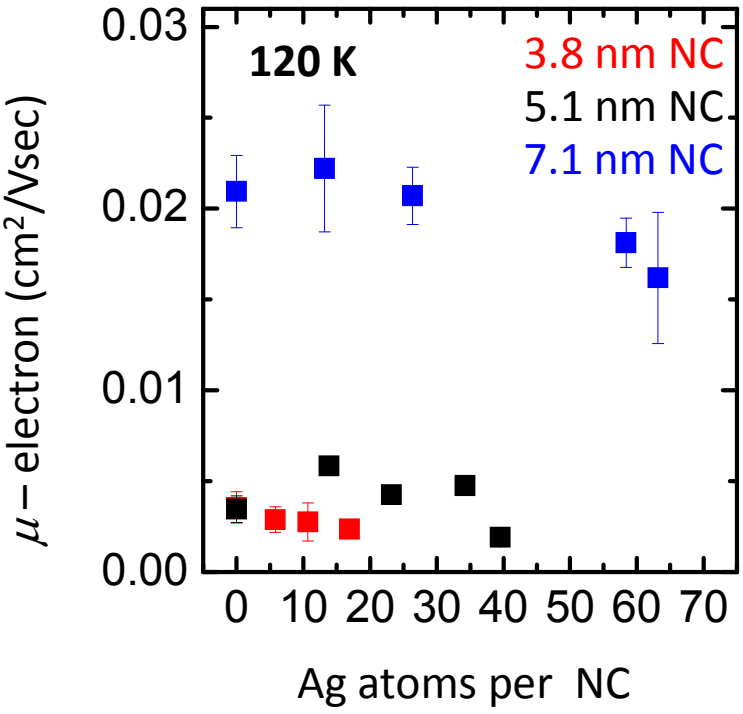

Figure 5.6: Comparison of the electron mobility measured at 120 K for 3.8-, 5.1-, and 7.1-nm-diameter Ag-doped PbSe nanocrystals (NCs) with different Ag concentrations. Error bars represent one standard deviation obtained from measurements on 3 devices.

However, more information can be obtained from the temperature dependence. For all films examined, a linear relation of μ versus T was observed when plotted in Arrhenius form, *i.e.* as $\mu=\mu_0 \exp[-E_A/k_BT]$, where μ_0 is the mobility pre-exponential factor, E_A is the charge-transport-activation energy, and k_B is the Boltzmann constant. For example, Figure 5.7a displays such Arrhenius plots for films of 3.8 nm nanocrystals with different doping concentrations. The linearity of the data suggests that the electron transport through these films follows the nearest-neighbor-hopping mechanism in the experimental temperature range.[42,58] Note that in contrast to Section 5.2, where we discussed all the data in term of conductivities (σ), here we shall be sticking with mobilities (μ) instead. Since $\sigma = e \times n \times \mu$, where e is the elemental charge and n is the carrier concentration, and we keep the carrier concentration constant, we can replace conductivity with mobility without affecting any of the trends.

Values of both μ_0 and E_A can be extracted from the y-intercept and slope of the Arrhenius plots, respectively. Figure 5.7b shows that values for μ_0 decrease upon doping, implying that the electronic coupling between nanocrystals is reduced with the introduction of Ag impurities. This decrease in μ_0 is also consistent with the lowering of the Fermi level due to *p*-type doping. Namely, transport occurs when an electron hops from the lowest conduction band state (conventionally denoted $1S_e$) of one nanocrystal to the $1S_e$ state of one of its neighbors. Due to variations in the nanocrystal size, a distribution in the energetic position of the $1S_e$ states will exist within the nanocrystal solid. This distribution is depicted in Figure 5.7c in terms of a $1S_e$ density of states (DOS). Transport will be more efficient if it occurs at an energy where the $1S_e$ DOS is high. This depends on the initial Fermi level of the nanocrystal solid as well as how many additional electrons are induced by the gate. However, as mentioned above, the gate-induced carrier density was approximately fixed for all of our measurements. In undoped nanocrystals, these additional electrons brought the transport level higher in the $1S_e$ energy distribution than when *p*-type Ag impurities were added (Figure 5.7c). In other words, because the initial Fermi level was lowered by doping, the gate-induced electrons were no longer sufficient to bring the transport level as high as in the undoped case. Rather, the transport occurred lower in the $1S_e$ distribution (where less states exist).

Because the electronic coupling between nanocrystals is reduced when fewer states are available, μ_0 should decrease, as observed.

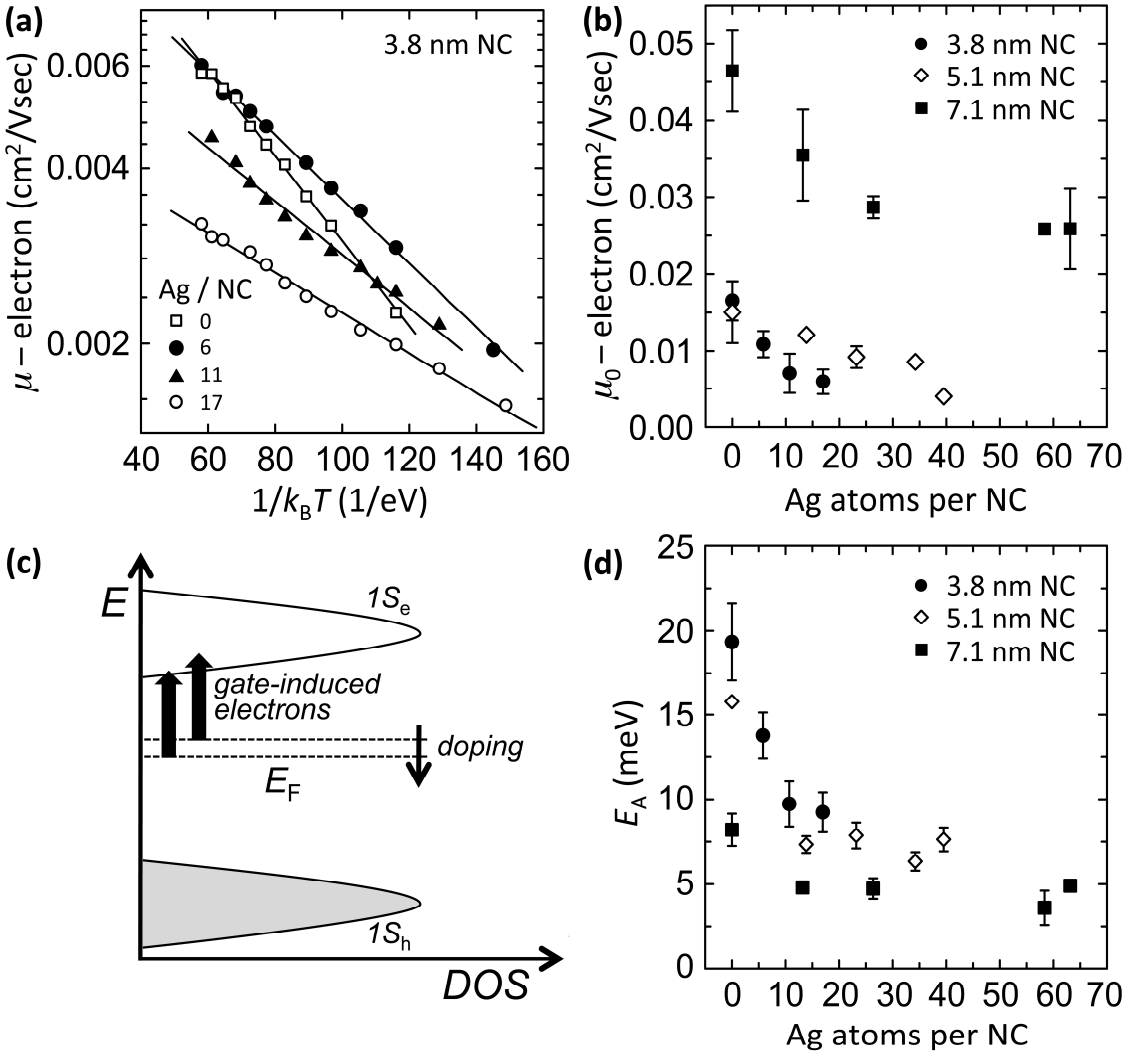

Figure 5.7: (a) Arrhenius plots of the electron mobility for 3.8-nm-diameter PbSe nanocrystals (NCs) doped with four different Ag concentrations. (b) The mobility pre-exponential factor for electron transport, μ_0, as a function of Ag concentration for 3.8-, 5.1-, and 7.1-nm-diameter PbSe NCs. Error bars represent one standard deviation obtained from measurements on 3 devices. (c) Schematic of the lowering of the Fermi level (E_F) upon *p*-type doping of Ag, which results in a reduction of μ_0 when electrons are induced by the gate. The density of states (DOS) for the lowest conduction band state ($1S_e$) and valence band state ($1S_h$) in the nanocrystal solid is depicted. (d) The charge-transport-activation energy, E_A, as a function of Ag concentration for 3.8-, 5.1-, and 7.1-nm-diameter PbSe NCs. The error bars represent one standard deviation obtained from measurements on 3 devices.

Figure 5.7d shows that E_A also decreases with increasing Ag doping, but then saturates for all three sizes of our PbSe nanocrystals. This might be an unexpected result

for electron transport in a system that is doped *p*-type, because *p*-type dopants can often behave as traps for electron transport and thus increase the activation energy for hopping. However, the electron transport in PbSe nanocrystal films still exhibits negligible hysteretic behavior in the I_D–V_G curves (right wing) even when the nanocrystals are doped (Figure 5.5b), suggesting that the impact of Ag atoms as electron traps is weak.

Instead, the trend in E_A can be explained by looking into the origin of the activation energy for charge transport. Our previous report[58] showed that the activation energy in undoped PbSe nanocrystals closely matched the sum of the Coulomb penalty (E_C) associated with hopping and the penalty for the energy disorder (E_D) of the $1S_e$ states (*e.g.* due to the size variation of the nanocrystals). If the same model is applied to describe the activation energy for charge transport in doped PbSe nanocrystals, E_C would be expected to be smaller. In general, the dielectric constant of a doped semiconductor increases with doping[62] and the Coulomb penalty is inversely proportional to the dielectric constant. Namely, E_C equals $0.35e^2/4\pi\varepsilon\varepsilon_0 D$, where e is the elemental charge, ε is the effective dielectric constant of the nanocrystal film, ε_0 is the vacuum permittivity, and D is the center-to-center distance between the nanocrystals.[46,55,56] Thus, the contribution from E_C to E_A should decrease with doping. In contrast, the energetic disorder is not altered significantly upon doping. For example, the full-width-at-half-maximum (FWHM) of the lowest energy peak in absorbance spectra does not change (Figure 5.4d). Therefore, the contribution of E_D to E_A should remain fixed with doping. Overall, one would then expect E_A to be reduced with doping and then saturate at the fixed value of E_D. This explanation is consistent with the trends observed in Figure 5.7d.

In summary, we have examined electron transport in films of Ag-doped PbSe nanocrystals between 78 and 200 K for three sizes of particles. The threshold voltage, the mobility pre-exponential factor, and the activation energy for electron transport were investigated. The results show that the Ag atoms behaved as electronically active impurities. Specifically, they lowered the Fermi level of the nanocrystal films, consistent with *p*-type dopants. The temperature dependence indicates that the electron transport followed a nearest-neighbor-hopping mechanism. Also the lowering of the charge

transport activation energy upon doping could be explained by the reduced Coulomb penalty for hopping.

5.5 EXPERIMENTAL SECTION

5.5.1 Chemicals and Substrates

Anhydrous methanol, anhydrous ethanol (≥99.5%), anhydrous butanol (99.8%), anhydrous octane (≥99%), anhydrous hexane (≥99%), toluene (HPLC grade, 99.9%), anhydrous acetonitrile (99.8%), 1,2-ethanedithiol (EDT, ≥98%), carbon tetrachloroethylene (TCE, spectrophotometric grade, ≥99%), tri-*n*-octylphosphine (TOP, technical grade, 90%), oleic acid (technical grade, 90%), 1-octadecene (90%), diphenylphosphine (DPP 98%), lead (II) oxide (PbO, 99.999%), selenium pellets (Se, 99.999%), hydrochloric acid (TraceSELECT®, for trace analysis, fuming, ≥37%), and nitric acid [TraceSELECT®, for trace analysis, ≥69.0% (T)] were purchased from Aldrich. Anhydrous acetone (extra dry, 99.8%) was purchased from Fisher Science Education. Silver nitrate ($AgNO_3$, 99.9995%) was purchased from Strem Chemicals. *n*-octadecyltrimethoxysilane (OTMS, 95%) was purchased from Gelest, Inc. All chemicals were used as delivered.

<100>-oriented, boron-doped silicon (Si) wafers (resistivity = 0.005–0.01 Ωcm, thickness = 525 ± 25 μm) coated with 300 nm of thermal oxide (SiO_2) growth were purchased from Silicon Valley Microelectronics.

5.5.2 Synthesis of PbSe Nanocrystals

PbSe nanocyrstals were prepared by following a modified literature procedure.[48,49] For example, in a typical synthesis of 6.0 nm PbSe nanocrysals, lead precursor solution consisting of lead oxide (1.25 g, 5.6 mmol), oleic acid (4.5 mL) and octadecene (17.8 mL) were degassed under vacuum (<20 millitorr) at 40 °C and purged with dry nitrogen gas. This degassing process was repeated three times. The temperature was elevated to 125 °C under nitrogen and was maintained at that temperature for 30 minutes while the

precursor solution turned optically clear. In the meantime, a mixture of a 1.0 M solution of Se in TOP (10.5 mL) and 0.03 mL of DPP was prepared. Separately, a 1.0 M solution of Se in TOP (3.0 mL) without adding any DPP was prepared. This TOP:Se solution (without DPP) was mixed with a clear solution of lead precursors (5.0 mL) that was taken out from the reaction vessel. Subsequently, the TOP:Se solution with DPP was injected rapidly into the reaction vessel at 125 °C. Upon injection, the temperature of the reaction solution dropped to 105 °C, but then it was elevated and maintained between 120–122 °C for the next 3 minutes to facilitate nanocyrstal growth. The mixture of TOP solution (without DPP) and lead precursor solution was then added slowly (dropwise) into the reaction vessel for the next 3 minutes and 20 seconds. Meanwhile, the temperature of the reaction solution was maintained between 123–126 °C. Nanocrystals were grown for an additional 1 minute and 40 seconds at 125 °C. Finally, 7.5 mL of anhydrous octane was injected and the reaction vessel was immersed in a water bath to quench the reaction. Once it cooled down to room temperature, the colloidal dispersion was cannulated from the reaction vessel into a Schlenk flask and transferred quickly into a nitrogen filled glove box to avoid air exposure. The PbSe nanocrystals were isolated from the mixture by adding anhydrous methanol, butanol, and ethanol, followed by centrifugation. Further purification was done by redispersing the precipitate using anhydrous hexane, followed by precipitation with anhydrous ethanol and acetone and centrifugation. The precipitates were dried under vacuum to remove excess solvent. The resulting precipitate yielded NCs which are primarily ligated with oleic acids. Different sized particles were obtained following the similar recipe but with different injection/growth times and temperatures.

5.5.3 Doping of PbSe Nanocrystals with Silver

To prepare Ag-doped PbSe nanocrystals, we first synthesized undoped particles following the above method. These nanocrystals were then doped via a cation-exchange reaction.[27] A typical procedure to obtain 5.1-nm-diameter PbSe nanocrystals doped on average with ~11 Ag atoms per nanocrystal (0.3 atomic percent) is as follows. 40 mg of the undoped nanocrystals is dispersed in toluene and heated to 60 °C in a glass vial. 0.3 mL of trioctylphosphine is then added followed by 0.3 mL of 0.1 M ethanolic $AgNO_3$ with stirring. After 1 minute, the reaction is quenched with the addition of 10 mL of

ethanol. The nanocrystals then precipitate, are collected by centrifugation, and redispersed in 1 mL of hexane. The nanocrystals are isolated again by precipitation with ethanol, centrifugation, and then dried under vacuum. The amount of Ag incorporated could be tuned by controlling the amount of Ag added to the exchange reaction (Figure 5.4a). It is important to note that the entire synthesis and doping process was performed under inert atmosphere (nitrogen).

5.5.4 Sample Characterization

X-ray diffraction (XRD), transmission electron microscopy (TEM), inductively coupled plasma optical emission spectroscopy (ICP-OES), inductively coupled plasma mass spectroscopy (ICP-MS), and ultraviolet-visible-near infrared (UV-Vis-NIR) absorption spectroscopy were used to characterize the size, shape, structure, composition, and optical properties of the doped nanocrystals.

For XRD, a Bruker-AXS microdiffractometer was utilized to collect wide-angle powder patterns (Cu-Kα). Samples were prepared from concentrated dispersions of nanocrystals in hexane. Films of these nanocrystals were deposited onto heavily doped Si wafers covered with a thermally grown 300-nm-thick SiO_2 layer.

For TEM, an FEI Tecnai G2 F30 microscope was used to image the nanocrystals with an acceleration voltage of 300 kV. Each sample was prepared by depositing a drop of a dilute dispersion of nanocrystals in hexanes onto a 400-mesh carbon-coated copper grid and allowing the solvent to evaporate at room temperature.

For optical characterization, as-prepared nanocrystals were dispersed in TCE and placed in a 1-cm-path-length quartz cuvette. Absorption spectra were obtained using a Cary 5E UV-Vis-NIR spectrophotometer. An average diameter of these particles was determined from a published correlation of size with the first absorbance peak.[50]

For ICP-MS, we used a Thermo Scientific XSeries2 instrument with a hexapole collision/reaction cell. For calibration, we compared the intensities of the unknown to

data from 4 multi-element standards purchased from SPEX Industries. Elements were analyzed at standard mass resolution using the helium/hydrogen collision reaction mode with kinetic energy discrimination. The mean and standard deviation were calculated from five measurements on each sample. The unknowns were introduced with an ESI PC3 (Peltier cooler) FAST system with sample loops to reduce oxide formation and carryover between samples. ^{89}Y was used as an internal standard.

For ICP-OES, we used a Thermo Scientific iCAP 6500 duo optical emission spectrometer with a simultaneous charge-induction detector. We measured each sample five times to determine the mean and standard deviation for each elemental wavelength. For calibration, we utilized NIST-traceable single or multi-element standards. To lessen matrix effects, we matched the matrix acid for all blanks, standards, and samples. We diluted each sample such that the elemental concentrations were in the linear range of the standard and detector combination. The probe and all tubing for introduction of the samples were made from Teflon and flushed for at least 45 seconds with clean matrix acid.

For both ICP-MS and ICP-OES, samples were prepared by dissolving ~1-2 mg of vacuum-dried nanocrystals in 5 ml of aqua regia (3:1 $HCl:HNO_3$). The resulting ions were then diluted to ~100 ppm with 18 MΩ deionized water. To avoid contamination, trace-grade acids (HCl and HNO_3) and HCl-leached plasticware and glassware were used.

5.5.5 Patterning of Si/SiO_2 for Field-Effect Transistors

Si wafers covered with a thermally grown 300 nm thick SiO_2 layer were patterned by standard photolithography, as detailed elsewhere.[51] Cr/Au (2.5 nm/32.5 nm) electrodes were used as source and drain electrodes. The length and the width of the channel varied from 50 to 200 μm and from 1 to 2 mm, respectively. A layer of Al/Au (10 nm/75 nm) was deposited on the backside of the Si/SiO_2 wafer to work as a gate electrode in contact with the heavily doped Si layer.

5.5.6 Device Fabrication

Si/SiO_2 wafers, with prepatterned source, drain, and gate electrodes, were subsequently rinsed with acetone, isopropanol, and methanol, followed by UV/ozone cleaning for 10 minutes. A 3 mM OTMS solution in trichloroethylene was spin-coated onto these wafers (3000 rpm for 10 seconds).[52] The wafers were then vapor annealed in ammonium hydroxide solution (28–30% in water) overnight, followed by rinsing with DI water and sonication in toluene. As prepared OTMS treated wafers were brought into a nitrogen glove box. Inside the glove box, PbSe NC films were spin-coated (10 seconds at 900 rpm followed by 15 seconds at 1200 rpm) from a 20 mg/ml dispersion of PbSe NCs in anhydrous octane passed through a 0.2 μm PTFE filter. The films were dried at 80 °C for 3 minutes and then at room temperature for more than 3 hours under nitrogen. Afterwards, the films were chemically treated with EDT by dipping the substrate in a 0.05 M EDT solution in anhydrous acetonitrile for 3 seconds at a rate of 0.5 cm/s.[51] To fill cracks formed during the EDT treatment, a second layer of NCs were spin-coated (10 seconds at 900 rpm followed by 15 seconds at 1200 rpm) from a 5 mg/mL dispersion of PbSe NCs in anhydrous octane, followed by the same drying procedure. Avoiding air exposure, these devices were then transferred into another glove box equipped with a Desert Cryogenic (Lakeshore) vacuum probe station. The devices were inserted into the vacuum probe station either at room temperature or at 235 K and stored under vacuum ($\sim 10^{-6}$ Torr) for more than two hours before taking electrical measurements. Note that only the hole conduction was observed for some of the devices when vacuum was applied at room temperature, probably due to removal of ethanedithiol. To achieve both the electron and hole conduction from these films, vacuum had to be applied at lower temperatures, for example at 235 K, where the vapor pressure of ethanedithiols is lower than that at room temperature. The influence of applying vacuum on the charge transport needs further investigation. Current–voltage characteristics were measured using Keithley 237 and 6517A electrometers. For temperature varying measurements, either liquid helium or liquid nitrogen was introduced into the cryogenic probe station. All the measurements were carried out under vacuum ($\sim 10^{-6}$ Torr).

5.6 REFERENCES

(1) Klimov, V. I. *Semiconductor and Metal Nanocrystals: Synthesis and Electronic and Optical Properties*; Marcel Dekker, Inc.: New York, 2004.

(2) Talapin, D. V.; Lee, J.-S.; Kovalenko, M. V.; Shevchenko, E. V. *Chemical Reviews* **2010**, *110*, 389.

(3) Alivisatos, A. P. *Science* **1996**, *271*, 933.

(4) Murray, C. B.; Kagan, C. R.; Bawendi, M. G. *Annual Review of Materials Science* **2000**, *30*, 545.

(5) Coe, S.; Woo, W. K.; Bawendi, M.; Bulovic, V. *Nature* **2002**, *420*, 800.

(6) Colvin, V. L.; Schlamp, M. C.; Alivisatos, A. P. *Nature* **1994**, *370*, 354.

(7) Konstantatos, G.; Howard, I.; Fischer, A.; Hoogland, S.; Clifford, J.; Klem, E.; Levina, L.; Sargent, E. H. *Nature* **2006**, *442*, 180.

(8) Huynh, W. U.; Dittmer, J. J.; Alivisatos, A. P. *Science* **2002**, *295*, 2425.

(9) Kamat, P. V. *Journal of Physical Chemistry C* **2008**, *112*, 18737.

(10) Nozik, A. J. *Physica E-Low-Dimensional Systems & Nanostructures* **2002**, *14*, 115.

(11) Murray, C. B.; Sun, S. H.; Gaschler, W.; Doyle, H.; Betley, T. A.; Kagan, C. R. *IBM Journal of Research and Development* **2001**, *45*, 47.

(12) Norris, D. J.; Efros, A. L.; Erwin, S. C. *Science* **2008**, *319*, 1776.

(13) Erwin, S. C.; Zu, L. J.; Haftel, M. I.; Efros, A. L.; Kennedy, T. A.; Norris, D. J. *Nature* **2005**, *436*, 91.

(14) Buonsanti, R.; Llordes, A.; Aloni, S.; Helms, B. A.; Milliron, D. J. *Nano Letters* **2011**, *11*, 4706.

(15) Fujii, M.; Yamaguchi, Y.; Takase, Y.; Ninomiya, K.; Hayashi, S. *Applied Physics Letters* **2005**, *87*, 211919.

(16) Ishizumi, A.; Kanemitsu, Y. *Journal of the Physical Society of Japan* **2010**, *79*, 093706.

(17) Knox, C. K.; Fillmore, S. D.; Call, D. M.; Allen, D. G.; Hess, B. C.; Davis, R. C.; Evenson, W. E.; Harrison, R. G. *Journal of Colloid and Interface Science* **2006**, *300*, 591.

(18) Meulenberg, R. W.; van Buuren, T.; Hanif, K. M.; Willey, T. M.; Strouse, G. F.; Terminello, L. J. *Nano Letters* **2004**, *4*, 2277.

(19) Orlinskii, S. B.; Schmidt, J.; Baranov, P. G.; Hofmann, D. M.; Donega, C. D.; Meijerink, A. *Physical Review Letters* **2004**, *92*.

(20) Pi, X. D.; Gresback, R.; Liptak, R. W.; Campbell, S. A.; Kortshagen, U. *Applied Physics Letters* **2008**, *92*, 123102.

(21) Roy, S.; Tuinenga, C.; Fungura, F.; Dagtepe, P.; Chikan, V.; Jasinski, J. *Journal of Physical Chemistry C* **2009**, *113*, 13008.

(22) Srivastava, B. B.; Jana, S.; Pradhan, N. *Journal of the American Chemical Society* **2011**, *133*, 1007.

(23) Stowell, C. A.; Wiacek, R. J.; Saunders, A. E.; Korgel, B. A. *Nano Letters* **2003**, *3*, 1441.

(24) Viswanatha, R.; Brovelli, S.; Pandey, A.; Crooker, S. A.; Klimov, V. I. *Nano Letters* **2012**, *11*, 4753.

(25) Geyer, S. M.; Allen, P. M.; Chang, L. Y.; Wong, C. R.; Osedach, T. P.; Zhao, N.; Bulovic, V.; Bawendi, M. G. *ACS Nano* **2010**, *4*, 7373.

(26) Mocatta, D.; Cohen, G.; Schattner, J.; Millo, O.; Rabani, E.; Banin, U. *Science* **2011**, *332*, 77.

(27) Sahu, A.; Kang, M. S.; Kompch, A.; Notthoff, C.; Wills, A. W.; Deng, D.; Winterer, M.; Frisbie, C. D.; Norris, D. J. *Nano Letters* **2012**, *12*, 2587.

(28) Stegner, A. R.; Pereira, R. N.; Klein, K.; Lechner, R.; Dietmueller, R.; Brandt, M. S.; Stutzmann, M.; Wiggers, H. *Physical Review Letters* **2008**, *100*, 026803.

(29) Wills, A. W.; Kang, M. S.; Wentz, K. M.; Hayes, S. E.; Sahu, A.; Gladfelter, W. L.; Norris, D. J. *Journal of Materials Chemistry* **2012**, *22*, 6335.

(30) Skinner, B.; Chen, T. R.; Shklovskii, B. I. *Physical Review B* **2012**, *85*, 205316.

(31) Nirmal, M.; Brus, L. *Accounts of Chemical Research* **1999**, *32*, 407.

(32) Norris, D. J.; Bawendi, M. G. *Physical Review B* **1996**, *53*, 16338.

(33) Wehrenberg, B. L.; Wang, C. J.; Guyot-Sionnest, P. *Journal of Physical Chemistry B* **2002**, *106*, 10634.

(34) Ellingson, R. J.; Beard, M. C.; Johnson, J. C.; Yu, P. R.; Micic, O. I.; Nozik, A. J.; Shabaev, A.; Efros, A. L. *Nano Letters* **2005**, *5*, 865.

(35) Nozik, A. J.; Beard, M. C.; Luther, J. M.; Law, M.; Ellingson, R. J.; Johnson, J. C. *Chemical Reviews* **2010**, *110*, 6873.

(36) Tisdale, W. A.; Williams, K. J.; Timp, B. A.; Norris, D. J.; Aydil, E. S.; Zhu, X. Y. *Science* **2010**, *328*, 1543.

(37) Talapin, D. V.; Murray, C. B. *Science* **2005**, *310*, 86.

(38) Kang, M. S.; Lee, J.; Norris, D. J.; Frisbie, C. D. *Nano Letters* **2009**, *9*, 3848.

(39) Wehrenberg, B. L.; Guyot-Sionnest, P. *Journal of the American Chemical Society* **2003**, *125*, 7806.

(40) Du, H.; Chen, C. L.; Krishnan, R.; Krauss, T. D.; Harbold, J. M.; Wise, F. W.; Thomas, M. G.; Silcox, J. *Nano Letters* **2002**, *2*, 1321.

(41) Murphy, J. E.; Beard, M. C.; Nozik, A. J. *Journal of Physical Chemistry B* **2006**, *110*, 25455.

(42) Romero, H. E.; Drndic, M. *Physical Review Letters* **2005**, *95*, 156801.

(43) Wehrenberg, B. L.; Yu, D.; Ma, J. S.; Guyot-Sionnest, P. *Journal of Physical Chemistry B* **2005**, *109*, 20192.

(44) Mentzel, T. S.; Porter, V. J.; Geyer, S.; MacLean, K.; Bawendi, M. G.; Kastner, M. A. *Physical Review B* **2008**, *77*, 075316.

(45) Liu, Y.; Gibbs, M.; Puthussery, J.; Gaik, S.; Ihly, R.; Hillhouse, H. W.; Law, M. *Nano Letters* **2010**, *10*, 1960.

(46) Yu, D.; Wang, C. J.; Wehrenberg, B. L.; Guyot-Sionnest, P. *Physical Review Letters* **2004**, *92*, 216802.

(47) Liu, H.; Pourret, A.; Guyot-Sionnest, P. *ACS Nano* **2010**, *4*, 5211.

(48) Steckel, J. S.; Yen, B. K. H.; Oertel, D. C.; Bawendi, M. G. *Journal of the American Chemical Society* **2006**, *128*, 13032.

(49) Luther, J. M.; Law, M.; Song, Q.; Perkins, C. L.; Beard, M. C.; Nozik, A. J. *ACS Nano* **2008**, *2*, 271.

(50) Moreels, I.; Lambert, K.; De Muynck, D.; Vanhaecke, F.; Poelman, D.; Martins, J. C.; Allan, G.; Hens, Z. *Chemistry of Materials* **2007**, *19*, 6101.

(51) Leschkies, K. S.; Kang, M. S.; Aydil, E. S.; Norris, D. J. *Journal of Physical Chemistry C* **2010**, *114*, 9988.

(52) Ito, Y.; Virkar, A. A.; Mannsfeld, S.; Oh, J. H.; Toney, M.; Locklin, J.; Bao, Z. A. *Journal of the American Chemical Society* **2009**, *131*, 9396.

(53) Egginger, M.; Bauer, S.; Schwodiauer, R.; Neugebauer, H.; Sariciftci, N. S. *Monatshefte Fur Chemie* **2009**, *140*, 735.

(54) Yildiz, A.; Serin, N.; Serin, T.; Kasap, M. *Japanese Journal of Applied Physics* **2009**, *48*, 111203.

(55) Efros, A. L.; Shklovskii, B. I. *Journal of Physics C - Solid State Physics* **1975**, *8*, L49.

(56) Shklovskii, B. I.; Efros, A. L. *Electronic Properties of Doped Semiconductors*; Springer-Verlag: Berlin; New York, 1984.

(57) Kang, M. S.; Sahu, A.; Norris, D. J.; Frisbie, C. D. *Nano Letters* **2010**, *10*, 3727.

(58) Kang, M. S.; Sahu, A.; Norris, D. J.; Frisbie, C. D. *Nano Letters* **2011**, *11*, 3887.

(59) Ashcroft, N. W.; Mermin, N. D. *Solid State Physics*; Saunders College Publ.: Fort Worth; Philadelphia; San Diego [etc.], 1976.

(60) Robinson, R. D.; Sadtler, B.; Demchenko, D. O.; Erdonmez, C. K.; Wang, L.-W.; Alivisatos, A. P. *Science* **2007**, *317*, 355.

(61) Son, D. H.; Hughes, S. M.; Yin, Y. D.; Alivisatos, A. P. *Science* **2004**, *306*, 1009.

(62) Dhar, S.; Marshak, A. H. *Solid-State Electronics* **1985**, *28*, 763.

CHAPTER 6

FACILE SYNTHESIS OF SILVER CHALCOGENIDE (Ag_2E, E=Se, S, and Te) SEMICONDUCTOR NANOCRYSTALS*

6.1 OVERVIEW

A general, one-pot, single-step method to produce colloidal silver chalcogenide (Ag_2E, E=Se, S, and Te) nanocrystals is presented, with an emphasis on Ag_2Se. The method avoids exotic chemicals, high temperatures, and high pressures, and requires only a few minutes of reaction time. While Ag_2S and Ag_2Te are formed in their low-temperature monoclinic phases, Ag_2Se is obtained in a metastable tetragonal phase not observed in the bulk.

6.2 INTRODUCTION

As a bulk material, silver selenide (Ag_2Se) is a narrow-bandgap semiconductor with many intriguing properties. First, it is a mixed conductor with high electronic and ionic mobility. Second, it undergoes a reversible first-order phase transition from a low-temperature phase (α-Ag_2Se) to a high-temperature phase (β-Ag_2Se) at 135 °C with a strong change in its electronic properties.[1] β-Ag_2Se is a superionic conductor that is used as an additive in highly conductive composite glasses for sensors, displays, and photo-chargeable secondary batteries, and has potential as a solid electrolyte.[2] α-Ag_2Se is widely used as a thermoelectric material due to its high electrical conductivity, large Seebeck coefficient, and low thermal conductivity, and as a photosensitizer in

* This chapter is reproduced with permission from Ayaskanta Sahu, Lejun Qi, Moon Sung Kang, Donna Deng, and David J. Norris, "Facile Synthesis of Silver Chalcogenide (Ag_2E, E=S, Se, and Te) Semiconductor Nanocrystals," Journal of American Chemical Society **2011**, 133 (17), 6509 (DOI: 10.1021/ja200012e).

photographic films and thermochromic materials.[3] Non-stoichiometric α-$Ag_{2+\delta}Se$ also shows giant magnetoresistance comparable to the colossal magnetoresistance observed in manganese perovskites.[4,5]

However, while all of these properties have been studied extensively in the bulk, very few reports have examined nanoscale Ag_2Se. In many semiconductors, decreasing the size of the material can provide a route to tune physical properties and observe new phenomena. In particular, colloidal semiconductor nanocrystals provide strongly size-specific optical and optoelectronic properties. These have been investigated for potential applications in solar cells,[6] light-emitting diodes,[7,8] thin-film transistors,[9,10] and in biological imaging.[11,12] Therefore, if Ag_2Se nanocrystals were available that were uniform in size, they could provide an interesting new system to investigate the dependence of optical, magnetic, mechanical, and transport properties on size. Furthermore, high quality Ag_2Se nanocrystals could lead to new applications or could significantly improve the performance of existing applications. These factors provide a compelling motivation to synthesize and explore the properties of silver selenide nanocrystals and extend the versatility of these materials simply by tailoring parameters such as size, stoichiometry, or crystal phase.

Despite this motivation, the synthesis of high-quality Ag_2Se semiconductor nanocrystals is far behind those of other materials such as the cadmium and zinc chalcogenides. Of the silver chalcogenides, Ag_2S has been the most studied.[13-17] Only a few reports exist on the preparation of Ag_2Se nanoparticles,[18,19] nanowires,[20] and nanoscale dendrites.[21] Other routes to obtain nano-sized Ag_2Se include vapor phase growth,[22] sonochemical methods,[23] and high-temperature[22] and high-pressure[24] solution-phase reactions. These methods often require the use of exotic precursors[25] and extreme conditions. Nevertheless, they still generate Ag_2Se nanocrystals that are polycrystalline and polydisperse, which can severely limit their use both for fundamental studies as well as potential applications.

To obtain crystalline nearly monodispere Ag_2Se particles, one could adapt a successful recipe for silver telluride nanocrystals.[26] Unfortunately, this synthesis requires two weeks. Alternatively, one could perform a cation exchange to transform Ag or CdSe nanocrystals to Ag_2Se.[18,19] However, this involves a two-step process, *i.e.*, the synthesis of either Ag or CdSe nanocrystals first followed by the cation exchange. Therefore, to the best of our knowledge, no reported method is direct, simple, and fast.

Herein, we demonstrate a one-pot, single-step synthesis of structurally well-defined and nearly monodisperse Ag_2Se nanocrystals. Our route is advantageous because it utilizes low temperature, atmospheric pressure, and standard chemicals. Instead of days, the reaction is completed within a few minutes. Moreover, the method also works for the synthesis of Ag_2S and Ag_2Te nanocrystals, thus providing a general and versatile technique to obtain the entire family of silver chalcogenides.

6.3 RESULTS AND DISCUSSION

6.3.1 Synthesis of Ag_2Se Nanocrystals

In a typical synthesis, 16.99 g of $AgNO_3$ and 7.896 g of selenium shot are dissolved separately in 100 mL tri-*n*-octylphosphine (TOP) to obtain 1M Ag-TOP and 1M TOP-Se, respectively. A mixture of 6.4 mL oleic acid (OA), 5.4 g 1-octadecylamine (ODA), and 12.8 mL 1-octadecene (ODE) is then combined in a 100 mL round-bottom flask, degassed, flushed three times with N_2 to remove water and oxygen, and heated to 70 °C under N_2. With continuous stirring, 4 mL of TOP-Se is added into the flask and the temperature is raised to 160 °C. 4 mL of Ag-TOP is then quickly injected and the reaction is allowed to proceed for ~5 minutes at 150 °C. The growth is quenched in an ice bath and 25 ml of butanol is added to prevent solidification of the reaction mixture while cooling. The nanocrystals are isolated by precipitating with ethanol and re-dispersing in hexanes. This process is repeated at least once to ensure a clean product.

6.3.2 Synthesis of Ag_2S and Ag_2Te Nanocrystals

A similar synthesis was developed to obtain Ag_2S and Ag_2Te nanocrystals. For the synthesis of Ag_2S nanocrystals, 72 mg of sulfur powder was added to the same mixture of OA, ODA, and ODE as used in the Ag_2Se synthesis and degassed. 4 ml of Ag-TOP was rapidly injected at 197 °C and the reaction was allowed to proceed for 12 minutes at 167 °C to obtain ~4 nm Ag_2S nanocrystals. Similarly, 2 mL of 1M TOP-Te was added to the mixture of OA, ODA, and ODE and degassed. 2 mL of Ag-TOP was then injected at 191 °C. A growth time of 5 minutes at ~150 °C produced ~7 nm Ag_2Te nanocrystals.

6.3.3 Role of Initial Ratio of Ag to Chalcogenide in the Synthesis of Ag_2E Nanocrystals

Among the three chalcogenides, tellurium is the most reactive toward silver, followed by selenium and then sulfur. Nearly monodisperse Ag_2Te and Ag_2Se could be obtained with an initial Ag:E ratio of 2:1. However, due to the slow reaction between S and Ag, we sometimes observed the formation of Ag nanocrystals during the synthesis of Ag_2S nanocrystals if we used this stoichiometric ratio. (In fact, in the absence of any chalcogenide, our synthetic procedure produced high quality silver nanocrystals.) To avoid the production of unwanted Ag nanocrystals, we decreased the Ag:S ratio to 1:1. We note that increasing the concentration of the chalcogenide is a fairly common strategy in the synthesis of metal chalcogenide nanocrystals. For example, common recipes for CdSe[27] and PbSe[28] nanocrystals use Cd:Se and Pb:Se ratios of 1:1.25 and 1:2, respectively. Because we were attempting to provide a general scheme for the synthesis of all three silver chalcogenides, we kept the Ag to chalcogenide ratio at 1:1 for all three syntheses. Varying the Ag to chalcogenide ratio (between 2:1 and 1:1) did not have any significant impact on the dispersity of any of the resulting products.

6.3.4 Size and Shape Control of Ag_2E Nanocrystals

For all three chalogenides, we could also obtain nanocrystals of different average sizes by varying reaction times and growth temperatures. By increasing the growth time, the average size of the Ag_2E nanocrystals could be increased. The shape of the Ag_2S and Ag_2Se nanocrystals remained roughly spherical regardless of the time of growth.

However, the Ag_2Te nanocrystals started to coagulate when grown for longer than about 20 minutes. This then resulted in randomly shaped Ag_2Te crystallites.

By varying the injection and growth temperatures and ligand concentrations, the average size of the samples could also be affected. For example, by reducing the ligand concentration by half, the initial nucleation burst produced a larger number of nuclei, resulting in a smaller final average size. During all of our experiments that involved changing growth temperatures or concentrations, we did not notice any significant changes in the shape of the roughly spherical nanocrystals.

6.3.5 Role of Surfactants in the Growth of Ag_2E Nanocrystals

We also wish to address the role of ODE, TOP, OA, and ODA in the nanocrystal growth. Our evidence suggests that ODE acts simply as a non-coordinating solvent. While TOP, OA, and ODA can all potentially act as surface ligands that stabilize the nanocrystals and mediate the growth, Fourier-transform infrared (FTIR) measurements (Figure 6.1) show that the surfaces of the Ag_2Se and Ag_2Te nanocrystals are covered almost entirely with TOP.[29] This is consistent with the precursors for these materials (Ag-TOP, TOP-Se, and TOP-Te). For Ag_2S, where sulfur powder was first dissolved in ODA and OA, these ligands were also detected on the nanocrystal surface, but weakly. We believe instead that ODA and OA are important for controlling the reaction rate. Without ODA, large precipitates of Ag_2Te and Ag_2Se formed in seconds and minutes, respectively. (With Ag_2S, large but stable 10-12 nm nanocrystals were obtained.) Without OA, the growth proceeded extremely slowly, yielding small, polydisperse nanocrystals. Thus, by balancing these two effects, a mixture of OA and ODA produces nearly monodisperse samples.

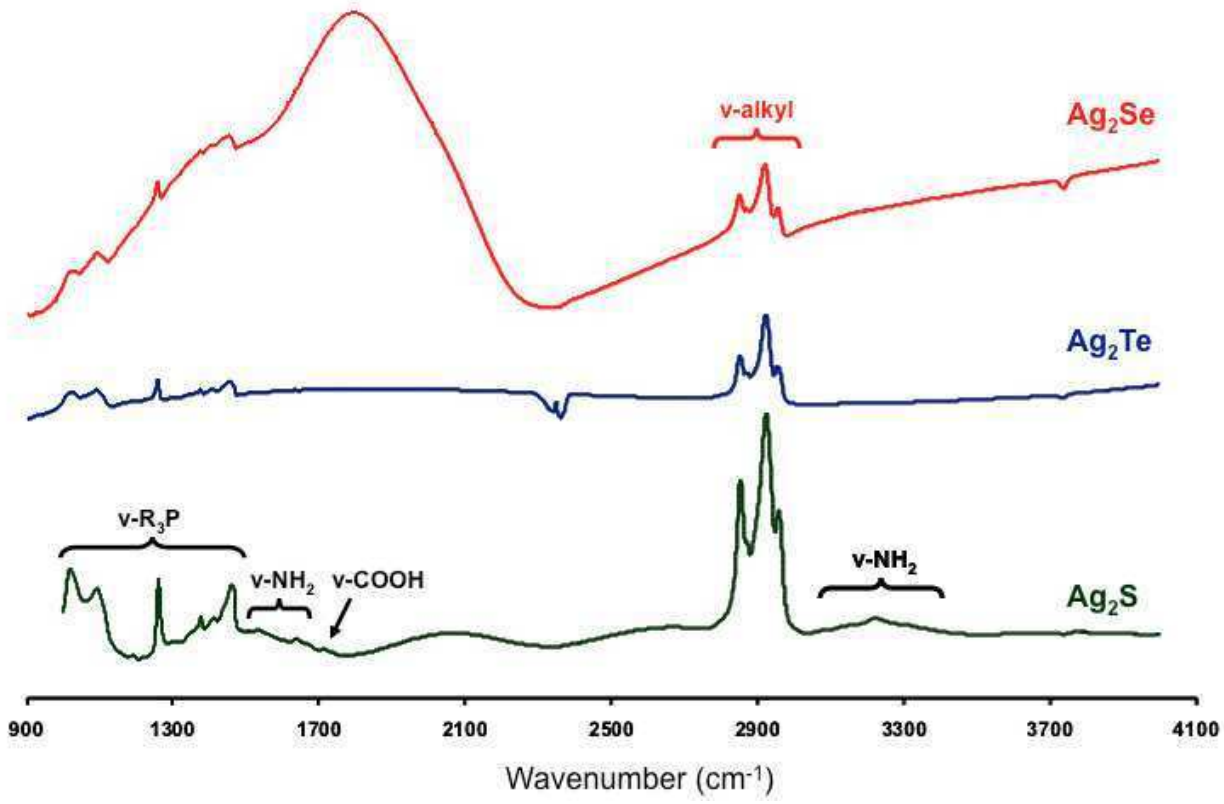

Figure 6.1: Infrared absorbance spectra of a film of as-synthesized Ag_2Se (red), Ag_2Te (blue), and Ag_2S (green) nanocrystals on a CaF_2 window. While the trioctylphosphine peaks exist for all three chalcogenides, one can observe weak amine and oleic acid peaks for the Ag_2S NCs which are absent for Ag_2Te and Ag_2Se NCs. The oscillating peaks in the Ag_2S data are due to interference fringes owing to the smooth surface of the film. The broad absorption feature in the Ag_2Se spectra peaking at around 1800 cm^{-1}, is due to band edge absorption which is discussed in the next chapter. The negative peak at 2350-2400 cm^{-1} for Ag_2Te is caused by residual CO_2 in the spectrometer that was present during the background scan. We assign the peaks at 1025, 1100, 1262, 1378, 1418, and 1467 cm^{-1} to trioctylphosphine, the peak at 1720 cm^{-1} to oleic acid, and the peaks at 1560, 1650, and 3200 cm^{-1} to octadecylamine.

6.3.6 Differences between the Present Synthesis and that of Urban et al.[26]

Our synthesis differs in several significant ways from that of Urban *et al.*[26] These differences explain the dramatic decrease in reaction time and versatility of our approach. The synthesis of Urban *et al.* injects TOP-Te at 85 °C resulting in a mixture of rod-like and spherical Ag_2Te nanocrystals. We believe that this mixture may be caused by a slow nucleation process at this low temperature. The reaction then requires a long aging process (9-12 days) to digest the rod-like nanocrystals and form a nearly monodisperse dispersion.

In contrast, we inject Ag-TOP at a higher temperature (around 190 °C) and proceed with a higher growth temperature (around 150 °C). At these temperatures, a fast and uniform nucleation is obtained, followed by steady growth. As discussed in the previous section, the mixture of ODA and OA is also important for tuning the speed of the growth.

6.3.7 Colloidal Stability of Ag_2E Nanocrystals

The as-obtained nanocrystals can be dispersed in various organic solvents, such as hexanes, toluene, or chloroform. In general, Ag_2E nanocrystals can plate a glass container with silver if stored under ambient conditions (exposed to light and air). We found that this effect was strongly dependent on the solvent in which the nanocrystals were dispersed. When dispersed in hexanes, this effect occurred for our Ag_2Se and Ag_2Te nanocrystals after ca. 4 and 3 weeks, respectively. However, by storing the nanocrystals at -20 °C in the dark, they remain stable for months. Our Ag_2S nanocrystals have been stable even under ambient conditions for months too. For all samples, the stability decreased if excess surface ligands were removed from the dispersion by repeated precipitations.

Solvents other than hexanes also reduced the stability. In octane, Ag_2Se and Ag_2Te nanocrystals plated out within a couple of days. Ag_2S remained stable. In chloroform and TCE, all three plated out within a couple of days. In carbon tetrachloride, Ag_2S plated out in ~2 days, Ag_2Se in 10 hours, and Ag_2Te in ~2 hours. In general, the stability was also a function of concentration. The length of time before plating decreased if the dispersion was more concentrated.

6.3.8 Structural Characterization of Ag_2E Nanocrystals

6.3.8.1 Transmission Electron Microscopy

Transmission electron microscope (TEM) images of a typical Ag_2Se sample are shown in Figure 6.2a,b. The nanocrystals are nearly monodisperse with a standard deviation of 5.1 % and an average size around 6.5 nm. This value is consistent with the

average size of the crystallographic domains calculated by fitting the X-ray diffraction (XRD) spectra (discussed below) using the Scherrer equation. A representative high-resolution TEM (HRTEM) image of the Ag_2Se nanocrystals demonstrates that they are single crystalline (Figure 6.2b).

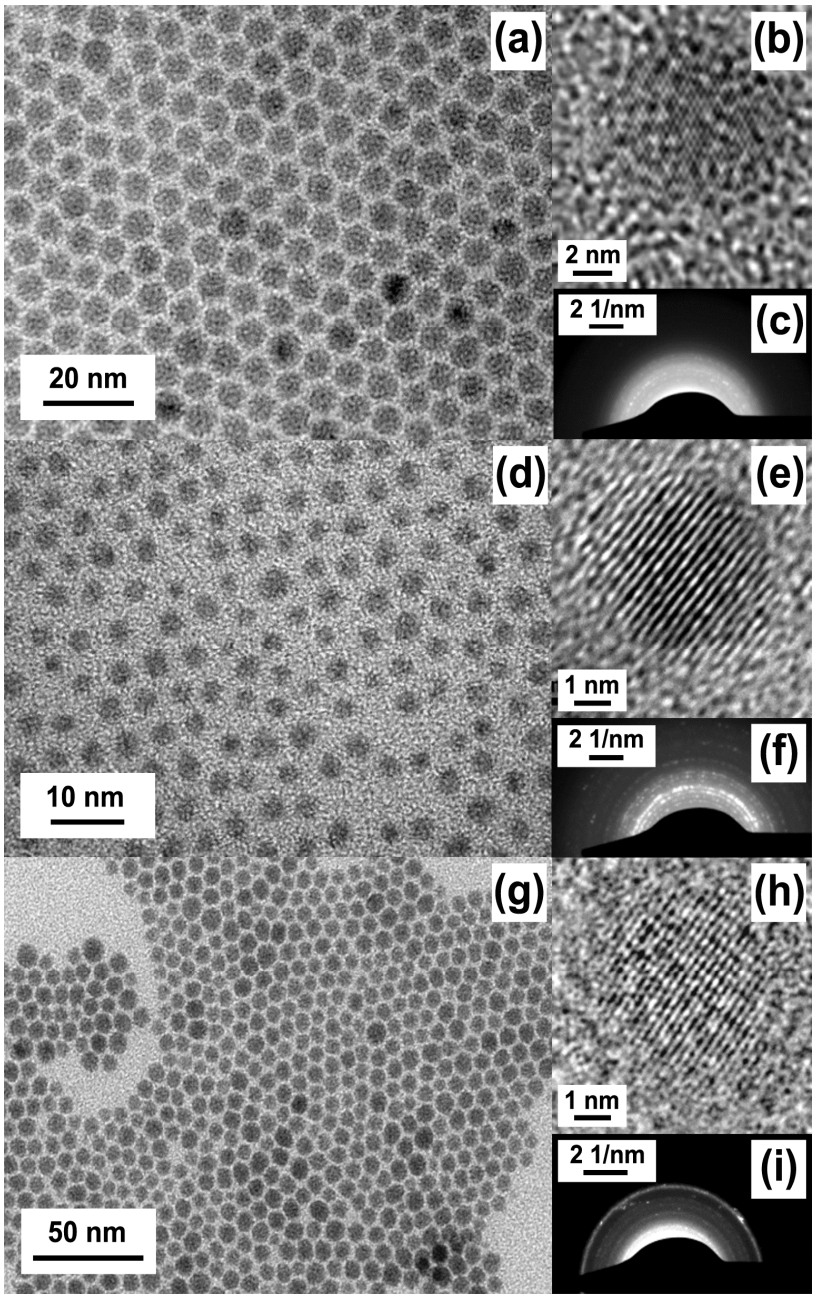

Figure 6.2: Low-magnification TEM micrographs and selected area electron diffraction patterns of an ensemble of as-synthesized nanocrystals of (a,c) Ag_2Se, (d,f) Ag_2S, and (g,i) Ag_2Te. Lattice-resolved HRTEM micrograph of a single (b) 7-nm diameter Ag_2Se, (e) 4-nm diameter Ag_2S, and (h) 7-nm diameter Ag_2Te nanocrystal.

Characteristic TEM images of Ag_2S (Figure 6.2d,e) and Ag_2Te (Figure 6.2g,h) nanocrystals are also shown. The standard deviations in size were 5.3% and 9.1% for Ag_2S and Ag_2Te, respectively. Our Ag_2Se and Ag_2Te nanocrystals exhibited sensitivity to electron irradiation in the TEM. The Ag_2Se and Ag_2Te samples shown in Figure 6.2 were stable for ca. 5-10 minutes under the 300 keV beam. The Ag_2S samples were much less sensitive, allowing one to work for at least an hour before deterioration of the nanocrystals was observed. This affected the quality of the HRTEM images.

6.3.8.2 X-Ray Photoelectron Spectroscopy

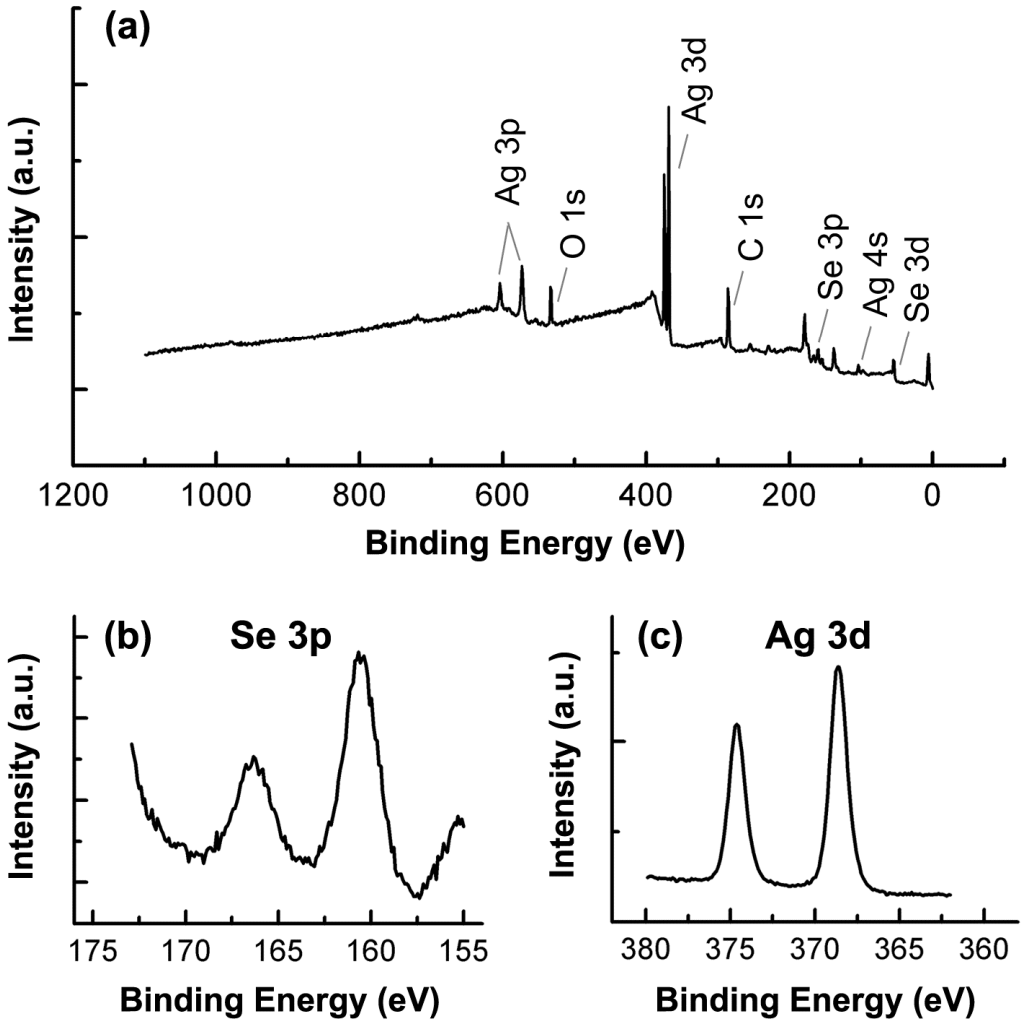

Figure 6.3: (a) XPS survey spectrum of Ag_2Se nanocrystals which shows that Ag and Se are present. XPS high resolution spectra of Ag_2Se from (b) Se 3p and (c) Ag 3d.

To clarify the sample composition and verify that both elements were present in the nanocrystals, several spectroscopic techniques were employed. Figure 6.3a-c presents X-ray photoelectron spectroscopy (XPS) data for the Ag_2Se nanocrystals. The survey spectrum combined with the core-level spectra, which clearly show Ag 3d and Se 3p peaks, indicate that Ag and Se are present. XPS data for Ag_2S and Ag_2Te nanocrystals are presented in Figures 6.4 and 6.5 respectively.

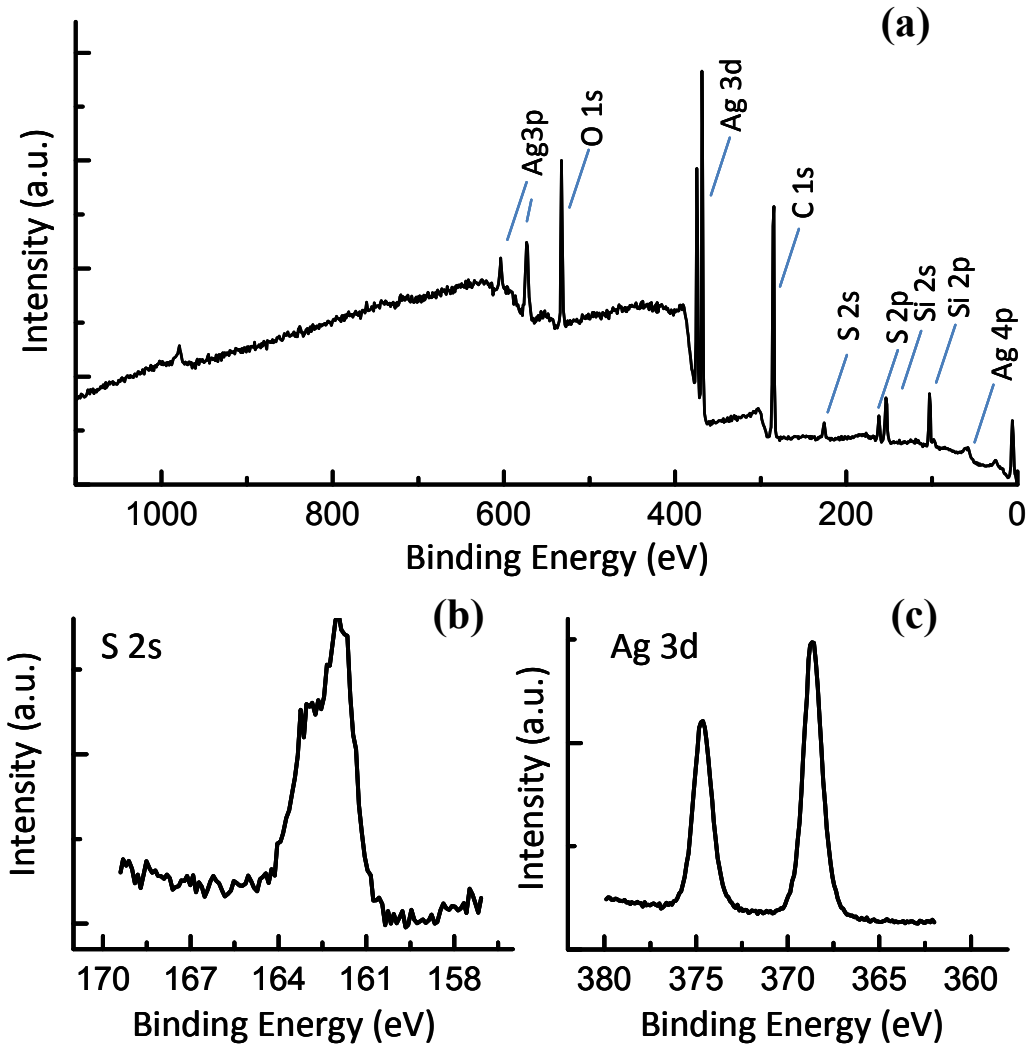

Figure 6.4: (a) XPS survey spectrum of Ag_2S nanocrystals which shows that Ag and S are present. XPS high resolution spectra of Ag_2S from (b) S 2s and (c) Ag 3d. The small peak at around 980 eV is an artifact due to an oxygen Auger peak.

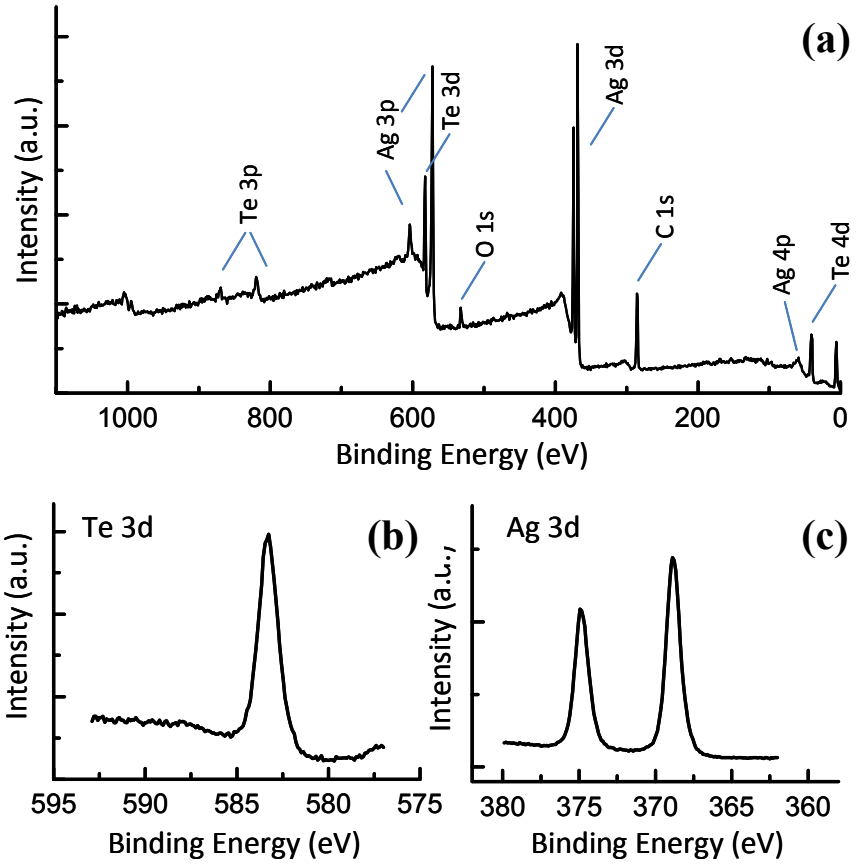

Figure 6.5: (a) XPS survey spectrum of Ag_2Te nanocrystals which shows that Ag and Te are present. XPS high resolution spectra of Ag_2Te from (b) Te 3d and (c) Ag 3d. The small peak at around 980 eV is an artifact due to an oxygen Auger peak.

6.3.8.3 Electron Probe Micro Analysis

Quantitative determination of the chemical composition was performed with electron probe micro analysis (EPMA). This showed that the elemental ratio of Ag:E (E=Se, Te, S) was 1.85:1 (±1.7%), 2.14:1 (±6.7%), and 1.94:1 (±1.5%), respectively, close to the expected ratio of 2:1.

The following tables (6.1-6.3) summarize the atomic ratios calculated from these various points on the films. The standard deviation (σ) in the ratios obtained was < 2 % for Ag_2S and Ag_2Se films, while it was around 6.7 % for the Ag_2Te film.

Table 6.1. EPMA data for films of Ag_2S nanocrystals.

No.	S	Ag	Comment	Atomic Ratio	
1	34.77	66.53	Ag_2S pnt 1	1.91	
2	33.90	65.66	Ag_2S pnt 2	1.94	
3	34.15	65.28	Ag_2S pnt 3	1.91	
4	34.02	67.06	Ag_2S pnt 4	1.97	
5	34.60	66.68	Ag_2S pnt 5	1.93	
6	34.67	67.13	Ag_2S pnt 6	1.94	
7	34.61	66.42	Ag_2S pnt 7	1.92	
8	34.60	65.08	Ag_2S pnt 8	1.88	
9	33.03	66.32	Ag_2S pnt 9	2.01	
10	34.07	66.29	Ag_2S pnt 10	1.95	
average	**34.24**	**66.24**		**1.94**	**Ag/S**
stdev	**0.50**	**0.66**		**0.03**	**1.94**
% stdev	**1.47**	**1.00**		**1.72**	

Table 6.2. EPMA data for films of Ag_2Te nanocrystals.

No.	Te	Ag	Comment	Atomic Ratio	
1	31.20	67.62	Ag_2Te pnt 1	2.17	
2	33.30	65.77	Ag_2Te pnt 2	1.98	
3	34.81	67.66	Ag_2Te pnt 3	1.94	
4	32.59	68.81	Ag_2Te pnt 4	2.11	
5	29.24	71.51	Ag_2Te pnt 5	2.45	
6	33.92	71.51	Ag_2Te pnt 6	2.11	
7	32.47	67.98	Ag_2Te pnt 7	2.09	
8	29.87	67.84	Ag_2Te pnt 8	2.27	
9	34.11	68.62	Ag_2Te pnt 9	2.01	
10	31.22	69.44	Ag_2Te pnt 10	2.22	
average	**32.27**	**68.68**		**2.14**	**Ag/Te**
stdev	**1.76**	**1.69**		**0.14**	**2.14**
% stdev	**5.45**	**2.46**		**6.70**	

Table 6.3. EPMA data for films of Ag_2Se nanocrystals.

No.	Se	Ag	Comment	Atomic Ratio	
1	34.56	64.83	Ag_2Se pnt 1	1.88	
2	35.14	64.04	Ag_2Se pnt 2	1.82	
3	34.75	64.05	Ag_2Se pnt 3	1.84	
4	33.99	64.81	Ag_2Se pnt 4	1.91	
5	35.14	64.05	Ag_2Se pnt 5	1.82	
6	35.24	64.10	Ag_2Se pnt 6	1.82	
7	34.49	63.37	Ag_2Se pnt 7	1.84	
8	34.37	64.22	Ag_2Se pnt 8	1.87	
9	35.38	64.19	Ag_2Se pnt 9	1.81	
10	34.51	63.96	Ag_2Se pnt 10	1.85	
average	**34.76**	**64.16**		**1.85**	**Ag/Se**
stdev	**0.43**	**0.40**		**0.03**	**1.85**
% stdev	**1.23**	**0.62**		**1.54**	

6.3.8.4 X-Ray Diffraction

All three silver chalcogenides are also expected to exhibit a temperature-dependent polymorphism. In our syntheses, even though the growth temperatures of Ag_2Se and Ag_2Te are above their respective $\alpha \rightarrow \beta$ phase transition temperatures (135 °C and 150 °C,[30] respectively), selected area electron diffraction patterns (Figure 6.2c, f, i) and powder XRD of the particles' crystallographic structure (Figure 6.6) reveal that none of the final products are in their high-temperature phases. For Ag_2S and Ag_2Te, the equilibrium low-temperature phases are observed, *i.e.* α-Ag_2S (monoclinic, JCPDS 00-014-0072) and α-Ag_2Te (monoclinic, JCPDS 00-034-0142).

However, the experimentally observed XRD pattern for our Ag_2Se nanocrystals is not consistent with either the cubic phase (JCPDS, 00-027-0619) or the orthorhombic phase (JCPDS, 00-024-1041) of Ag_2Se. For Ag_2Se, two low-temperature phases have previously been postulated to exist depending on the crystallite size (stable orthorhombic and metastable tetragonal).[31,32] Although XRD patterns were not available in the database

for the tetragonal phase of Ag_2Se, a careful analysis of our data indicates that all of our Ag_2Se nanocrystals are in the metastable tetragonal phase (having lattice constants a=b=0.706 nm, and c=0.498 nm) instead of the more stable orthorhombic phase.

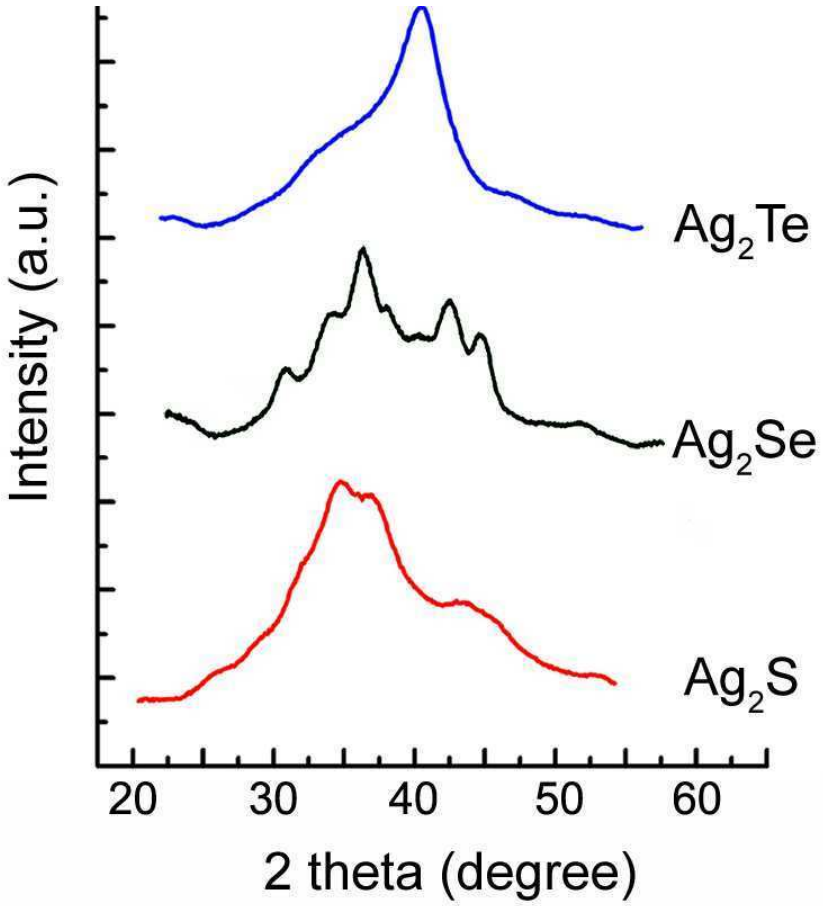

Figure 6.6: XRD patterns of as-synthesized Ag_2Te, Ag_2Se and Ag_2S nanocrystals. The observed peak broadening in the reflections is expected due to size.

Assuming a tetragonal phase with a=b=0.706 nm and c=0.498 nm, we calculated the various possible spacings between crystal planes (*i.e.*, d_{hkl}, where h, k, and l are the three Miller indices for a particular crystal plane). The results are shown in Table 6.4 below.

Table 6.4. Calculated interplanar spacings d_{hkl} for tetragonal Ag_2Se with a=b=0.706 nm and c=0.498 nm.

a (nm)	b (nm)	c (nm)	h	k	l	$1/d_{hkl}^2$	$1/d_{hkl}$ (1/nm)	d_{hkl} (nm)
0.706	0.706	0.498	1	0	0	2.00627563	1.416430595	**0.706**
0.706	0.706	0.498	1	1	0	4.01255126	2.003135357	**0.499217388**
0.706	0.706	0.498	2	0	0	8.025102521	2.83286119	**0.353**
0.706	0.706	0.498	2	1	0	10.03137815	3.167235096	**0.315732798**
0.706	0.706	0.498	3	0	0	18.05648067	4.249291785	**0.235333333**
0.706	0.706	0.498	2	2	0	16.05020504	4.006270715	**0.249608694**
0.706	0.706	0.498	3	1	0	20.0627563	4.479146827	**0.223256803**
0.706	0.706	0.498	4	0	0	32.10041008	5.66572238	**0.1765**
0.706	0.706	0.498	3	2	0	26.08158319	5.107013138	**0.195809169**
0.706	0.706	0.498	4	1	0	34.10668571	5.840092954	**0.171230151**
0.706	0.706	0.498	5	0	0	50.15689075	7.082152975	**0.1412**
0.706	0.706	0.498	0	0	1	4.032193029	2.008032129	**0.498**
0.706	0.706	0.498	1	0	1	6.038468659	2.457329579	**0.40694582**
0.706	0.706	0.498	1	1	1	8.044744289	2.836325843	**0.3525688**
0.706	0.706	0.498	2	0	1	12.05729555	3.472361667	**0.287988434**
0.706	0.706	0.498	2	1	1	14.06357118	3.750142821	**0.266656511**
0.706	0.706	0.498	3	0	1	22.0886737	4.699858902	**0.212772345**
0.706	0.706	0.498	2	2	1	20.08239807	4.48133887	**0.223147597**
0.706	0.706	0.498	3	1	1	24.09494933	4.908660645	**0.203721559**
0.706	0.706	0.498	4	0	1	36.13260311	6.011040102	**0.16636056**
0.706	0.706	0.498	3	2	1	30.11377622	5.487602047	**0.182228957**
0.706	0.706	0.498	4	1	1	38.13887874	6.175668283	**0.161925796**
0.706	0.706	0.498	5	0	1	54.18908378	7.361323508	**0.135845137**
0.706	0.706	0.498	0	0	2	16.12877212	4.016064257	**0.249**
0.706	0.706	0.498	1	0	2	18.13504775	4.258526476	**0.234823009**
0.706	0.706	0.498	1	1	2	20.14132338	4.487908575	**0.222820938**
0.706	0.706	0.498	2	0	2	24.15387464	4.914659158	**0.20347291**
0.706	0.706	0.498	2	1	2	26.16015027	5.114699431	**0.19551491**
0.706	0.706	0.498	3	0	2	34.18525279	5.846815611	**0.171033271**
0.706	0.706	0.498	2	2	2	32.17897716	5.672651687	**0.1762844**
0.706	0.706	0.498	3	1	2	36.19152842	6.015939529	**0.166225075**
0.706	0.706	0.498	4	0	2	48.2291822	6.944723335	**0.143994217**

Based on these calculations and the XRD data, we assigned the experimental d-spacings. Since we do not have the exact location of the atoms in the structure, and hence, the structure factor, we could not calculate the systematic absences which could explain why all the planes in Table 6.4 are not observed. Moreover, as seen in Table 6.5, multiple (hkl) values result in almost the same d-spacing. If we had knowledge of the systematic absences, we could eliminate some of these spacings from our assignments. It is also possible that more than one of these overlapping d-spacings contribute to the XRD pattern, but since they are so close they appear as one peak due to Scherrer broadening. This issue could be resolved by reducing the line broadening by growing larger crystallites. Unfortunately, it was not possible to grow nanocrystals larger than 10 nm while keeping them stable in dispersion. However, all the peaks that were observed in the XRD pattern could be indexed to at least one plane (Figure 6.7). A more detailed structural analysis of tetragonal Ag_2Se could be performed but is beyond the scope of this thesis.

Table 6.5. XRD assignments for our Ag_2Se data using the calculations in Table 6.4. Our peaks match the expected positions for the tetragonal phase. However, some peaks could be assigned to more than one plane.

λ (Cu K_α) =	1.5418 Å			n=1				
2θ	θ	sin θ	λ / 2 sinθ (Å)	d_{hkl}/n (nm)	(hkl)	d_{hkl} calc (nm)	(hkl)	d_{hkl} calc (nm)
28.7	14.35	0.247845	3.110417	0.3110417	120	0.315732		
30.4	15.2	0.262189	2.940243	0.2940243	201	0.287988		
33.6	16.8	0.289032	2.667180	0.2667181	211	0.266656		
36	18	0.309017	2.494684	0.2494685	220	0.249608		
38	19	0.325568	2.367860	0.2367861	102	0.234823	300	0.23533
40.1	20.05	0.34284	2.248570	0.224857	221	0.223147	310	0.22325
42.6	21.3	0.363251	2.122222	0.2122223	301	0.212772		
44.6	22.3	0.379456	2.031591	0.2031592	202	0.203472	311	0.203721
46.7	23.35	0.396347	1.945013	0.1945014	212	0.195514	320	0.19580
51.7	25.85	0.436017	1.768051	0.1768052	222	0.176284	400	0.1765

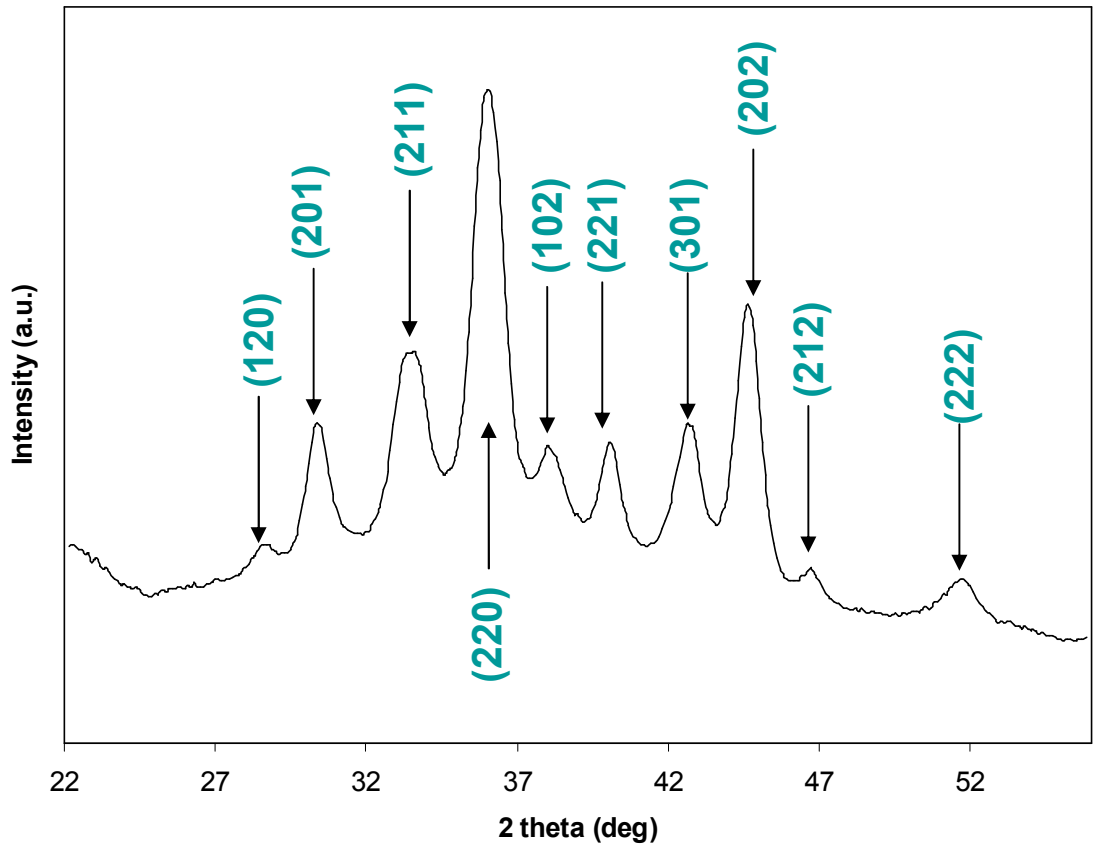

Figure 6.7: XRD pattern of nearly 10-nm Ag_2Se nanocrystals. All of the peaks can be indexed to the tetragonal phase.

In Figure 6.8, we plot the XRD patterns for various sized Ag_2Se nanocrystals (3-10 nm) and observe the gradual narrowing of the peak widths with increasing size. (Transmission electron microscopy was used to confirm the crystallite diameters.) The smallest nanocrystals (~3 nm in size) could also be assigned to the cubic phase because the most prominent peaks from the tetragonal phase overlap with those of the cubic phase. Moreover, due to Scherrer broadening, these prominent peaks overlap with the peaks with lower intensities.

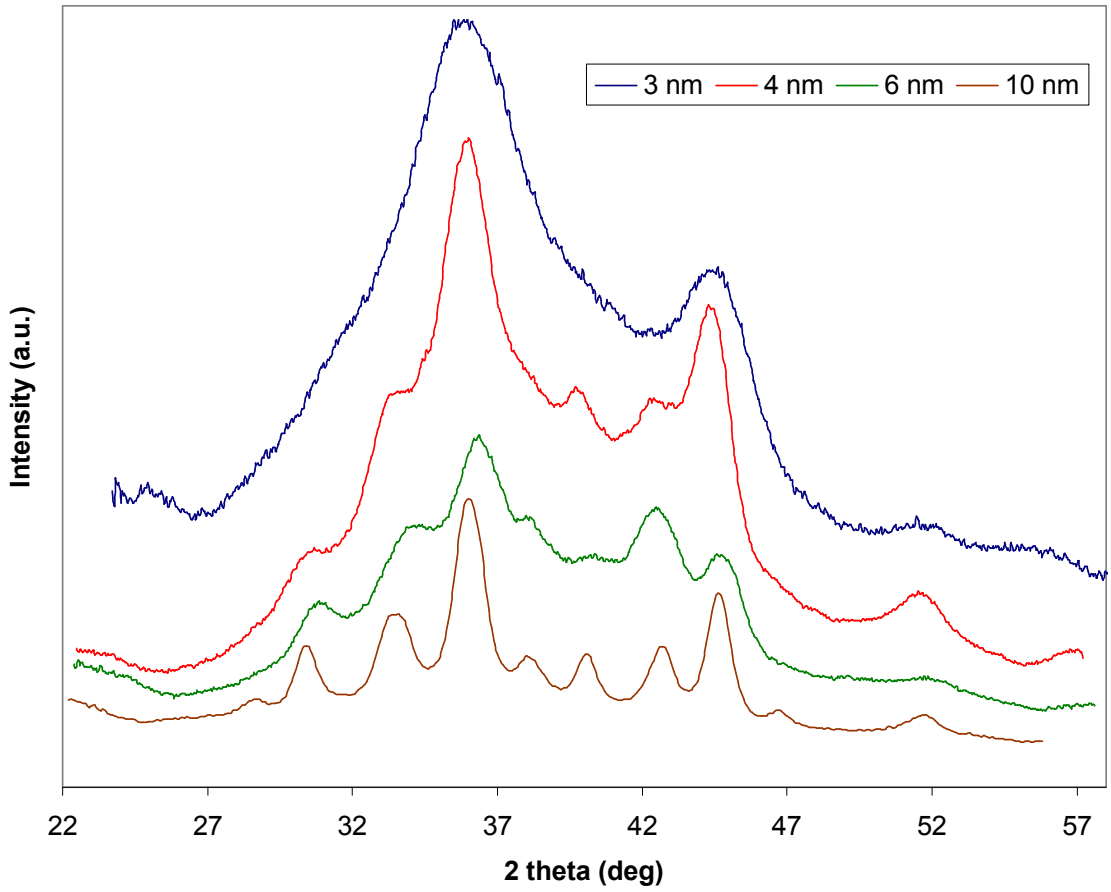

Figure 6.8: XRD Patterns of various sized Ag_2Se nanocrystals ranging from 3 to 10 nm.

However, if one assumes the 3 nm nanocrystals are in the cubic phase and then tries to fit the peaks with Gaussians that account for the Scherrer broadening, one does not obtain the appropriate crystallite size of 3 nm but rather ~1.5 nm (Table 6.6). This profile fitting was performed using JADE 9 software. The output from this program is shown in Figure 6.9 in which the last column of data represents the estimated size in Angstroms. If one does the same analysis with the peaks from the tetragonal phase (Figure 6.10), one obtains a better estimate (~2.5 – 3.5 nm) of the actual crystallite size (Table 6.7).

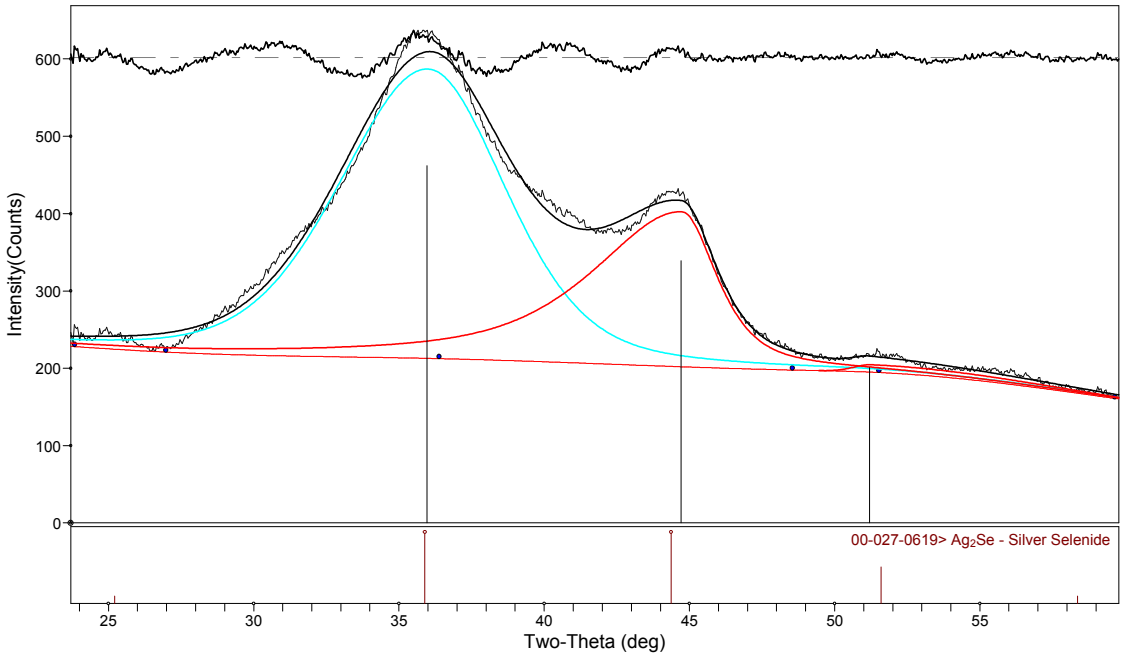

Figure 6.9: Peak fitting of the cubic phase of Ag_2Se to the observed XRD pattern for 3-nm Ag_2Se nanocrystals. The software JADE 9 was used. The last column of numbers represents the estimated size based on Scherrer broadening in Angstroms. The fit predicts a size of ~1.5 nm, which is inconsistent with the actual size determined by transmission electron microscopy. The lower stick spectrum is the expected pattern for bulk cubic Ag_2Se (JCPDS, 00-027-0619).

Table 6.6. Report for peak fitting of the cubic phase of Ag_2Se to the observed XRD pattern for 3-nm Ag_2Se nanocrystals.

Profile Fitting Report	**(Assuming cubic Ag_2Se)**					
R = 3.02%						
@ 2-Theta	**d(Å)**	**Height**	**Area**	**Area%**	**FWHM**	**XS(Å)**
35.963 (0.053)	2.4952 (0.0071)	250 (5)	48481 (1162)	100	6.730 (0.140)	12 (1)
44.709 (0.078)	2.0253 (0.0067)	134 (2)	22490 (474)	46.4	5.116 (0.112)	17 (1)
51.198 (0.892)	1.7828 (0.0579)	6 (1)	1007 (305)	2.1	6.369 (1.709)	14 (5)

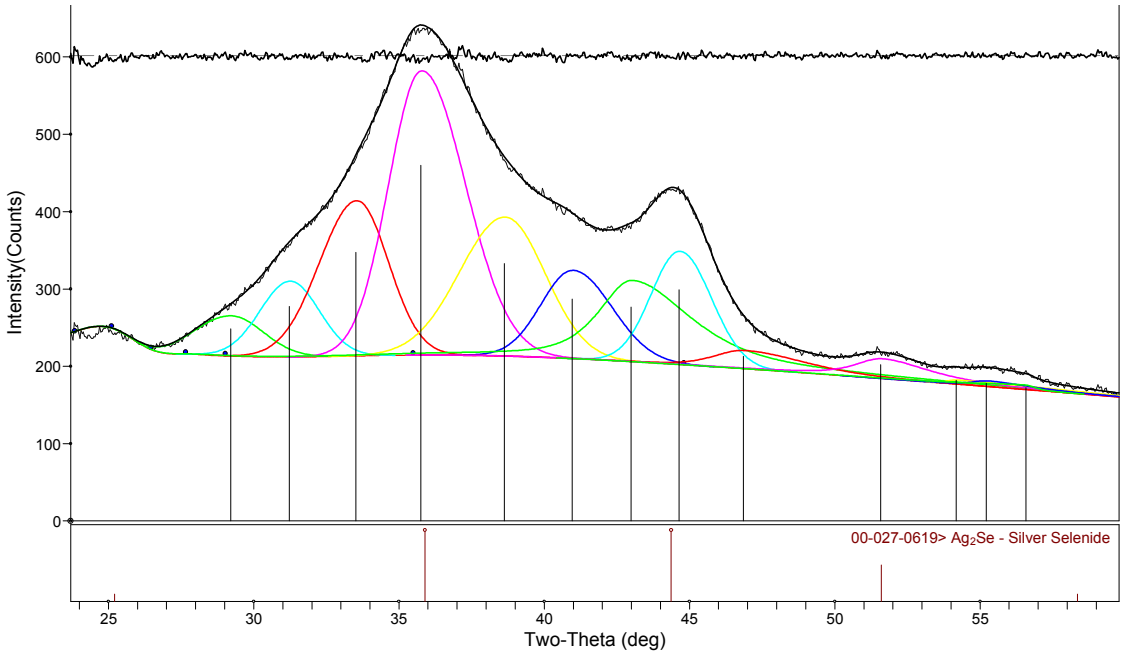

Figure 6.10: Peak fitting of the tetragonal phase of Ag_2Se to the observed XRD pattern for 3-nm Ag_2Se nanocrystals, using JADE 9 as in Figure 6.9. The fit predicts a size of ~2.5 to ~3.5 nm, which is consistent with the actual size determined by transmission electron microscopy. The lower stick spectrum is the expected pattern for bulk cubic Ag_2Se (JCPDS, 00-027-0619).

Table 6.7. Report for peak fitting of the tetragonal phase of Ag_2Se to the observed XRD pattern for 3-nm Ag_2Se nanocrystals.

Profile Fitting Report	(Assuming tetragonal phase)					
R = 1.11%						
@ 2-Theta	d(Å)	Height	Area	Area%	FWHM	XS(Å)
29.212 (2.022)	3.0546 (0.4137)	35	2571	12.7	2.774	30
31.230 (2.316)	2.8618 (0.4138)	65	4192	20.8	2.406	35
33.524 (0.906)	2.6710 (0.1402)	134	9940	49.2	2.788	30
35.750 (0.401)	2.5096 (0.0544)	245	20191	100	3.094	27
38.627 (1.657)	2.3290 (0.1922)	120	10997	54.5	3.446	25
40.961 (1.604)	2.2016 (0.1651)	76	5795	28.7	2.858	30
42.988 (0.598)	2.1023 (0.0558)	70	8737	43.3	3.740	23
44.637 (0.715)	2.0284 (0.0617)	98	6342	31.4	2.435	36
46.858 (1.439)	1.9373 (0.1123)	16	1689	8.4	3.587	24
51.580 (0.656)	1.7705 (0.0419)	17	1741	8.6	3.053	29
54.181 (1.545)	1.6915 (0.0892)	4	426	2.1	4.849	18
55.218 (1.120)	1.6621 (0.0621)	5	370	1.8	2.379	38
56.576 (0.479)	1.6254 (0.0252)	4	347	1.7	2.366	39

These results suggest that: (i) Ag_2Se and Ag_2Te nanocrystals undergo first-order phase transitions to a low temperature phase upon cooling from the reaction temperature, and (ii) Ag_2Se nanocrystals are kinetically trapped in a metastable phase that is not observed in the bulk. TEM and XRD studies with *in-situ* heating to test these two conclusions shall be discussed in Chapter 8.

We also note that similar XRD patterns for Ag_2Se nanocrystals have previously been assigned to other crystal structures. Based on our analysis, we believe the prior assignment to the orthorhombic phase is incorrect.[19] Also, small Ag_2Se nanocrystals (roughly 4 nm in size) had been assigned to the cubic phase.[18] Our smallest nanocrystals (~3 nm in size) do indeed exhibit an XRD pattern that could be attributed to the cubic phase. However, the most prominent XRD peaks from the tetragonal and cubic overlap. Thus, with Scherrer broadening, these two phases are difficult to distinguish in small nanocrystals. Because our larger Ag_2Se nanocrystals are clearly in the tetragonal phase (Figure 6.8), we believe it is more likely that all of our sizes have the tetragonal structure. This conclusion also agrees with other reports.[31,32] This implies that all of our Ag_2Se nanocrystals are trapped in a metastable crystal structure.

6.3.9 Optical Absorption Spectroscopy of Ag_2E Nanocrystals

The optical absorption spectra of dispersions in tetrachloro-ethylene are shown in Figure 6.11. The Ag_2Te spectrum shows three clearly resolved transitions, as observed previously.[26,33] Surprisingly, the spectra from our Ag_2S and Ag_2Se samples are featureless despite having much narrower size distributions (~5%) than our Ag_2Te sample (~9%). We also find that the Ag_2Te absorption features are not size dependent, at least over the size range accessible to us (~3 to ~8 nm in diameter). The explanation for these transitions and the absence of similar features in Ag_2S nanocrystals is still under investigation. Absorption in Ag_2Se nanocrystals will be discussed further in the next chapter.

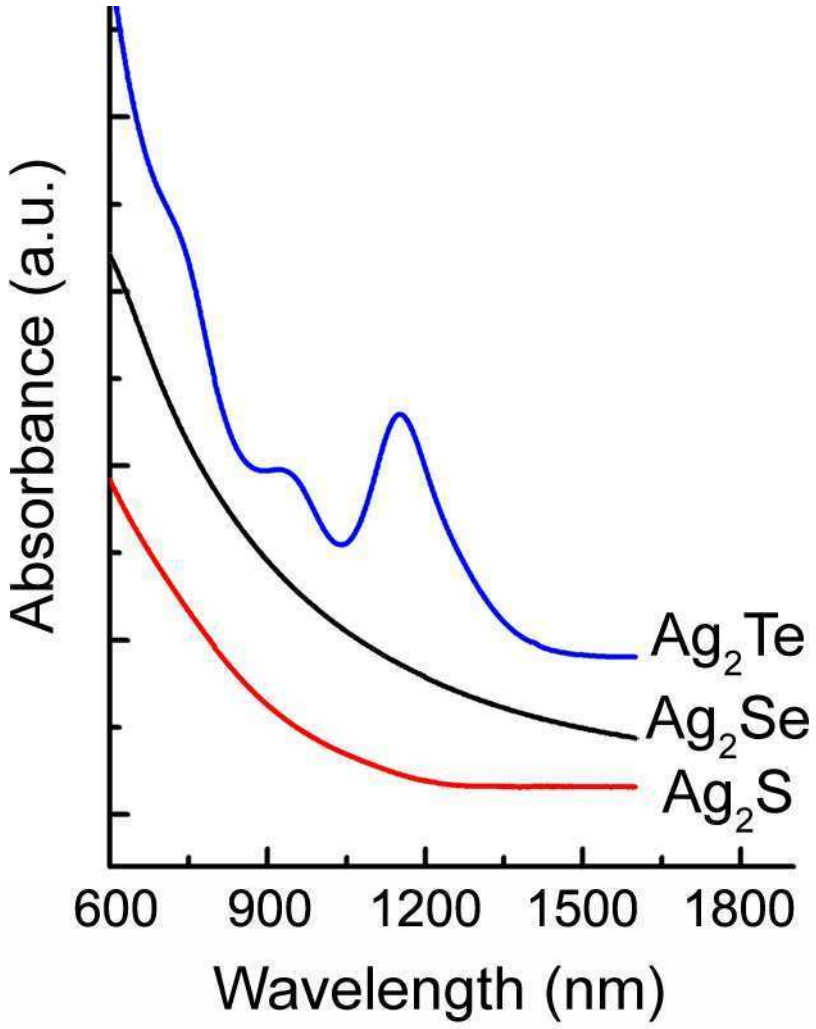

Figure 6.11: Room temperature optical absorption spectra of as-synthesized Ag_2Te, Ag_2Se and Ag_2S nanocrystals.

6.4 CONCLUSION

In conclusion, a simple route to nearly monodisperse colloidal Ag_2Se nanocrystals has been presented. This synthesis can also be adapted to yield Ag_2S and Ag_2Te nanocrystals. The particles are nearly stoichiometric and single crystalline. Ag_2S and Ag_2Te are produced in their low-temperature equilibrium phases. For Ag_2Se, the metastable tetragonal phase is obtained. Due to the simplicity and adaptability of the synthesis in terms of size and material, a variety of new nanoscale silver chalcogenides

can be obtained. These materials have unique properties and the nanocrystals should allow new phenomena and applications to be explored.

6.5 EXPERIMENTAL SECTION

6.5.1 Chemicals

Carbon tetrachloride (reagent grade, 99.9%), chloroform (HPLC grade, ≥99.8%), methyl alcohol (HPLC grade, ≥99.9%), 1-octadecene (ODE, technical grade, 90%), octadecylamine (ODA, technical grade, 90%), octane (reagent grade, 98%), oleic acid (OA, technical grade, 90%), selenium pellets (Se, 99.999%), sulfur powder (S, 99.95%), tellurium shot (Te, 1-2 mm, 99.999%), tetrachloroethylene (TCE, spectrophotometric grade, ≥99.9%), toluene (HPLC grade, 99.9%), and tri-*n*-octylphosphine (TOP, technical grade, 90%) were purchased from Sigma-Aldrich. Hexanes (ACS grade) was purchased from VWR International. Reagent alcohol (histological grade, 90% ethyl alcohol, 5% methyl alcohol, 5% butyl alcohol) and butyl alcohol were obtained from Fisher Scientific. Silver nitrate ($AgNO_3$, 99.9995%) was purchased from Strem Chemicals. All chemicals were used as delivered without further purification.

6.5.2 Sample Characterization

A Bruker-AXS microdiffractometer was utilized to collect X-ray diffraction (XRD) patterns (Cu-K_α). An FEI Tecnai G^2 F30 transmission electron microscope (TEM) was used to image the nanocrystals with an acceleration voltage of 300 kV. Optical absorption data were measured with a Cary 5 (Varian) ultraviolet-visible-near-infrared (UV-VIS-NIR) spectrometer. Electron probe micro analysis (EPMA) was performed using a JEOL 8900R electron probe micro analyzer with an acceleration voltage of 10 kV and a beam current of 50 nA with a 75 micron beam diameter. Each element was analyzed in its own wavelength-dispersive spectrometer and pure metals or binary compounds were used as standards. A JEOL thin-film correction algorithm was used for the quantitative elemental analyses. Films of Ag_2E (E = S, Se, and Te) nanocrystals (NCs) were spin-coated from dispersions of these NCs in anhydrous octane on a heavily

doped Si wafer covered with a thermally grown 300 nm thick SiO_2 layer. Data for EPMA was collected from 10 different points on each sample and analyzed. Films were prepared for FTIR spectroscopy by drop-casting a dispersion of nanocrystals in an 8:1 hexane:octane mixture on CaF_2 windows. Spectra were obtained on a Nicolet Magna 560 spectrometer. Peak assignments were made with the assistance of Ref. 29. X-ray photoelectron spectroscopy (XPS) measurements were performed on drop-cast silver chalcogenide films using an SSX-100 system (Surface Science Instruments) with Al K_α X-ray radiation.

6.6 REFERENCES

(1) Schoen, D. T.; Xie, C.; Cui, Y. *Journal of the American Chemical Society* **2007**, *129*, 4116.

(2) Boolchand, P.; Bresser, W. J. *Nature* **2001**, *410*, 1070.

(3) Ferhat, M.; Nagao, J. *Journal of Applied Physics* **2000**, *88*, 813.

(4) Parish, M. M.; Littlewood, P. B. *Nature* **2003**, *426*, 162.

(5) Xu, R.; Husmann, A.; Rosenbaum, T. F.; Saboungi, M. L.; Enderby, J. E.; Littlewood, P. B. *Nature* **1997**, *390*, 57.

(6) Gur, I.; Fromer, N. A.; Geier, M. L.; Alivisatos, A. P. *Science* **2005**, *310*, 462.

(7) Colvin, V. L.; Schlamp, M. C.; Alivisatos, A. P. *Nature* **1994**, *370*, 354.

(8) Tessler, N.; Medvedev, V.; Kazes, M.; Kan, S.; Banin, U. *Science* **2002**, *295*, 1506.

(9) Klein, D. L.; Roth, R.; Lim, A. K. L.; Alivisatos, A. P.; McEuen, P. L. *Nature* **1997**, *389*, 699.

(10) Talapin, D. V.; Murray, C. B. *Science* **2005**, *310*, 86.

(11) Bruchez, M., Jr.; Moronne, M.; Gin, P.; Weiss, S.; Alivisatos, A. P. *Science* **1998**, *281*, 2013.

(12) Chan, W. C. W.; Nie, S. *Science* **1998**, *281*, 2016.

(13) Du, Y. P.; Xu, B.; Fu, T.; Cai, M.; Li, F.; Zhang, Y.; Wang, Q. B. *Journal of the American Chemical Society* **2010**, *132*, 1470.

(14) Gao, F.; Lu, Q. Y.; Zhao, D. Y. *Nano Letters* **2003**, *3*, 85.

(15) Hoyer, P.; Weller, H. *Chemical Physics Letters* **1994**, *224*, 75.

(16) Huxter, V. M.; Mirkovic, T.; Nair, P. S.; Scholes, G. D. *Advanced Materials* **2008**, *20*, 2439.

(17) Motte, L.; Billoudet, F.; Lacaze, E.; Douin, J.; Pileni, M. P. *Journal of Physical Chemistry B* **1997**, *101*, 138.

(18) Son, D. H.; Hughes, S. M.; Yin, Y.; Paul Alivisatos, A. *Science* **2004**, *306*, 1009.

(19) Wang, D.; Xie, T.; Peng, Q.; Li, Y. *Journal of the American Chemical Society* **2008**, *130*, 4016.

(20) Gates, B.; Wu, Y. Y.; Yin, Y. D.; Yang, P. D.; Xia, Y. N. *Journal of the American Chemical Society* **2001**, *123*, 11500.

(21) Xiao, J.; Xie, Y.; Tang, R.; Luo, W. *Journal of Materials Chemistry* **2002**, *12*, 1148.

(22) Safran, G.; Geszti, O.; Radnoczi, G.; Barna, P. B. *Thin Solid Films* **1998**, *317*, 72.

(23) Wang, W. Z.; Geng, Y.; Qian, Y. T.; Ji, M. R.; Xie, Y. *Materials Research Bulletin* **1999**, *34*, 877.

(24) Henshaw, G.; Parkin, I. P.; Shaw, G. A. *Journal of the Chemical Society-Dalton Transactions* **1997**, 231.

(25) Ng, M. T.; Boothroyd, C.; Vittal, J. J. *Chemical Communications* **2005**, 3820.

(26) Urban, J. J.; Talapin, D. V.; Shevchenko, E. V.; Kagan, C. R.; Murray, C. B. *Nature Materials* **2007**, *6*, 115.

(27) Reiss, P.; Bleuse, J.; Pron, A. *Nano Letters* **2002**, *2*, 781.

(28) Murphy, J. E.; Beard, M. C.; Nozik, A. J. *Journal of Physical Chemistry B* **2006**, *110*, 25455.

(29) Silverstein, R. M.; Bassler, G. C.; Morrill, T. C. *Spectrometric Identification of Organic Compounds*; Wiley: New York, 1981.

(30) Qin, A. M.; Fang, Y. P.; Tao, P. F.; Zhang, J. Y.; Su, C. Y. *Inorganic Chemistry* **2007**, *46*, 7403.

(31) Gates, B.; Mayers, B.; Wu, Y. Y.; Sun, Y. G.; Cattle, B.; Yang, P. D.; Xia, Y. N. *Advanced Functional Materials* **2002**, *12*, 679.

(32) Gunter, J. R.; Keusch, P. *Ultramicroscopy* **1993**, *49*, 293.

(33) Ko, D.-K.; Urban, J. J.; Murray, C. B. *Nano Letters* **2010**, *10*, 1842.

CHAPTER 7

QUANTUM CONFINEMENT IN SILVER SELENIDE SEMICONDUCTOR NANOCRYSTALS*

7.1 OVERVIEW

We prepare Ag_2Se nanocrystals with average diameters between 2.7 and 10.4 nm that exhibit narrow optical absorption features in the near to mid infrared. We demonstrate that these features are broadly tunable due to quantum confinement. They provide the longest wavelength absorption peaks (6.5 μm) yet reported for colloidal nanocrystals.

7.2 INTRODUCTION

Efficient mid-infrared (IR) light sources, lasers and detectors are critical for many commercial, military and scientific applications, including remote sensing, thermography and astronomy. Commercial devices based on InSb and HgCdTe photodiodes exist, but their expense and low operating temperatures prevent some large-scale applications.[1,2] For example, chemical gas analysis, meteorology and pollution monitoring, could benefit from new multi-spectral IR photodetectors that are inexpensive and operate near room temperature.[3] Organic laser dyes and rare-earth-doped crystals could potentially provide alternative IR sources, but dyes are restricted to the near IR[4] and rare earths offer limited tunability in the mid IR.[5] Epitaxial quantum dots (EQDs)[6] have led to efficient mid-IR emitters with commercially viable performance. However, they are grown with ultra-high

* This chapter is reproduced with permission from Ayaskanta Sahu, Ankur Khare, Donna D. Deng, and David J. Norris, "Quantum Confinement in Silver Selenide Semiconductor Nanocrystals," Chemical Communications **2012**, 48, 5458 (DOI:10.1039/C2CC30539A).

vacuum techniques, such as molecular beam epitaxy, and are not chemically processible, both leading to high cost.

Colloidal QDs, also known as semiconductor nanocrystals, may provide an attractive alternative IR material.[7] Nanocrystals can be chemically synthesized with narrow size distributions and then dispersed in a range of organic and inorganic solvents. This can lead to low-cost films of QDs that are highly uniform and densely packed, properties that are potentially useful for the active region of an optical device. Unfortunately, although a variety of semiconductor nanocrystals have been chemically synthesized for applications in the visible and the near IR,[8-10] only a few examples exist with tunabilty in the mid IR, most significantly HgTe nanocrystals.[11-13]

In general, tunability can arise in nanocrystals due to quantum confinement,[14,15] which increases the energy of electronic transitions between the valence- and conduction-band states. Thus, in sufficiently small nanocrystals, the lowest energy absorption feature can shift blue from the bulk bandgap with decreasing particle size. Each bulk band also evolves into a set of discrete electronic states. Thus, a second approach to tunable IR absorption is to utilize "intraband" transitions between these states, *e.g.* within the conduction band.[16,17] However, this requires a steady population of electrons in the conduction band states of the nanocrystals. Achieving this through optical excitation or charge injection presents challenges for devices.

Herein, we instead utilize a relatively unexplored nanocrystal material, silver selenide (Ag_2Se), to obtain wavelength-tunable absorption in the near to mid IR. Because Ag_2Se has a narrow bulk bandgap of ~0.15 eV,[18] it presents an interesting material system to obtain tunable mid-IR absorption (>2.5 μm) with quantum confinement. It is also environmentally more benign than the mercury chalcogenides. Below we demonstrate colloidal QDs that exhibit spectrally narrow absorption peaks in the mid IR that are tunable with particle size down to 0.19 eV (6.5 μm).

Recently, the first syntheses of high-quality Ag_2Se nanocrystals have appeared.[19-22] However, only one demonstrated quantum confinement in optical spectra[22] and, in this case, the transitions were in the near IR. To explore applications in the mid IR as well as other size-dependent phenomena, one needs single-crystalline, nearly monodisperse Ag_2Se nanocrystals over a large range of sizes. In Chapter 6, we presented a route to obtain fairly monodisperse single-crystalline silver chalcogenide nanocrystals (S, Se and Te).[19] Herein, we adapt our approach to synthesize Ag_2Se nanocrystals from 2.8 to 10.4 nm for optical studies.

7.3 RESULTS AND DISCUSSION

A typical synthesis began by heating a mixture of 7.8 g of tri-octylphosphine oxide (TOPO) and 6.6 mL of oleylamine (OM) in a 50-mL round-bottom flask to 70 °C and degassing and flushing with N_2 three times. Simultaneously, 16.99 g of $AgNO_3$ and 7.896 g of selenium shot was dissolved in 100 mL tri-*n*-octylphosphine (TOP) to obtain 1M Ag-TOP and 1M TOP-Se, respectively, in a N_2-filled glovebox. 4 mL of TOP-Se was added to the flask and the temperature was raised to 150 °C. 4 mL of Ag-TOP was then quickly injected into the rapidly stirring mixture and the reaction was allowed to proceed for ~4 minutes at 140 °C. The growth was quenched in a water bath and 20 ml of butanol was added to prevent solidification of the reaction mixture while cooling. The nanocrystals were precipitated with ethanol and re-dispersed in hexanes. This precipitation was repeated at least twice to remove all unreacted oleylamine. No additional size-selection was used.

The procedure above generates nanocrystals with an average size of 7.3 nm and a standard deviation of 0.67 nm (~9%) as determined by transmission electron microscopy (TEM, Figure 7.1a). High-resolution TEM (Figure 7.1b) demonstrates that the nanocrystals are single crystal. The IR absorption spectrum (Figure 7.1c) exhibits a distinct peak around 0.22 eV (5.6 μm).

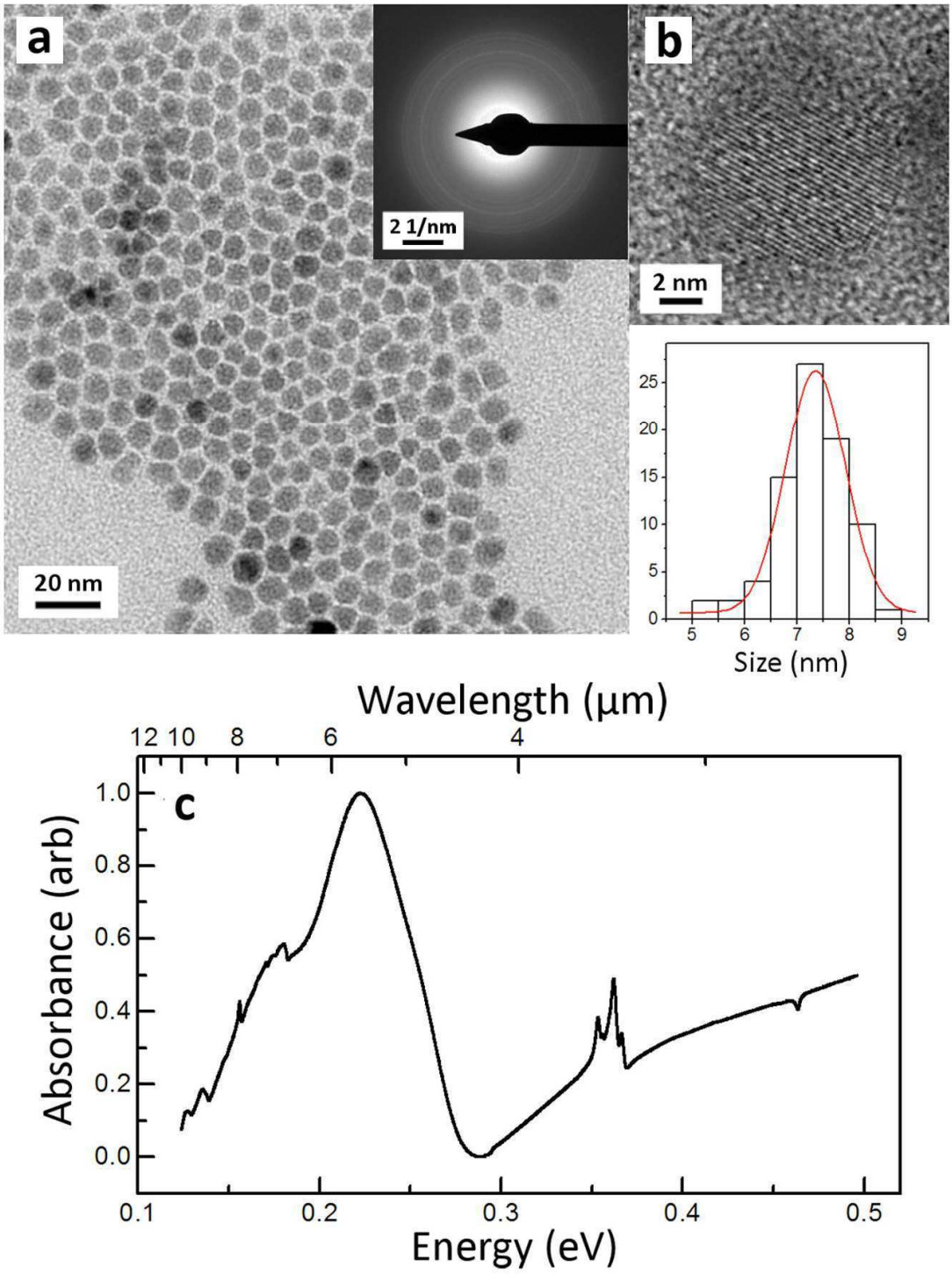

Figure 7.1: (a) Low-magnification TEM image, selected-area electron-diffraction pattern and size histogram of Ag_2Se nanocrystals with an average diameter of 7.3-nm. (b) Lattice-resolved high-resolution TEM image of an 8.2-nm-diameter single-crystalline Ag_2Se nanocrystal. (c) Room temperature infrared absorbance spectra of a film of the same nanocrystals in (a). The features at 0.35-0.37 eV are due to C-H stretches in the organic ligands that coat the nanocrystal surfaces.

To obtain nanocrystals of different sizes, we could simply vary the growth time. For the synthesis of the smallest sized Ag_2Se nanocrystals (~2.8 nm ±16%), an approach similar to the one described earlier was followed. 4 ml of TOP-Se was added to the mixture of OM and TOPO and the temperature raised to 150 °C. The heating mantle was then removed and the reaction flask was cooled down using a water bath. As the temperature dropped, 4 ml of Ag-TOP was rapidly injected at 130 °C and the reaction was quenched within 15 seconds by addition of 24 mL butanol.

Following the recipe mentioned above, we were able to obtain fairly monodisperse (σ~10%) nanocrystals with sizes less than 7.5 nm by varying the growth times between 1 to 6 minutes. Growing the particles longer did result in an increase of the average size. However, the size distribution also broadened, presumably due to Ostwald ripening. To obtain bigger nanocrystals, we therefore modified the synthesis by using a different precursor to introduce silver. Instead of a TOP complex with $AgNO_3$, we used an AgCl-TOP complex instead. In a N_2-filled glovebox, 14.32 g of AgCl was dissolved in 100 mL TOP to obtain 1M AgCl-TOP. 2 mL of TOP-Se was added to the mixture of OM and TOPO after degassing and the temperature was raised to 180 °C. 2 mL of AgCl-TOP was injected to this rapidly stirring mixture and the reaction was allowed to proceed for nearly 20 minutes at 170 °C to yield 10.4-nm Ag_2Se nanocrystals. The reaction was quenched using a water bath and 10 mL of butanol was injected to prevent the unreacted TOPO from solidifying. Around 8 mL of ethanol was added to precipitate the nanocrystals. Care was taken while purifying these particles. Owing to their large size, they tend to crash out of solution and are unrecoverable if excess alcohol is added during the cleaning procedure.

In Figure 7.2 we show representative low- and high-resolution TEM images, as well as the size histograms for our smallest (~2.8 nm ±16%) and largest (~10.4 nm ±11%) nanocrystals. Figure 7.3 shows representative TEM images for various sized Ag_2Se nanocrystals obtained using the second approach with AgCl-TOP as the silver precursor.

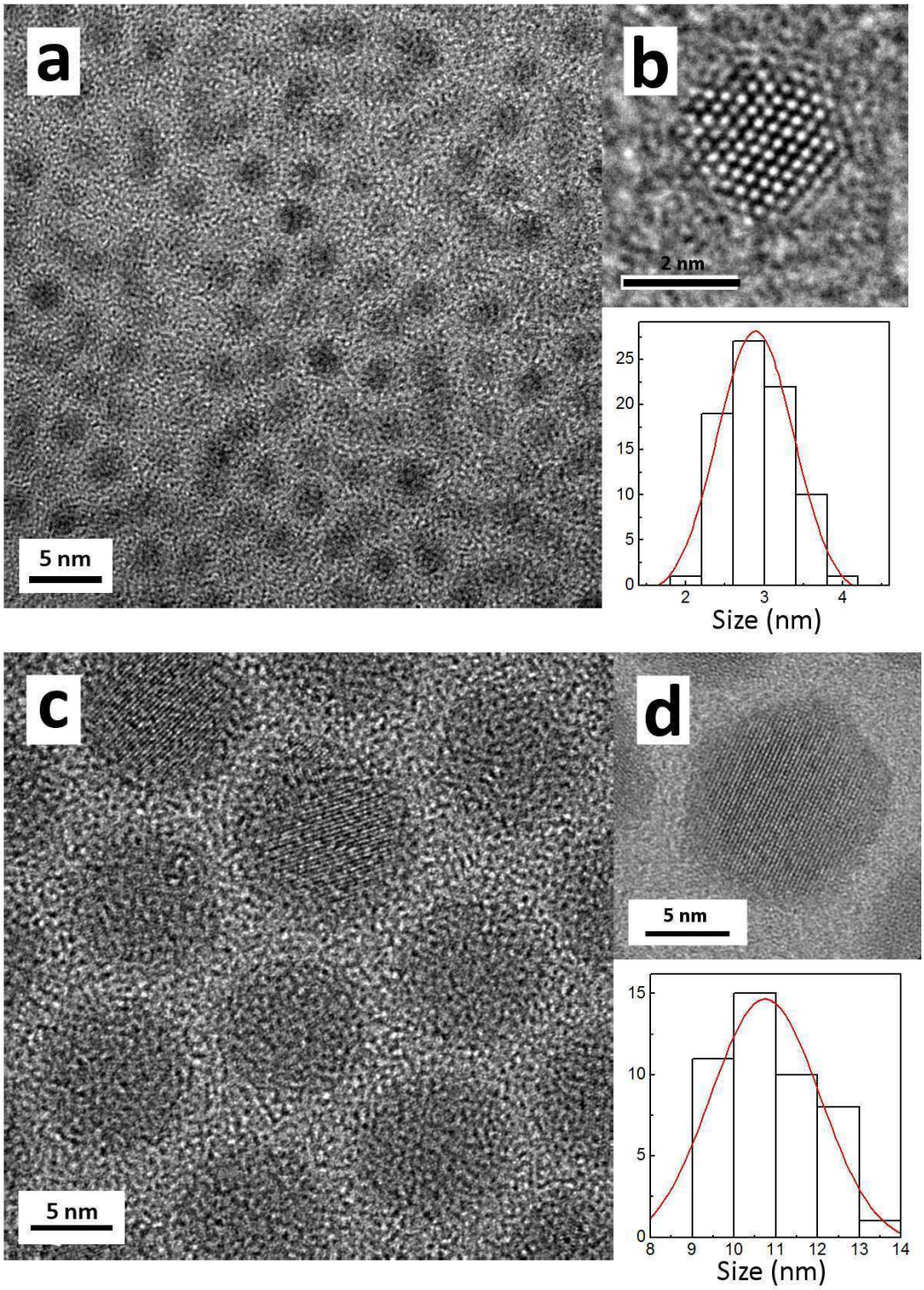

Figure 7.2: (a, c) Low-magnification transmission electron microscope (TEM) images and size histograms showing the size distribution of an ensemble of Ag_2Se nanocrystals with average sizes of 2.8- and 10.4-nm, respectively. (b, d) Lattice-resolved high-resolution TEM micrographs of 2.3- and 10.3-nm single-crystalline Ag_2Se nanocrystals, respectively.

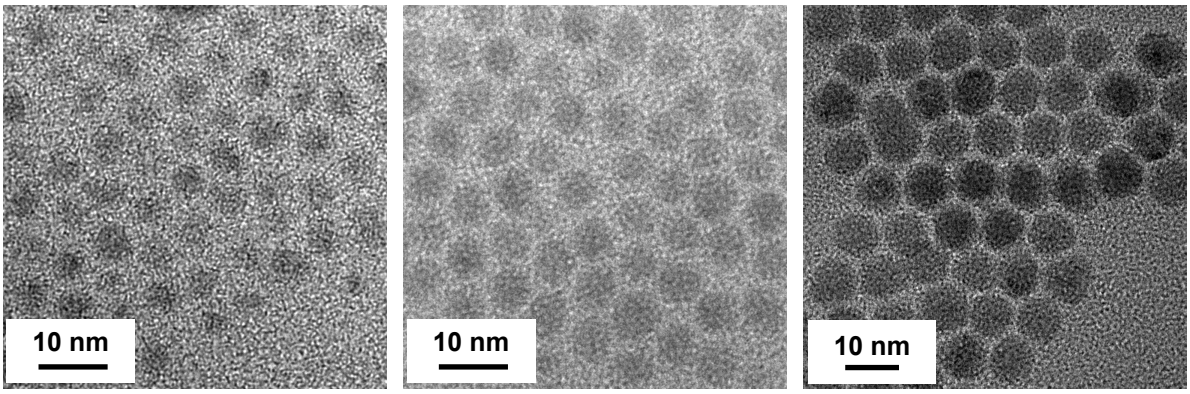

Figure 7.3: Transmission electron microscope (TEM) images for 4.2-nm, 5.9-nm and 8.6-nm Ag_2Se nanocrystals.

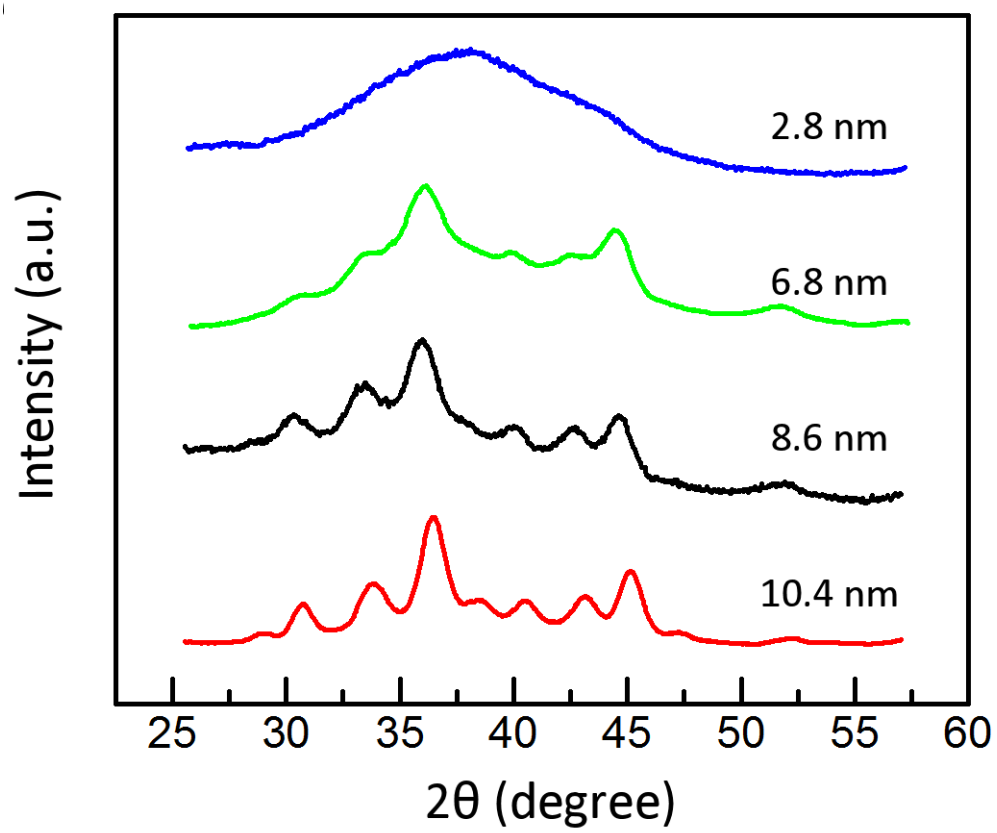

Figure 7.4: X-ray diffraction patterns of different-sized Ag_2Se nanocrystals. The average diameter obtained from transmission electron microscopy is indicated next to each pattern. The observed peak broadening with decreasing diameter is expected due to size effects.

Nanoscale Ag_2Se has been reported to exhibit two room-temperature polymorphs: orthorhombic, which is the stable bulk phase, and tetragonal, which is a metastable

phase.[23,24] Previously, we obtained Ag_2Se nanocrystals that existed in the tetragonal phase.[19] X-ray diffractograms (Figure 7.4) and selected-area diffraction patterns (Figure 7.1a) confirmed that all of the Ag_2Se nanocrystals presented here were also in the tetragonal phase.

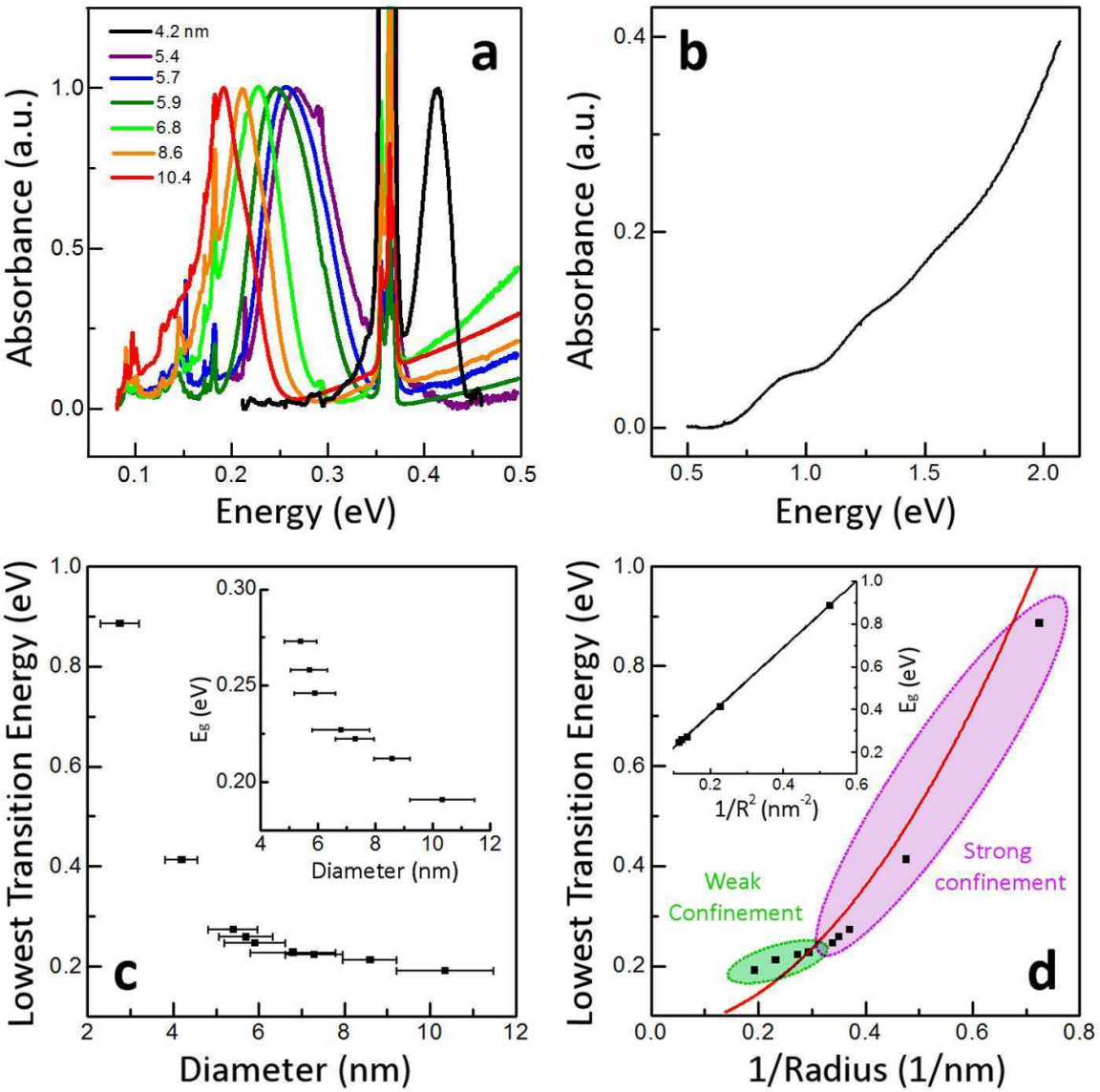

Figure 7.5: (a) Room-temperature mid-IR absorbance spectra of films of Ag_2Se nanocrystals of different sizes. The strong peak around 0.36 eV is due to C-H stretches in the organic ligands that coat the nanocrystal surfaces. (b) Room-temperature near-IR absorbance spectrum of 2.8-nm Ag_2Se nanocrystals dispersed in tetrachloroethylene. (c) The energy of the lowest optical transition versus size for our Ag_2Se nanocrystals. The error bars represent one standard deviation in the average diameter. The inset is a blow-up for nanocrystals larger than 5 nm. (d) The energy of the lowest optical transition versus 1/radius. The solid red line represents effective mass theory using literature parameters. The transition energy does not vary as 1/radius but rather $1/(\text{radius})^2$ for nanocrystals <6 nm, which are strongly confined (inset). The solid black line is a linear fit to the experimental data with a coefficient of determination of 0.9998.

When the nanocrystal size was varied, the lowest energy absorption feature could be tuned over the mid IR (Figure 7.5a). These features are narrow with a full-width-at-half-maximum (FWHM) typically <75 meV. Only the smallest nanocrystals, which were the most polydisperse, exhibited a broader feature, with a FWHM of ~200 meV (Figure 7.5b). In this case, the reaction was quenched right after nucleation and the nanocrystals may not have had sufficient time to undergo any size-focusing. Figure 7.5c presents a correlation between QD size (from TEM) and the energy of the lowest optical transition (from the absorption peak).

Table 7.1. Electron Probe Micro Analysis (EPMA) data for films of 6.8-nm-diameter Ag_2Se nanocrystals.

No.	Se	Ag	Comment	Atomic Ratio	
1	34.25	65.09	Ag_2Se pnt 1	1.900	
2	33.76	65.27	Ag_2Se pnt 2	1.933	
3	33.70	65.53	Ag_2Se pnt 3	1.945	
4	33.30	65.67	Ag_2Se pnt 4	1.972	
5	33.04	67.19	Ag_2Se pnt 5	2.033	
6	34.45	64.78	Ag_2Se pnt 6	1.881	
7	34.04	65.31	Ag_2Se pnt 7	1.919	
8	34.87	65.90	Ag_2Se pnt 8	1.890	
9	34.46	65.35	Ag_2Se pnt 9	1.896	
10	34.05	66.45	Ag_2Se pnt 10	1.951	
Average	**33.99**	**65.65**		**1.932**	**Ag/Se**
Stdev	**0.53**	**0.67**		**0.046**	**1.932**
% Stdev	**1.56**	**1.02**		**2.4**	

While quantum confinement can explain the size dependence of the absorption feature (more below), we first consider another explanation. IR absorption in non-stoichiometric copper chalcogenides has recently been explained by free-carrier absorption.[25-27] To give rise to a similar effect at 0.23 eV (5.5 μm) for our 6.8-nm Ag_2Se nanocrystals, we estimated that each particle would need ~7 vacancies, or a stoichiometric ratio of 1.9984 (Ag:Se). However, a quantitative analysis of the stoichiometry of our 6.8-nm sample by electron probe micro analysis (EPMA, see Table

7.1) gave a value of 1.9321 (±0.046). Table 7.1 summarizes the atomic ratios calculated from various points on a film of 6.8-nm-diameter Ag_2Se nanocrystals. The standard deviation (σ) in the ratios obtained was ~ 2.4 %. This suggests that the observed peak is not due to free carriers. Further, peaks due to free-carrier absorption are generally much broader (typically with linewidths of hundreds of meVs). Finally, to explain the data, the stoichiometery would need to decrease monotonically with increasing size, which seems unlikely.

Rather, we argue that the size dependence is due to quantum confinement. In this case, we can estimate the position of the lowest-energy electronic transitions using a simple particle-in-a-sphere effective-mass model.[14,15] To do this, we need the dielectric constant and effective masses for bulk Ag_2Se. Using a dielectric constant of 11 (Ref. 28) and effective masses for the electron, m_e^*, and hole, m_h^*, of $0.32m$ and $0.54m$, respectively,[18,28] where m is the free-electron mass, we obtain an exciton Bohr radius of 2.9 nm. Thus, as a first approximation, nanocrystals with diameters <5.8 nm should exhibit quantum confinement.

Specifically, according to simple effective-mass theory, the energy of the lowest electronic transition in our nanocrystals, E_g^{NC}, should vary as

$$E_g^{NC}(R) = E_g^{bulk} + \frac{\hbar^2 \pi^2}{2R^2}\left[\frac{1}{m_e} + \frac{1}{m_h}\right]$$

where E_g^{bulk} is the bulk bandgap, R is the radius of the nanocrystal and $\hbar$ is Planck's constant. Two values for the bulk bandgap of Ag_2Se have been reported. For the orthorhombic phase, it has been determined to be 0.15-0.18 eV.[18,22,29-33] The existence of another phase with a bandgap of 0.05-0.07 eV has also been discussed[29-32] and has been assigned to the tetragonal phase.[29] The red line in Figure 7.5d plots the expected size dependence of E_g^{NC} for our Ag_2Se nanocrystals assuming $m_e^* = 0.32\,m$ and $m_h^* = 0.54\,m$ and a bulk bandgap gap of 0.07 eV.[29] This bandgap was chosen since our nanocrystals are in the tetragonal phase. The experimental energies are close to but systematically lower than the values predicted by the simple model until ~6 nm (Figure 7.5d). We

postulate that particles below this size are in the strongly confined regime (since the calculated excitonic Bohr diameter was 5.8 nm). Nanocrystals larger than this size are more weakly confined and show weaker size dependence. These strong and weak confinement regimes are qualitatively indicated by the purple and green ovals in Figure 7.5d.

For particles smaller than 6 nm, we performed a linear least squares analysis on the plot of E_g^{NC} versus $1/R^2$ (the black line in the inset of Figure 7.5d). The size dependence of the data is well approximated by E_g^{NC} [eV] = 0.064 + 1.566 (R[nm])$^{-2}$. The y-intercept at infinite R should represent the bulk bandgap. The value from the fit (0.064 eV) is consistent with the previously reported value for the bulk bandgap (0.07 eV) of the tetragonal phase of Ag_2Se. The fit is also in agreement with Ref. 22, where a distinct absorption peak was observed at ~750 nm (1.653 eV) for Ag_2Se nanocrystals with a diameter of 2 ± 0.6 nm. Our formula predicts that this absorption peak should be at 1.63 ± 0.47 eV.

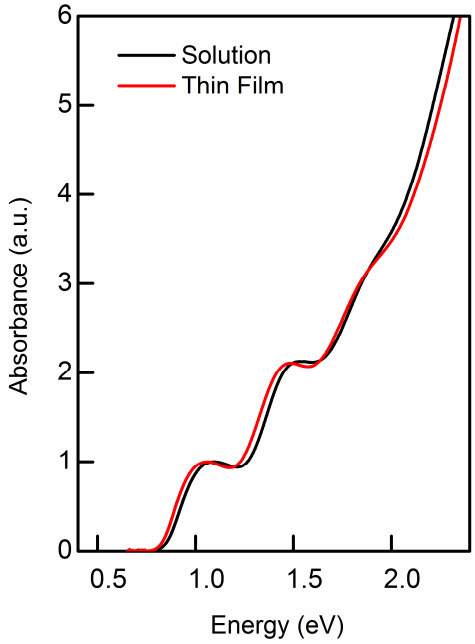

Figure 7.6: Room-temperature near-IR absorbance spectra of 2.7-nm Ag_2Se nanocrystals dispersed in carbon tetrachloride (black) and as a thin solid film on a sapphire disk (red). The energy of the lowest optical transition undergoes a red shift of nearly 26 meV when cast as a thin film due to a combination of changes in the dielectric function of the film and increased electronic coupling between the quantum dots (Ref. 34).

We note that, except for the 2.8-nm sample, all absorption measurements (Figure 7.5) were performed on films of nanocrystals. Thus, the lowest energy peaks are slightly red-shifted from what would be obtained from dispersions due to the solvatochromic effect and possibly electronic coupling.[34] Indeed, we observe a 26 meV shift for 2.7 nm Ag_2Se nanocrystals (Figure 7.6).

Photoluminescence was also observed in the same sample. A large Stokes shift (390 meV) exists between the lowest energy absorption peak and the fluorescence maximum (Figure 7.7).

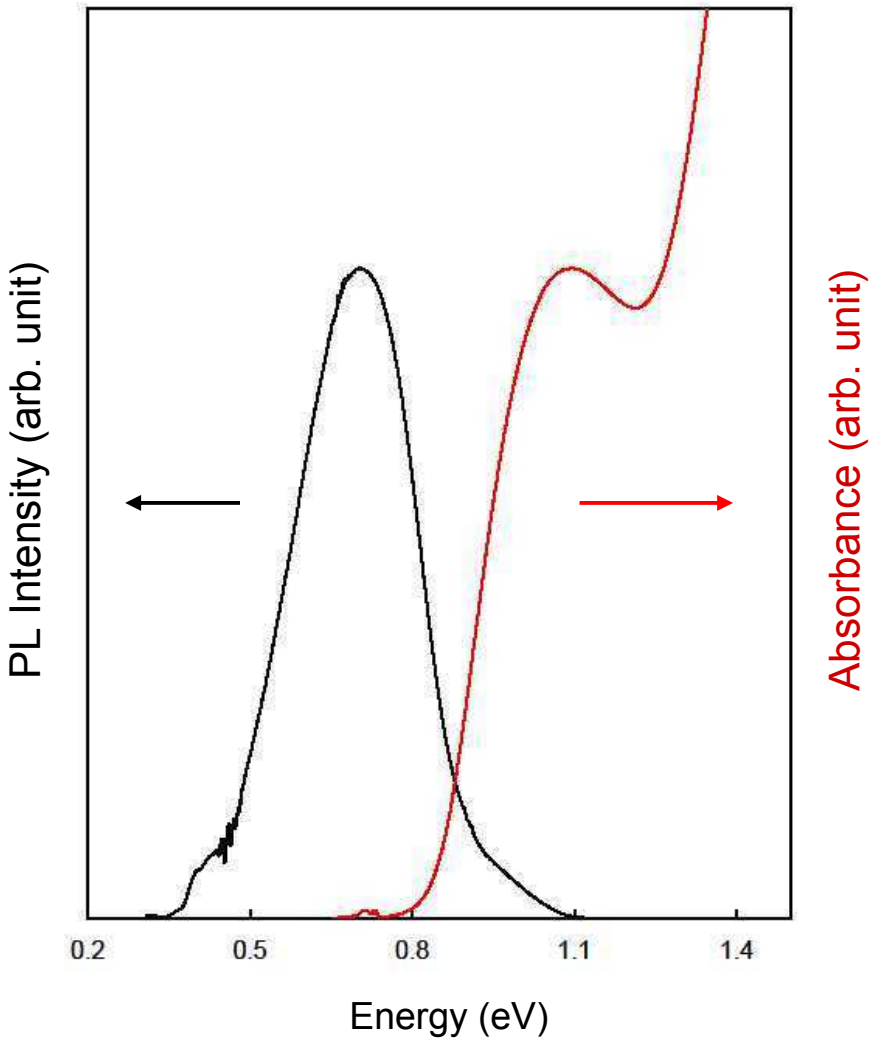

Figure 7.7: Absorbance (red) and emission (black) spectra of 2.7-nm Ag_2Se nanocrystals dispersed in carbon tetrachloride. The absorption and photoluminescence maxima are at 1.093 and 0.703 eV, respectively, indicating a large Stokes shift of ~390 meV.

7.4 CONCLUSION

In conclusion, we demonstrate a wet-chemical synthesis to produce fairly monodisperse Ag_2Se nanocrystals ranging from 2.8 to 10.4 nm in diameter. These nanocrystals exhibit quantum confinement with an absorption peak that can be tuned with size from 0.19 (6.5 μm) to 0.89 eV (1.4 μm). With potential applications in IR optical and optoelectronic devices like solar cells, molecular detectors and thermal imagers, Ag_2Se nanocrystals provide an excellent alternative to other IR-active materials with heavy metals such as Pb or Hg.

7.5 EXPERIMENTAL SECTION

7.5.1 Chemicals

Carbon tetrachloride (reagent grade, 99.9%), tetrachloroethylene (TCE, spectrophotometric grade, ≥99%), selenium pellets (Se, 99.999%), tri-*n*-octylphosphine oxide (TOPO, technical grade, 90%), oleyl amine (OM, technical grade, 70%), octane (reagent grade, 98%) and tri-*n*-octylphosphine (TOP, technical grade, 90%) were purchased from Sigma-Aldrich. Hexanes (ACS grade) was purchased from VWR International. Reagent alcohol (histological grade, 90% ethyl alcohol, 5% methyl alcohol, 5% butyl alcohol) and butyl alcohol were obtained from Fisher Scientific. Silver nitrate ($AgNO_3$, 99.9995%) and silver chloride (AgCl, 99.9%) were purchased from Strem Chemicals. All chemicals were used as delivered without further purification.

7.5.2 Sample Characterization

FEI Tecnai T12 and G^2 F30 transmission electron microscopes (TEM) were used to image the nanocrystals with an acceleration voltage of 120 kV and 300 kV, respectively. Films were prepared for X-ray diffraction (XRD) by drop-casting a dispersion of nanocrystals in an 8:1 hexane:octane mixture on heavily doped Si wafers covered with a thermally grown 300-nm-thick SiO_2 layer and the patterns (Cu-K_α) were collected using a Bruker-AXS microdiffractometer. Optical absorption data for the

smallest nanocrystals (dispersed in carbon tetrachloride or TCE) were measured with a Cary 5 (Varian) ultraviolet-visible-near-infrared (UV-VIS-NIR) spectrometer. A JEOL 8900R electron probe micro analyzer was used for electron probe micro analyses (EPMA) with an acceleration voltage of 10 kV and a beam current of 50 nA with a 75 micron beam diameter. Pure metals or binary compounds were used as standards for Ag and Se. Both elements were analyzed in their respective wavelength-dispersive spectrometers. For subsequent quantitative elemental analyses, we used a JEOL thin-film correction algorithm. Films of Ag_2Se nanocrystals were spin-coated from dispersions in octane on a heavily doped Si wafer covered with a thermally grown 300-nm-thick SiO_2 layer. Data for EPMA was collected from 10 different points on the film and analyzed. Films were prepared for attenuated total internal reflection Fourier transform infrared (ATR-FTIR) spectroscopy by drop-casting a dispersion of nanocrystals in hexanes onto a trapezoidal-shaped Germanium (Ge) ATR crystal ($5 \times 1 \times 0.1$ cm^3) and allowing the deposit to dry for nearly 20 minutes. FTIR absorption spectra were collected using a Nicolet Magna 550 series II FTIR spectrophotometer with an ATR accessory (Harrick Scientific) and a Glowbar source. The infrared beam was focused normal onto the 45° beveled edge of the trapezoidal Ge ATR crystal. All spectra were obtained by averaging 100 interferograms at 4 cm^{-1} resolution. Peak assignments[35] were made with the assistance of Ref. 35. The fluorescence spectrum was measured in a Bruker Vertex 80 Fourier-transform infrared (FTIR) spectrometer. The excitation source was an OSRAM OSTAR® model SFH 4751 infrared light source emitting at a wavelength of 940 nm. The photoluminescence was detected by a liquid nitrogen-cooled InSb photodiode from Bruker.

7.6 REFERENCES

(1) Rogalski, A. *Infrared Physics & Technology* **2002**, *43*, 187.

(2) Rogalski, A.; Antoszewski, J.; Faraone, L. *Journal of Applied Physics* **2009**, *105*, 091101.

(3) Xu, H. Z.; Zhao, E.; Majumdar, A.; Jayasinghe, L.; Shi, Z. *Electronics Letters* **2003**, *39*, 659.

(4) Resch-Genger, U.; Grabolle, M.; Cavaliere-Jaricot, S.; Nitschke, R.; Nann, T. *Nature Methods* **2008**, *5*, 763.

(5) Shaw, L. B.; Cole, B.; Thielen, P. A.; Sanghera, J. S.; Aggarwal, I. D. *IEEE Journal of Quantum Electronics* **2001**, *37*, 1127.

(6) Bhattacharya, P.; Ghosh, S.; Stiff-Roberts, A. D. *Annual Review of Materials Research* **2004**, *34*, 1.

(7) Murray, C. B.; Sun, S. H.; Gaschler, W.; Doyle, H.; Betley, T. A.; Kagan, C. R. *IBM Journal of Research and Development* **2001**, *45*, 47.

(8) Battaglia, D.; Peng, X. G. *Nano Letters* **2002**, *2*, 1027.

(9) Hines, M. A.; Scholes, G. D. *Advanced Materials* **2003**, *15*, 1844.

(10) Murray, C. B.; Kagan, C. R.; Bawendi, M. G. *Annual Review of Material Science* **2000**, *30*, 545.

(11) Keuleyan, S.; Lhuillier, E.; Brajuskovic, V.; Guyot-Sionnest, P. *Nature Photonics* **2011**, *5*, 489.

(12) Keuleyan, S.; Lhuillier, E.; Guyot-Sionnest, P. *Journal of the American Chemical Society* **2011**, *133*, 16422.

(13) Kovalenko, M. V.; Kaufmann, E.; Pachinger, D.; Roither, J.; Huber, M.; Stangl, J.; Hesser, G.; Schaffler, F.; Heiss, W. *Journal of the American Chemical Society* **2006**, *128*, 3516.

(14) Brus, L. E. *Journal of Chemical Physics* **1984**, *80*, 4403.

(15) Efros, A. L.; Efros, A. L. *Soviet Physics Semiconductors - USSR* **1982**, *16*, 772.

(16) Guyot-Sionnest, P.; Hines, M. A. *Applied Physics Letters* **1998**, *72*, 686.

(17) Wehrenberg, B. L.; Wang, C. J.; Guyot-Sionnest, P. *Journal of Physical Chemistry B* **2002**, *106*, 10634.

(18) Junod, P.; Hediger, H.; Kilchor, B.; Wullschleger, J. *Philosophical Magazine* **1977**, *36*, 941.

(19) Sahu, A.; Qi, L.; Kang, M. S.; Deng, D.; Norris, D. J. *Journal of the American Chemical Society* **2011**, *133*, 6509.

(20) Wang, D.; Xie, T.; Peng, Q.; Li, Y. *Journal of the American Chemical Society* **2008**, *130*, 4016.

(21) Wang, S. B.; Hu, B.; Liu, C. C.; Yu, S. H. *Journal of Colloid and Interface Science* **2008**, *325*, 351.

(22) Yarema, M.; Pichler, S.; Sytnyk, M.; Seyrkammer, R.; Lechner, R. T.; Fritz-Popovski, G.; Jarzab, D.; Szendrei, K.; Resel, R.; Korovyanko, O.; Loi, M. A.; Paris, O.; Hesser, G.; Heiss, W. *ACS Nano* **2011**, *5*, 3758.

(23) Gates, B.; Mayers, B.; Wu, Y. Y.; Sun, Y. G.; Cattle, B.; Yang, P. D.; Xia, Y. N. *Advanced Functional Materials* **2002**, *12*, 679.

(24) Gunter, J. R.; Keusch, P. *Ultramicroscopy* **1993**, *49*, 293.

(25) Deka, S.; Genovese, A.; Zhang, Y.; Miszta, K.; Bertoni, G.; Krahne, R.; Giannini, C.; Manna, L. *Journal of the American Chemical Society* **2010**, *132*, 8912.

(26) Luther, J. M.; Jain, P. K.; Ewers, T.; Alivisatos, A. P. *Nature Materials* **2011**, *10*, 361.

(27) Zhao, Y. X.; Pan, H. C.; Lou, Y. B.; Qiu, X. F.; Zhu, J. J.; Burda, C. *Journal of the American Chemical Society* **2009**, *131*, 4253.

(28) Gorbachev, V. V.; Putilin, I. M. *Physica Status Solidi B - Basic Research* **1975**, *69*, K153.

(29) Abdullayev, A. G.; Shafizade, R. B.; Krupnikov, E. S.; Kiriluk, K. V. *Thin Solid Films* **1983**, *106*, 175.

(30) Baer, Y.; Frohlich, C.; Steigmeier, E.; Busch, G. *Zeitschrift Fur Naturforschung Part A - Astrophysik Physik Und Physikalische Chemie* **1962**, *A 17*, 886.

(31) Boettcher, A.; Haase, G.; Treupel, H. *Zeitschrift fur Angewandte Physik* **1955**, *7*, 478.

(32) Dalven, R.; Gill, R. *Physical Review* **1967**, *159*, 645.

(33) Dalven, R.; Gill, R. *Journal of Applied Physics* **1967**, *38*, 753.

(34) Leatherdale, C. A.; Bawendi, M. G. *Physical Review B* **2001**, *63*, 165315.

(35) Silverstein, R. M.; Bassler, G. C.; Morrill, T. C. *Spectrometric Identification of Organic Compounds*; Wiley: New York, 1981.

CHAPTER 8

PHASE TRANSITIONS IN SILVER CHALCOGENIDE NANOCRYSTALS

8.1 INTRODUCTION

In the previous chapters, we have discussed extensively ways to expand the range of available properties in solid state materials, firstly by doping (silver in CdSe and PbSe nanocrystals),[1] and secondly by shrinking the size of the material (quantum confinement in Ag_2Se nanocrystals)[2,3] and in fact, combining both of these effects when we dope the nanocrystals. While the properties of nano-scale materials are different from those observed in bulk, some of these properties vary continuously as one shrinks the size of the material. The most notable example in this case would be the systematic reduction in melting points with decreasing size (the melting temperature of CdS decreases from 1600 °C in bulk crytals to ~400 °C for nanocrystals).[4] Other properties like quantum confinement arise only below a certain size (exciton Bohr radius of the material).[5,6] Studies of properties like temperature-dependent structural transformations and phase transitions in bulk materials have not been yet expanded fully to the nano-scale. Whether or not these transitions are a continuous or discrete function of the size of the material or even depend on the crystal size at all, will depend on the material. In fact, we have already observed the existence of a metastable tetragonal phase in silver selenide nanocrystals not observed in bulk in Chapters 6 and 7.[2,3] Discovering novel pathways to tap into metastable and high energy structures at or close to ambient conditions will further advance control over material properties.

Traditional studies of phase transitions in bulk systems define the pressure, temperature and composition of the material as the key parameters that

determine the transition point and subsequent behavior. Only in the last few decades has it been appreciated that the physical size of the material also plays a key role in determining the transition point.[7] Solid-solid phase transitions in bulk systems do not occur spontaneously at ambient conditions because there exists a certain barrier to these transitions which is deeply correlated to the difference in their Gibbs free energies. In nanocrystalline systems where a huge fraction of the atoms are on the surface, with substantially different energies compared to in bulk crsytals, one can imagine that the barriers to these phase transitions should be altered significantly. Even in the highest quality bulk crystals, a certain number of defects always exist at equilibrium. The new phase nucleates typically at these defect sites and then expands systematically throughout the crystal. The case is very different for nanocrystals.

Especially in nanocrystals synthesized by the high-temperature hot-injection methods described in this thesis, the nanocrystals are in general single crystalline and free of structural defects.[8] Additionally, using high-temperature synthetic techniques helps anneal any defects that might exist during nucleation and/or growth since the high-energy defect is always only a few lattice lengths away from the surface. Thus one can safely assume the defect concentrations in nanocrystals are much lower than what one would expect in bulk crystals. Hence, there exist very few nucleation sites in these pristine crystals for the onset of phase transitions that progress by the nucleation and growth mechanism. Even if the new phase manages to nucleate in a certain nanocrystal, the maximum distance it can propagate is restricted to within the dimension of that nanocrystal and cannot extend to neighboring crystals. This is very unlike the case in bulk systems where even a single nucleation event can trigger a huge change as it can propagate to great lengths. Subsequent interfacial forces associated between the parent and the product phases in the bulk crystal can generate more defects and as a result form new nucleation sites which start to propagate as well, eventually leading to an avalanche of nucleation and growth. However, since nanocrystals do not have a well-defined or rather strained structure at the surface, the surface can provide potential nucleation sites which then change the dynamics of the nucleation and growth event entirely, as one could have potentially 30-40 % of the atomic sites acting as defect sites. While studying

the changes in phase transitions with size is of fundamental interest, it also provides a device engineer an opportunity to obtain materials with tunable properties. If a certain material shows significant deviation in its phase behavior with size, it allows us to alter the phase diagrams of these at will and extend the versatility of existing material systems.

8.2 BACKGROUND

Before delving deeply into phase transitions in nanocrystalline systems, we need to first distinguish between two terms - *phase transformation* and *phase transition* - that are often used interchangeably. In this study, when we refer to *phase transition,* we are restricting ourselves to transitions between two phases which do not involve any compositional changes *i.e.* the parent phase and the product phase have identical chemical compositions. The phase transition only involves a structural transition. In general, any other phenomena that involve a compositional change would be included under *phase transformations*.[9] A word of caution though needs to be exercised when one refers to identical chemical composition. Instances such as transformation of oxygen to ozone and isomeric transitions should not be considered phase transitions because ozone and oxygen, and isomers, are each two different individual components. In this sense, the definition of *phase transition* shall be further restricted to a transformation that only involve phases of a single component with different crystal structures.

As proposed by Ehrenfest,[10] phase transitions may be classified based on the differential of any thermodynamic parameter [most common of which is the Gibbs free energy function (G)] with respect to the transition parameter (which can be the pressure, temperature or composition of the system). The order of the transition is then defined by the least derivative which is non-zero at the phase transition point. In our studies, we shall be dealing with phase transitions as a function of temperature keeping pressure and compositions constant. Thus, in our case, for a n-th order transition

$$\Delta\left(\frac{\partial^n G}{\partial T^n}\right) \neq 0; \qquad \Delta\left(\frac{\partial^{n-1} G}{\partial T^{n-1}}\right) = 0 \quad at \quad T = T_c \tag{8.1}$$

where T denotes the temperature of the system, T_c the phase transition temperature

Now substituting n=1 for a first order transition and n=2 for a second order transition in equation 8.1, we obtain

$$\Delta\, G = 0; \qquad \Delta\left(\frac{\partial G}{\partial T}\right)_P = -\Delta S = \frac{\Delta H}{T_c} \quad at \quad T = T_c \tag{8.2}$$

$$\Delta\left(\frac{\partial G}{\partial T}\right)_P = -\Delta S = \frac{\Delta H}{T_c} = 0; \quad \Delta\left(\frac{\partial^2 G}{\partial T^2}\right)_P = \frac{1}{T_c}\Delta\left(\frac{\partial H}{\partial T}\right)_P = \Delta\frac{C_P}{T_c} \neq 0 \quad at \quad T = T_c \tag{8.3}$$

Here, for first and second order transitions respectively, S denotes the entropy, H the enthalpy and C_p the specific heat of the system at constant pressure, P.

Thus, *first-order transitions* are accompanied by a discrete change in entropy, enthalpy and specific volume of the material. Typically but not exclusively, all first-order transitions are discrete events involving nucleation and growth. The change in enthalpy leads to the generation of a latent heat during the transition process. In contrast, *second-order transitions* do not involve any latent heat of transition. While it is common to classify transitions as first- or second-order, in reality it is difficult to pinpoint whether a transition occurs as either of these two types. Going strictly by definition, first-order transitions should undergo sharply at *Tc* and the high- and low-temperature phases of the material should not coexist at any other temperatures other than *Tc*. However, in reality it is known that in a finite temperature interval near the transition temperature for most transitions classified as first-order transitions, both the low- and the high-temperature phases do coexist.

In contrast to the thermodynamic mode of classification introduced by Ehrenfest, Burger proposed another way of classifying these transitions based on the structural mechanism as *diffusional* or *displacive* transitions.[11] In various nomenclatures,

diffusional transitions are analogous to "*reconstructive*" or "*nucleation and growth*" transitions while *displacive* transitions can be related to "*martensitic*" or "*cooperative*" transitions. The nomenclature of "*nucleation and growth*" is very confusing as both displacive and diffusional transitions occur via the nucleation and growth mechanism. In a displacive transition, a homogeneous lattice deformation takes place with an ordered relative displacement of lattice planes and atoms, such that there always exists a correspondence between the parent crystallographic structure and the product structure. Thus, transitions that involve a small deformation in lattice parameters between the two phases generally follow the displacive mechanism. In contrast, as the name suggests, diffusional transitions involve diffusive events where atoms can move around from the parent to the product lattice sites at random. The process involves breaking of bonds between neighboring atoms in the parent structure and reconstruction of the structure to grow the product structure. In general, no correspondence exists between the parent and product lattice structures in these transitions and more often than not, these are accompanied with huge changes in lattice parameters. However, in real world systems, this strict distinction between different modes of transitions disappears. There exist transitions which can be classified under either class and hence these are referred to as "hybrid" transitions.[11]

8.3 PHASE TRANSITIONS IN SILVER SELENIDE NANOCRYSTALS

Silver selenide (Ag_2Se) exhibits a reversible first-order reversible phase transition from a low-temperature orthorhombic phase (α-Ag_2Se) to a high-temperature cubic phase (β-Ag_2Se) at 135 °C. While β-Ag_2Se is a superionic conductor that is used as an additive in highly conductive composite glasses for sensors, displays, and photo-chargeable secondary batteries, and has potential as a solid electrolyte, α-Ag_2Se is widely used as a thermoelectric material, and as a photosensitizer in photographic films and thermochromic materials.[2] From a fundamental standpoint as well as from an application point of view, it becomes extremely interesting to observe how the existence of both these phases is affected by varying the crystal size. Many groups have probed the size

dependence in solid-solid phase transitions, focusing mostly on pressure-induced ones.[12-15] However, these transitions occur typically in the giga-pascal range which makes them highly unlikely to be incorporated in most practical applications. In contrast, only a few reports have studied the size dependence of temperature-induced phase transitions.[16] One reason for this limited study could be due to the lack of reliable synthetic techniques to obtain fairly monodisperse crystals of small size, sintering of small crystals and/or sublimation on heating. In this regard, Ag_2Se presents itself as an attractive proposition to study these temperature-induced transitions. Firstly, we have developed robust synthetic methods to synthesize fairly monodisperse Ag_2Se nanocrystals within a size range of 3-10 nm.[2,3] Secondly, bulk Ag_2Se undergoes a phase-transition at a relatively low temperature of 135 °C which is lower than the sintering temperature (typically ~ 200-250 °C) for the Ag_2Se nanocrystals. Indeed, whether the phase transition temperature goes up or down with reducing size remains to be seen. However, the Ag_2Se system provides us with a fairly large window (-268 °C to 200 °C) to study the effect of size in temperature-induced phase transitions.

Prior to investigating the effect of temperature on the phase transition in our Ag_2Se nanocrystals, it is important to note that they do not exist in the stable orthorhombic phase observed in bulk but in a metastable tetragonal phase,[2,3] which is not unusual. Solid-solid phase transformations can be drastically affected by crystallite size as is evidenced by widespread experimental observations of metastable structures existing at room temperature and pressures for nanostructured materials over the last three decades.[12-14,17-44] In Chapters 6 and 7, we observe the same with our Ag_2Se nanocrystals wherein these exist in a tetragonal phase as against the bulk low temperature stable orthorhombic phase.[2,3] For the sizes studied in the range from nearly 3-10 nm, we found all our nanocrystal samples to exist in the tetragonal phase. This implies, however, that there ought to exist a certain upper bound on the size below which Ag_2Se crystallites favor the tetragonal phase as compared to the bulk orthorhombic phase. In order to investigate this phase-transition size, we prepare samples with increasing size and probe their structure using X-ray diffraction. As mentioned in Chapter 6, using colloidal syntheses, we were unable to grow nanocrystals stable in solution with sizes greater than

10 nm. To overcome this limitation, firstly we deposit our largest sized nanocrystals as a thin film on a substrate and replace the long chain surfactants capping these nanocrystals with shorter ones, and secondly we sinter these films at relatively mild temperatures to promote sintering and hence obtain controlled crystallite growth on the substrate. Replacing the bulky capping ligands with short-chain ligands is essential because this allows us to perform the sintering at very slow rates at modest temperatures of around 60 °C as against nearly 250 °C wherein the sintering takes place at an uncontrolled rate. For the ligand exchange, we follow a protocol described in Chapter 4 for CdSe nanocrystal films[1,45] and replace the long ligands with hydroxyl ligands (see Section 8.4.7 for details). We then proceed to sinter these exchanged films at ~ 60 °C for varying periods to obtain different crystallite sizes. The x-ray diffraction data for one of these sintered films with an average crystallite size of roughly 28 nm (as calculated by the Scherrer broadening of the peak width) is shown in Figure 8.1.

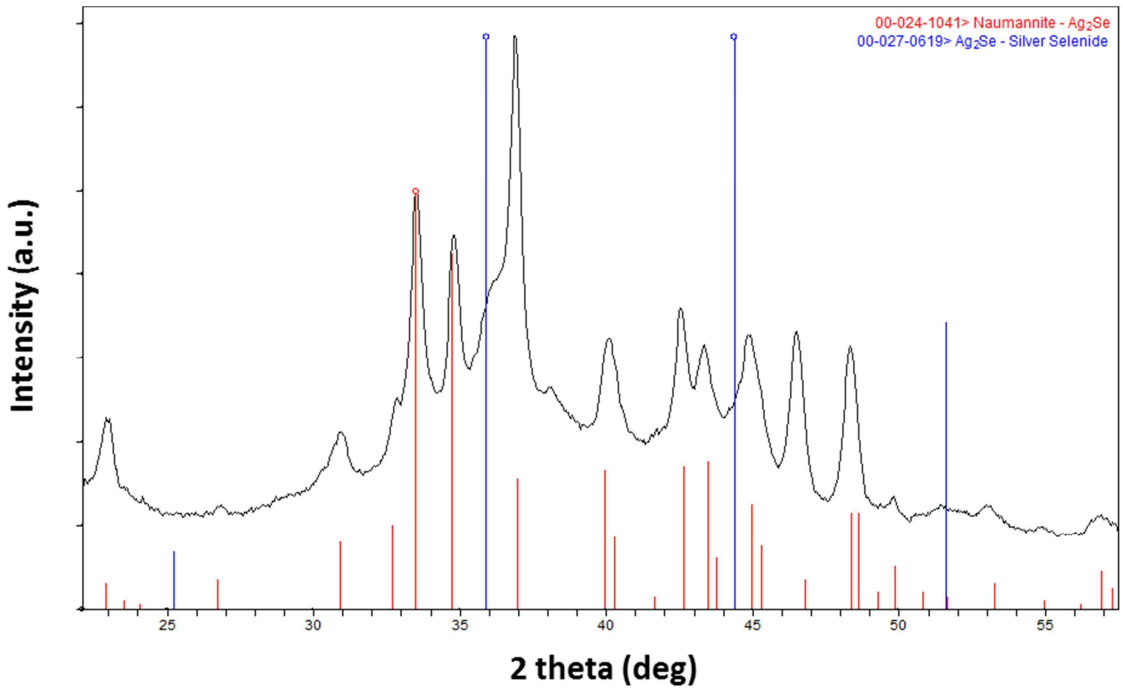

Figure 8.1: X-ray diffraction data of a Ag_2Se nanocrystal sintered film with ~ 28-nm average crystallite size.

One can clearly observe peaks that match the orthorhombic phase of Ag_2Se while there also exist peaks that remain from the tetragonal phase. The red peaks correspond to

the low-temperature orthorhombic phase (naumannite) and the blue peaks to that of the high-temperature cubic phase that exists in bulk. A word of caution that needs to be exercised in these data is that as against to calculating crystal sizes from X-ray diffraction data from a fairly monodisperse sample of nanocrsytals deposited on a substrate, the sizes calculated here are from a sintered polycrystalline sample wherein there is no control over grain size across the entire film. Since one obtains just an average crystallite size, there might be regions where one has crystallites either solely in the tetragonal phase or in the orthorhombic phase. However, since we have no other technique to grow controlled grains of the same size at our disposal, we continue our analyses with this approach.

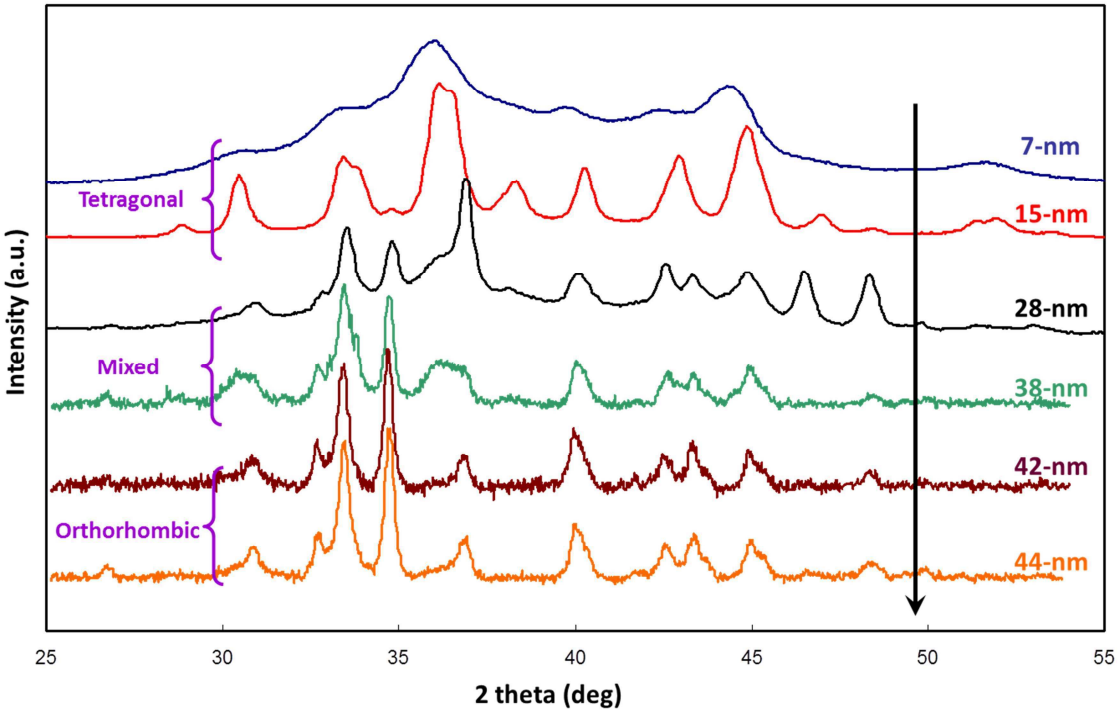

Figure 8.2: X-ray diffraction data showing the transition from the metastable tetragonal phase to the stable orthorhombic phase with increasing grain size in Ag_2Se crystals.

Figure 8.2 depicts the X-ray diffraction data obtained from a set of sintered samples with increasing sintering times (and hence larger crystallite sizes) and compares it with the X-ray diffractogram of an unsintered 7-nm nanocrystal film. We observe that crystallites roughly greater than 38-nm in size show no signs of the tetragonal phase and almost exist entirely in the orthorhombic phase which leads us to believe a size

corresponding to ~ 40-nm marks an upper boundary for the tetragonal phase to exist in Ag_2Se crystallites. We have good reason to be confident about this result since Ag_2Se nanowires with diameters below 40-nm do exist in the tetragonal phase while those greater than 40-nm in diameter exist in the orthorhombic phase.[46] To the best of our knowledge, this is the first report which tracks a systematic change from a metastable phase to a stable phase in nanocrystalline systems at ambient conditions simply as a function of their crystallite size.

Having mapped out the first section of our phase diagram for Ag_2Se as a function of size at room temperature and pressure, we now proceed to examine the effect of temperature on the Ag_2Se nanocrystals. As against bulk Ag_2Se, where the phase transition occurs from the orthorhombic phase to cubic phase at 135 °C, instead we are probing the transition from the tetragonal phase to the cubic phase as a function of temperature. Since, in either case, the transition should involve a change in crystal structure, we use *in-situ* X-ray diffraction (XRD) with heating as a tool to track the changes in the structure as a function of temperature. Also, since in bulk, the transition to the high-temperature phase is known to be of first order, it should be accompanied by a discrete change in the enthalpy, specific heat, entropy and specific volume as discussed in Section 8.2. Thus, we also employ differential scanning calorimetry (DSC), which tracks the enthalpy and specific heat, as an alternative tool to track the phase transition in conjunction with XRD.

Figure 8.3 shows XRD data portraying the phase change from the tetragonal phase to cubic phase for ~6-nm Ag_2Se nanocrystals. The phase change takes place around 100 °C and the nanocrystals transform completely to the cubic phase as observed in bulk. The red sticks in the figure show the expected positions of the peaks from the cubic phase [Joint Committee on Powder Diffraction Standards (JCPDS) # 00-027-0619]. Whether the depressed phase transition temperature from 135 °C to 100 °C is due to the reduced size of the crystals or due to a transition from the tetragonal to the cubic phase instead of a transition from the orthorhombic to the cubic phase needs to be investigated further.

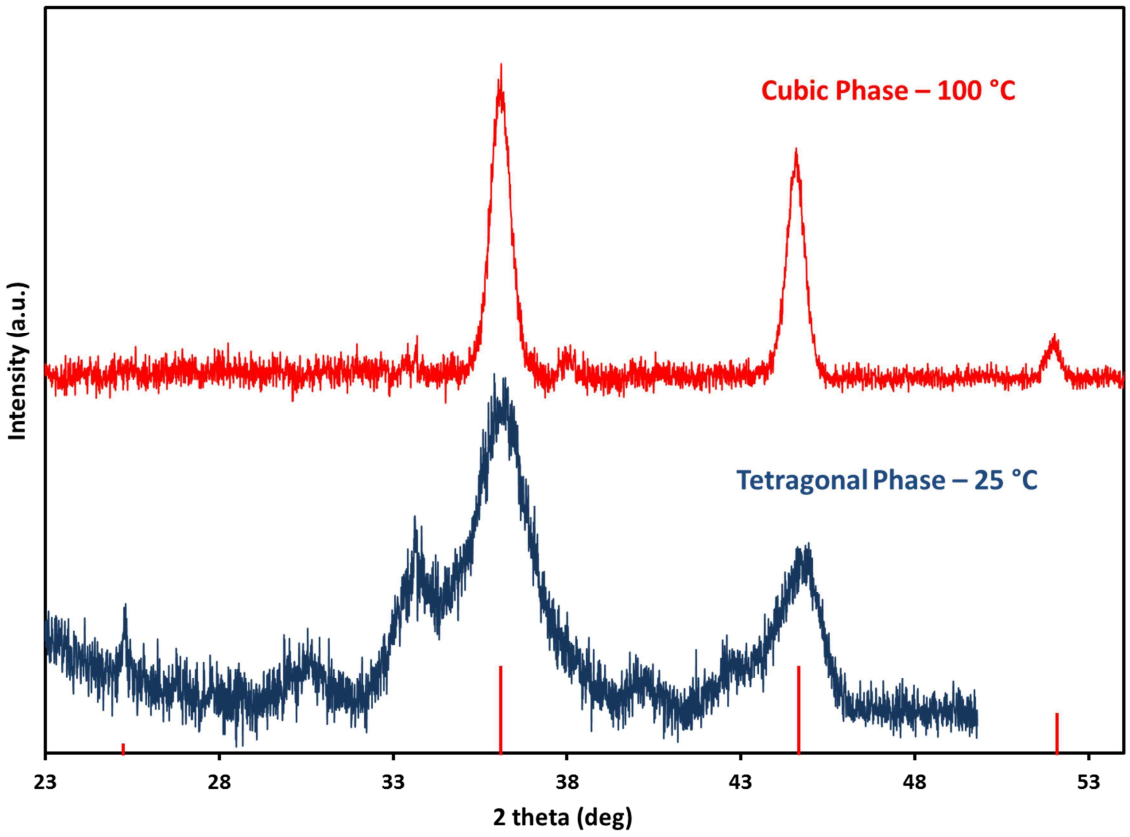

Figure 8.3: Changes in X-ray diffraction patterns with increased temperature showing the transition from the low-temperature tetragonal phase to the high-temperature cubic phase for ~6-nm Ag_2Se nanocrystals.

Figure 8.4 shows the DSC plot for one thermal cycle (heating followed by cooling) for a sample of ~8.6-nm Ag_2Se nanocrystals. For comparison, we also performed a DSC analysis on bulk Ag_2Se purchased from Sigma Aldrich (Figure 8.4). The vertical axis shows the amount of heat flow into the sample during heating. Thus it is an endothermic heat flow – a positive peak implies that the sample takes up heat and a negative peak implies the sample releases heat. The sharp peak in the DSC plot at around 100 °C for the nanocrystals and around 136 °C for the bulk samples (fairly close to the bulk expected value of 135 °C from literature) shows that both the nanocrystals as well as the bulk crystals absorb heat to undergo the phase transition which can be attributed to the latent heat involved during the transition. This proves that the transition is of first order. It is evident that the nanocrystals have a lower phase transition temperature than the bulk crystals.

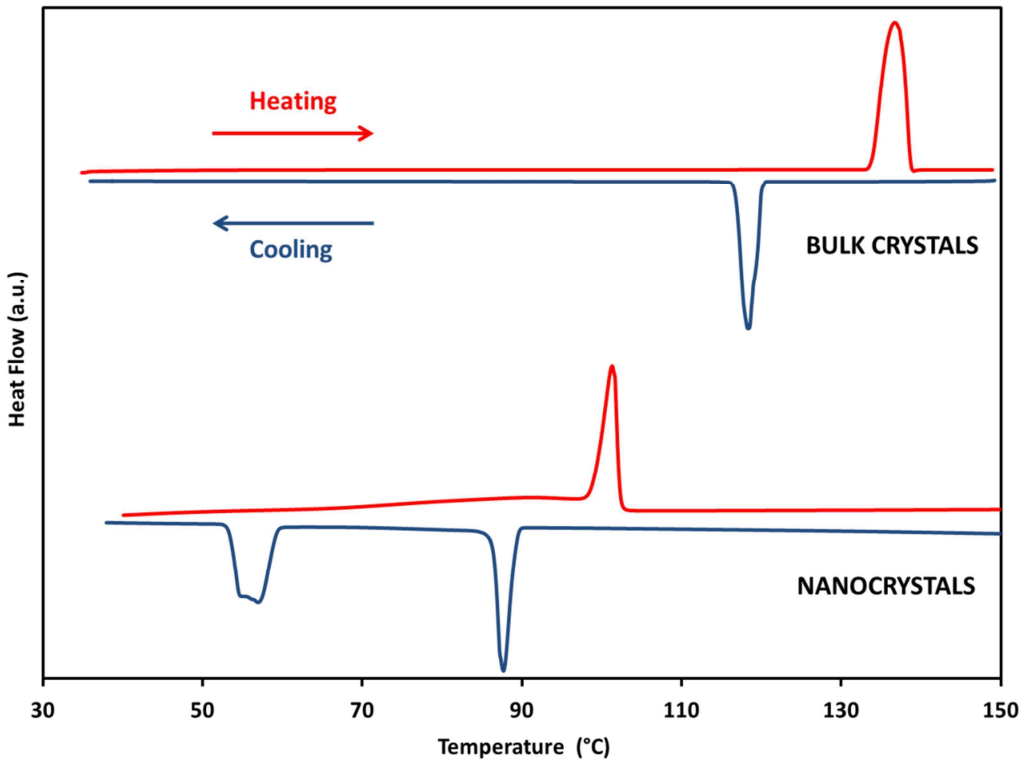

Figure 8.4: DSC thermogram of ~8.6-nm Ag_2Se nanocrystals for one thermal (heating/cooling) cycle. The data for Ag_2Se bulk crystals are also included for comparison.

Furthermore, to verify whether the phase transition was reversible or not, we performed a cooling cycle to observe if the crystals reverted back to their original phase. As expected from the bulk sample, we did observe a peak on the cooling cycle close to 120 °C. Hysteresis is a common phenomenon in reversible cycles and its origins are related to the fact that we have different phases nucleating and growing during the heating and the cooling cycle. On one hand during the heating cycle, we nucleate a cubic phase inside the tetragonal phase which then grows. The activation barrier for these nuclei to nucleate and grow will be different from what one would expect for the nuclei during the cooling cycle wherein the tetragonal phase tries to grow in the cubic phase. Interestingly enough, for the nanocrystal sample, we observe two peaks in the cooling cycle – one centered around 85 °C and the other around 57 °C. These two peaks were observed in all our Ag_2Se samples. From the DSC thermogram, one can not determine the origin of these two peaks. Hence, we perform a thermal cycle with *in-situ* XRD analyses to probe this further. Figure 8.5 shows the heating cycle while Figure 8.6 shows the cooling cycle.

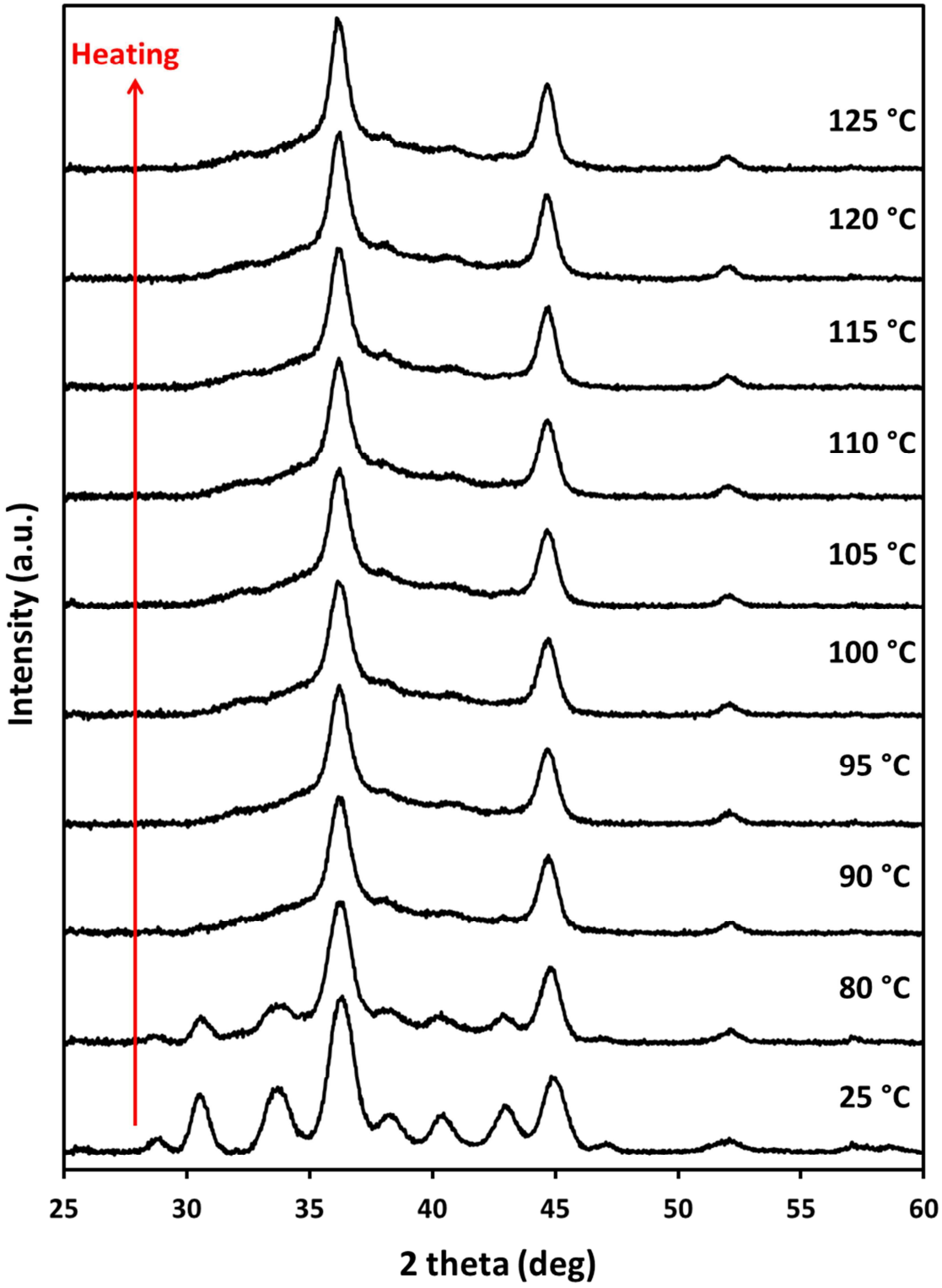

Figure 8.5: Changes in X-ray diffraction patterns with increasing temperature showing the transition from the low-temperature tetragonal phase to the high-temperature cubic phase for ~8.6-nm Ag_2Se nanocrystals.

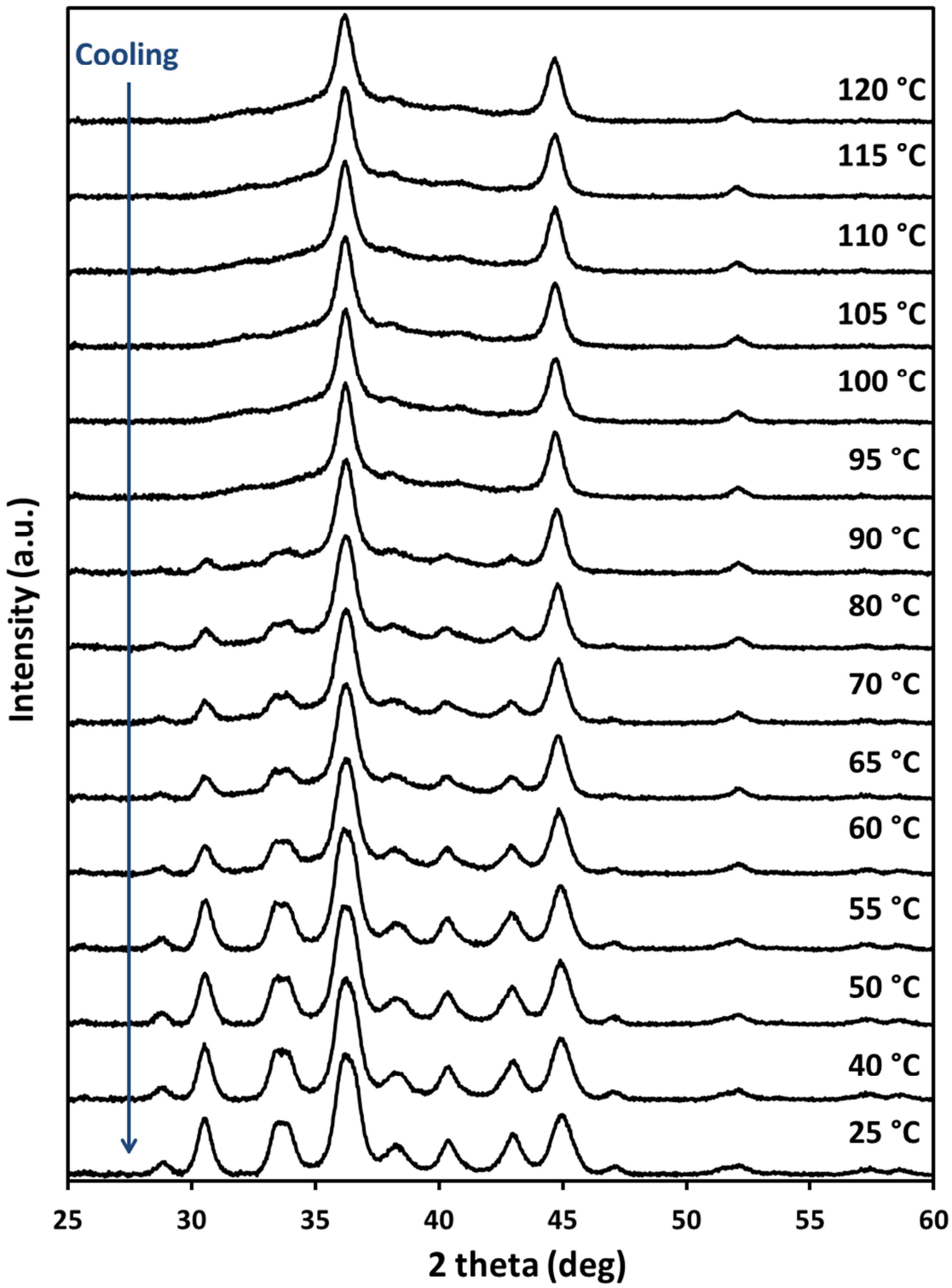

Figure 8.6: Changes in X-ray diffraction patterns with decreasing temperature showing the transition from the high-temperature cubic phase to the low-temperature tetragonal phase for ~8.6-nm Ag_2Se nanocrystals.

As is evident from Figure 8.5, the transition from the low-temperature tetragonal phase to the high-temperature cubic phase starts somewhere around 80 °C and is complete by 90 °C. The difference between the DSC data and the XRD data might be due to the fact that the samples for XRD are cast as a thin film on a substrate which might have some influence on the phase transition. Moreover, the temperature read from the XRD data is the set-point temperature and not the actual sample temperature. In spite of the inconsistency between the two sets of data, they more or less agree with each other within a temperature range of ~ 10 °C. Figure 8.6 plots the cooling cycle for the same nanocrystal sample used for Figure 8.5. We observe that the onset of the reverse transition does indeed take place somewhere between 95 °C - 90 °C with signs of the tetragonal phase creeping in. However, the sample does not revert back to the original structure until the temperature reaches about 60 °C - 55 °C. This proves that there are two different regimes in the phase transition to the original tetragonal phase while cooling down the sample. Since the tetragonal phase is not observed in bulk, we could not find any reports on this phenomenon.

One assumption is that the transition might not directly occur from the cubic to the tetragonal phase but might progress through some other metastable phase which exists roughly between 80 °C- 60 °C. However, in that temperature range we observe that the XRD pattern more or less matches the tetragonal phase observed at room temperature even though the intensities are somewhat different. This leads us to believe that there might be some subtle differences in the crystal structure and/or the atomic positions of the silver and the selenium atoms between the intermediate phase and the tetragonal phase. With no knowledge of the atomic locations in the tetragonal phase observed by us at room temperature, we cannot claim if there would be any differences in those locations in the intermediate phase. However, we found one single report by Okabe *et al.* where they observe the existence of another metastable tetragonal phase for grain sizes of Ag_2Se less than 50-nm with lattice parameters a=b=0.698 nm, and c=0.496 nm using high resolution transmission electron microscopy.[47] These values of lattice constants are only marginally different from what we observe (a=b=0.706 nm, and c=0.498 nm).

Using their lattice constants, we would get peaks very close to where we observe (within 0.5 degrees of each other). However, a peak fitting using their lattice constants do not match the experimental data at room temperature from the nanocrystals as well as the constants used by us. Hence, most likely, we observe the tetragonal phase proposed by us at room temperature while there exists a distinct possibility that we might be observing this metastable tetragonal phase (with lattice constants proposed by Okabe *et al.*) as the intermediate phase which exists between 80 °C-60 °C during the cooling cycle. Since all the peaks are not fully developed in this temperature regime and additionally with the huge Scherrer broadening due to the small crystallite sizes, it is hard to locate the peak positions and do any rigorous curve fitting.

Another fact that might lend credence to our postulate is that this phase can be observed using high-resolution transmission electron microscopy wherein localized heating would most certainly take place. In fact, recently, a phase transition was observed in copper sulfide nanorods with unintentional heating under the electron beam.[48] A similar effect might have been observed by Okabe *et al.* where they observed their metastable tetragonal phase due to mild heating of the sample. It is not unreasonable for the local sample temperature to rise to about 70-80 °C under high intensity electron beams. A recent report by Yin *et al.* discusses the phase transition of Ag_2Se thin films under the electron beam.[49] One way to discern what is going on would be to study the local structure of the atoms using techniques such as Extended X-Ray Absorption Fine Structure (EXAFS) spectroscopy. Even though it is extremely challenging to analyze systems which go through such a disordered-ordered phase transition and draw reliable conclusions, EXAFS may be able to figure out the nature of this intermediate phase.

The ratio of the two DSC peaks in the cooling cycle – one around 85 °C and the other around 57 °C – varies from sample to sample. In samples where the 85 °C is small compared to the peak at 57 °C, the XRD data shows that there is no noticeable change in the crystal structure in between 85 °C – 60 °C, and the sample changes phase directly from the cubic to the tetragonal phase without passing through the metastable intermediate phase. Again, this hints at the peak at 85 °C corresponding to a

transformation from the cubic to the metastable intermediate phase and the peak around 57 °C to the tetragonal phase. Figure 8.7 shows the DSC thermogram of one such sample and Figures 8.8 and 8.9 show the corresponding X-ray heating and cooling cycle diffractograms of the sample. One can observe from the cooling cycle that there is no hint of phase transition until 65 °C and then between 65 °C to 50 °C, the sample switches back to the original tetragonal phase.

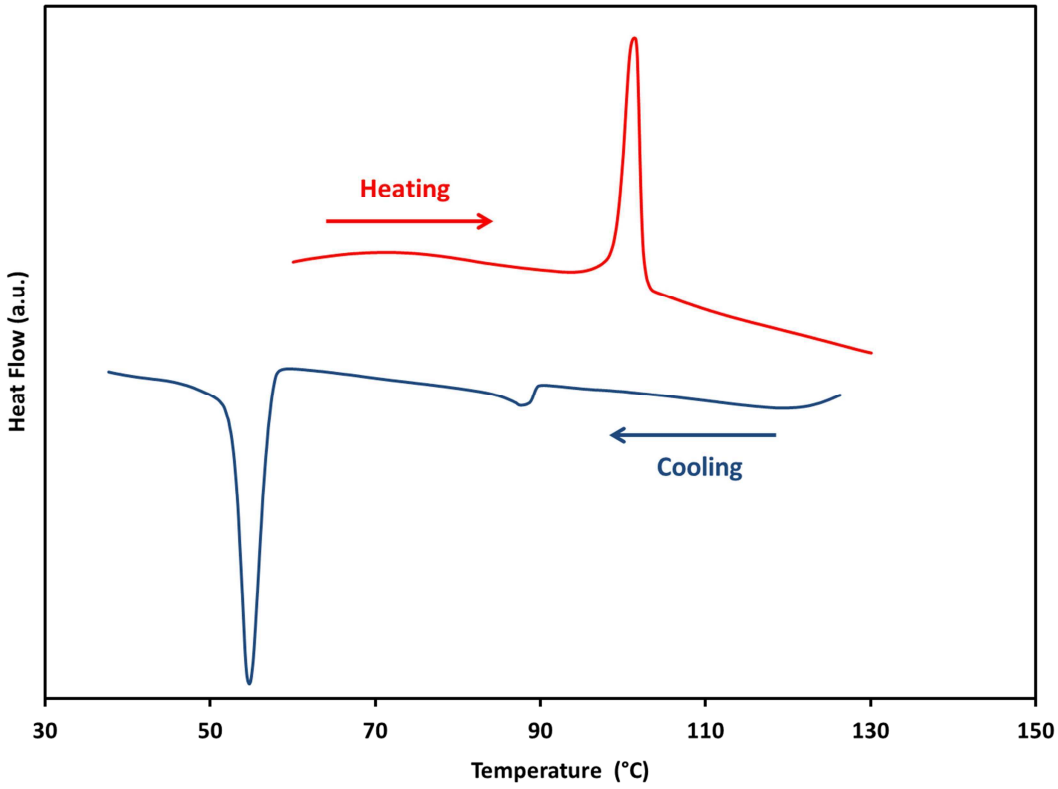

Figure 8.7: DSC thermogram of ~8-nm Ag_2Se nanocrystals for one thermal (heating/cooling) cycle.

The samples were made to go through multiple thermal cycles of heating and cooling to check if the phase transition and its reversibility were consistent over numerous cycles. Figure 8.10 shows the XRD data obtained from a sample of ~8-nm Ag_2Se nanocrystals in the second thermal cycle. Note that this was the same sample used for Figures 8.8 and 8.9 (first thermal cycle). The sample retained its properties on the second cycle, going from the low-temperature tetragonal phase to the high-temperature cubic phase somewhere between 80 °C and 100 °C and changing back to the original tetragonal phase somewhere around 60 °C, which is as observed from the DSC data in Figure 8.7 and the X-ray diffractograms in Figures 8.8 and 8.9.

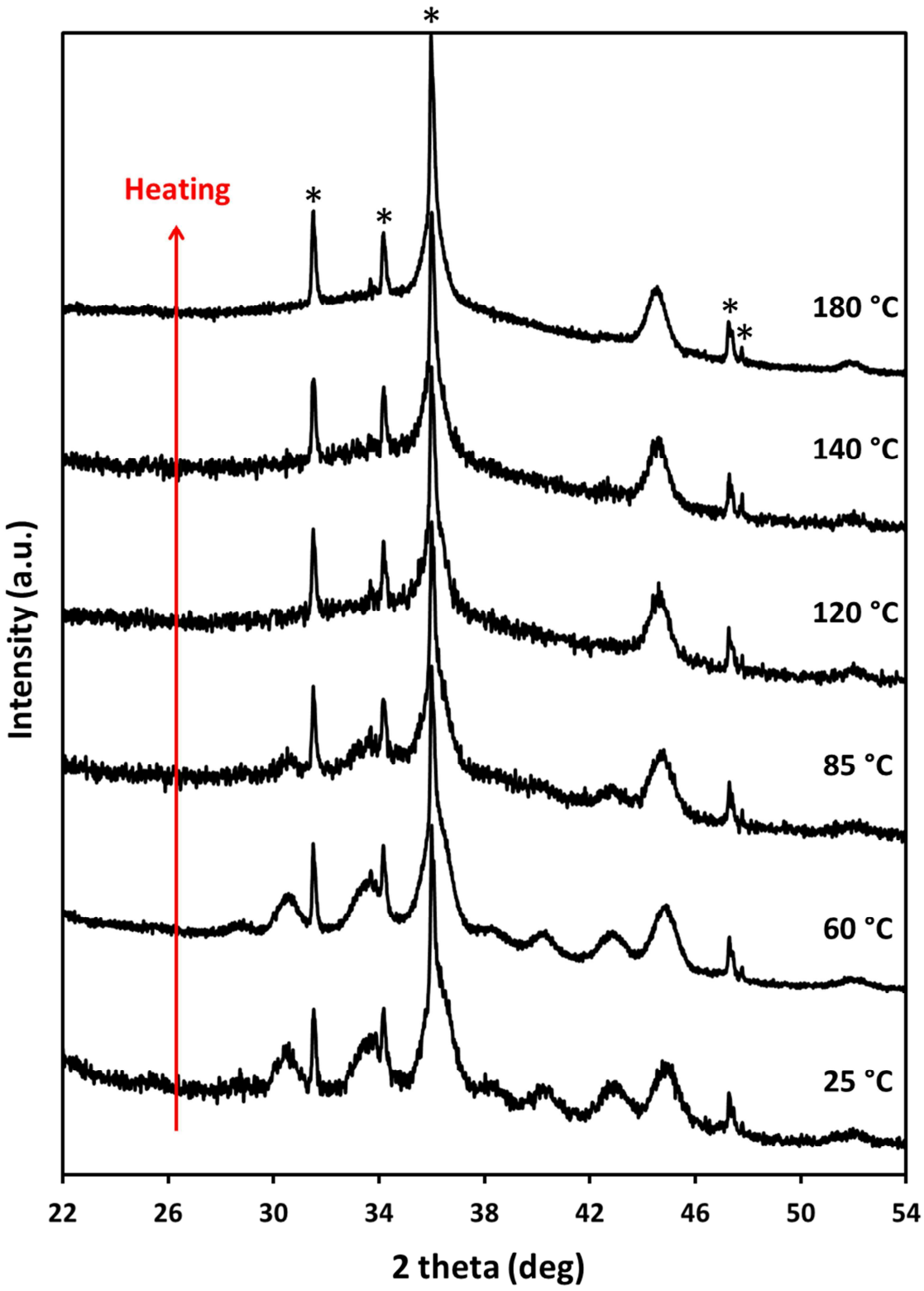

Figure 8.8: Changes in X-ray diffraction patterns with increasing temperature showing the transition from the low-temperature tetragonal phase to the high-temperature cubic phase for ~8-nm Ag_2Se nanocrystals. The sharp peaks marked by asterisks are zincite peaks from the conductive grease on the substrate holder.

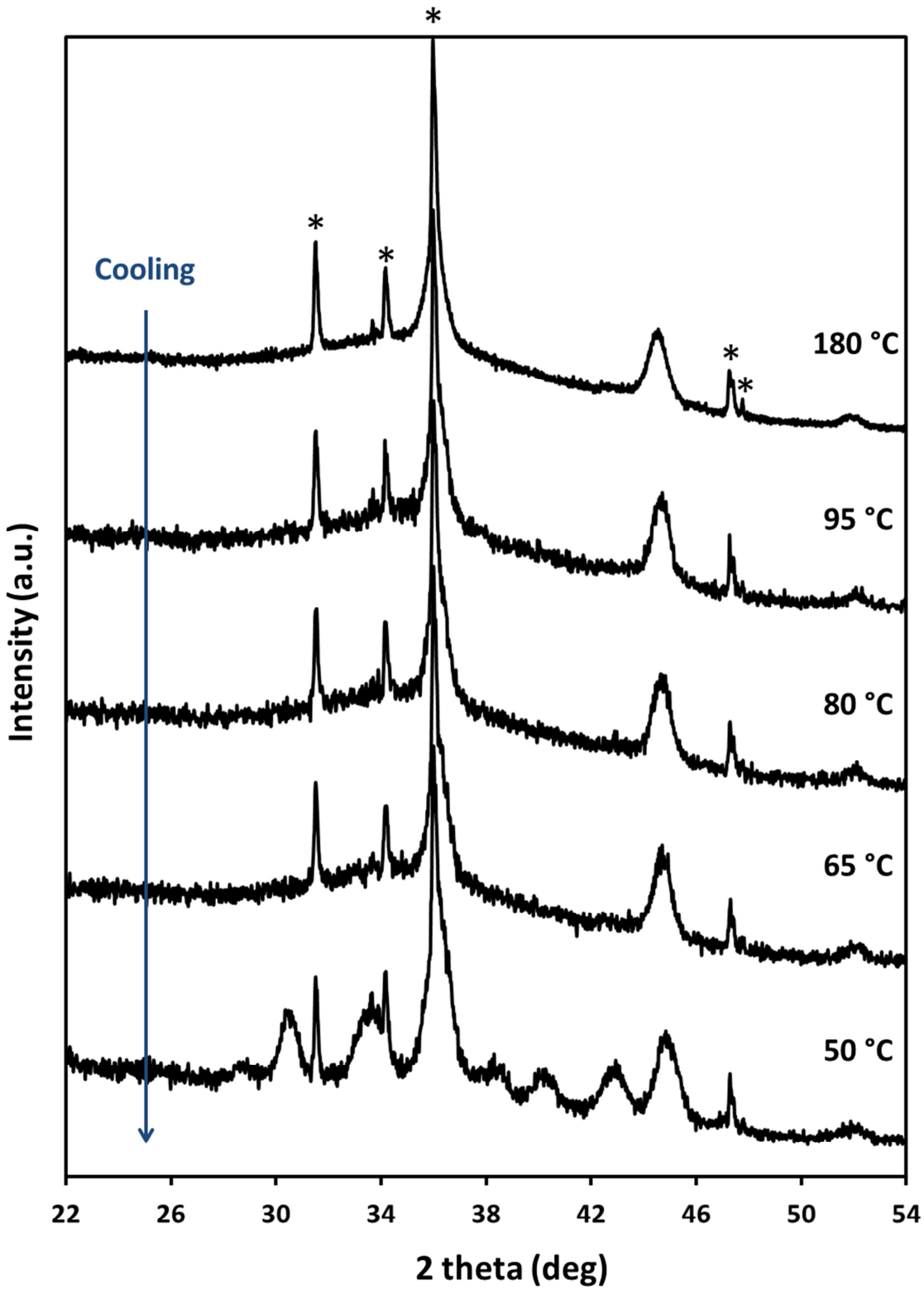

Figure 8.9: Changes in X-ray diffraction patterns with decreasing temperature showing the transition from the high-temperature cubic phase to the low-temperature tetragonal phase for ~8-nm Ag_2Se nanocrystals. The sharp peaks marked by asterisks are zincite peaks from the conductive grease on the substrate holder.

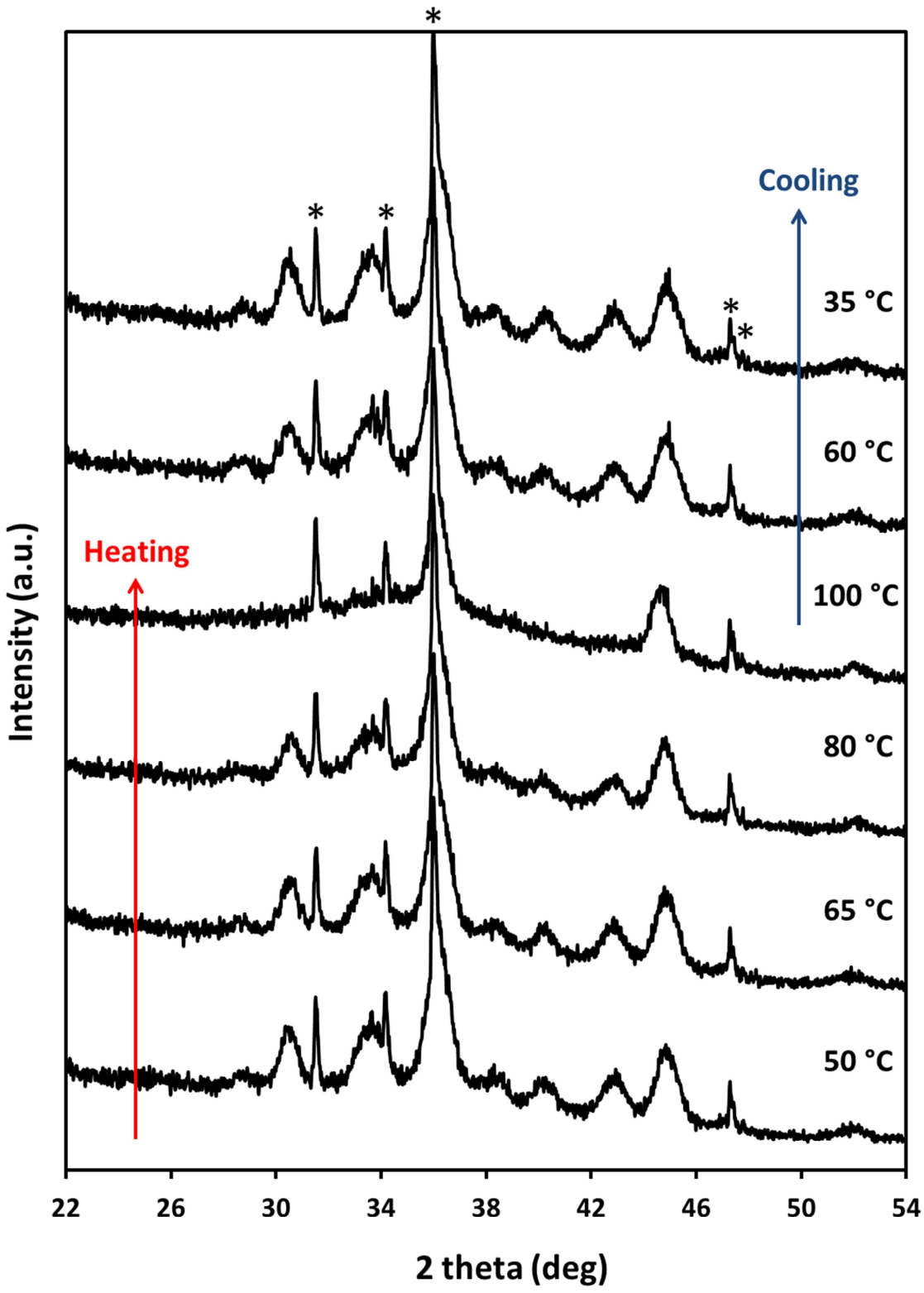

Figure 8.10: Changes in X-ray diffraction patterns with temperature showing the transition from the low-temperature tetragonal phase to the high-temperature cubic phase and back to the original phase for ~8-nm Ag_2Se nanocrystals in the second thermal cycle of heating and cooling. The sharp peaks marked by asterisks are zincite peaks from the conductive grease on the substrate holder.

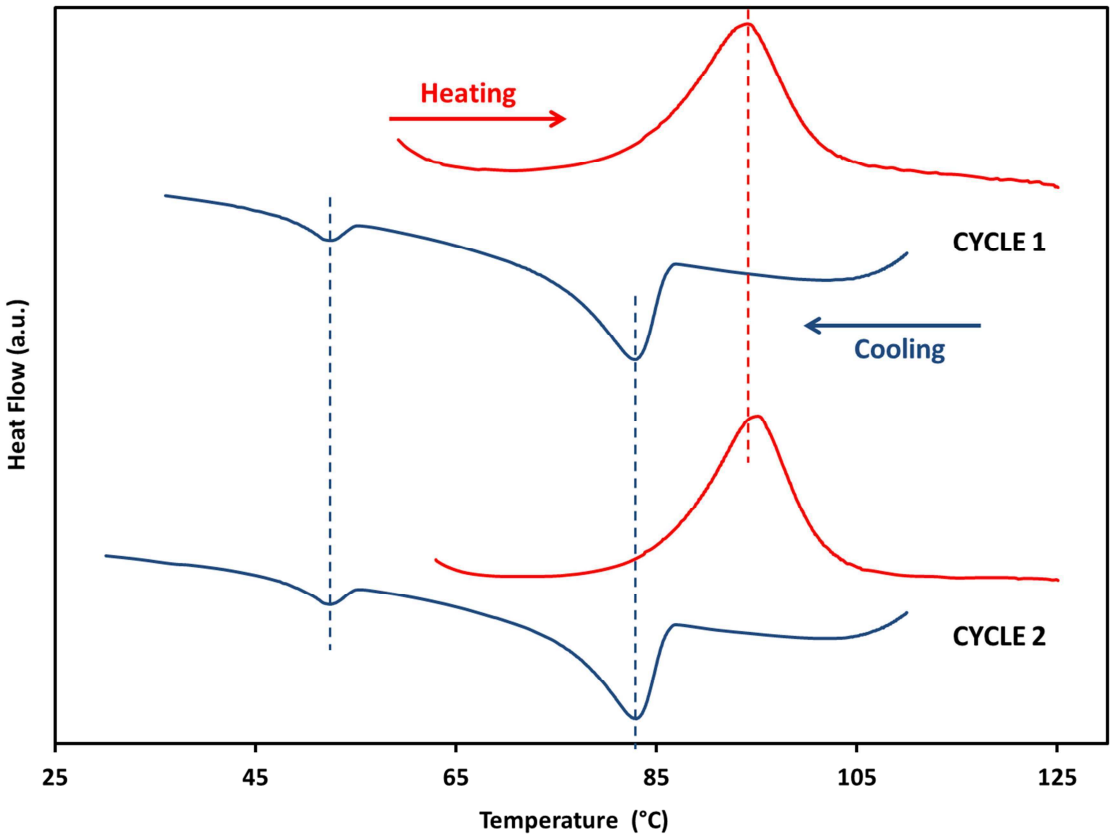

Figure 8.11: DSC thermograms of ~6.5-nm Ag_2Se nanocrystals for two thermal (heating/cooling) cycles. The dotted red and blue lines are meant to serve as guide lines to locate the shift in relative peak positions between the two cycles for the heating and cooling cycles, respectively.

Figure 8.11 shows the DSC thermograms of a sample of 6.5-nm Ag_2Se nanocrystals for two consecutive thermal cycles. Two interesting observations from the figure are that firstly, the phase transition temperatures during heating in both cycles are within 1.5 °C of each other while those during cooling are within 0.5 °C of each other implying sample stability over multiple thermal cycles. Secondly, the phase transition temperatures during heating are suppressed by almost 6-7 °C compared to the previous samples which were ~8-nm to 8.6-nm in size and by nearly 3 °C (for the peak around 85 °C) and 5 °C (for the peak around 57 °C) in the corresponding cooling cycles which implies that the phase transition depends on the size of the crystals. However, while the smaller nanocrystals (~6.5-nm) are stabilized by oleic acid, octadecylamine and tri-octylphosphine, the bigger ones used in the previous figures possess a different set of capping ligands (oleyl amine, tri-octylphosphine and tri-octylphosphine oxide). Hence, before attributing this reduction in phase-transition temperature to a reduction in size of

the crystals, first and foremost, we need to confirm whether the observation is simply an effect of different surfactants capping the nanocrystals. For PVP-capped AgI nanocrystals, Makiura *et al.* observe a huge change in the phase-transition temperature during cooling, which they correlate to a mixture of the size effect, presence of defects and a charge balance induced by PVP, the surfactant.[50] Thus, we proceed to synthesize Ag_2Se nanocrystals of approximately the same size with various different ligands and check the phase transition temperatures. Details of the synthesis methods employed for each type of surfactant can be found in the experimental section at the end of the Chapter (Sections 8.4.3-8.4.6). The results are summarized in Figure 8.12 with DSC thermograms for each type of ligand combination.

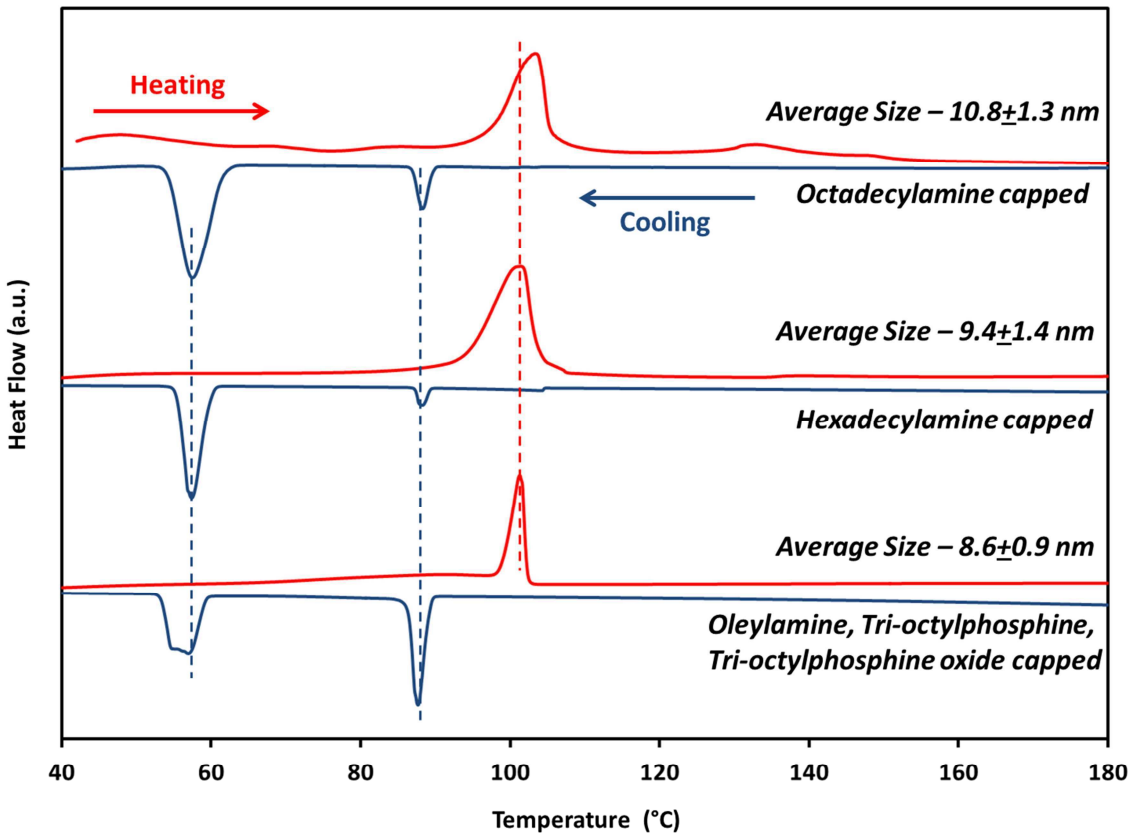

Figure 8.12: DSC thermograms of 8.6-nm oleylamine-, tri-octylphosphine-, tri-octylphosphine oxide-capped, 9.4-nm hexadecylamine-capped and 10.8-nm octadecylamine-capped Ag_2Se nanocrystals. The dotted red and blue lines are meant to serve as guide lines to locate the shift in relative peak positions between the three samples for the heating and cooling cycles, respectively.

The phase-transition temperatures during the heating cycle were within 2 °C of each other for the three nanocrystal samples capped with different ligands. Notably, the

nanocrystals capped with octadecylamine (ODA) with an average size 10.8-nm underwent the transition at 103.3 °C while those capped with hexadecylamine (HDA) having an average size of 9.4-nm, and a mixture of oleylamine (OM), tri-octylphosphine (TOP) and tri-octylphosphine oxide (TOPO) having an average size of 8.6-nm, did the same at 101.5 °C and 101.3 °C respectively. During the cooling cycle, the first and second transitions took place around 88.3 °C and 57.4 °C, respectively for the ODA-capped nancrystals. For the HDA-capped ones, they took place at 88.2 °C and 57.3 °C respectively, while for the OM, TOP, TOPO-capped nanocrystals, the reverse transitions took place around 87.7 °C and 57 °C. Three noteworthy points here are that firstly, within our error, the phase transition does not seem to depend largely on the surface-capping ligands. Secondly, with increasing size, the transition temperature on the heating cycle shifts to progressively higher temperatures even though it is a very weak function of size. Finally, the HDA- and the ODA-capped nanocrystals possessing a larger size distribution (σ~15%) as compared to those capped with OM, TOP and TOPO (σ~10%), demonstrate a broader peak in the DSC thermogram during the heating cycle again implying that the transition temperature is indeed a function of the size of the nanocrystals.

Having more or less established that the shifting of the phase-transition temperature is a weak function of the size of the nanocrystal, we proceed to synthesize even smaller nanocrystals and study their phase-transition behavior (Figure 8.13). For all our samples, we observe that during the cooling cycle, the phase-transition temperatures are almost the same (88 °C and between 55-58 °C). Only for the smallest samples (~ 4.6-nm) did we observe a significant deviation in these transition temperatures (83 °C and 52.5 °C respectively). Also for the two smallest samples with average sizes roughly around 6.7-nm and 4.6-nm, the phase-transition temperatures for the heating cycle were around 95 °C and 76.5 °C respectively, while that for the 6.5-nm sample shown in Figure 8.11, it was nearly 94 °C. Hence, we can conclude that the phase-transition temperature of Ag_2Se nanocrystals shifts uniformly lower with decreasing size. The observation matches with what is generally postulated of melting of nanocrystals wherein the melting temperature at the solid-liquid phase transition also decreases with decreasing size[7] and the depression in the melting varies inversely as the crystal size.

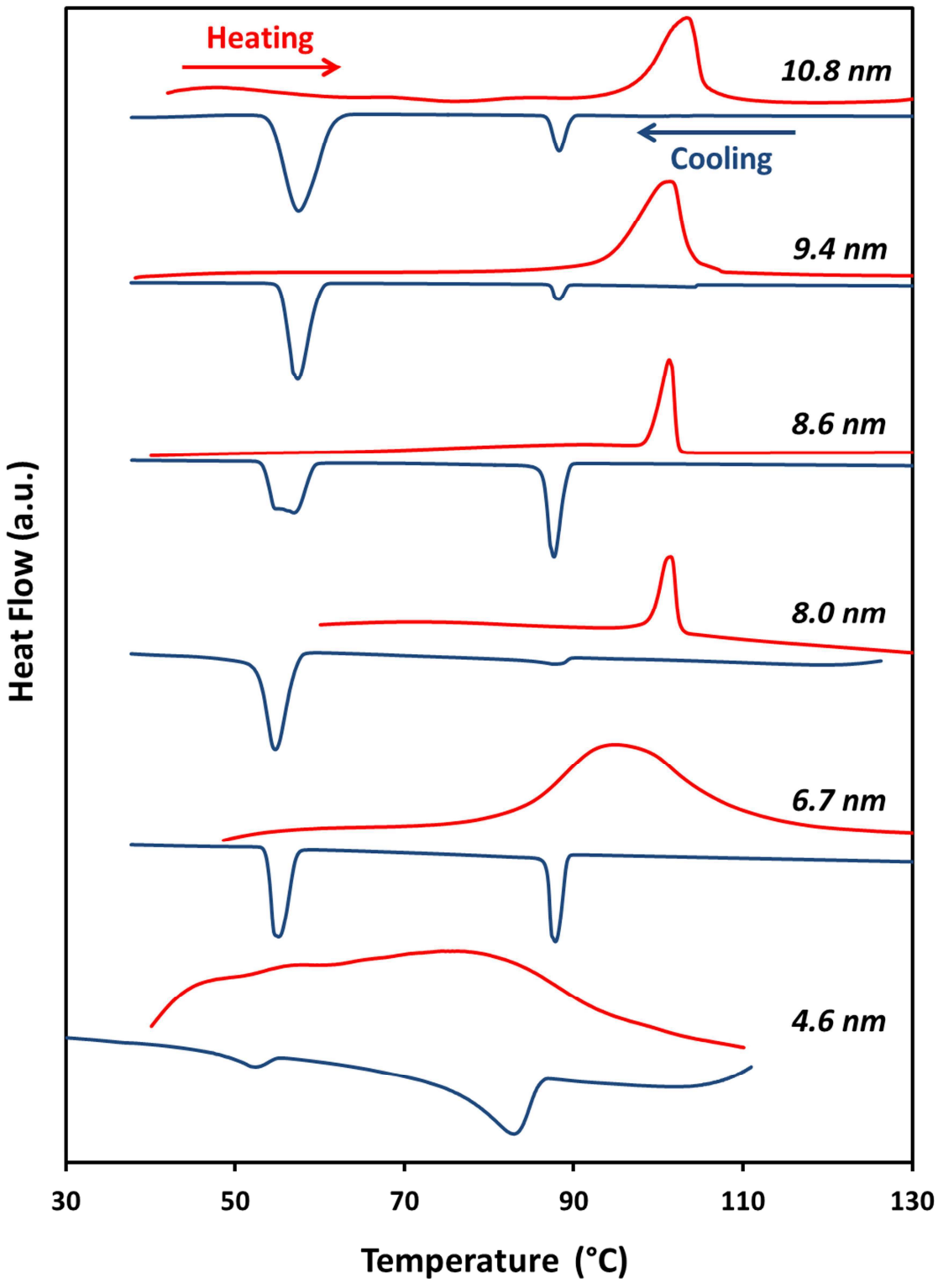

Figure 8.13: DSC thermograms of 4.6-nm, 6.7-nm, 8.0-nm, 8.6-nm, 9.4-nm and 10.8-nm Ag_2Se nanocrystals showing the size dependence of the phase-transition temperatures.

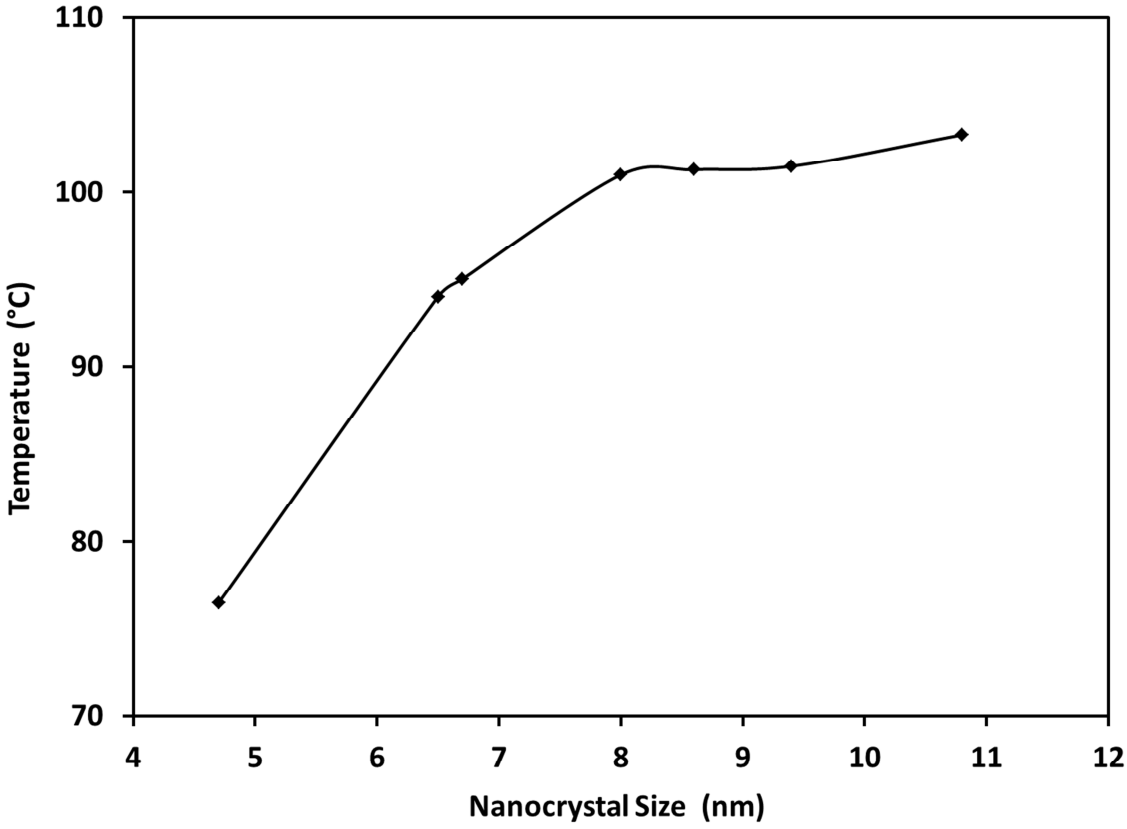

Figure 8.14: Phase-transition temperature dependence on Ag_2Se nanocrystal size as observed from experimental data.

For melting of nanocrystals, the following equation has been proposed,[7]

$$T_b - T_m = \frac{2T_m}{\Delta H^0 \rho_1 R}\left[\gamma_1 - \gamma_2\left(\frac{\rho_1}{\rho_2}\right)^{2/3}\right] \qquad (8.4)$$

where T_b and T_m are the bulk and the nanocrystal melting temperatures, respectively, ΔH^0 the latent heat of fusion, R the size of the nanocrystal, γ the surface tension and ρ the density of each phase (1-liquid and 2-solid). For a solid-solid transition case, the corresponding phases would both be solids. In our case, since the transition takes place from the tetragonal phase to the cubic phase and the tetragonal phase does not exist in bulk, we cannot estimate the bulk phase-transition temperature (T_b). We can somewhat estimate the latent heat evolved during the phase change through DSC. However, the data is very approximate as it is hard to determine the exact mass undergoing the transition.

Since the nanocrystals are capped by ligands which can contribute from nearly 20-70% of the mass of the nanocrystal depending on the size of the nanocrystal and the identity of the ligands. Moreover, the complexity is compounded by the fact that the surface of the nanocrystal may be strained or distorted (and is usually amorphous) and hence the role of the surface atoms during the transition is not known, *i.e.* if they actually contribute to the phase transition or not. Again, depending on the size of the nanocrystals, as many as 40% of the atoms of the nanocrystal can exist at the surface. Finally, since the Ag_2Se system has not been studied very extensively (especially the tetragonal and the cubic phase), we were unable to find any reliable values of the density and surface tension (surface energy) of these two phases. Nevertheless, we try to plot our data as a function of size to get a rough estimate of how the phase diagram would look like (Figure 8.14).

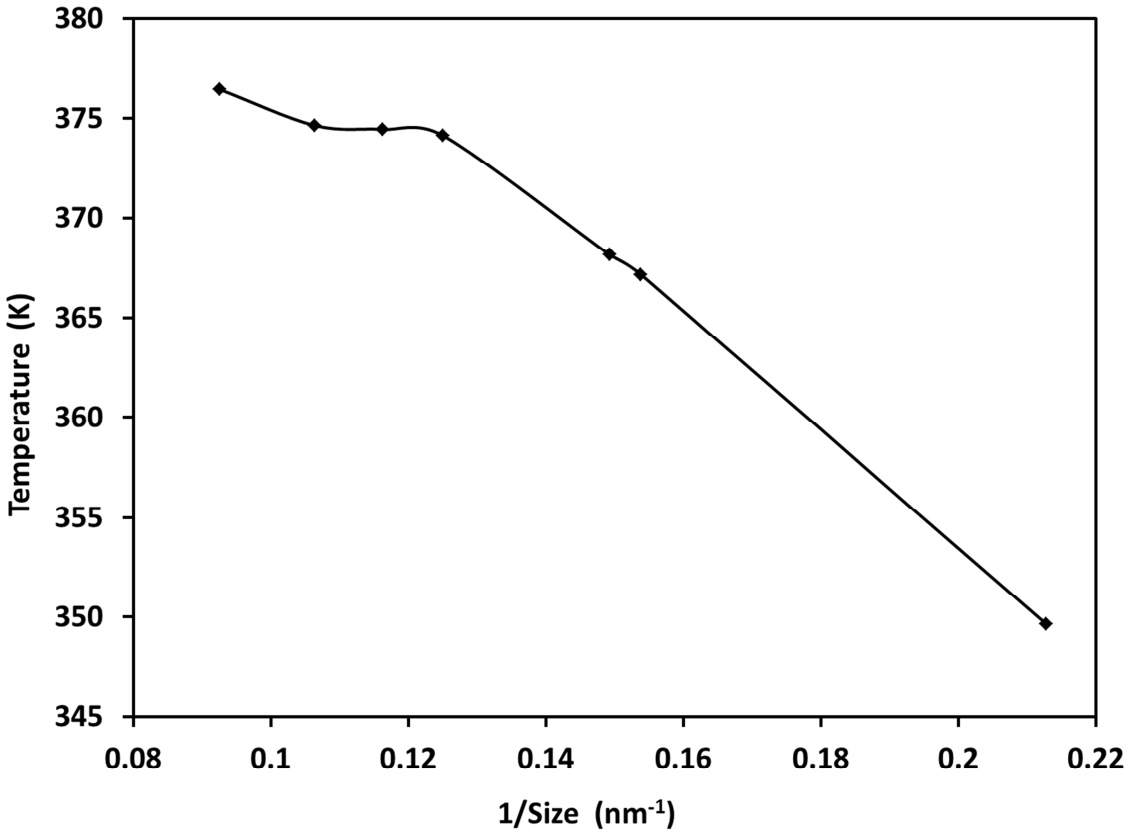

Figure 8.15: Phase-transition temperature as in Figure 8.14 of Ag_2Se nanocrystals as a function of their inverse size.

Figure 8.15 plots the phase-transition temperature of the Ag_2Se nanocrystals against their corresponding inverse size. Even though the data does not seem to lie on a

straight line, a linear fit to the data above when extrapolated to infinity gives a phase transition for bulk Ag_2Se (if it existed in the tetragonal phase) to be around 400 K *i.e.* 127 °C which is pretty close, but still lower than, the bulk phase-transition (from the orthorhombic phase to the cubic phase) temperature of 135 °C.

We would get a better idea regarding the phase diagram of Ag_2Se, if we were able to discern if nano- to micro-sized Ag_2Se crystals in the orthorhombic phase also displayed a size-dependent phase-transition behavior. To achieve the same, using a ligand exchange and sintering technique described previously, we prepared a thin film of Ag_2Se of nearly 100-nm average grain sizes existing in the orthorhombic phase and conducted XRD experiments with *in-situ* heating to determine the phase transition temperature. Note that to determine the phase transition temperature of these samples, we needed to perform DSC measurements. However, we were unable to do so as we could only synthesize these as thin films which are not amenable for the DSC measurements. Regardless, we could get a fair idea of the transition temperatures for these big Ag_2Se crystals which lie in an intermediate regime somewhere between nanocrystals and bulk Ag_2Se. Figures 8.16 and 8.17 show the XRD patterns for these crystals for the heating and the cooling cycles, respectively. We can observe immediately from Figure 8.16 that around 130 °C, the phase has almost changed from the orthorhombic to the cubic phase. The high-intensity peak around 37 degrees (2-theta) has almost disappeared and the other two centered around 33.5 and 35 degrees have reduced substantially in intensity. Given that in all the previous samples, we have determined the phase-transition temperature from the peak in the DSC curve and not at the temperature where the peak merges into the baseline, it is fair to assume that the phase-transition temperature for this sample is somewhere around 130 °C. By the same analogy, we can assume that the phase-transition temperature for the sample during the cooling cycle lies somewhere around 110 °C. Thus, compared to the bulk sample (Figure 8.4), we observe a depression in the transition temperature during the heating cycle from 135 °C to 130 °C, and from 120 °C to 110 °C during the cooling cycle for the 100-nm Ag_2Se crystals. Hence, there is reduction in the transition temperatures with decreasing size for the macro- to micro-sized crystals existing in the orthorhombic phase as well.

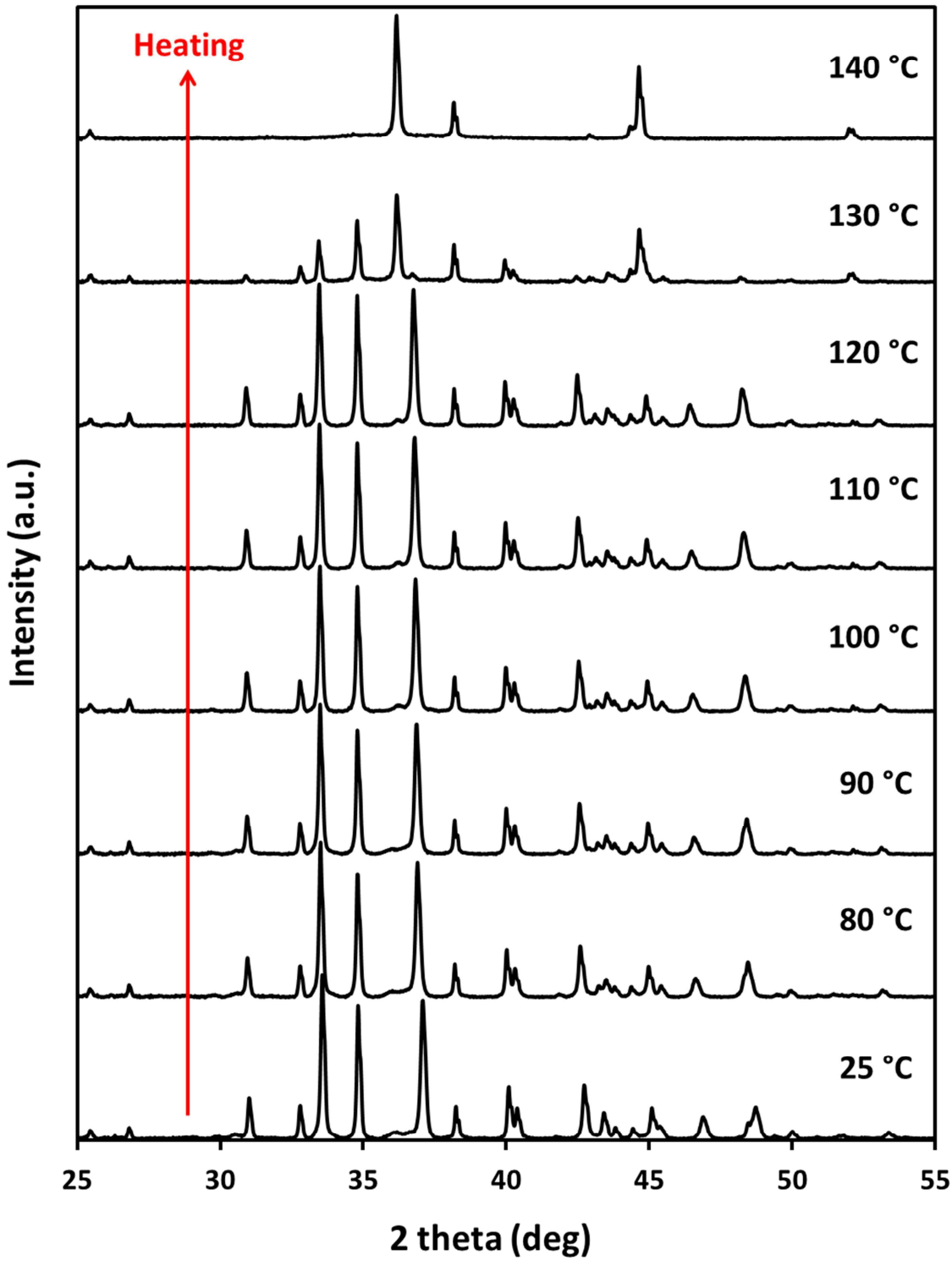

Figure 8.16: Changes in X-ray diffraction patterns with increasing temperature showing the transition from the low-temperature orthorhombic phase to the high-temperature cubic phase for ~100-nm Ag_2Se crystals.

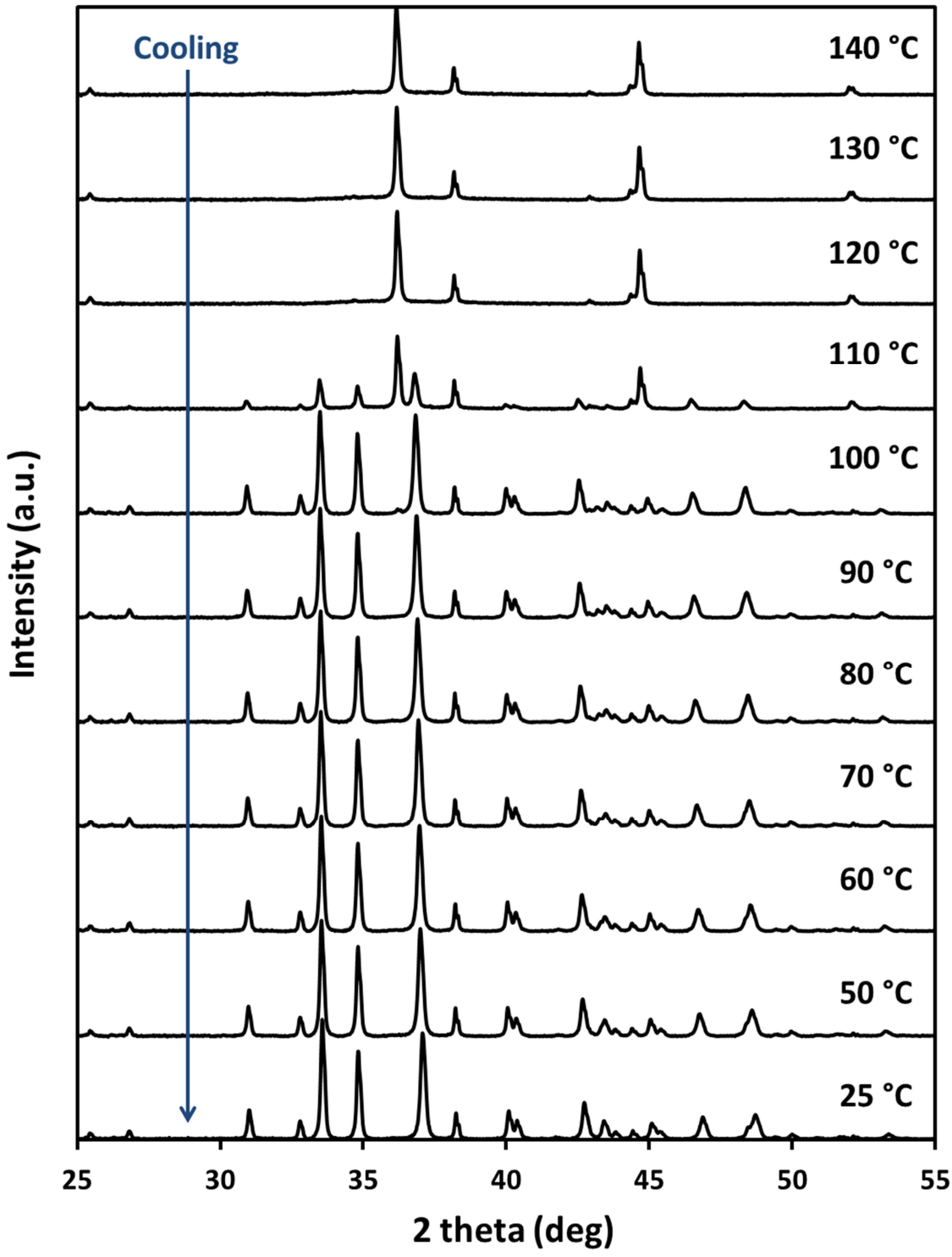

Figure 8.17: Changes in X-ray diffraction patterns with decreasing temperature showing the transition from the high-temperature cubic phase to the low-temperature orthorhombic phase for ~100-nm Ag_2Se crystals.

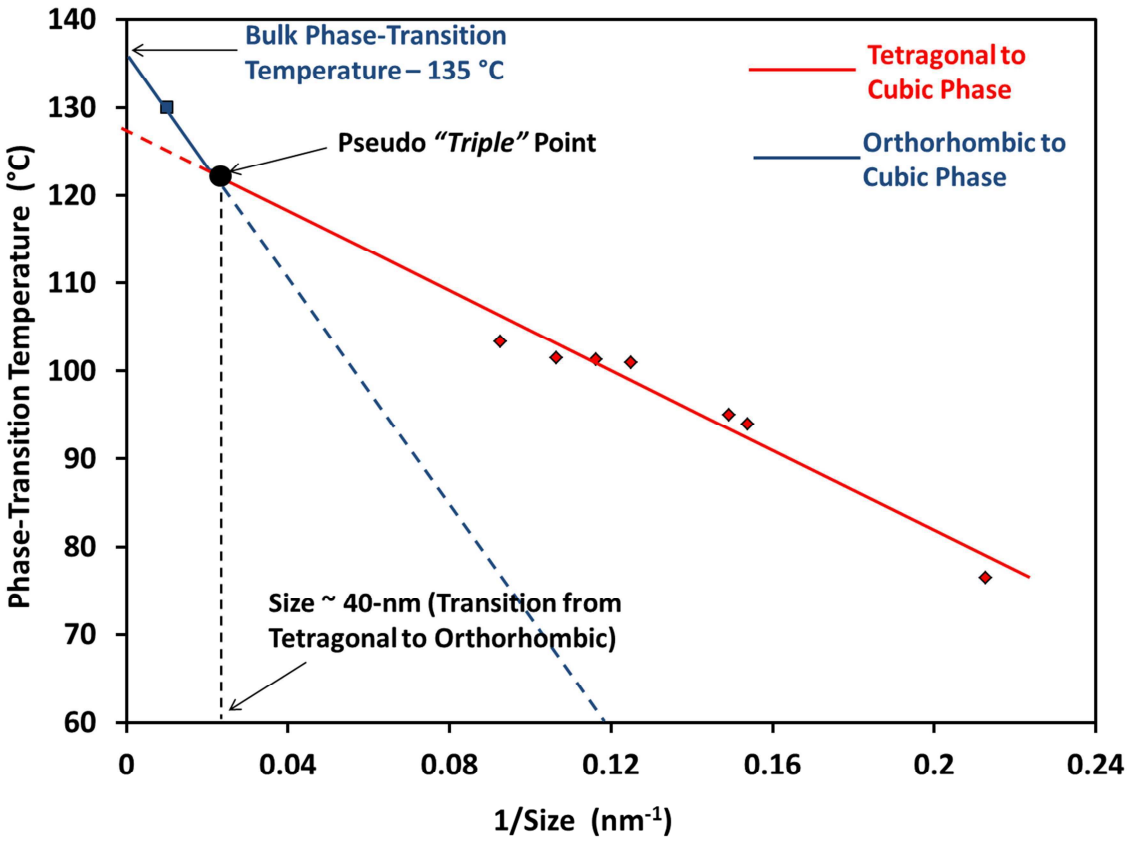

Figure 8.18: Size- and temperature-dependent phase diagram for Ag_2Se crystals. The dotted lines indicate the expected transition lines if the corresponding phases existed at those temperatures. The red diamonds indicate the position of the phase-transition temperatures for Ag_2Se nanocrystals existing in the tetragonal phase. The blue cube does the same for ~100 nm crystals in the orthorhombic phase.

Now putting together all the information we have accumulated regarding the phase-transition behavior of Ag_2Se crystals in Figure 8.18, we construct a hypothetical phase diagram for Ag_2Se with temperature and size of the crystals as the two parameters. The solid red line is a linear fit from the data points corresponding to experimentally obtained phase-transition temperatures for different nanocrystal samples existing in the tetragonal phase at room temperature as a function of their size. The extrapolated line has a y-intercept of 127 °C corresponding to the expected value of the phase transition temperature if bulk crystals were to exist in the tetragonal phase under ambient conditions. Similarly, the solid blue does the same for the phase-transition temperature for a bulk sample (infinite size) and an experimentally obtained point for 100-nm crystals existing in the orthorhombic phase. The point at which these two solid lines intersect should determine the triple point where all three phases can co-exist. We name this a

pseudo triple point as it is between three solid phases instead of the more conventional solid-liquid-gas systems. A vertical line from this triple point onto the x-axis helps us extract the size of the crystal at which this triple point should exist. Interestingly, this size turns out to be 40-nm – the size at ambient conditions which determines the transition from the tetragonal to the orthorhombic phase. Thus, we have more or less sketched a new phase diagram for Ag_2Se with temperature and crystal size as the axes.

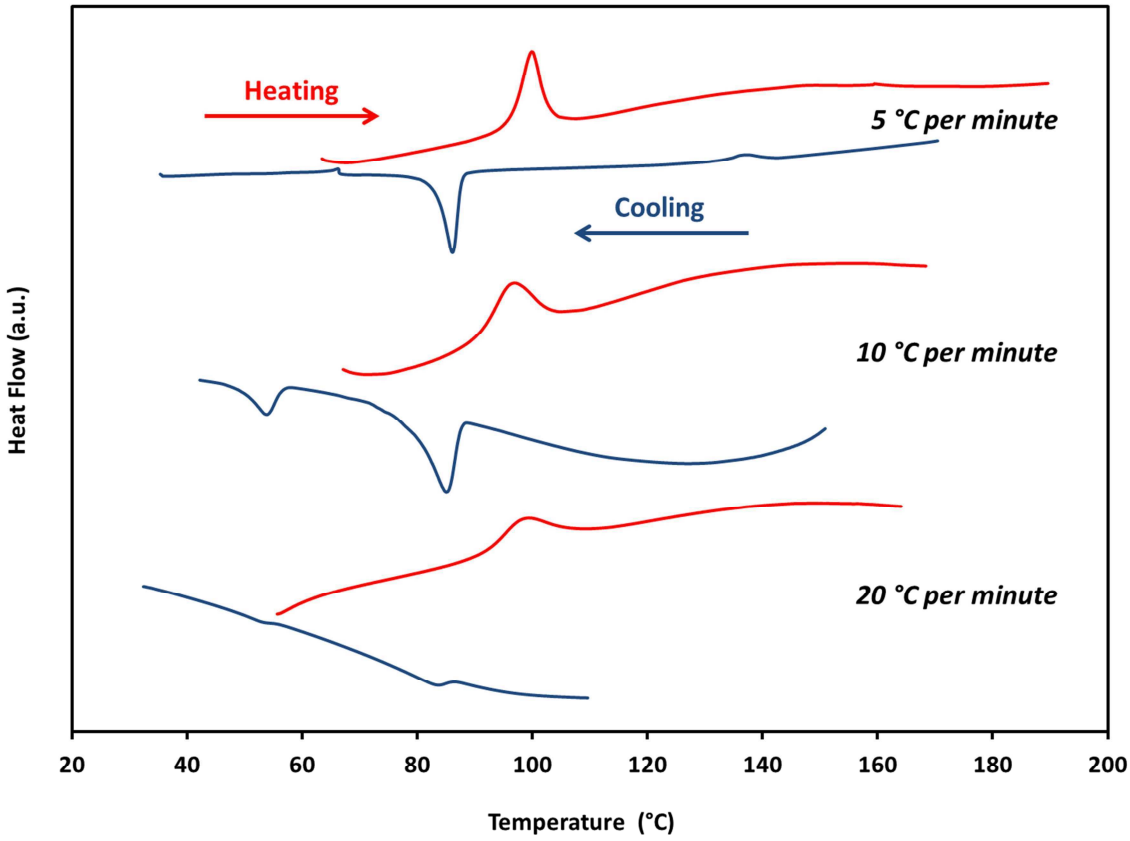

Figure 8.19: DSC thermograms of ~6.5-nm Ag_2Se nanocrystals for three thermal (heating/cooling) cycles at different scan speeds.

Before proceeding any further though, we needed to check a few key issues that exist in systems undergoing phase transitions which would help us in manipulating the phase diagram even further. Firstly, we wanted to see if the phase transitions were a function of the heating and cooling rates. Figure 8.19 shows the phase transitions for the same sample at different heating and cooling rates of 5 °C, 10 °C and 20 °C per minute. Note that for all the previous DSC thermograms, the heating/cooling rates were 10 °C per

minute. It is evident that while slower rates lead to sharp transitions, faster scan rates lead to more diffuse transitions spread out over a range of temperature. However, the phase-transition temperatures for the three scan rates studied did not vary much and were within 3-4 °C during the heating cycle and 2 °C during the cooling cycle, which perhaps explains the excellent agreement between the XRD and the DSC data for the other samples. XRD scans take much longer (nearly an hour at each temperature) as compared to DSC scans. Since the scanning rate does not affect the transitions too much, both sets of data agree well with each other.

The only major difference in the three sets of data was the relative ratio of the two phase transition peaks (88 °C and 57°C) during the cooling cycle. While the peak positions were almost the same for different scan speeds, the intensity of the 88 °C peak was much higher when scanned at a slower rate. In fact, we were barely able to observe the peak at 57 °C when the sample was scanned at a rate of 5 °C per minute. As discussed earlier, assuming that the first transition corresponds to the transition from the cubic to the metastable tetragonal phase and the second from the metastable to the stable tetragonal phase in nanocrystals, the data implies that when the sample passes through an extremely slow rate of cooling, it mostly transitions straight to the stable tetragonal phase since it has ample time to do so and is not trapped in the metastable phase. This leads us to believe that under extremely high cooling rates, one might be able to stabilize the metastable tetragonal phase at room temperature long enough to study it better.

For our biggest Ag_2Se samples (sizes > 10-nm) capped with OM, TOP, TOPO, at times we observe sintering when heated above the phase transition temperature. Since the sintering leads to a huge distribution of grain sizes, we observe a tailing of the DSC heating curve towards higher temperatures and during cooling we observe a third peak centered around 99 °C corresponding most likely to the sintered part of the film (Figure 8.20).

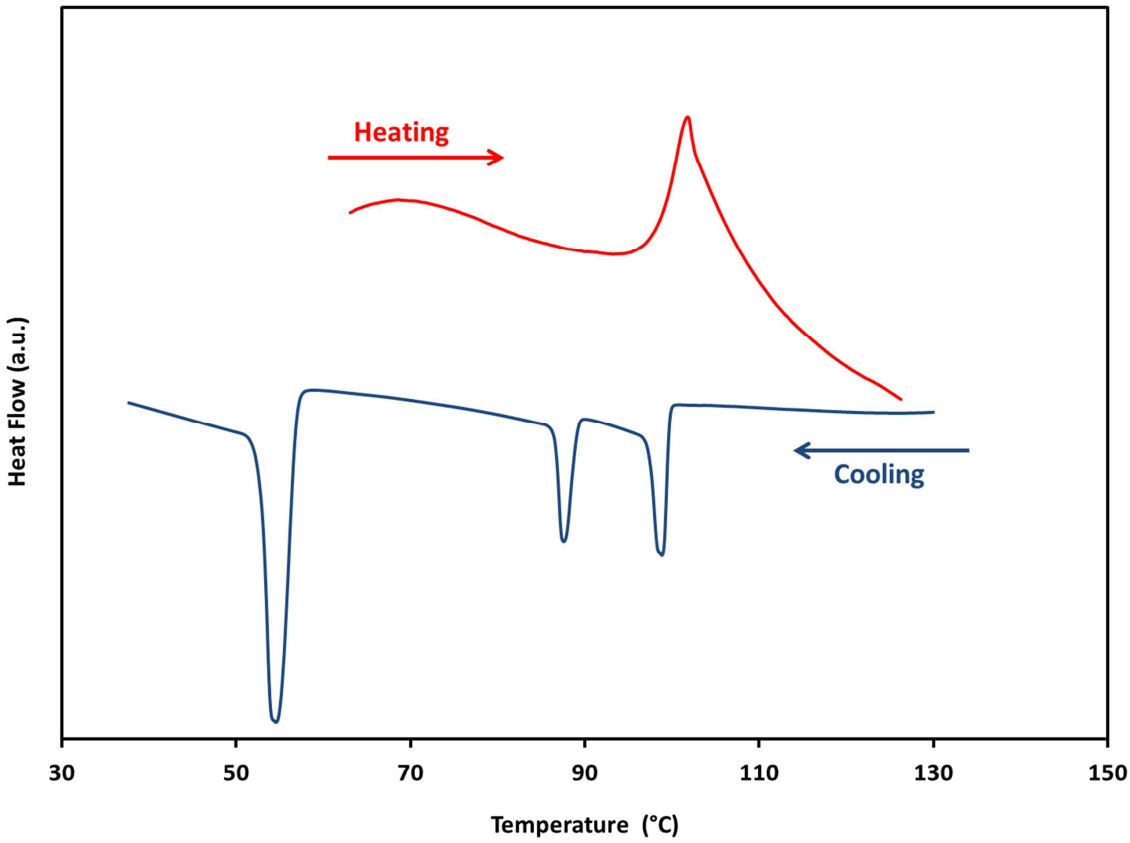

Figure 8.20: DSC thermogram of oleylamine-, tri-octylphosphine- and tri-octylphosphine oxide-capped ~10.5-nm Ag_2Se nanocrystals for one thermal (heating/cooling) cycle. The broad peak during the heating cycle is representative of sintering.

However, in order to make sure that the broadening corresponds to sintering and not some other effect in the sample, we performed XRD studies with *in-situ* heating on the same sample. If there is any sintering we should be able to notice it in the peak widths in the X-ray diffractograms. As expected, the peaks seem to sharpen after the phase transition takes place during the heating cycle (Figure 8.21). During the cooling cycle (Figure 8.22), one can observe that the XRD pattern recovered at room temperature does not match the initial one. This can easily be noticed by comparing the corresponding patterns at 25 °C for the heating and the cooling cycles. The peaks in the cooling cycle are much sharper and in fact, we can observe new peaks starting to appear. Most notably, the broad peak at ~36 °C with the highest intensity for the heating cycle, splits up into two distinct and relatively sharp peaks in the XRD pattern for the cooling cycle upon recovery.

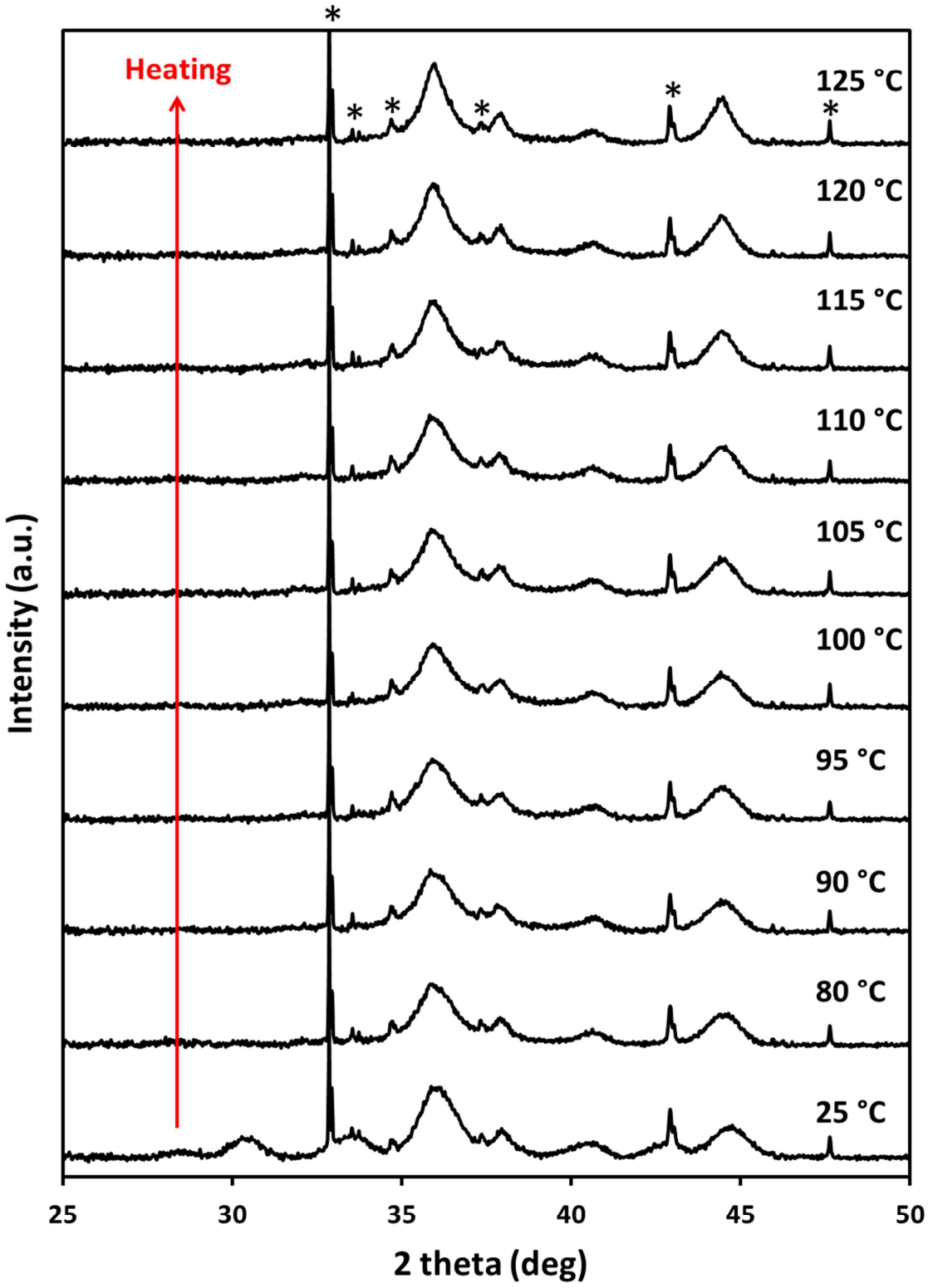

Figure 8.21: Changes in X-ray diffraction patterns with increasing temperature showing the transition from the low-temperature tetragonal phase to the high-temperature cubic phase for ~10.5-nm Ag_2Se nanocrystals. The sharp peaks marked by asterisks are zincite peaks from the conductive grease on the substrate holder.

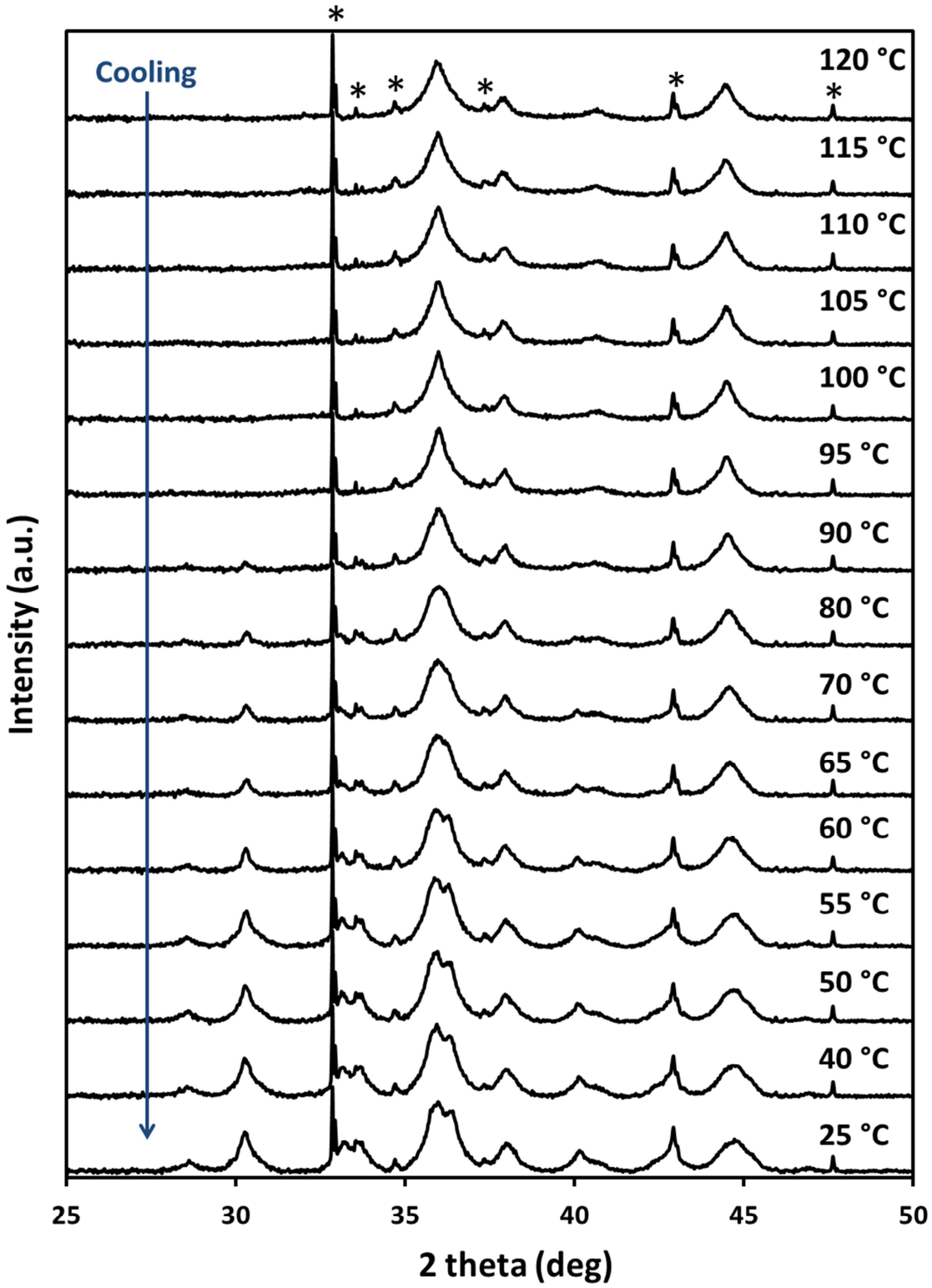

Figure 8.22: Changes in X-ray diffraction patterns with decreasing temperature showing the transition from the high-temperature cubic phase to the low-temperature tetragonal phase for ~10.5-nm Ag_2Se nanocrystals. The sharp peaks marked by asterisks are zincite peaks from the conductive grease on the substrate holder.

Any size-dependent study involving nanocrystals, including phase-transition studies, is likely to suffer if the size distribution of the sample changes due to sintering. In order to overcome this undesirable state of affairs, we proceed to exchange the native as-synthesized ligands capping these nanocrystals with bulky polymeric ligands (see Section 8.4.8 for details). The ligand exchange serves three important purposes. First, since these ligands have a strong affinity for the surface atoms on the nanocrystals, they bind strongly to the nanocrystals and do not come off easily on thermal treatment. Moreover, they sublime at very high temperatures as against the common OM, OA, ODA, TOP, TOPO ligands which sublime between 200 °C – 300 °C. Thus they provide extremely good thermal stability and prevent the nanocrystals from sintering both when heated as a powder or when cast on a thin film. Secondly, since they are much longer than the other ligands, they help to keep the particles separate and hence, prevent any particle-particle interaction. It is extremely important for the phase-transition studies in nanocrystals that they do not talk to each other. As discussed earlier, one of the key differences between phase transitions in bulk materials and nanocrystals is that the new phase is restricted to the dimensions of the individual nanocrystal where it nucleates. Especially in the silver chalcogenide system, wherein the ionic conductivity goes up by orders of magnitude upon phase transition, it is not impossible to fathom that the ions from one nanocrystal might diffuse to the neighboring crystals and influence the transition in those and/or promote sintering. Thus, by increasing the inter-particle separation using these bulky polymer ligands, we hope to avoid any such issues. Finally, these ligands render the nanocrystals hydrophilic and hence these can be dispersed in polar solvents like water and methanol which make them extremely compatible for any bio-based application. Hence, we proceed to perform the ligand exchange with the same sample that showed sintering and then study the XRD patterns again with *in-situ* heating. As observed in Figures 8.23 and 8.24 and DSC analyses, we see no evidence of sintering post-ligand exchange. Both the XRD patterns at 30 °C for the heating and the cooling cycle are exactly the same. Moreover, after the ligand exchange, the phase-transition properties remain the same, with the transition during the heating cycle taking place somewhere between 80 °C and 90 °C and the reverse transition taking place between 60 °C and 50 °C.

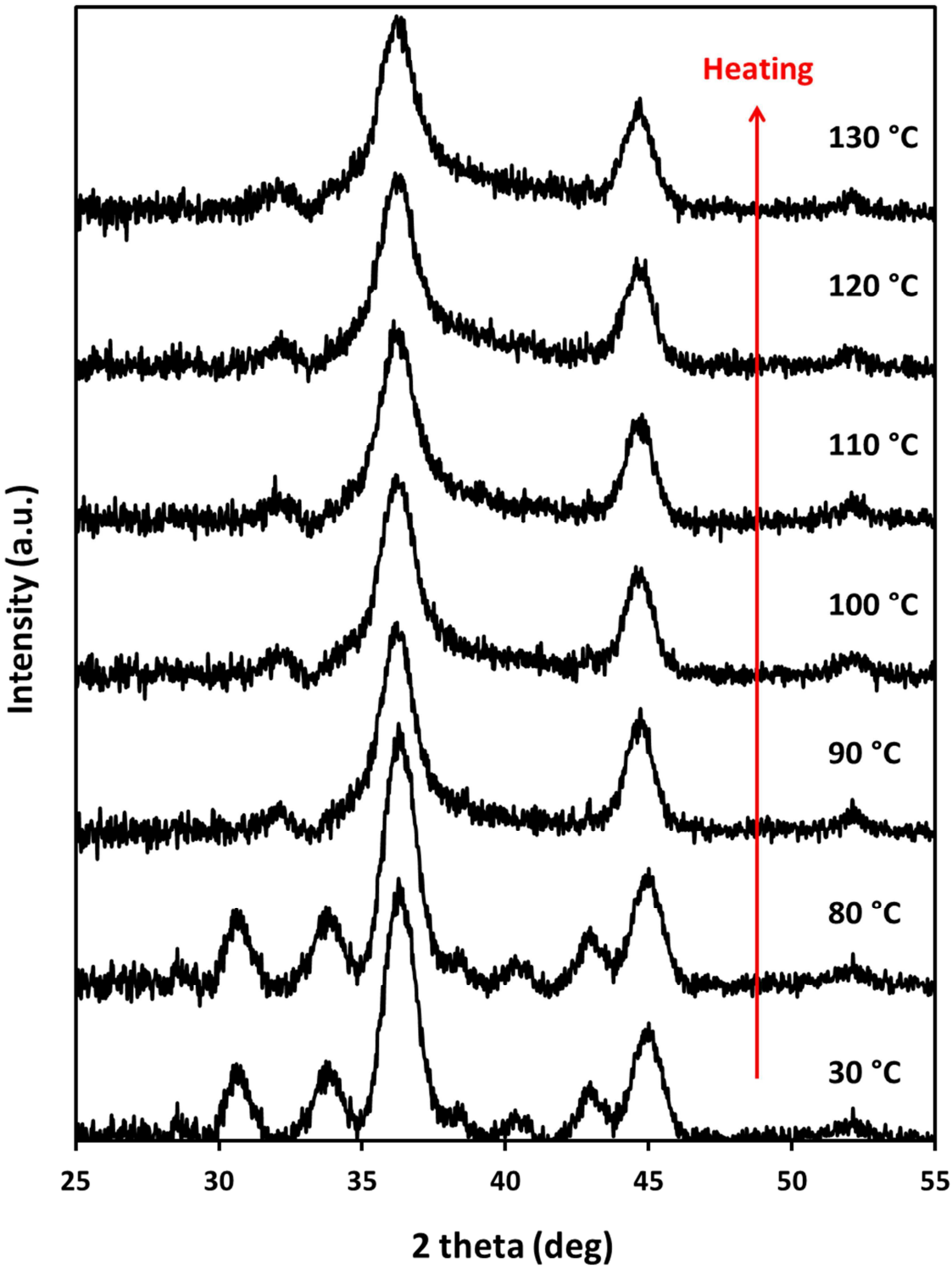

Figure 8.23: Changes in X-ray diffraction patterns with increasing temperature showing the transition from the low-temperature tetragonal phase to the high-temperature cubic phase for ~10.5-nm Ag_2Se nanocrystals capped with bulky polymer ligands.

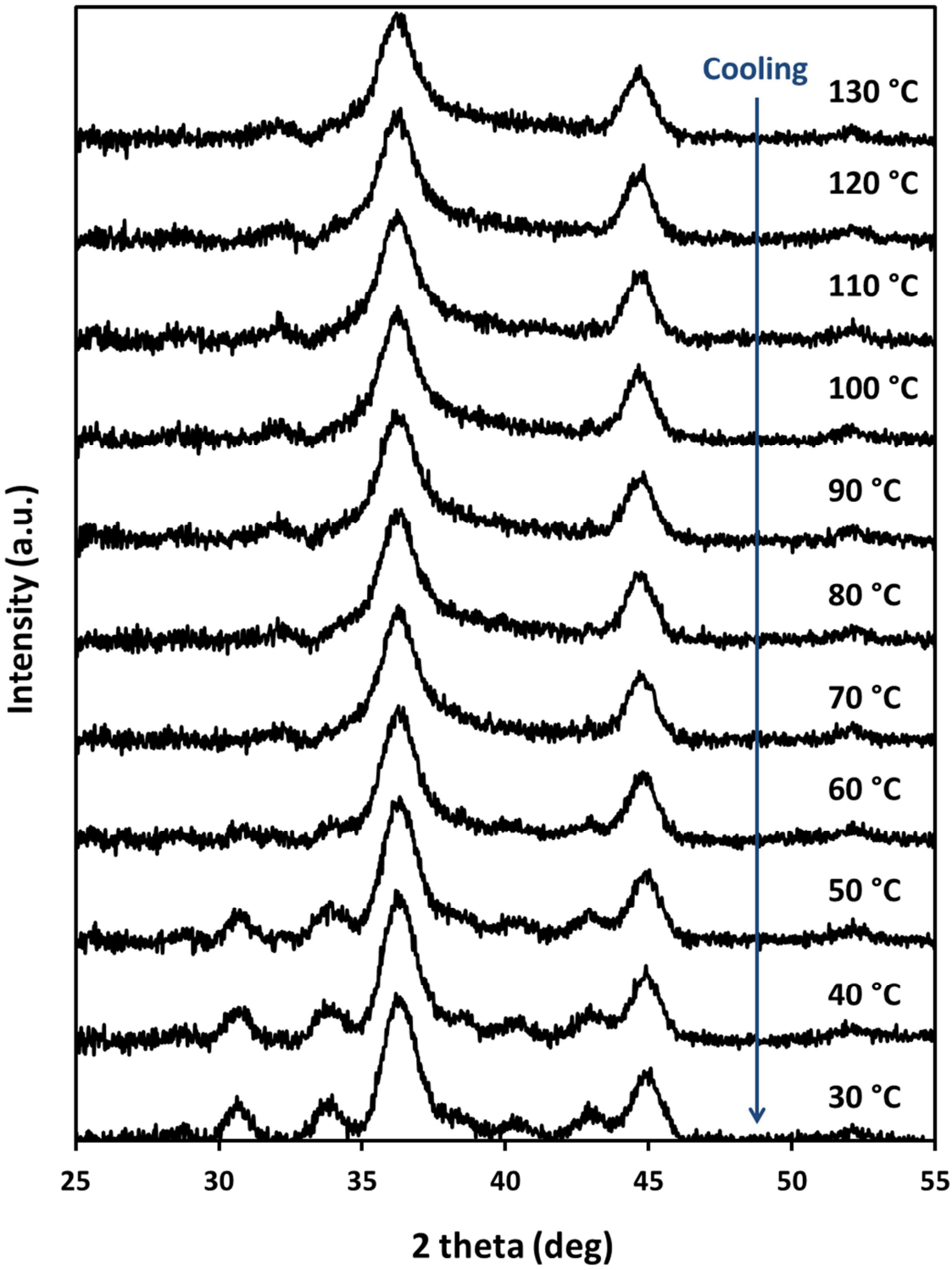

Figure 8.24: Changes in X-ray diffraction patterns with decreasing temperature showing the transition from the high-temperature cubic phase to the low-temperature tetragonal phase for ~10.5-nm Ag_2Se nanocrystals capped with bulky polymer ligands.

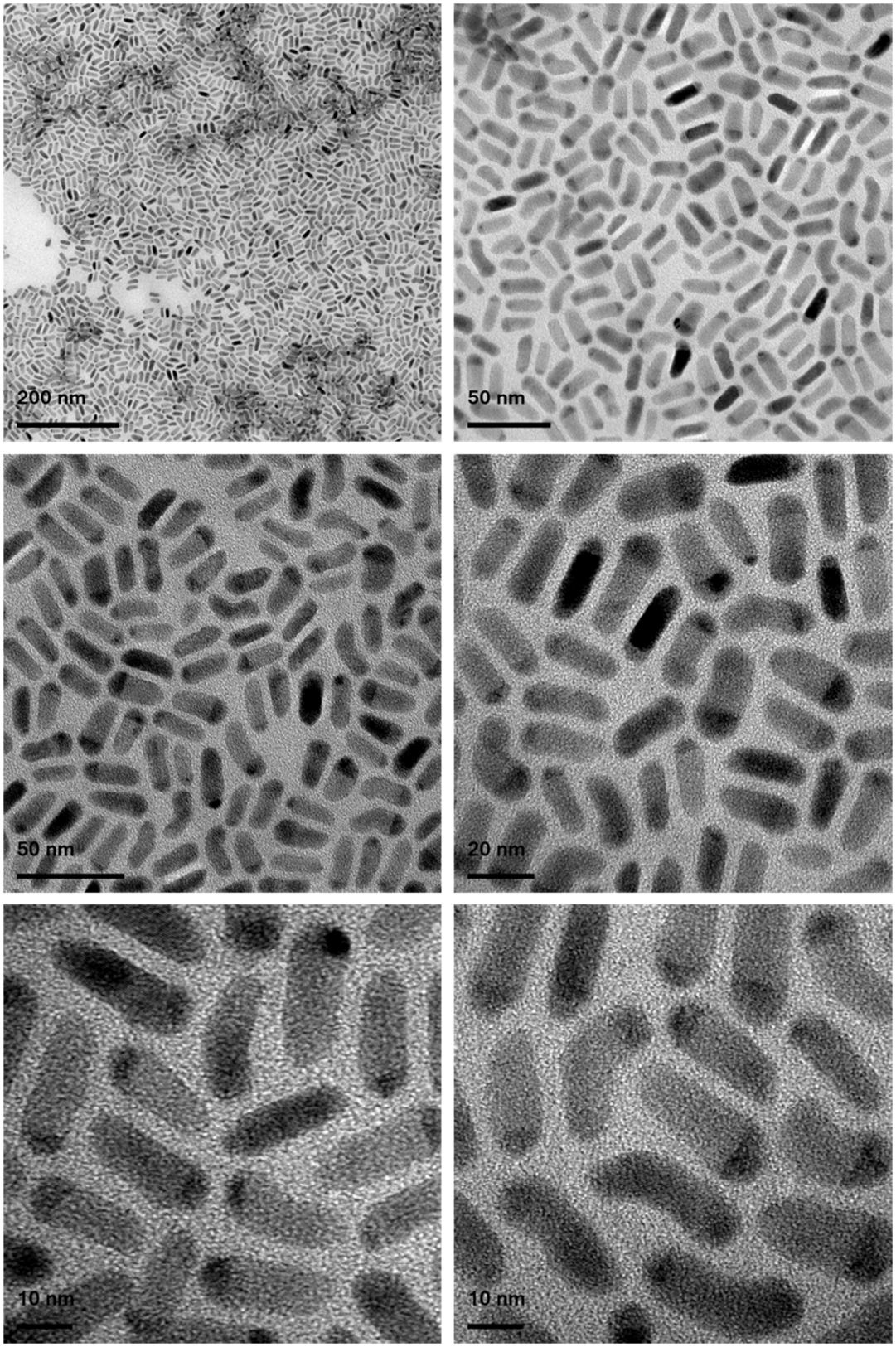

Figure 8.25: Low-magnification transmission electron micrographs of an ensemble of as-synthesized Ag_2Se–CdS core-shell nanocrystals.

Lastly, we wanted to investigate the phase transition properties of these nanocrystals in a confined geometry. Adding a shell of a wide band-gap material like CdS and ZnS to core semiconductor nanocrystals like CdSe and PbS is a well-established technique to avoid surface oxidation and passivate surface traps at the core surface, thus improving their optical and electronic properties.[51] In order to take full advantage of the near- and mid-IR light emitting properties of Ag_2Se nanocrystals[3] as discussed in Chapter 7, it might be essential to add a shell to the nanocrystals. Also, to investigate the opto-electronic properties of the high temperature phase, a shell might be required. But this shell might affect the phase transition properties of the core Ag_2Se nanocrystal. Hence, we proceed to synthesize Ag_2Se-CdS core shell nanocrystals and study their phase transition properties.

We employ a successive ionic layer adsorption and reaction (SILAR) synthesis technique similar to those used for CdSe nanocrystals to grow a CdS shell around the Ag_2Se nanocrystals (see Section 8.4.9 for details).[52] We first synthesize Ag_2Se nanocrystals following the protocol described in Chapter 7 with average sizes of around 7.5-nm and capped with oleyamine, tri-octylphosphine and tri-octylphosphine oxide. After cleaning these as-synthesized nanocrystals, we proceed to grow shells of CdS around them by alternate additions of cadmium and sulfur precursors (amounts in each addition corresponding to growth of one monolayer), respectively, at around temperatures of 200 °C – 250 °C. Representative transmission electron micrographs of the same are shown in Figures 8.25 and 8.26. As is evident from the images, the CdS shell does not grow uniformly as a sphere around the nanocrystals but has preferential growth across certain facets and hence we end up with a dot-in-rod structure with Ag_2Se being the dot and CdS the rod. Key features that can be seen in Figure 8.26 are that the diameters of the rods are roughly around 7.6-nm as expected. The nanorod having a diameter of 7.38 nm and the one just above that in Figure 8.26 show well defined lattice fringes running almost all the way across the nanorod, thus displaying their high crystallinity.

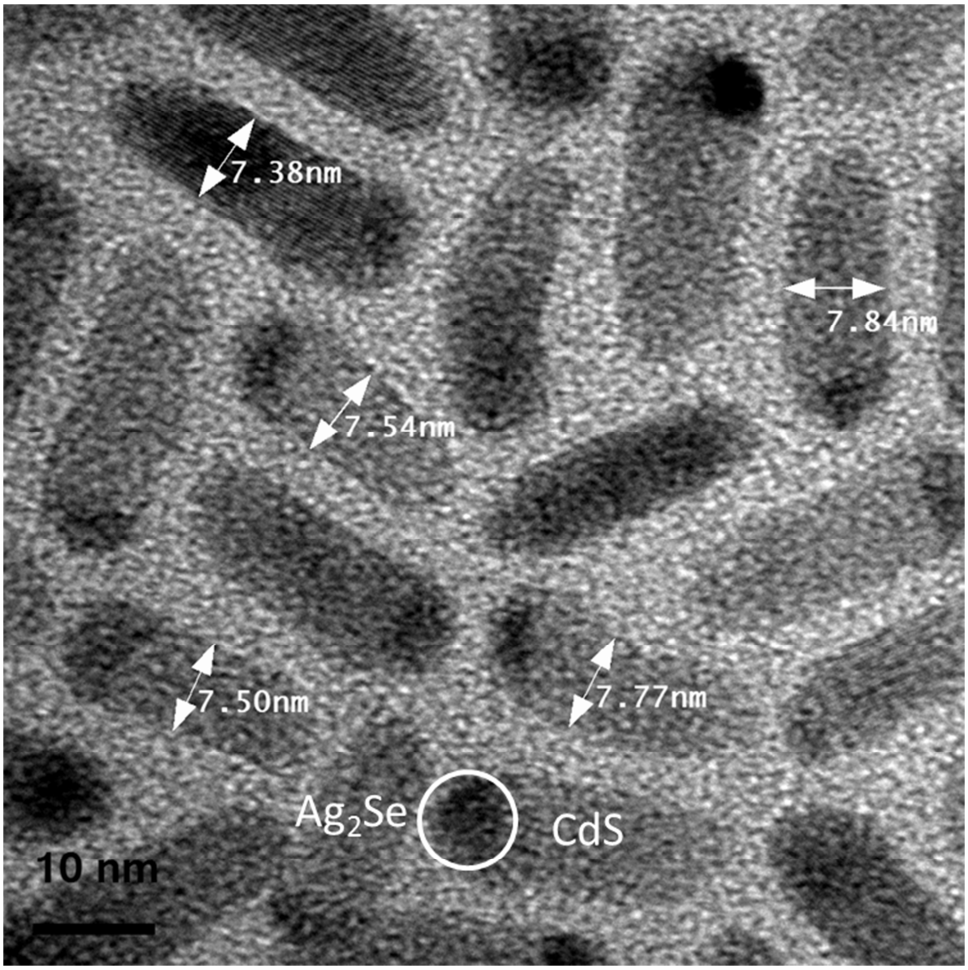

Figure 8.26: Low-magnification transmission electron micrograph of an ensemble of as-synthesized Ag_2Se–CdS core-shell nanocrystals showing the size of the rod like structures and pointing out the Ag_2Se and the CdS portions.

While the diameter of the rod can be controlled by the size of the Ag_2Se nanocrystal used, the length can be tuned by the amount of cadmium and sulfur precursors added. Figure 8.27 shows low-resolution transmission electron micrographs of such a structure where we only add a little amount of cadmium and sulfur. We used the same seed Ag_2Se nanocrystals as were used in the previous figure with an average size of nearly 7.5-nm. We can observe that in this case too, the CdS again shows a preferential growth direction (which is perhaps expected since in a depleted system the precursors would only add to the high binding energy facets). The structures correspond more to an acorn like structure rather than to a dot-in-rod structure. As against rod lengths of roughly 20-nm in Figure 8.26, we obtain rod lengths of nearly 7-nm in this case.

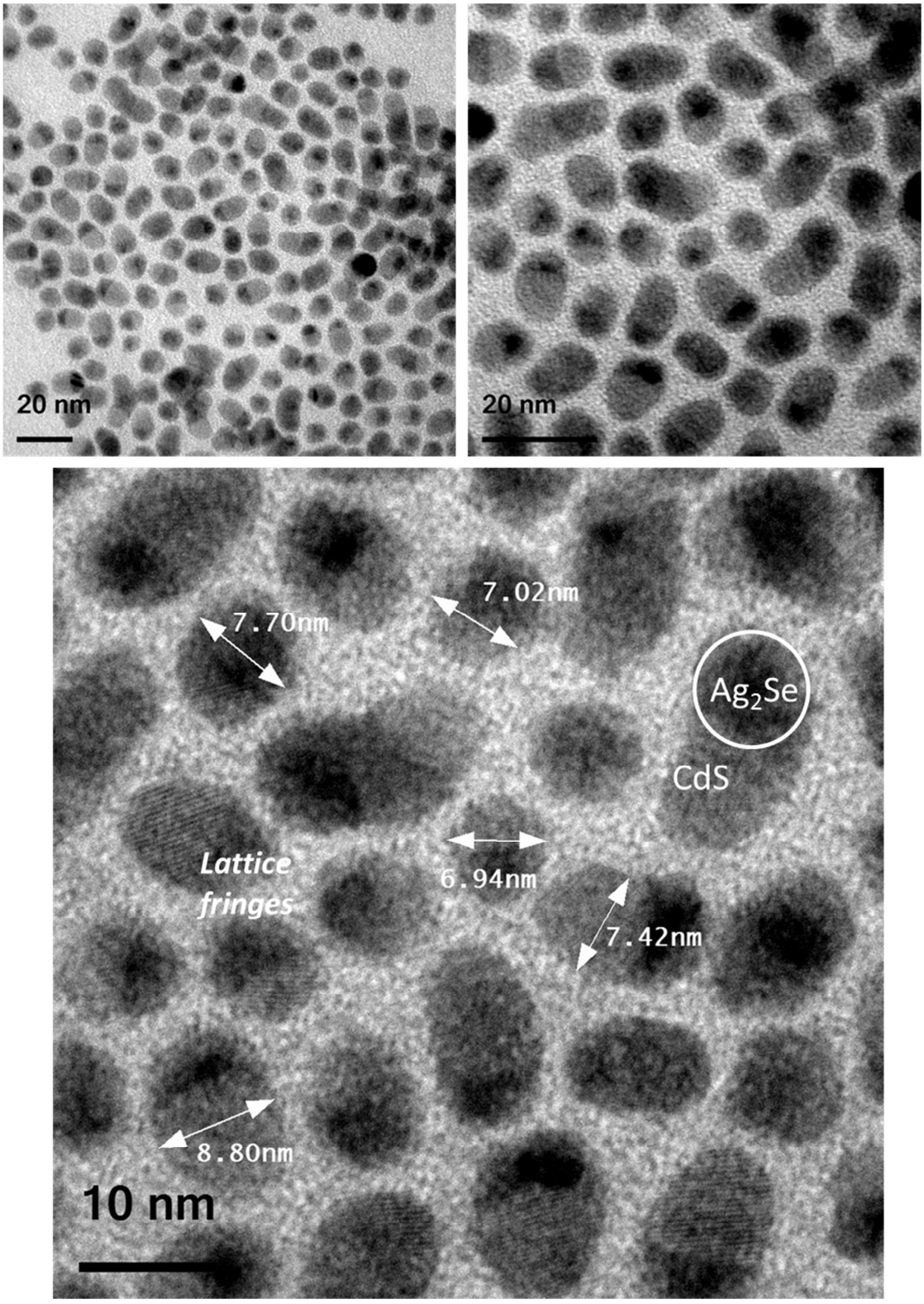

Figure 8.27: Low-magnification transmission electron micrographs of an ensemble of as-synthesized Ag_2Se–CdS acorn-shaped nanocrystals showing the size of the structures and pointing out the Ag_2Se and the CdS portions.

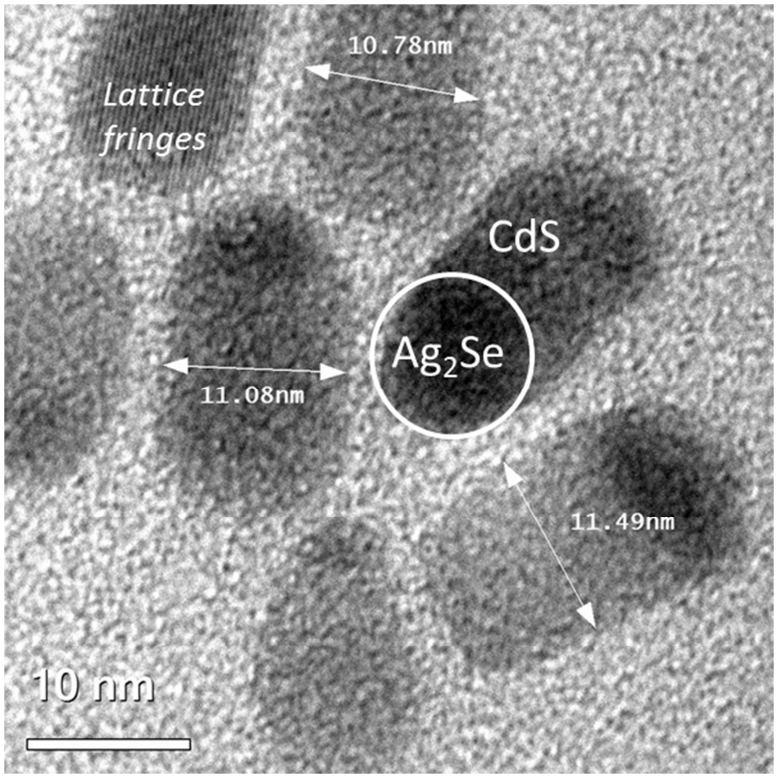

Figure 8.28: Low-magnification transmission electron micrograph of an ensemble of as-synthesized Ag_2Se–CdS dot-in-rod nanocrystals showing the size of the nanostructures and pointing out the Ag_2Se and the CdS portions.

Figure 8.28 shows a low-resolution transmission electron micrograph of an ensemble of Ag_2Se-CdS dot-in-rod structures where we start off with our largest sized Ag_2Se nanocrystals (~10.5-nm average size) as the seed material. As in the previous two cases, we observe the same preferential growth of CdS with the rod-diameters being comparable to the seed nanocrystal size. Here, we add intermediate amounts of cadmium and sulfur precursor to restrict the rod lengths to nearly 14-nm. Thus, we demonstrate that we can control both the diameter and the length of these dot-in-rod structures.

Now we proceed to study the phase transitions characteristics of these nanocrystals. We were not able to perform XRD studies with these nanoctructures because the diffraction peaks from CdS overlapped with those from the Ag_2Se portion of the structure and also were stronger in intensity (Figure 8.29). One way to get around this problem was to grow smaller CdS grains. However, even with the acorn-shaped CdSe-Ag_2Se nanocrystals, we were unable to differentiate the two sets of peaks (Figure 8.29).

Additionally, the CdS peaks start to broaden when their grain size gets smaller and this compounds the issue even further. Also with no JCPDS information on the tetragonal phase of Ag_2Se, we were not able to carry out Rietveld analyses in order to fit peaks to the observed diffractograms. While we were able to identify the strongest Ag_2Se related peaks in the acorn-shaped nanocrystals, these peaks from the tetragonal phase at room temperature overlap with the peaks from the cubic phase at high temperature. It is usually the disappearance of the lower intensity peaks that helps us track the transition. Under such a scenario, it did not make sense to carry out XRD studies with *in-situ* heating to observe the phase transition. Rather, we used DSC to determine the phase transition temperatures.

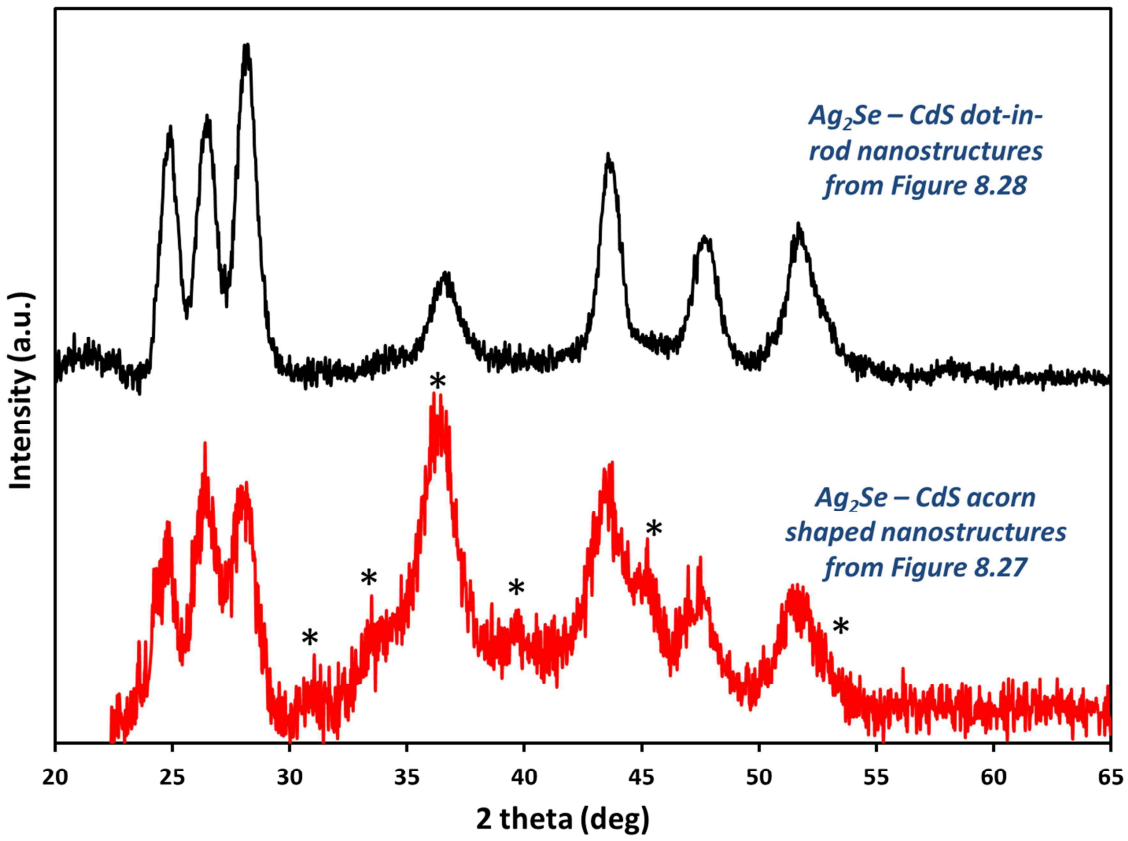

Figure 8.29: X-ray diffraction patterns of Ag_2Se–CdS dot-in-rod and acorn-shaped nanocrystals. All the sharp peaks in the black pattern correspond to CdS peaks. The asterisks show the location of the peaks expected from tetragonal phase Ag_2Se.

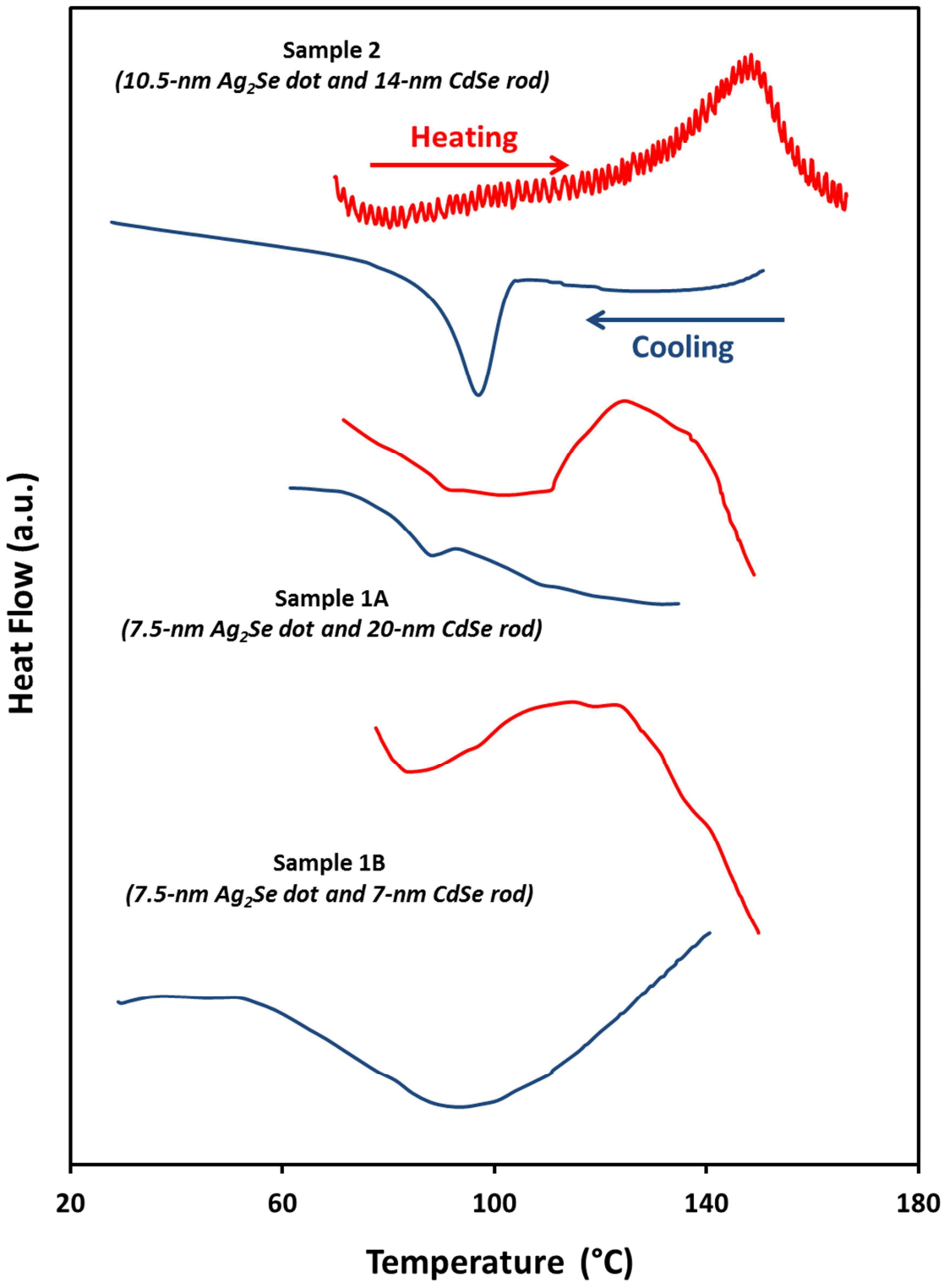

Figure 8.30: DSC thermograms of dot-in-rod Ag_2Se-CdS nanocrystals showing the size dependence of the phase-transition temperatures.

The DSC results are summarized in Figure 8.30. Henceforth, we shall name the sample in Figures 8.25 and 8.26 as Sample 1A (7.5-nm Ag_2Se dot and 20-nm CdSe rod), the one is Figure 8.27 as Sample 1B (7.5-nm Ag_2Se dot and 7-nm CdSe rod) and the sample in Figure 8.28 as Sample 2 (10.5-nm Ag_2Se dot and 14-nm CdSe rod). For samples 1A and 1B, one can see that the peaks in the DSC thermograms are much broader than what we observed for the seed nanocrystals earlier, which might be attributed to the fact that there is probably some alloying between Ag_2Se and the CdS at the interface which would vary across random nanorystals in an ensemble and hence the actual size of the Ag_2Se nanostructure undergoing the phase transition would vary across the sample. More notably, in both cases the phase transition shifts to nearly 124 °C which is more than 20 °C higher than the corresponding seed nanocrystals. Thus the first observation is that the phase transition temperature shifts to a higher temperature in a confined geometry. The transition peaks are much sharper in Sample 1A as compared to 1B probably because sample 1A has a much more well-defined structure than sample 1B in terms of the Ag_2Se–CdS interface. It is probably the strain at this interface that drives the phase transition temperature higher. Also, the length of the rod does not seem to have an effect on the transition temperature.

Now in Sample 2, where the seed nanocrystal is much bigger than in Sample 1, the phase transition peaks are much sharper. Since the interfacial surface is much less (per unit volume of Ag_2Se material), hence the alloying is probably also lower and restricted to only a few monolayers at most. In a smaller nanocrystal, alloying of a few monolayers would correspond to a more drastic effect on the effective size distribution that undergoes phase transition as compared to a larger nanocrystal. Hence, the sample with larger seeds has sharper peaks. Also the phase transition temperature (147 °C) is much higher than the phase temperatures of both the seed nanocrystal and Sample 1 with smaller seeds. In fact, it is even higher than the bulk Ag_2Se phase-transition temperature (135 °C). This might be explained from the previous size-dependence analogy provided for the seed nanocrystals where the phase-transition temperature increased uniformly with increasing size. Samples 1 and 2 are in the same confined geometry with the same material (CdS) and hence, with increasing size, the phase-transition temperature rises.

Most interestingly, we can now tune the phase-transition temperatures of these materials by confinement and push it even above the bulk transition temperature. Now, with the dot-in-rod system, we are confining the seed nanocrystals only in one direction and we have already achieved nearly a 50 °C increase in phase transition temperature. Hence, the next step would be to subject these nanocrystals to 3-D confinement by growing a uniform shell around them. We do so by growing a shell of ZnS around the Ag_2Se nanocrystals.

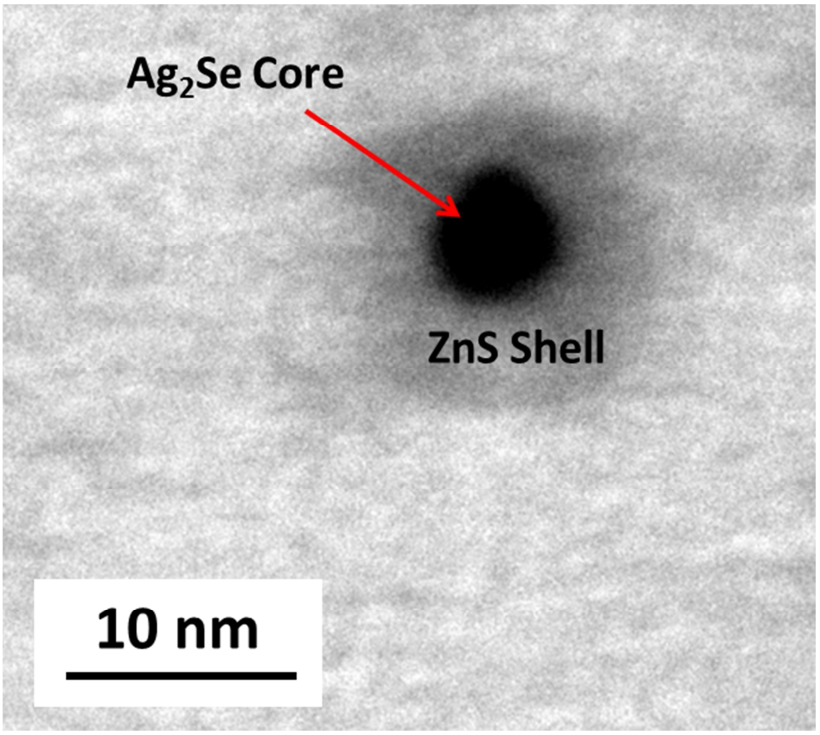

Figure 8.31: Low-magnification transmission electron micrograph of a single Ag_2Se – ZnS core-shell nanocrystal.

For the growth of the ZnS shell, we used a synthesis method that involves a single precursor – zinc diethyldithiocarbamate (see Section 8.4.10 for details).[53] The advantage of this method over shelling techniques is that it allows us to grow a shell at relatively low temperatures of ~110 °C. Thus, we avoid the alloying problem encountered for the CdS shell growth as well as prevent sintering of the seed Ag_2Se nanocrystals during the shelling process. Also, since the shell overgrowth is very slow at these temperatures, it

allows us to control the shell size precisely and hence, the possibility to study the phase transitions at different shell thicknesses presents itself.

Figure 8.31 show a low-resolution transmission electron microscopy (TEM) image of a single Ag_2Se-ZnS core shell nanocrystal. The ZnS shell encompasses the Ag_2Se core uniformly and is very unlike the dot-in-rod structures encountered earlier. Having been assured that we do indeed achieve 3D confinement, we proceed to study the DSC patterns for these nanocrystals.

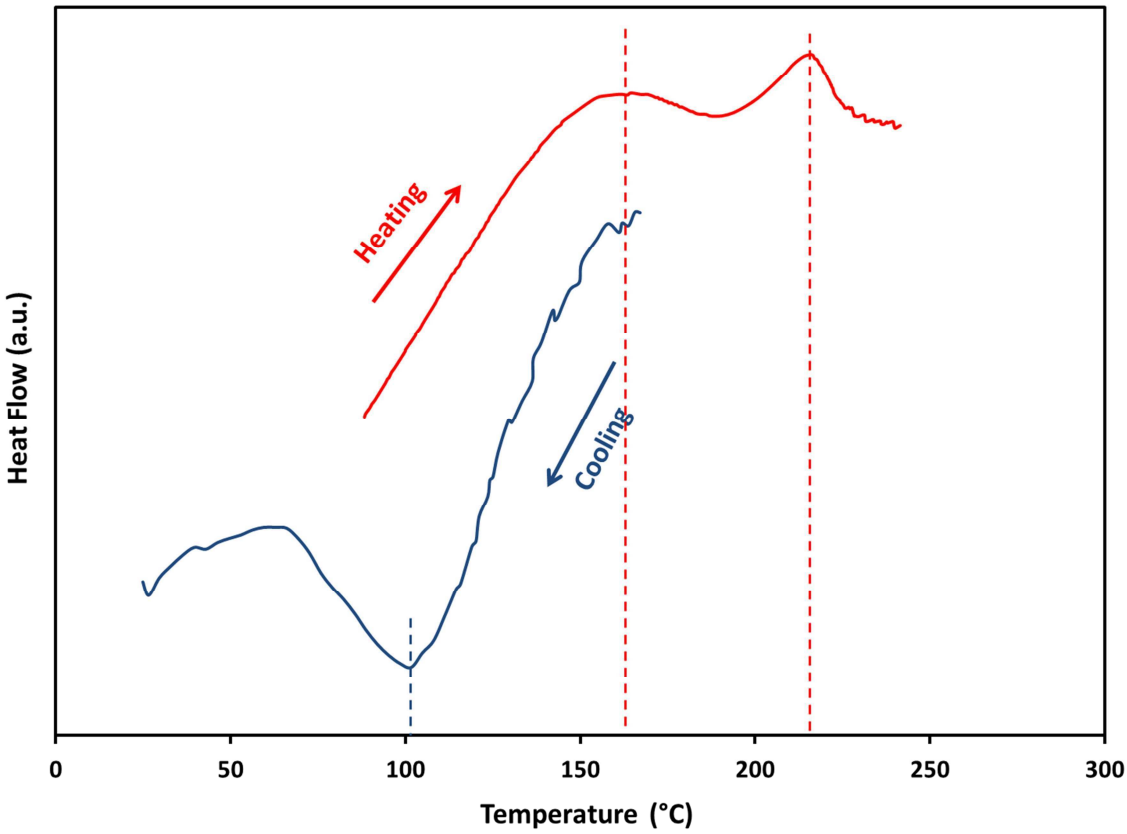

Figure 8.32: DSC thermograms of Ag_2Se-ZnS core-shell nanocrystals. The dotted red and blue lines are meant to serve as guide lines to locate the peak positions for the heating and cooling cycles, respectively.

Figure 8.32 shows the DSC thermogram for the core-shell nanocrystals. During the heating cycle, we observe a broad peak centered around 165 °C and a much sharper one centered around 215 °C. Whether the first peak corresponds to the transition from the tetragonal phase to the cubic phase or the second or if there exists a new phase in between these peaks remains to be answered. Regardless of the identity of these peaks,

we observe some phase transition which is indeed, higher than bulk Ag_2Se and higher than the cases where we had 1D confinement (Samples 1 and 2) and the core-only nanocrystals. In the cooling cycle we only have a single broad peak centered on 101 °C. To address the question what the peaks correspond to, we need to perform XRD studies on these samples. By growing extremely thin ZnS shells on our biggest nanocrystals (so that we can observe the Ag_2Se peaks), we hope to achieve this. These studies are currently in progress.

The increase in the phase-transition temperature in confined systems has also been observed by other groups as well. In fact, Tangirala *et al.* observe a similar effect with Ag_2S nanocrystals in an inorganic matrix[54] and Leon *et al.* with Ag_2Se nanocrystals in mesoporous silica.[55] For confined organic molecules too, a similar increase in the melting temperature has been reported.[56,57] The results are not totally unexpected. Any phase transition in these nanocrystalline systems leads to a change in crystal structure and unit cell volume. Free standing nanocrystals would have all three degrees of freedom, *i.e.* either to expand or contract depending on the volume differences between the corresponding phases. However, nanocrystals in confined systems lose this freedom. If the transition involves a huge change in volume, it would lead to extremely high stresses at the interface of the nanocrystal and the encompassing matrix and hence, the system would try to resist this change. Thus, this would lead to an increase in phase-transition temperatures. This is exactly what we observe for our Ag_2Se system. While free-standing nanocrystals exhibit a phase-transition temperature of nearly 100 °C, the dot-in-rod structures with one degree of confinement transition between 125-147 °C (depending on size of the seed nanocrystal) and finally, core-shell nanocrystals, where the nanocrystal is entirely confined, undergo the phase transition at an even higher temperature of either 165 °C or 215 °C (needs to be determined). To summarize our studies on phase transitions in Ag_2Se so far, we demonstrate the extremely malleable nature of this exciting class of materials wherein on one hand, by reducing the size of the crystal, we can decrease the phase-transition temperature uniformly and on the other hand, by confining these nanocrystals within a matrix with different degrees of freedom, we can increase the phase-transition temperature uniformly. Modifying the size and the surface

of these nanocrystals provides us with a useful and extremely facile tool to modify the phase behavior of this material system.

In bulk Ag_2Se, it is well known that the high-temperature cubic phase Ag_2Se behaves as a super-ionic conductor with extremely high ionic and electronic conductivities. Now that we are convinced that we indeed see a phase transition in our nanocrystals, this transition should also affect electrical transport in our nanocrystal samples. In order to probe the conductivity of the Ag_2Se nanocrystal films, we fabricate a simple two terminal device. Figure 8.33a shows a schematic cross section of such a device. Films of nancorystals (~60-nm thick) were spin-coated from a dispersion of nanocrystals in chloroform onto Si/SiO_2 substrates that were prepatterned with source and drain electrodes (Cr/Au) similar to all the devices used in Chapters 4 and 5. Figures 8.33b and 8.33c show the current voltage (I-V) characteristics of these films at various temperatures. Since the films are insulating due to the bulky ligands attached on the nanocrystal surface, we hardly observe any current (~picoamperes) at room temperature until about 60 °C (Figure 8.33b). The conductivity of the sample can be measured from the slope of the I-V curves shown in Figures 8.33b and 8.33c. One can observe that as we raise the temperature, the slope goes on increasing steadily, thus implying an increase in the conductance of the film. Around 90 °C, the current increases to the order of nanoamperes and further heating raises the current levels by orders of magnitude. If we recall from our previous experiments, one would expect the onset of the phase transition around these temperatures. The current levels reach microamperes with further heating to about 130 °C and then saturates at that level. Any further increase in temperature leads to a marginal increase in current levels. Figure 8.33d plots the absolute value of current versus the voltage at various temperatures. We can observe that it is absolutely symmetric such that sweeping the voltage in either positive or negative direction gives similar results.

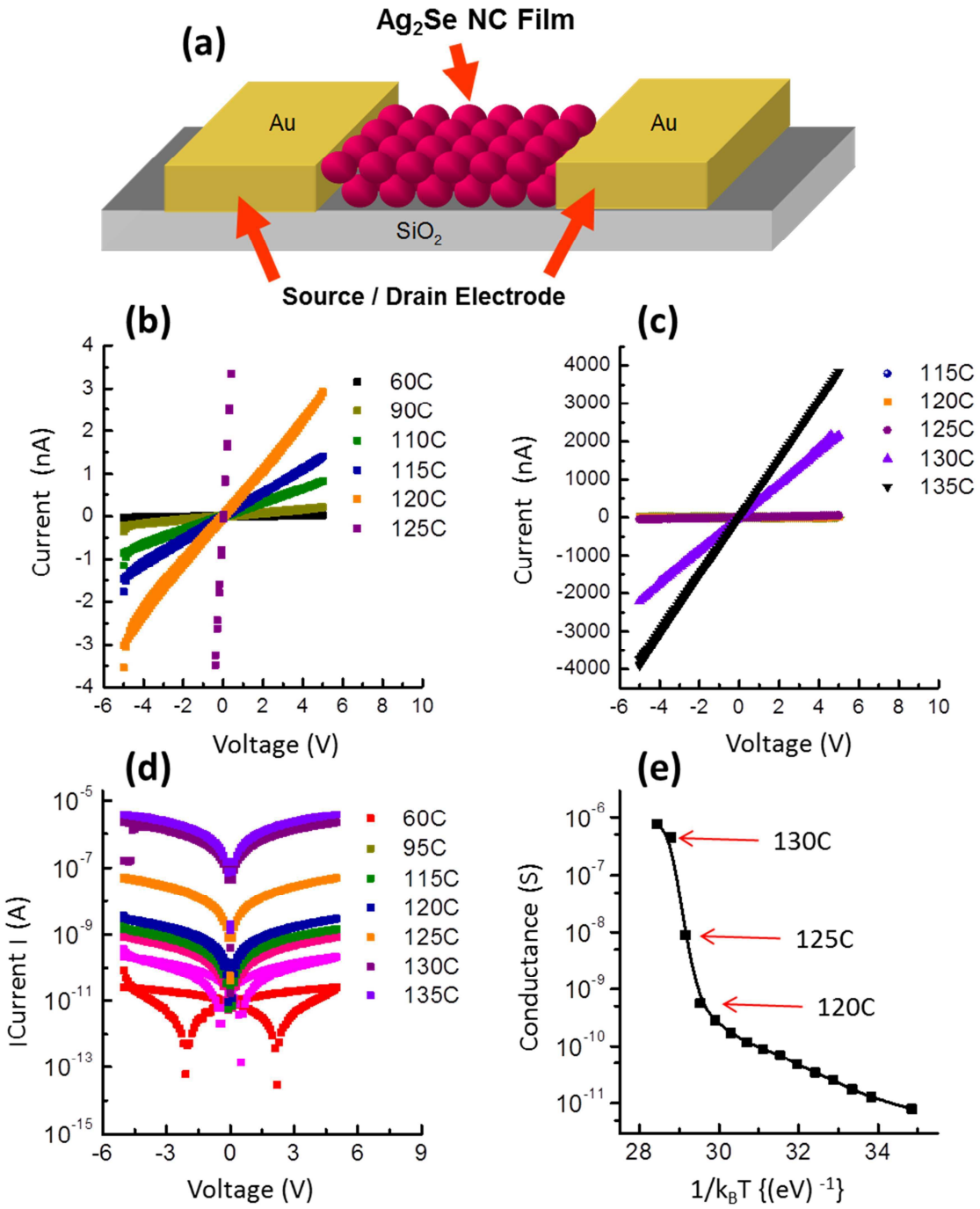

Figure 8.33: (a) Schematic cross section (not to scale) of two-terminal device structure used to characterize the electrical properties of ~7.5-nm OM-, TOP-, TOPO-capped Ag_2Se nanocrystals (NCs). The length and width of the channel were 50 μm and 1 mm, respectively. (b) and (c) Current-voltage characteristics of the nanocrystal film at different temperatures. (d) Absolute value of the current versus drain voltage at different temperatures. (e) Conductance of the nanocrystal film versus inverse temperature plotted as a log-linear plot. One can observe four orders of magnitude increase in the conductance due to the phase transition.

Finally, in Figure 8.33e, we calculate the conductance of the nanocrystal film and plot it against temperature inverse (log-linear plot). While we increase the conductance of the film by an order of magnitude when we heat the sample from room temperature to the onset of phase transition (~110-115 °C), during the phase transition (~120-130 °C) we increase it by almost four orders of magnitude. Note that the samples were heated from the bottom with a hot plate and hence, the temperatures recorded were not on the sample but the set point on the hot plate. There would exist a temperature difference between the bottom surface of the sample which is in contact with the hot plate and the top surface (nanocrystal film) which is exposed to ambient conditions (~25 °C). Hence, the difference in the phase-transition temperatures observed by the electrical measurements (~120 °C) and the XRD and DSC measurements (~100 °C) could be attributed to the fact that the actual film temperature in the electrical measurements is most likely lower than what we record from the hot plate. Thus, we observe huge increases in the conductivity due to the phase transition similar to what one would expect from bulk Ag_2Se. Plotting the logarithm of conductance against inverse temperature gives us a linear curve which shows that it is a thermally activated process. However, the net conductivity will be a sum of both the electrical and the ionic conductivity and we cannot decouple those from a simple two probe experiment. Moreover, our temperature range is way too narrow to extract a fit and investigate the transport mechanism. Regardless, converting the conductance to conductivity we find that after the phase transition, the conductivity of the sample is nearly 0.01 S/cm which is to the best of our knowledge, one of the highest obtained conductivity from any film of semiconductor nanocrystals without ligand exchange.

However, with a two probe measurement, one cannot be sure if the increase in conductance due to the phase transition can be attributed to a change in the conductance of the actual nanocrystal film or simply to a change in the contact resistance at the respective contacts. Since, the phase transition induces a change in the crystal structure and hence a change in the surface energy, what we observe might just be a surface effect at the contacts and would then have nothing to do with the actual electrical properties of the nanocrystal films. In order to address this issue, we proceed to conduct four-probe

measurements on our Ag_2Se nanocrystal films. Another way to circumvent this problem would be by fabricating thin-film transistors and studying their properties. However, with the bulky ligands, we were not able to make working transistors that were gateable. By performing a ligand exchange with short chain ligands, one would be able to get working transistors. However, even with mild heating, the films sinter and hence we lose the nanocrystalline character of the films. Thus, we proceed with four-probe measurements which allow us to decouple the actual film resistance from the contact resistance so that we can extract both values.

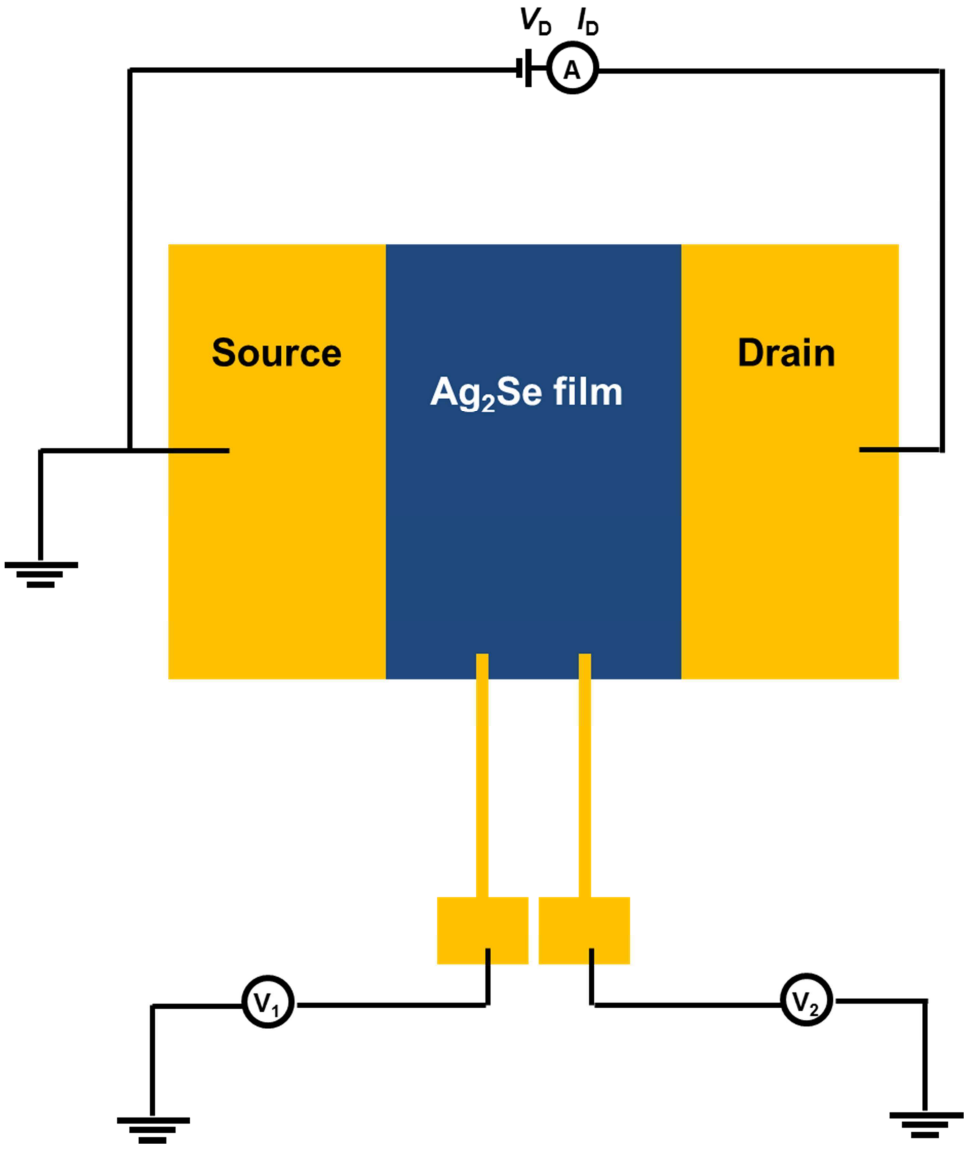

Figure 8.34: Circuit schematic for the four-probe measurement configuration. During I_D-V_D sweeps, the source electrode is held at ground as V_D is swept. The other two probes measure the potentials (V_1 and V_2) at two different regions in the channel.

We used a four-probe geometry proposed by Pesavento *et al.*.[58] Figure 8.34 shows a schematic for the four-terminal measurement configuration used. To minimize the probes' effect on the distribution of the electric field in the conductive channel, devices were fabricated with channel length and width, respectively, 30 and 10 times larger than the probe width and its penetration in the channel. We performed experiments with two different configurations. For the first set which we shall refer to as configuration 1, the length (L) of the channel was 300 μm and the width (W) was 2000 μm. The two additional probes were spaced apart by 100 μm each such that L_{V1} = 100 μm and L_{V2} = 200 μm. For the second set which we shall refer to as configuration 2, the length (L) of the channel was 450 μm and the width (W) was 1500 μm. The two additional probes were spaced apart by 150 μm each such that L_{V1} = 150 μm and L_{V2} = 300 μm. The two additional probes are meant to probe the potential at two intermediate points in the film away from the contacts. These were aligned such that they barely touched the nanocrystal film and did not penetrate the film so much that they start to affect the conduction. The penetration was kept less than 10% of the net channel width *i.e.* 200 μm for the first set and 150 μm for the second.

Films of Ag_2Se nanocrystals, typically ~100-nm thick, were spin coated onto these substrates. Electrical characterization of the films was carried out by sweeping the drain voltage (V_D) while keeping the source grounded (V_S = 0) and monitoring the drain current (I_D) as well as the potentials at the two probes (V_1 and V_2). These two probes allow us to monitor the channel potential at any two random points *in situ* while sweeping the drain voltage. Now, by linearly extrapolating the voltage difference across these two points, we can determine the expected potentials near the contacts. However, we do know the applied potentials at the contacts (V_D and V_S). Thus, we can calculate the potential drops at the contacts (ΔV_D and ΔV_S). Since we know the drain current (I_D), which is constant for a certain V_D, we can easily calculate the contact resistances at the drain (R_D) and the source (R_S) as well as the actual film resistance (R_F). In order to determine the actual sample temperature, we attached a thermocouple to the film. The film was scanned between -0.2 V to 0.2 V at a sweep speed of 0.01 V/s. Figure 8.35 shows the variation of the I_D-V_D curves with increasing temperature. As in the previous

two-terminal measurements, the curves are linear and their slope increases with increasing temperature thus implying an increase in the film conductivity.

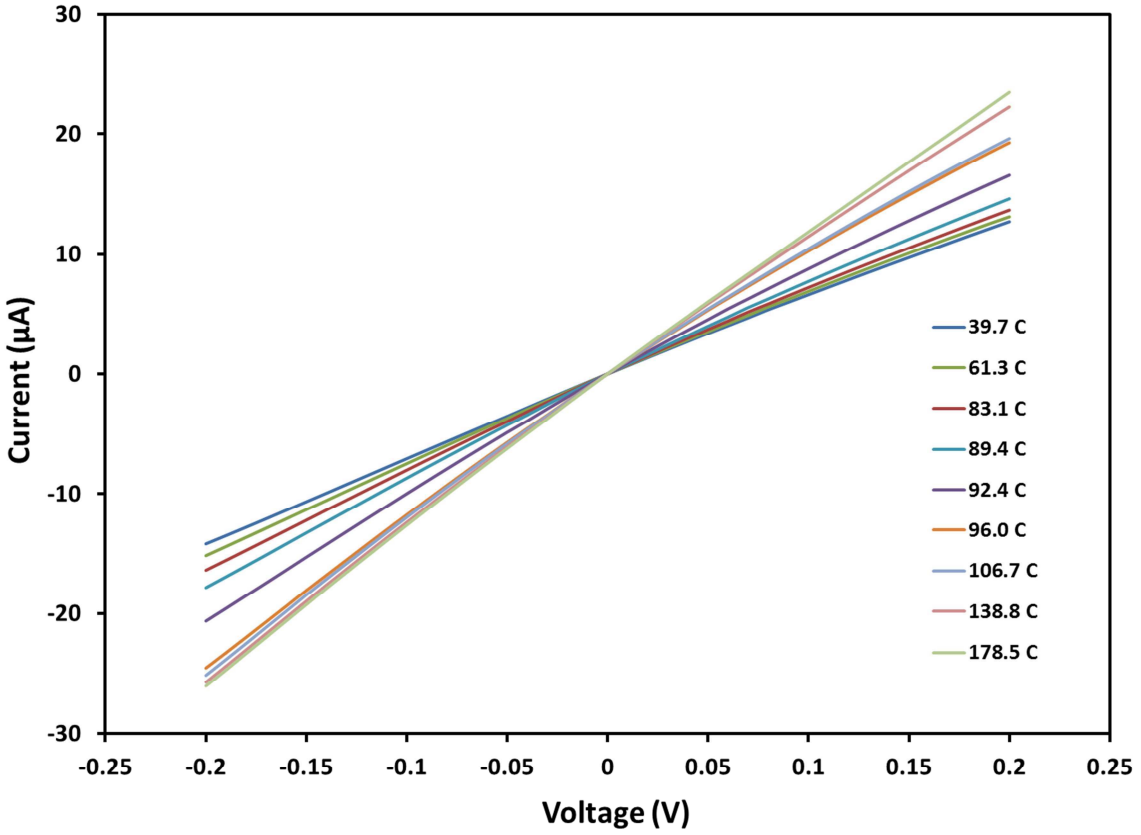

Figure 8.35: Current-voltage characteristics of the nanocrystal film at different temperatures.

At higher temperatures, since the temperature fluctuated a bit while taking the measurement, the slopes of the curves during the negative sweep are a little different from those during the positive sweep. Both temperatures were however recorded, and the temperatures indicated in the figure and all further analyses correspond to those during the positive sweep. As in Figure 8.32, the slope of the curves in Figure 8.35 increased significantly during the phase transition between 83.1 °C and 96 °C, and then plateaued with further increase in temperature. Now we proceed to calculate the actual film resistance and the contact resistances and compare those as a function of temperature. At room temperature, we obtain a film resistance (R_F) of 11.95 kΩ and a contact resistance of 3.23 kΩ (R_D) at the drain electrode while the contact resistance at the source was almost zero (since the source was grounded). In all further analyses, when we refer to the contact resistance, we shall be referring to R_D. We can observe that while R_D is much

lower than R_F, they are of the same order. So we need to be careful in our analyses taking into account the contact resistances whenever applicable.

With the current sample geometry (configuration 1) and assuming a film thickness of roughly 100-nm, we obtain a conductivity value of 1.03 S/cm at room temperature which is, to the best of our knowledge, a record conductivity value for any colloidal semiconductor nanocrystal system capped with bulky long chain ligands. Figure 8.36 plots the conductivity of the film as a function of the temperature for both the heating (forward) cycle as well as the cooling (reverse) cycle.

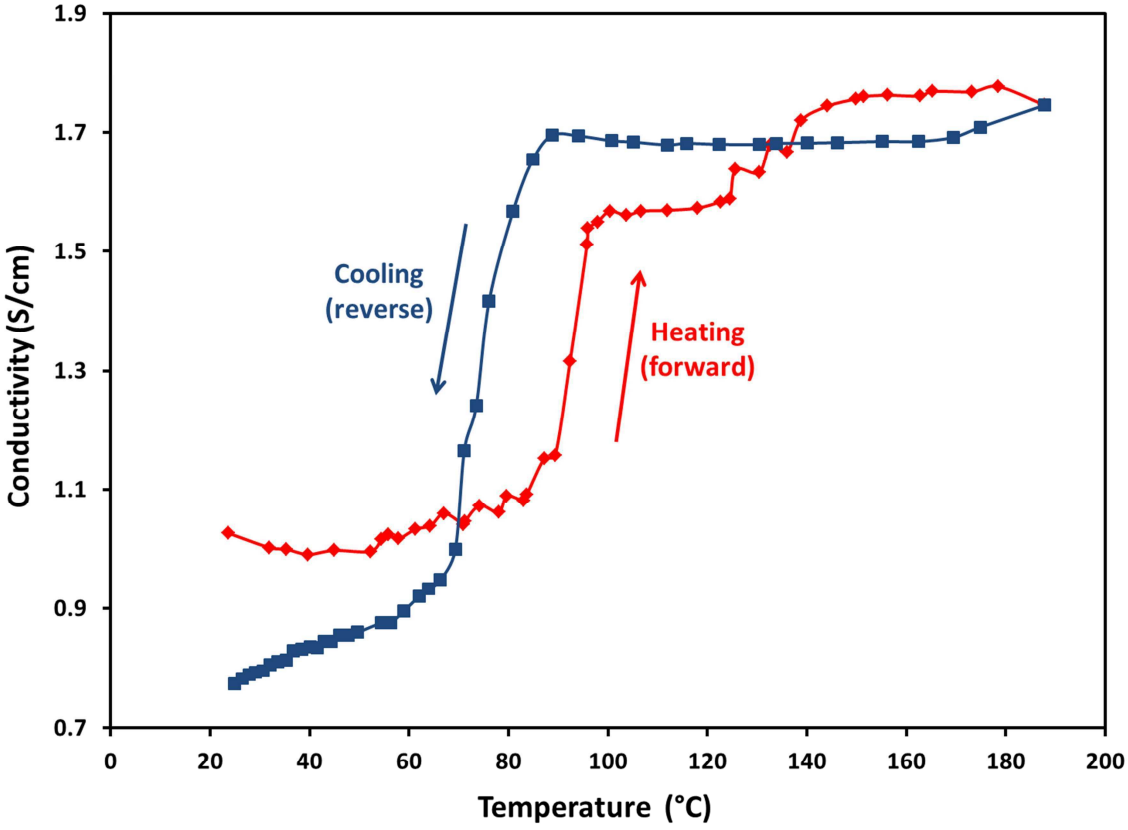

Figure 8.36: Change in film conductivity of the Ag_2Se nanocrystal film for the heating cycle (red) and the cooling cycle (blue) portraying the phase transition with configuration 1.

We can observe a sharp change in the conductivity of the film during the phase transition for both the forward and the reverse cycle. Also we observe a hysteresis in both the curves similar to that obtained from the DSC and the XRD data. Since we were heating using a hot plate, we were unable to control completely the heating rate. Hence,

the curve for the heating cycle is not smooth. However, the cooling was much better controlled and hence the data points lie on a smooth curve and we do not observe any spikes.

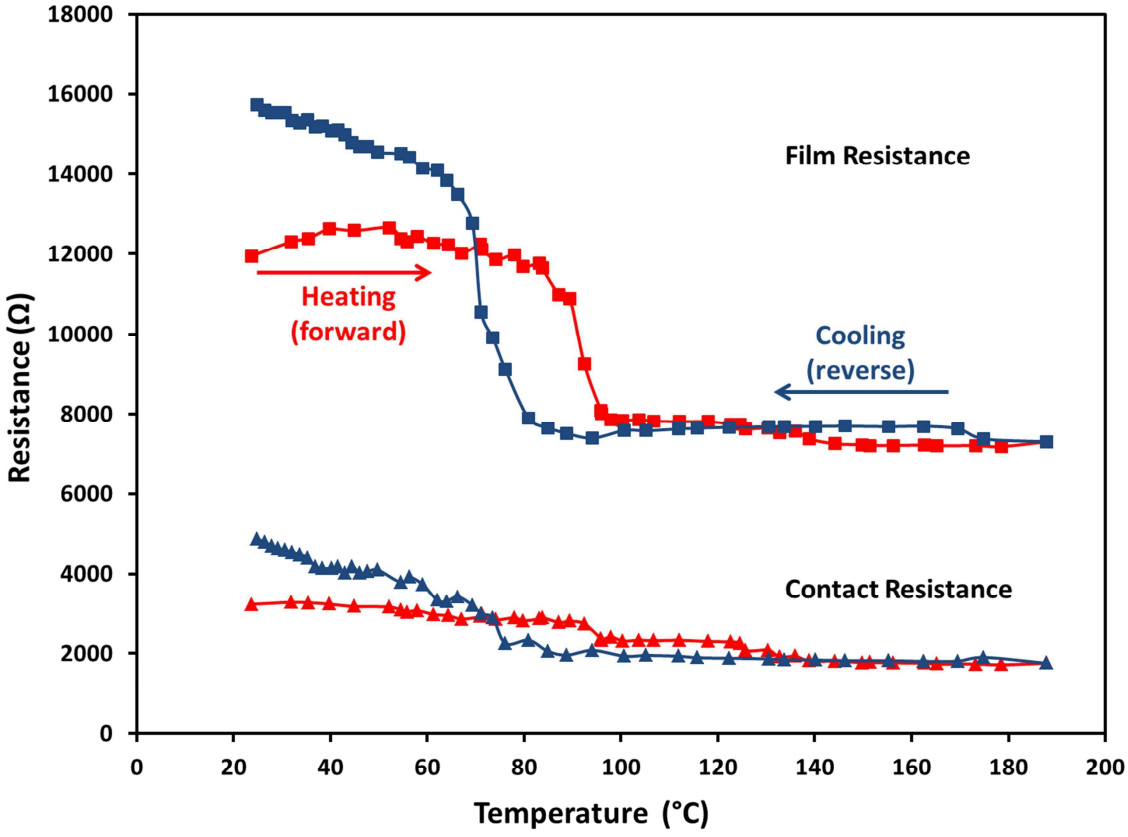

Figure 8.37: Change in film resistance (squares) and contact resistance (triangles) for the Ag_2Se nanocrystal film for the heating cycle (red) and the cooling cycle (blue) in configuration 1.

In Figure 8.37, we plot the film resistance and the contact resistances as a function of the sample temperature. We can observe that the contact resistances are much lower and systematically remain lower throughout the thermal cycle. Thus, the increase in conductivity can be attributed to changes in film resistance and is a property of Ag_2Se. We wanted to check if the increase in conductivity was consistent across other channels and hence, we repeated the experiment with configuration 2. Figure 8.38 plots the conductivity of the film as a function of the temperature for both the heating (forward) cycle as well as the cooling (reverse) cycle with a channel having configuration 2.

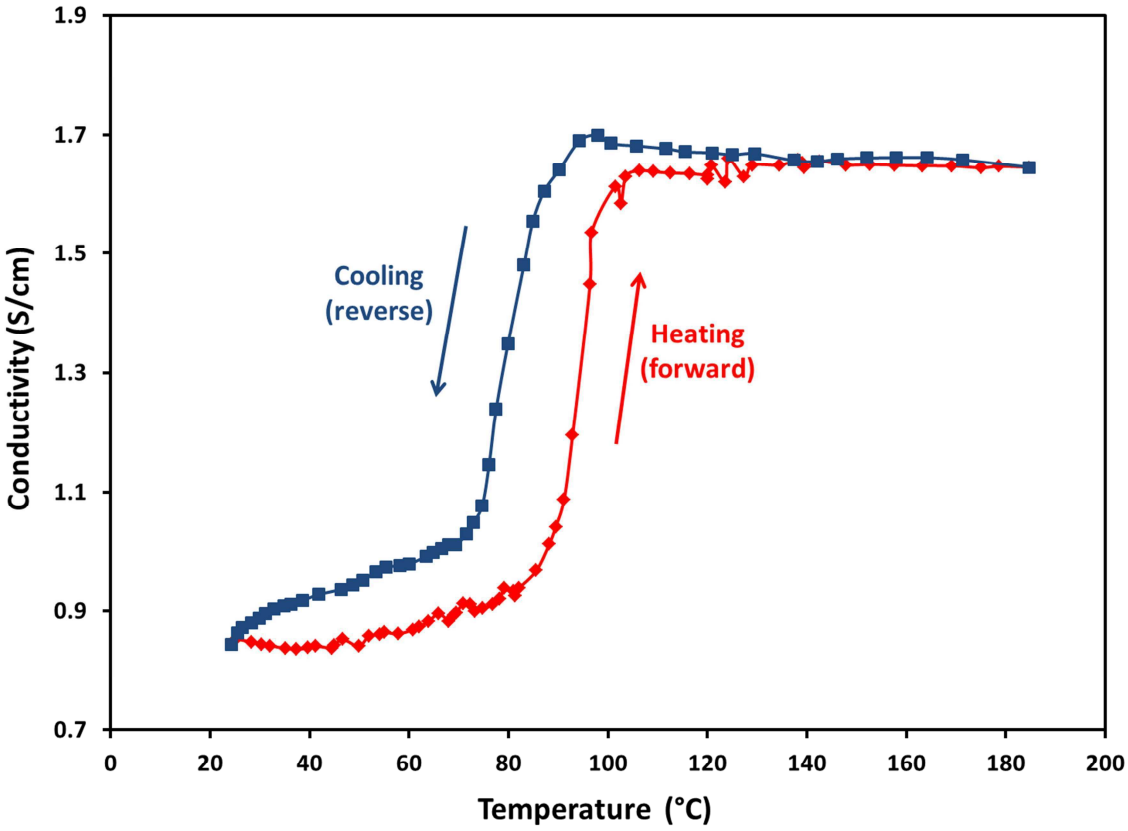

Figure 8.38: Change in film conductivity of the Ag_2Se nanocrystal film for the heating cycle (red) and the cooling cycle (blue) portraying the phase transition with configuration 2.

For configuration 2, we obtain almost exactly the same conductivities as we did with configuration 1 lending further credence to the fact that the observed trends are due to the inherent material property and do not depend on the geometry of the device. The heating cycle in this case was started immediately after the end of the cooling cycle with configuration 1. Hence, the room temperature conductivity we start with in this case is a little lower than that observed during the experiment with configuration 1.

Figure 8.39 plots the film and the contact resistances as a function of temperature. In configuration 2, we have a larger channel length of 450 μm as compared to that of 300 μm with configuration 1. Thus, we should observe a larger film resistance as can be seen in the figure. With increased channel lengths, the film resistance dominates the contact resistances and is higher than the contact resistances by nearly 20-40 times. With such an overwhelmingly high film resistance, the contact resistances have negligible effect on any

of the trends observed during the thermal cycles. Also, the phase transition has almost no effect on the contact resistances.

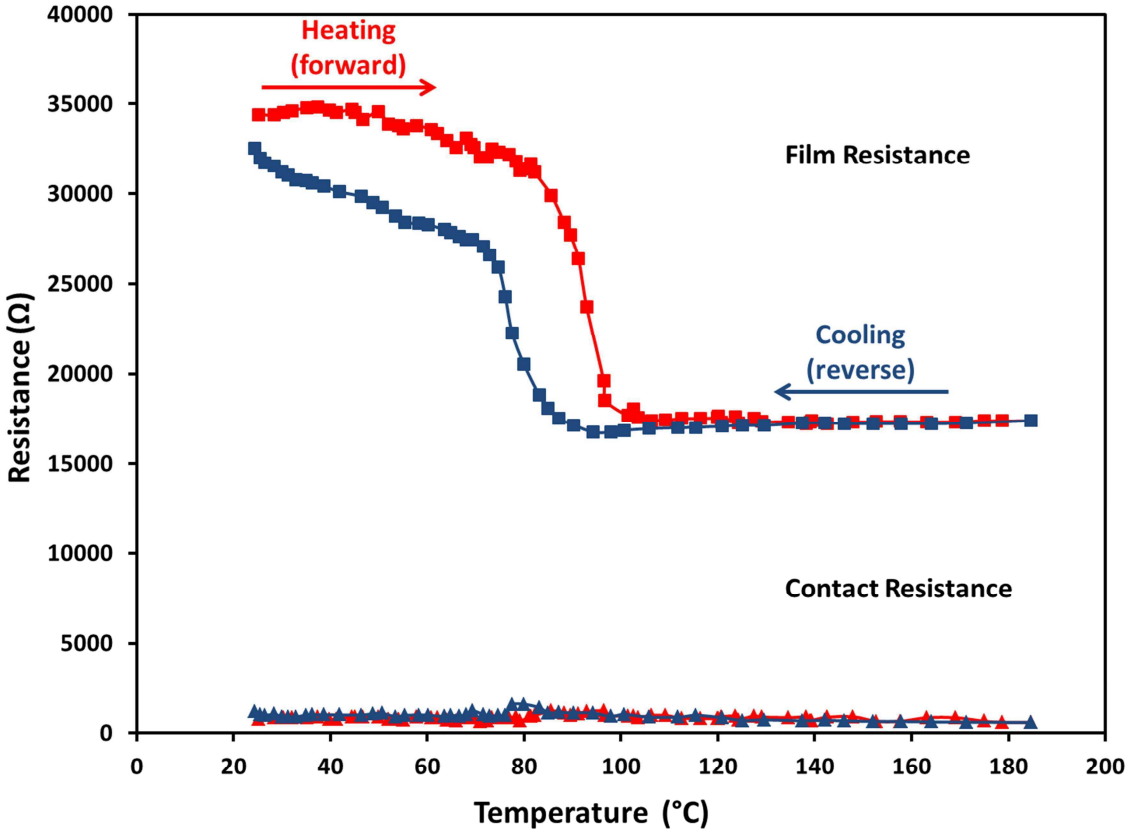

Figure 8.39: Change in film resistance (squares) and contact resistance (triangles) for the Ag_2Se nanocrystal film for the heating cycle (red) and the cooling cycle (blue) in configuration 2.

Figure 8.40 tries to correlate the changes in conductivity that we observe from the electrical measurements to the phase transitions observed from DSC measurements. Indeed, by plotting the resistance of the film versus the temperature, we observe two different regimes during the heating cycle and three regimes for the cooling cycle. During heating, we see a huge drop in the film resistance around 85 °C which continues until 100 °C, which would correspond to the transition from the tetragonal phase to the cubic phase (indicated by the red dotted line in Figure 8.40). In the cubic phase, the rigid lattice structure breaks down with the selenium atoms settling into a BCC lattice while all the silver atoms are free to move about in the lattice fluidly. This results in a huge increase in the ionic conductivity which probably leads to the decrease in the film resistance.

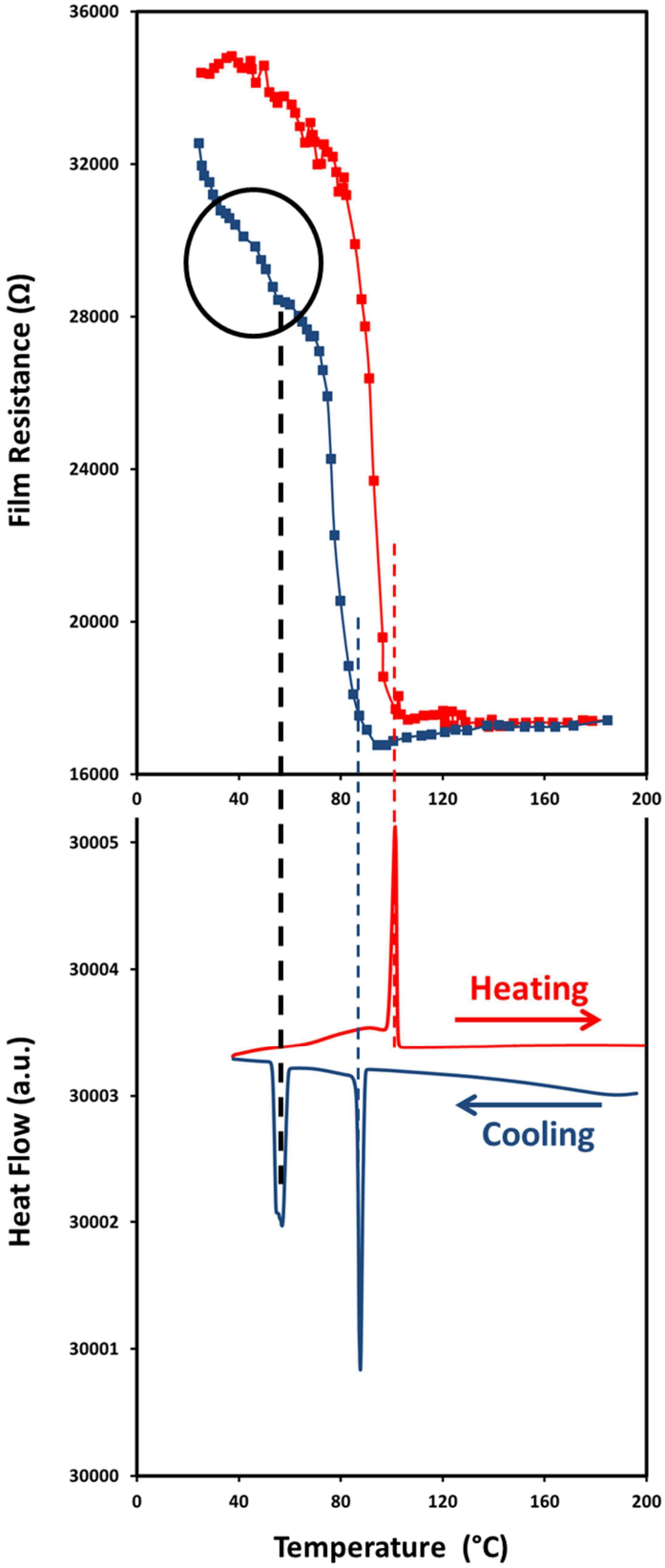

Figure 8.40: Correlation between changes in film resistance and phase transitions identified through DSC measurements for a thermal cycle in Ag_2Se nanocrystals.

However, in a nanocrystal, the ionic conductivity will be limited in the sense that howsoever fluid the Ag ions become, their motion will be restricted within the nanocrystal itself. Thus, there exists an upper bound to the increase in conductivity due to the free motion of the ions (unless the ions start to diffuse out of the nanocrystal into the neighboring nanocrystals which is highly unlikely since the crystals are separated by long ligands and this would lead to a breakdown in the entire shape and structure of the nanocrystals which would be non-recoverable). Once this bound is reached (say after the phase transition), any further increase in temperature cannot raise the conductivity any further and the conductivity starts to saturate. In fact, after a certain point, scattering might start to dominate within the nanocrystal and any further increase in temperature would probably lead to a decrease in conductivity. In our case, probably we hit this bound around 100 °C and then the conductivity is almost constant with temperature and in fact drops down a bit.

This effect is more pronounced during the cooling cycle, where we can clearly observe that as the temperature is decreased, the conductivity increases probably due to lower scattering between the ions. Upon cooling the sample even further, the ions are more and more restricted in their movement and this leads to a decrease in the conductivity. Around 85 °C, suddenly the phase changes from the cubic phase to the metastable tetragonal phase and the atoms are tied down to their respective sites. This leads to a sudden decrease in conductivity. Since the major drop in conductivity occurs around 85 °C, we postulate that this phase transition should correspond to the cubic-tetragonal transition as this structural transition would curb the ionic conductivity. Further cooling leads to a more subtle transition from the metastable tetragonal phase to the stable tetragonal phase. Since this transition corresponds to a minor change in the lattice positions of the atoms, there is no significant change in the conductivity. However, we can see that the trend of variation in conductivity with temperature is fairly different which leads us to believe that these are two separate phases with similar structures. Figure 8.41 summarizes the discussion into a chart where one can observe the different regimes in conductivities (represented as film resistance instead) correlated to the different phases with a variation in temperature.

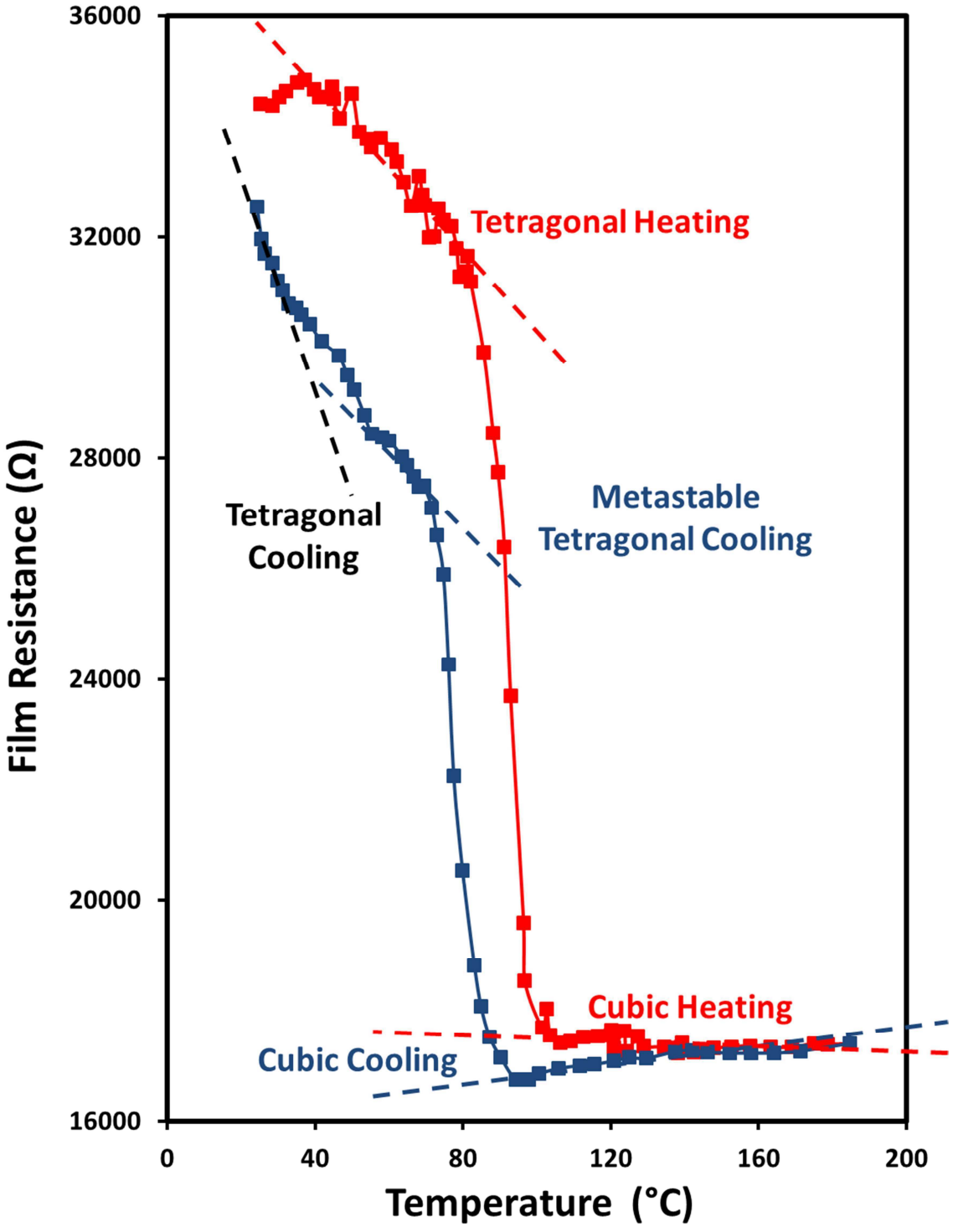

Figure 8.41: Trends of resistance of the film of Ag_2Se nanocrystals in various phases during a thermal cycle.

In order to have a better understanding of the conduction mechanism in the various phases, we need to fit a model to the data and extract the temperature dependence

of conductivity. From the above data, however, we can only extract the net conductivity of the film as a function of temperature in different phases. Since Ag_2Se behaves as a mixed conductor exhibiting both ionic and electronic conduction, we need to de-convolute both these parts and address them separately. Hence, we need to perform impedance spectroscopy in order to extract the ionic and the electronic contributions to the conductivity. With ongoing experiments involving impedance spectroscopy on these Ag_2Se nanocrystalline systems, very soon we shall be able to analyze the transport mechanism for these mixed conductors in the nanocrystalline regime.

8.4 EXPERIMENTAL SECTION

8.4.1 Chemicals and Substrates

Chloroform (HPLC grade, ≥99.8%), acetone (ACS spectrophotometric grade, ≥99.5%), tri-*n*-octylphosphine oxide (TOPO, technical grade, 90%), oleyl amine (OM, technical grade, 70%), octane (reagent grade, 98%), 1-octadecene (ODE, technical grade, 90%), octadecylamine (ODA, technical grade, 90%), hexadecylamine (HDA, technical grade, 90%), octane (reagent grade, 98%), oleic acid (OA, technical grade, 90%), selenium pellets (Se, 99.999%), selenium powder (Se, 99.999%), sodium hydroxide pellets, sulfur powder (S, 99.95%), poly (ethylene glycol) methyl ether (PEG, $M_n \sim 2000$, flakes), zinc diethyldithiocarbamate (97%), hexamethylene diisocyanate (HMDI, purum, ≥98%), diethyl ether (reagent grade, ≥98%) and tri-*n*-octylphosphine (TOP, technical grade, 90%) were purchased from Sigma-Aldrich. Hexanes (ACS grade) was purchased from VWR International. Isopropanol (IPA, ACS analytical grade) was purchased from Schlarlau Chemicals. Poly-ethyleneimine (PEI, branched, MW 600, 99%) was purchased from Alfa Aesar. Reagent alcohol (histological grade, 90% ethyl alcohol, 5% methyl alcohol, 5% butyl alcohol), methanol and butyl alcohol were obtained from Fisher Scientific. Cadmium (II) oxide (CdO, 99.999%) and silver nitrate ($AgNO_3$, 99.9995%) were purchased from Strem Chemicals. *n*-octadecyltrimethoxysilane (OTMS, 95%) was purchased from Gelest, Inc. All chemicals were used as delivered without further purification.

Circular sapphire windows, 12.7 mm (0.5") in diameter and 1.0 mm (0.040") thick, were purchased from Esco Products Inc. <100>-oriented, boron-doped silicon (Si) wafers (resistivity=0.005–0.01 Ωcm, thickness=525±25 μm) coated with 300 nm of thermal oxide (SiO_2) were purchased from Silicon Valley Microelectronics.

8.4.2 Sample Characterization

A Philips CM12 transmission electron microscope (TEM) was used to image the nanocrystals with an acceleration voltage of 100 kV. Films were prepared for X-ray diffraction (XRD) by drop-casting a dispersion of hydrophobic nanocrystals in an 8:1 hexane:octane mixture or hydrophilic nanocrystals dispersed in chloroform either on heavily doped Si wafers covered with a thermally grown 300-nm-thick SiO_2 layer or sapphire windows and the patterns (Cu-K_α) were collected using a Bruker D8 Advance diffractometer with a Lynks-eye detector and a heating stage which was constantly purged with nitrogen during the thermal cycling. Films of Ag_2Se nanocrystals were spin-coated from dispersions in chloroform on a heavily doped Si wafer covered with a thermally grown 300-nm-thick SiO_2 layer for electrical measurements. Measurements of the phase-transition temperatures were made on a TA Instruments STD 2960 differential scanning calorimeter under a nitrogen atmosphere. The apparatus was calibrated with indium (156.6 °C, 28.7 J/g) and tin (232.1 °C, 60.5 J/g).

8.4.3 Synthesis of OA-ODA-TOP-TOPO-capped Ag_2Se Nanocrystals[2]

In a typical synthesis, 16.99 g of $AgNO_3$ and 7.896 g of selenium shot are dissolved separately in 100 mL tri-*n*-octylphosphine (TOP) to obtain 1M Ag-TOP and 1M TOP-Se, respectively. A mixture of 6.4 mL oleic acid (OA), 5.4 g 1-octadecylamine (ODA), and 12.8 mL 1-octadecene (ODE) is then combined in a 100 mL round-bottom flask, degassed, flushed three times with N_2 to remove water and oxygen, and heated to 70 °C under N_2. With continuous stirring, 4 mL of TOP-Se is added into the flask and the temperature is raised to 160 °C. 4 mL of Ag-TOP is then quickly injected and the reaction is allowed to proceed for ~5 minutes at 150 °C. The growth is quenched in an ice bath and 25 ml of butanol is added to prevent solidification of the reaction mixture while

cooling. The nanocrystals are isolated by precipitating with ethanol and re-dispersing in hexanes. This process is repeated at least once to ensure a clean product.

8.4.4 Synthesis of OM-TOP-TOPO-capped Ag_2Se Nanocrystals[3]

A typical synthesis began by heating a mixture of 7.8 g of tri-octylphosphine oxide (TOPO) and 6.6 mL of oleylamine (OM) in a 50-mL round-bottom flask to 70 °C and degassing and flushing with N_2 three times. Simultaneously, 16.99 g of $AgNO_3$ and 7.896 g of selenium shot was dissolved in 100 mL tri-*n*-octylphosphine (TOP) to obtain 1M Ag-TOP and 1M TOP-Se, respectively, in a N_2-filled glovebox. 4 mL of TOP-Se was added to the flask and the temperature was raised to 150 °C. 4 mL of Ag-TOP was then quickly injected into the rapidly stirring mixture and the reaction was allowed to proceed for ~4 minutes at 140 °C. The growth was quenched in a water bath and 20 ml of butanol was added to prevent solidification of the reaction mixture while cooling. The nanocrystals were precipitated with ethanol and re-dispersed in hexanes. This precipitation was repeated at least twice to remove all unreacted oleylamine. No additional size-selection was used.

8.4.5 Synthesis of HDA-capped Ag_2Se Nanocrystals

The synthesis is adapted from a recipe proposed by Wang *et al*.[59] In a typical synthesis, 7.7 g of HDA was heated to 180 °C in a 50-mL round-bottom flask. 0.5 g of $AgNO_3$ was added to the flask with rapid stirring. The reaction was allowed to proceed for ~5 minutes at 180 °C, following which 0.12 g of Se powder was added to the mixture. After 10 minutes, the growth is quenched in a water bath and 20 mL of toluene is added to prevent solidification of the reaction mixture while cooling. The nanocrystals are precipitated with methanol and re-dispersed in toluene. The precipitation is repeated at least thrice to remove all unreacted HDA.

8.4.6 Synthesis of ODA-capped Ag_2Se Nanocrystals

The synthesis is adapted from a recipe proposed by Wang *et al*.[59] In a typical synthesis, 8.6 g of ODA was heated to 180 °C in a 50-mL round-bottom flask. 0.5 g of $AgNO_3$ was added to the flask with rapid stirring. The reaction was allowed to proceed

for 10 minutes at 180 °C, following which 0.12 g of Se powder was added to the mixture. After 10 minutes, the growth is quenched in a water bath and 20 mL of toluene is added to prevent solidification of the reaction mixture while cooling. The nanocrystals are precipitated with methanol and re-dispersed in toluene. The precipitation is repeated at least thrice to remove all unreacted ODA.

8.4.7 Ligand Exchange with Sodium Hydroxide

Films of Ag_2Se nanocrystals were drop-cast from highly concentrated dispersions in hexanes on sapphire discs. These films were then dipped into 20 mL of 0.08 M sodium hydroxide (NaOH) in methanol for at least 30 minutes followed by rinsing in pure methanol to remove any unbound NaOH and the bulky ligands that were replaced by NaOH.

8.4.8 Ligand Exchange with Bulky Polymeric Ligands

The first step in the ligand exchange involved synthesizing these ligands. The synthesis is adapted from a recipe put forth by Nikolic *et al*.[60,61] 2.22 g of PEG is dissolved in 20 mL of chloroform in a 50-mL round-bottom flask. 4.5 mL of HMDI is then added to and the mixture is refluxed for 24 hours at 63.5 °C with rapid stirring. The mixture turns yellow after a few hours. Following 24 hours of reflux, it is cooled down to room temperature and mixed with nearly 180 mL of cold diethylether to precipitate the complex and then re-dispersed in chloroform. The cleaning procedure is repeated twice to remove any reactants that have not formed the requisite complex. After the final round of precipitation, the precipitate is dried and dissolved in 20 mL chloroform. 2 mL of PEI is added to it and the mixture is again refluxed for 24 hours at 56 °C with rapid stirring to form the PEG-PEI complex. As earlier, cold diethylether is used to precipitate the complex. After cleaning at least twice, the precipitate is dissolved in chloroform and stored as such in the glove box.

For the ligand exchange, the nanocrystals with hydrophobic ligands are dispersed in chloroform. Assuming that the entire surface of the nanocrystal is covered by these ligands, the amount of polymeric ligands needed to cap the sample of nanocrystals is

calculated. An excess of ligands corresponding to nearly 5 times the required amount are added to the nanocrystals in chloroform and rapidly stirred for nearly 5 minutes. The ligand exchange is usually complete within a minute or two. The nanocrystals are then precipitated out by adding large amounts of hexanes followed by re-dispersion in chloroform. The cleaning procedure with hexanes is carried out at least a couple of times to clean out all the original hydrophobic ligands. Finally, the polymer-capped nanocrystals are precipitated in any polar solvent like methanol, chloroform or water.

8.4.9 Synthesis of Dot-in-Rod Ag_2Se-CdS Nanocrystals

0.308 g CdO is added to 6 mL OA and 54 mL ODE in a 100-mL flask, degassed 3 times at 40 °C with rapid stirring and then heated to 250 °C for ~ 30 minutes to form a 0.04 M cadmium-oleate complex. The complex is cooled down to nearly 80 °C and kept stirring at that temperature. 77 mg sulfur is added to 60 mL ODE, degassed 3 times at °C with rapid stirring, and then heated to 180 °C for ~ 30 minutes to form the 0.04 M S-ODE complex. Typically, 1-2 μmol of as-synthesized Ag_2Se nanocrystals are mixed with 37.5 mL of ODE and 9 g ODA in a 250-mL round-bottom flask, flushed with nitrogen for nearly an hour at 70 °C and then the mixture is heated to 150 °C. The amount of Cd- and S-precursors required to grow one monolayer on the Ag_2Se nanocrystals are calculated (depending on the size of the nanocrystals and the amount in the reaction flask). First, the Cd-oleate precursor is added and the mixture is heated to 200 °C and allowed to progress for nearly 15 minutes. It is then cooled back to 150 °C following which the S-ODE precursor is added. Again, the mixture is heated to 200 °C and allowed to progress for 15 minutes. Depending on how many shells need to be grown, one can go back and forth numerous times. Finally, the reaction is quenched in a water bath and nearly 20 mL butanol is added to prevent the mixture from solidifying while cooling. The nanocrystals are precipitated out by adding ethanol and then re-dispersed in hexanes. The cleaning procedure is carried out at least a couple of times to ensure a clean product.

8.4.10 Synthesis of Core-Shell Ag_2Se-ZnS Nanocrystals

Depending on the amount of Ag_2Se nanocrystals used and the desired thickness of the ZnS shell, the number of moles of zinc required is calculated. Since each mole of zinc

diethyldithiocarbamate provides one mole of ZnS, the quantity of the dithiocarbamate needed is obtained. The requisite quantity of the dithiocarbamate is added to a round-bottom flask containing the Ag_2Se nanocrystals and a mixture of 20 mL ODE, 8 mL OM and 6 mL TOP and flushed with nitrogen for ~ 30 minutes. Then the mixture is heated under nitrogen slowly to 120 °C over the course of an hour. Once the temperature reaches 120 °C, it is kept steady at that temperature for nearly an hour and then cooled back to room temperature. The shell thickness can be varied by adding more dithiocarbamate or increasing the reaction time to about 3 hours. The nanocrystals are cleaned by adding 20 mL butanol, 30 mL acetone and 20 mL ethanol. The precipitate is re-dispersed in hexanes and cleaned again with ethanol. One more round of re-dispersion in hexanes and precipitation with ethanol gives a clean sample of nanocrystals.

8.4.11 Conductivity Measurements

For the conductivity measurements, Si/SiO_2 wafers, with prepatterned source, drain, and gate electrodes, were rinsed with acetone, isopropanol, and methanol, followed by UV/ozone cleaning for 10 minutes. A 3 mM OTMS solution in trichloroethylene was spin-coated onto these wafers (3000 rpm for 10 seconds). The wafers were then vapor annealed in ammonium hydroxide solution (28–30% in water) overnight, followed by rinsing with DI water and sonication in toluene. As prepared OTMS-treated wafers were brought into a nitrogen glove box. The self-assembled monolayer on the Si/SiO_2 surface improves the morphological characteristics of the nanocrystal-based thin films and a better adhesion on the substrate surface. Inside the glove box, Ag_2Se nanocrystal films were spin-coated (30 seconds at 1700 rpm) from a 30 mg/mL dispersion of Ag_2Se NCs in chloroform passed through a 0.2 μm PTFE filter. The films were dried at 80 °C for 3 minutes and then at room temperature for more than 3 hours under nitrogen.

Electrical characterizations were performed in air with a Keithley 4200 semiconductor parameter analyzer equipped with two 4200-PA remote pre-amplifiers. The sample was placed on a hot-plate and its temperature was carefully monitored with a K-type Kapton insulated thermocouple placed on the substrate surface. Linear current-voltage characteristics were recorded between ± 0.2 V as a function of the temperature

with temperature steps of ΔT = 1-5 K in both forward and reverse temperature scans, in order to monitor the temperature stability of the device. The scan rate was 10 mV/s. The conductivity was determined from the linear *I-V* relationship in the bias voltage range of -0.0 V to 0.1 V. The voltage sweep was applied to the drain electrode while the source electrode was grounded.

8.5 REFERENCES

(1) Sahu, A.; Kang, M. S.; Kompch, A.; Notthoff, C.; Wills, A. W.; Deng, D.; Winterer, M.; Frisbie, C. D.; Norris, D. J. *Nano Letters* **2012**, *12*, 2587.

(2) Sahu, A.; Qi, L.; Kang, M. S.; Deng, D.; Norris, D. J. *Journal of the American Chemical Society* **2011**, *133*, 6509.

(3) Sahu, A.; Khare, A.; Deng, D. D.; Norris, D. J. *Chemical Communications* **2012**, *48*, 5458.

(4) Buffat, P.; Borel, J. P. *Physical Review A* **1976**, *13*, 2287.

(5) Efros, A. L.; Efros, A. L. *Soviet Physics Semiconductors - USSR* **1982**, *16*, 772.

(6) Brus, L. E. *Journal of Chemical Physics* **1983**, *79*, 5566.

(7) Goldstein, A. N.; Echer, C. M.; Alivisatos, A. P. *Science* **1992**, *256*, 1425.

(8) Murray, C. B.; Kagan, C. R.; Bawendi, M. G. *Annual Review of Material Science* **2000**, *30*, 545.

(9) Rao, C. N. R.; Rao, K. J. *Phase Transitions in Solids*; McGraw-Hill: New York, 1978.

(10) Ehrenfest, P. *Proceedings of the Koninklijke Akademie Van Wetenschappen Te Amsterdam* **1933**, *36*, 153.

(11) Smoluchowski, R. *Phase Transformations in Solids*; Wiley: New York, NY, 1951.

(12) Gribb, A. A.; Banfield, J. F. *American Mineralogist* **1997**, *82*, 717.

(13) Tolbert, S. H.; Alivisatos, A. P. *Science* **1994**, *265*, 373.

(14) McHale, J. M.; Auroux, A.; Perrotta, A. J.; Navrotsky, A. *Science* **1997**, *277*, 788.

(15) Tolbert, S. H.; Alivisatos, A. P. *Annual Review of Physical Chemistry* **1995**, *46*, 595.

(16) Rivest, J. B.; Fong, L. K.; Jain, P. K.; Toney, M. F.; Alivisatos, A. P. *Journal of Physical Chemistry Letters* **2011**, *2*, 2402.

(17) Li, H.; Zanella, M.; Genovese, A.; Povia, M.; Falqui, A.; Giannini, C.; Manna, L. *Nano Letters* **2011**, *11*, 4964.

(18) Garvie, R. C.; Goss, M. F. *Journal of Materials Science* **1986**, *21*, 1253.

(19) Garvie, R. C.; Swain, M. V. *Journal of Materials Science* **1985**, *20*, 1193.

(20) Garvie, R. C. *Journal of Physical Chemistry* **1978**, *82*, 218.

(21) Chraska, T.; King, A. H.; Berndt, C. C.; Karthikeyan, J. Phase Transformation as a Function of Particle Size in Nanocrystalline Zirconia. In *Phase Transformations and Systems Driven Far from Equilibrium*; Materials Research Society: Warrendale, 1998; Vol. 481; pp 613.

(22) Chraska, T.; King, A. H.; Berndt, C. C. *Materials Science and Engineering A-Structural Materials Properties Microstructure and Processing* **2000**, *286*, 169.

(23) Akdogan, E. K.; Mayo, W.; Safari, A.; Rawn, C. J.; Payzant, E. A. *Ferroelectrics* **1999**, *223*, 11.

(24) Alivisatos, A. P. *Berichte Der Bunsen-Gesellschaft - Physical Chemistry Chemical Physics* **1997**, *101*, 1573.

(25) Begg, B. D.; Vance, E. R.; Nowotny, J. *Journal of the American Ceramic Society* **1994**, *77*, 3186.

(26) Skandan, G.; Hahn, H.; Roddy, M.; Cannon, W. R. *Journal of the American Ceramic Society* **1994**, *77*, 1706.

(27) Schlag, S.; Eicke, H. F. *Solid State Communications* **1994**, *91*, 883.

(28) Sato, H.; Kitakami, O.; Sakurai, T.; Shimada, Y.; Otani, Y.; Fukamichi, K. *Journal of Applied Physics* **1997**, *81*, 1858.

(29) Nitsche, R.; Winterer, M.; Hahn, H. *Nanostructured Materials* **1995**, *6*, 679.

(30) Rossetti, G. A.; Cline, J. P.; Navrotsky, A. *Journal of Materials Research* **1998**, *13*, 3197.

(31) Winterer, M.; Nitsche, R.; Redfern, S. A. T.; Schmahl, W. W.; Hahn, H. *Nanostructured Materials* **1995**, *5*, 679.

(32) Zhang, H. Z.; Banfield, J. F. Phase Stability in the Nanocrystalline TiO_2 System. In *Phase Transformations and Systems Driven Far from Equilibrium*; Materials Research Society: Warrendale, 1998; Vol. 481; pp 619.

(33) Zhang, H. Z.; Banfield, J. F. *Journal of Physical Chemistry B* **2000**, *104*, 3481.

(34) Zhang, H. Z.; Banfield, J. F. *Journal of Materials Chemistry* **1998**, *8*, 2073.

(35) Suresh, A.; Mayo, M. J.; Porter, W. D. *Journal of Materials Research* **2003**, *18*, 2912.

(36) Ji, Z.; Haynes, J. A.; Ferber, M. K.; Rigsbee, J. M. *Surface & Coatings Technology* **2001**, *135*, 109.

(37) Frey, M. H.; Payne, D. A. *Physical Review B* **1996**, *54*, 3158.

(38) Chen, C. C.; Herhold, A. B.; Johnson, C. S.; Alivisatos, A. P. *Science* **1997**, *276*, 398.

(39) Luther, J. M.; Zheng, H. M.; Sadtler, B.; Alivisatos, A. P. *Journal of the American Chemical Society* **2009**, *131*, 16851.

(40) Pietryga, J. M.; Werder, D. J.; Williams, D. J.; Casson, J. L.; Schaller, R. D.; Klimov, V. I.; Hollingsworth, J. A. *Journal of the American Chemical Society* **2008**, *130*, 4879.

(41) Sadtler, B.; Demchenko, D. O.; Zheng, H.; Hughes, S. M.; Merkle, M. G.; Dahmen, U.; Wang, L. W.; Alivisatos, A. P. *Journal of the American Chemical Society* **2009**, *131*, 5285.

(42) Xi, B. J.; Xiong, S. L.; Xu, D. C.; Li, J. F.; Zhou, H. Y.; Pan, J.; Li, J. Y.; Qian, Y. T. *Chemistry - A European Journal* **2008**, *14*, 9786.

(43) Liu, S. Y.; Choy, W. C. H.; Jin, L.; Leung, Y. P.; Zheng, G. P.; Wang, J. B.; Soh, A. K. *Journal of Physical Chemistry C* **2007**, *111*, 9055.

(44) Reiss, P. *New Journal of Chemistry* **2007**, *31*, 1843.

(45) Kang, M. S.; Sahu, A.; Norris, D. J.; Frisbie, C. D. *Nano Letters* **2010**, *10*, 3727.

(46) Gates, B.; Mayers, B.; Wu, Y. Y.; Sun, Y. G.; Cattle, B.; Yang, P. D.; Xia, Y. N. *Advanced Functional Materials* **2002**, *12*, 679.

(47) Okabe, T.; Ura, K. *Journal of Applied Crystallography* **1994**, *27*, 140.

(48) Zheng, H.; Rivest, J. B.; Miller, T. A.; Sadtler, B.; Lindenberg, A.; Toney, M. F.; Wang, L.-W.; Kisielowski, C.; Alivisatos, A. P. *Science* **2011**, *333*, 206.

(49) Yin, K. B.; Xia, Y. D.; Liu, Z. G.; Yin, J.; Sun, L. T. *Physica Status Solidi A - Applications and Materials Science* **2012**, *209*, 135.

(50) Makiura, R.; Yonemura, T.; Yamada, T.; Yamauchi, M.; Ikeda, R.; Kitagawa, H.; Kato, K.; Takata, M. *Nature Materials* **2009**, *8*, 476.

(51) Hines, M. A.; Guyot-Sionnest, P. *Journal of Physical Chemistry* **1996**, *100*, 468.

(52) Li, J. J.; Wang, Y. A.; Guo, W. Z.; Keay, J. C.; Mishima, T. D.; Johnson, M. B.; Peng, X. G. *Journal of the American Chemical Society* **2003**, *125*, 12567.

(53) Dethlefsen, J. R.; Dossing, A. *Nano Letters* **2011**, *11*, 1964.

(54) Tangirala, R.; Baker, J. L.; Alivisatos, A. P.; Milliron, D. J. *Angewandte Chemie - International Edition* **2010**, *49*, 2878.

(55) Leon, V.; Ren, Y.; Saboungi, M.-L. *Journal of Applied Physics* **2008**, *103*, 016105.

(56) Jackson, C. L.; McKenna, G. B. *Journal of Chemical Physics* **1990**, *93*, 9002.

(57) Alba-Simionesco, C.; Dosseh, G.; Dumont, E.; Frick, B.; Geil, B.; Morineau, D.; Teboul, V.; Xia, Y. *European Physical Journal E* **2003**, *12*, 19.

(58) Pesavento, P. V.; Chesterfield, R. J.; Newman, C. R.; Frisbie, C. D. *Journal of Applied Physics* **2004**, *96*, 7312.

(59) Wang, D.; Xie, T.; Peng, Q.; Li, Y. *Journal of the American Chemical Society* **2008**, *130*, 4016.

(60) Nikolic, M. S.; Krack, M.; Aleksandrovic, V.; Kornowski, A.; Forster, S.; Weller, H. *Angewandte Chemie - International Edition* **2006**, *45*, 6577.

(61) Nikolic, M. S.; Olsson, C.; Salcher, A.; Kornowski, A.; Rank, A.; Schubert, R.; Fromsdorf, A.; Weller, H.; Forster, S. *Angewandte Chemie-International Edition* **2009**, *48*, 2752.

BIBLIOGRAPHY

(1) Abdullayev, A. G.; Shafizade, R. B.; Krupnikov, E. S.; Kiriluk, K. V. *Thin Solid Films* **1983**, *106*, 175.

(2) Akdogan, E. K.; Mayo, W.; Safari, A.; Rawn, C. J.; Payzant, E. A. *Ferroelectrics* **1999**, *223*, 11.

(3) Alba-Simionesco, C.; Dosseh, G.; Dumont, E.; Frick, B.; Geil, B.; Morineau, D.; Teboul, V.; Xia, Y. *European Physical Journal E* **2003**, *12*, 19.

(4) Alivisatos, A. P. *Science* **1996**, *271*, 933.

(5) Alivisatos, A. P. *Berichte Der Bunsen-Gesellschaft - Physical Chemistry Chemical Physics* **1997**, *101*, 1573.

(6) Ashcroft, N. W.; Mermin, N. D. *Solid State Physics*; Saunders College Publ.: Fort Worth; Philadelphia; San Diego [etc.], 1976.

(7) Avinor, M.; Meijer, G. *Journal of Chemical Physics* **1960**, *32*, 1456.

(8) Baer, Y.; Frohlich, C.; Steigmeier, E.; Busch, G. *Zeitschrift Fur Naturforschung Part A - Astrophysik Physik Und Physikalische Chemie* **1962**, *A 17*, 886.

(9) Baranovski, S. *Charge Transport in Disordered Solids with Applications in Electronics*; Wiley: Chichester, England; Hoboken, NJ, 2006.

(10) Barber, D. J.; Freestone, I. C. *Archaeometry* **1990**, *32*, 33.

(11) Battaglia, D.; Peng, X. G. *Nano Letters* **2002**, *2*, 1027.

(12) Begg, B. D.; Vance, E. R.; Nowotny, J. *Journal of the American Ceramic Society* **1994**, *77*, 3186.

(13) Bhargava, R. N.; Gallagher, D.; Hong, X.; Nurmikko, A. *Physical Review Letters* **1994**, *72*, 416.

(14) Bhattacharya, P.; Ghosh, S.; Stiff-Roberts, A. D. *Annual Review of Materials Research* **2004**, *34*, 1.

(15) Bimberg, D.; Grundmann, M.; Ledentsov, N. N. *MRS Bulletin* **1998**, *23*, 31.

(16) Boettcher, A.; Haase, G.; Treupel, H. *Zeitschrift Fur Angewandte Physik* **1955**, *7*, 478.

(17) Boolchand, P.; Bresser, W. J. *Nature* **2001**, *410*, 1070.

(18) Brovelli, S.; Galland, C.; Viswanatha, R.; Klimov, V. I. *Nano Letters* **2012**, *12*, 4372.

(19) Bruchez, M., Jr.; Moronne, M.; Gin, P.; Weiss, S.; Alivisatos, A. P. *Science* **1998**, *281*, 2013.

(20) Brus, L. *Applied Physics A - Materials Science & Processing* **1991**, *53*, 465.

(21) Brus, L. *Journal of Physics and Chemistry of Solids* **1998**, *59*, 459.

(22) Brus, L. E. *Journal of Chemical Physics* **1983**, *79*, 5566.

(23) Brus, L. E. *Journal of Chemical Physics* **1984**, *80*, 4403.

(24) Bryan, J. D.; Gamelin, D. R. Doped Semiconductor Nanocrystals: Synthesis, Characterization, Physical Properties, and Applications. In *Progress in Inorganic Chemistry, Vol 54*, 2005; Vol. 54; pp 47.

(25) Buffat, P.; Borel, J. P. *Physical Review A* **1976**, *13*, 2287.

(26) Buonsanti, R.; Llordes, A.; Aloni, S.; Helms, B. A.; Milliron, D. J. *Nano Letters* **2011**, *11*, 4706.

(27) Cardona, M.; Yu, P. Y. *Fundamentals of Semiconductors*; Springer-Verlag Berlin Heidelberg: [New York], 2005.

(28) Chadi, D. J. *Annual Review of Materials Science* **1994**, *24*, 45.

(29) Chamonal, J. P.; Molva, E.; Pautrat, J. L.; Revoil, L. *Journal of Crystal Growth* **1982**, *59*, 297.

(30) Chan, W. C. W.; Nie, S. M. *Science* **1998**, *281*, 2016.

(31) Chen, C. C.; Herhold, A. B.; Johnson, C. S.; Alivisatos, A. P. *Science* **1997**, *276*, 398.

(32) Chiang, C. K.; Druy, M. A.; Gau, S. C.; Heeger, A. J.; Louis, E. J.; Macdiarmid, A. G.; Park, Y. W.; Shirakawa, H. *Journal of the American Chemical Society* **1978**, *100*, 1013.

(33) Cho, J. H.; Lee, J.; Xia, Y.; Kim, B.; He, Y. Y.; Renn, M. J.; Lodge, T. P.; Frisbie, C. D. *Nature Materials* **2008**, *7*, 900.

(34) Chraska, T.; King, A. H.; Berndt, C. C. *Materials Science and Engineering A - Structural Materials Properties Microstructure and Processing* **2000**, *286*, 169.

(35) Chraska, T.; King, A. H.; Berndt, C. C.; Karthikeyan, J. Phase Transformation as a Function of Particle Size in Nanocrystalline Zirconia. In *Phase Transformations and Systems Driven Far from Equilibrium*; Materials Research Society: Warrendale, 1998; Vol. 481; pp 613.

(36) Coe, S.; Woo, W. K.; Bawendi, M.; Bulovic, V. *Nature* **2002**, *420*, 800.

(37) Cohen-Tannoudji, C.; Diu, B.; Laloë, F. *Quantum Mechanics*; Wiley: New York,NY, 1977.

(38) Colvin, V. L.; Schlamp, M. C.; Alivisatos, A. P. *Nature* **1994**, *370*, 354.

(39) Colvin, V. L.; Schlamp, M. C.; Alivisatos, A. P. *Nature* **1994**, *370*, 354.

(40) Counio, G.; Esnouf, S.; Gacoin, T.; Boilot, J. P. *Journal of Physical Chemistry* **1996**, *100*, 20021.

(41) Dabbousi, B. O.; Bawendi, M. G.; Onitsuka, O.; Rubner, M. F. *Applied Physics Letters* **1995**, *66*, 1316.

(42) Dabbousi, B. O.; RodriguezViejo, J.; Mikulec, F. V.; Heine, J. R.; Mattoussi, H.; Ober, R.; Jensen, K. F.; Bawendi, M. G. *Journal of Physical Chemistry B* **1997**, *101*, 9463.

(43) Dalpian, G. M.; Chelikowsky, J. R. *Physical Review Letters* **2006**, *96*.

(44) Dalven, R.; Gill, R. *Physical Review* **1967**, *159*, 645.

(45) Dalven, R.; Gill, R. *Journal of Applied Physics* **1967**, *38*, 753.

(46) Deka, S.; Genovese, A.; Zhang, Y.; Miszta, K.; Bertoni, G.; Krahne, R.; Giannini, C.; Manna, L. *Journal of the American Chemical Society* **2010**, *132*, 8912.

(47) Dethlefsen, J. R.; Dossing, A. *Nano Letters* **2011**, *11*, 1964.

(48) Dhar, S.; Marshak, A. H. *Solid-State Electronics* **1985**, *28*, 763.

(49) Dow, J. D.; Hong, R. D.; Klemm, S.; Ren, S. Y.; Tsai, M. H.; Sankey, O. F.; Kasowski, R. V. *Physical Review B* **1991**, *43*, 4396.

(50) Drexler, K. E. *Nanosystems: Molecular Machinery, Manufacturing, and Computation*; Wiley: New York, 1992.

(51) Drndic, M.; Jarosz, M. V.; Morgan, N. Y.; Kastner, M. A.; Bawendi, M. G. *Journal of Applied Physics* **2002**, *92*, 7498.

(52) Du, H.; Chen, C. L.; Krishnan, R.; Krauss, T. D.; Harbold, J. M.; Wise, F. W.;

Thomas, M. G.; Silcox, J. *Nano Letters* **2002**, *2*, 1321.

(53) Du, M. H.; Erwin, S. C.; Efros, A. L.; Norris, D. J. *Physical Review Letters* **2008**, *100*, 179702.

(54) Du, M.-H.; Erwin, S. C.; Efros, A. L. *Nano Letters* **2008**, *8*, 2878.

(55) Du, Y. P.; Xu, B.; Fu, T.; Cai, M.; Li, F.; Zhang, Y.; Wang, Q. B. *Journal of the American Chemical Society* **2010**, *132*, 1470.

(56) Dzhafarov, T. D.; Serin, M.; Oren, D.; Sungu, B.; Sadigov, M. S. *Journal of Physics D - Applied Physics* **1999**, *32*, L5.

(57) Efros, A. L.; Efros, A. L. *Soviet Physics Semiconductors - USSR* **1982**, *16*, 772.

(58) Efros, A. L.; Shklovskii, B. I. *Journal of Physics C - Solid State Physics* **1975**, *8*, L49.

(59) Egginger, M.; Bauer, S.; Schwodiauer, R.; Neugebauer, H.; Sariciftci, N. S. *Monatshefte Fur Chemie* **2009**, *140*, 735.

(60) Ehrenfest, P. *Proceedings of the Koninklijke Akademie Van Wetenschappen Te Amsterdam* **1933**, *36*, 153.

(61) Einstein, A. *Annalen Der Physik* **1905**, *17*, 549.

(62) Ekimov, A. I.; Efros, A. L.; Onushchenko, A. A. *Solid State Communications* **1985**, *56*, 921.

(63) Ekimov, A. I.; Kudryavtsev, I. A.; Ivanov, M. G.; Efros, A. L. *Journal of Luminescence* **1990**, *46*, 83.

(64) Ellingson, R. J.; Beard, M. C.; Johnson, J. C.; Yu, P. R.; Micic, O. I.; Nozik, A. J.; Shabaev, A.; Efros, A. L. *Nano Letters* **2005**, *5*, 865.

(65) Erwin, S. C.; Petukhov, A. G. *Physical Review Letters* **2002**, *89*, 227201.

(66) Erwin, S. C.; Zu, L. J.; Haftel, M. I.; Efros, A. L.; Kennedy, T. A.; Norris, D. J. *Nature* **2005**, *436*, 91.

(67) Fafarman, A. T.; Koh, W.-k.; Diroll, B. T.; Kim, D. K.; Ko, D.-K.; Oh, S. J.; Ye, X.; Doan-Nguyen, V.; Crump, M. R.; Reifsnyder, D. C.; Murray, C. B.; Kagan, C. R. *Journal of the American Chemical Society* **2011**, *133*, 15753.

(68) Faraday, M. *Philosophical Transactions of the Royal Society of London* **1857**, *147*, 145.

(69) Ferhat, M.; Nagao, J. *Journal of Applied Physics* **2000**, *88*, 813.

(70) Fowler, A. B.; Wainer, J. J.; Webb, R. A. *IBM Journal of Research and Development* **1988**, *32*, 372.

(71) Frey, M. H.; Payne, D. A. *Physical Review B* **1996**, *54*, 3158.

(72) Fujii, M.; Yamaguchi, Y.; Takase, Y.; Ninomiya, K.; Hayashi, S. *Applied Physics Letters* **2005**, *87*, 211919.

(73) Furdyna, J. K. *Journal of Applied Physics* **1988**, *64*, R29.

(74) Furdyna, J. K.; Kossut, J. *Semiconductors and Semimetals. Volume 25, Diluted Magnetic Semiconductors*; Academic Press: Boston, 1988.

(75) Gans, R. *Annalen Der Physik* **1912**, *37*, 881.

(76) Gans, R. *Annalen Der Physik* **1915**, *47*, 270.

(77) Gao, F.; Lu, Q. Y.; Zhao, D. Y. *Nano Letters* **2003**, *3*, 85.

(78) Garvie, R. C. *Journal of Physical Chemistry* **1978**, *82*, 218.

(79) Garvie, R. C.; Goss, M. F. *Journal of Materials Science* **1986**, *21*, 1253.

(80) Garvie, R. C.; Swain, M. V. *Journal of Materials Science* **1985**, *20*, 1193.

(81) Gates, B.; Mayers, B.; Wu, Y. Y.; Sun, Y. G.; Cattle, B.; Yang, P. D.; Xia, Y. N. *Advanced Functional Materials* **2002**, *12*, 679.

(82) Gates, B.; Wu, Y. Y.; Yin, Y. D.; Yang, P. D.; Xia, Y. N. *Journal of the American Chemical Society* **2001**, *123*, 11500.

(83) Gelmont, B. L.; Dyakonov, M. I. *Soviet Physics Semiconductors - USSR* **1972**, *5*, 1905.

(84) Georgobiani, A. N.; Aminov, U. A.; Dravin, V. A.; Lepnev, L. S.; Mullabaev, I. D.; Ursaki, V. V.; Iljukhina, Z. P. *Nuclear Instruments & Methods in Physics Research Section A - Accelerators Spectrometers Detectors and Associated Equipment* **1999**, *426*, 164.

(85) Geyer, S. M.; Allen, P. M.; Chang, L. Y.; Wong, C. R.; Osedach, T. P.; Zhao, N.; Bulovic, V.; Bawendi, M. G. *ACS Nano* **2010**, *4*, 7373.

(86) Goldstein, A. N.; Echer, C. M.; Alivisatos, A. P. *Science* **1992**, *256*, 1425.

(87) Gorbachev, V. V.; Putilin, I. M. *Physica Status Solidi B - Basic Research* **1975**, *69*, K153.

(88) Gribb, A. A.; Banfield, J. F. *American Mineralogist* **1997**, *82*, 717.

(89) Gunawan, A. A.; Mkhoyan, K. A.; Wills, A. W.; Thomas, M. G.; Norris, D. J. *Nano Letters* **2011**, *11*, 5553.

(90) Gunter, J. R.; Keusch, P. *Ultramicroscopy* **1993**, *49*, 293.

(91) Gur, I.; Fromer, N. A.; Geier, M. L.; Alivisatos, A. P. *Science* **2005**, *310*, 462.

(92) Guyot-Sionnest, P.; Hines, M. A. *Applied Physics Letters* **1998**, *72*, 686.

(93) Guyot-Sionnest, P.; Wang, C. *Journal of Physical Chemistry B* **2003**, *107*, 7355.

(94) Guyot-Sionnest, P.; Wehrenberg, B.; Yu, D. *Journal of Chemical Physics* **2005**, *123*, 074709.

(95) Hadjichristidis, N.; Pispas, S.; Floudas, G. *Block Copolymers: Synthetic Strategies, Physical Properties, and Applications*; Wiley-Interscience: Hoboken, N.J., 2003.

(96) Han, J. P.; Shen, M. R.; Cao, W. W.; Senos, A. M. R.; Mantas, P. Q. *Applied Physics Letters* **2003**, *82*, 67.

(97) Hartmann, H.; Mach, R.; Selle, B. *Wide Gap II-VI Compounds as Electronic Materials*; Akad. d. Wiss. d. DDR, Zentralinst. für Elektronenphysik: Berlin, 1982.

(98) Henglein, A. *Berichte Der Bunsen-Gesellschaft - Physical Chemistry Chemical Physics* **1982**, *86*, 301.

(99) Henry, C. H.; Nassau, K.; Shiever, J. W. *Physical Review B* **1971**, *4*, 2453.

(100) Henshaw, G.; Parkin, I. P.; Shaw, G. A. *Journal of the Chemical Society - Dalton Transactions* **1997**, 231.

(101) Higginson, K. A.; Kuno, M.; Bonevich, J.; Qadri, S. B.; Yousuf, M.; Mattoussi, H. *Journal of Physical Chemistry B* **2002**, *106*, 9982.

(102) Hines, M. A.; Guyot-Sionnest, P. *Journal of Physical Chemistry* **1996**, *100*, 468.

(103) Hines, M. A.; Scholes, G. D. *Advanced Materials* **2003**, *15*, 1844.

(104) Hoffman, D. M.; Meyer, B. K.; Ekimov, A. I.; Merkulov, I. A.; Efros, A. L.; Rosen, M.; Couino, G.; Gacoin, T.; Boilot, J. P. *Solid State Communications* **2000**, *114*, 547.

(105) Hoyer, P.; Weller, H. *Chemical Physics Letters* **1994**, *224*, 75.

(106) Hu, J. T.; Odom, T. W.; Lieber, C. M. *Accounts of Chemical Research* **1999**, *32*, 435.

(107) Huang, X. Y.; Lindgren, E.; Chelikowsky, J. R. *Physical Review B* **2005**, *71*.

(108) Huxter, V. M.; Mirkovic, T.; Nair, P. S.; Scholes, G. D. *Advanced Materials* **2008**, *20*, 2439.

(109) Huynh, W. U.; Dittmer, J. J.; Alivisatos, A. P. *Science* **2002**, *295*, 2425.

(110) Inoue, M. *Journal of Physics and Chemistry of Solids* **1979**, *40*, 857.

(111) Ipe, B. I.; Lehnig, M.; Niemeyer, C. M. *Small* **2005**, *1*, 706.

(112) Ishizumi, A.; Kanemitsu, Y. *Journal of the Physical Society of Japan* **2010**, *79*, 093706.

(113) Ito, Y.; Virkar, A. A.; Mannsfeld, S.; Oh, J. H.; Toney, M.; Locklin, J.; Bao, Z. A. *Journal of the American Chemical Society* **2009**, *131*, 9396.

(114) Jackson, C. L.; McKenna, G. B. *Journal of Chemical Physics* **1990**, *93*, 9002.

(115) Jain, P. K.; Beberwyck, B. J.; Fong, L. K.; Polking, M. J.; Alivisatos, A. P. *Angewandte Chemie - International Edition* **2012**, *51*, 2387.

(116) Jarosz, M. V.; Porter, V. J.; Fisher, B. R.; Kastner, M. A.; Bawendi, M. G. *Physical Review B* **2004**, *70*, 195327.

(117) Jasieniak, J.; Pacifico, J.; Signorini, R.; Chiasera, A.; Ferrari, M.; Martucci, A.; Mulvaney, P. *Advanced Functional Materials* **2007**, *17*, 1654.

(118) Jha, P. P.; Guyot-Sionnest, P. *ACS Nano* **2009**, *3*, 1011.

(119) Ji, Z.; Haynes, J. A.; Ferber, M. K.; Rigsbee, J. M. *Surface & Coatings Technology* **2001**, *135*, 109.

(120) JoseYacaman, M.; Rendon, L.; Arenas, J.; Puche, M. C. S. *Science* **1996**, *273*, 223.

(121) Junod, P.; Hediger, H.; Kilchor, B.; Wullschleger, J. *Philosophical Magazine* **1977**, *36*, 941.

(122) Kamat, P. V. *Journal of Physical Chemistry C* **2008**, *112*, 18737.

(123) Kang, M. S.; Lee, J.; Norris, D. J.; Frisbie, C. D. *Nano Letters* **2009**, *9*, 3848.

(124) Kang, M. S.; Sahu, A.; Norris, D. J.; Frisbie, C. D. *Nano Letters* **2010**, *10*, 3727.

(125) Kang, M. S.; Sahu, A.; Norris, D. J.; Frisbie, C. D. *Nano Letters* **2011**, *11*, 3887.

(126) Kennedy, T. A.; Glaser, E. R.; Klein, P. B.; Bhargava, R. N. *Physical Review B* **1995**, *52*, 14356.

(127) Kershaw, S. V.; Harrison, M.; Rogach, A. L.; Kornowski, A. *IEEE Journal of*

Selected Topics in Quantum Electronics **2000**, *6*, 534.

(128) Keuleyan, S.; Lhuillier, E.; Brajuskovic, V.; Guyot-Sionnest, P. *Nature Photonics* **2011**, *5*, 489.

(129) Keuleyan, S.; Lhuillier, E.; Guyot-Sionnest, P. *Journal of the American Chemical Society* **2011**, *133*, 16422.

(130) Klein, D. L.; Roth, R.; Lim, A. K. L.; Alivisatos, A. P.; McEuen, P. L. *Nature* **1997**, *389*, 699.

(131) Klimov, V. I. *Semiconductor and Metal Nanocrystals: Synthesis and Electronic and Optical Properties*; Marcel Dekker, Inc.: New York, 2004.

(132) Klimov, V. I.; Ivanov, S. A.; Nanda, J.; Achermann, M.; Bezel, I.; McGuire, J. A.; Piryatinski, A. *Nature* **2007**, *447*, 441.

(133) Klimov, V. I.; Mikhailovsky, A. A.; McBranch, D. W.; Leatherdale, C. A.; Bawendi, M. G. *Science* **2000**, *287*, 1011.

(134) Knox, C. K.; Fillmore, S. D.; Call, D. M.; Allen, D. G.; Hess, B. C.; Davis, R. C.; Evenson, W. E.; Harrison, R. G. *Journal of Colloid and Interface Science* **2006**, *300*, 591.

(135) Ko, D.-K.; Urban, J. J.; Murray, C. B. *Nano Letters* **2010**, *10*, 1842.

(136) Koenraad, P. M.; Flatte, M. E. *Nature Materials* **2011**, *10*, 91.

(137) Konstantatos, G.; Howard, I.; Fischer, A.; Hoogland, S.; Clifford, J.; Klem, E.; Levina, L.; Sargent, E. H. *Nature* **2006**, *442*, 180.

(138) Kovalenko, M. V.; Bodnarchuk, M. I.; Zaumseil, J.; Lee, J. S.; Talapin, D. V. *Journal of the American Chemical Society* **2010**, *132*, 10085.

(139) Kovalenko, M. V.; Kaufmann, E.; Pachinger, D.; Roither, J.; Huber, M.; Stangl, J.; Hesser, G.; Schaffler, F.; Heiss, W. *Journal of the American Chemical Society* **2006**, *128*, 3516.

(140) Kovalenko, M. V.; Scheele, M.; Talapin, D. V. *Science* **2009**, *324*, 1417.

(141) Kuno, M.; Lee, J. K.; Dabbousi, B. O.; Mikulec, F. V.; Bawendi, M. G. *Journal of Chemical Physics* **1997**, *106*, 9869.

(142) Laiho, R.; Lashkul, A. V.; Lahderanta, E.; Nedeoglo, D. D.; Nedeoglo, N. D.; Shakhov, M. A. *Semiconductor Science and Technology* **2006**, *21*, 654.

(143) Lamer, V. K.; Dinegar, R. H. *Journal of the American Chemical Society* **1950**, *72*, 4847.

(144) Lauhon, L. J.; Gudiksen, M. S.; Wang, C. L.; Lieber, C. M. *Nature* **2002**, *420*, 57.

(145) Leatherdale, C. A.; Bawendi, M. G. *Physical Review B* **2001**, *63*, 165315.

(146) Lee, J. S.; Kovalenko, M. V.; Huang, J.; Chung, D. S.; Talapin, D. V. *Nature Nanotechnology* **2011**, *6*, 348.

(147) Leon, V.; Ren, Y.; Saboungi, M.-L. *Journal of Applied Physics* **2008**, *103*, 016105.

(148) Leschkies, K. S.; Kang, M. S.; Aydil, E. S.; Norris, D. J. *Journal of Physical Chemistry C* **2010**, *114*, 9988.

(149) Levy, L.; Hochepied, J. F.; Pileni, M. P. *Journal of Physical Chemistry* **1996**, *100*, 18322.

(150) Li, H.; Zanella, M.; Genovese, A.; Povia, M.; Falqui, A.; Giannini, C.; Manna, L. *Nano Letters* **2011**, *11*, 4964.

(151) Li, J. J.; Wang, Y. A.; Guo, W. Z.; Keay, J. C.; Mishima, T. D.; Johnson, M. B.; Peng, X. G. *Journal of the American Chemical Society* **2003**, *125*, 12567.

(152) Liu, H.; Pourret, A.; Guyot-Sionnest, P. *ACS Nano* **2010**, *4*, 5211.

(153) Liu, S. Y.; Choy, W. C. H.; Jin, L.; Leung, Y. P.; Zheng, G. P.; Wang, J. B.; Soh, A. K. *Journal of Physical Chemistry C* **2007**, *111*, 9055.

(154) Liu, Y.; Gibbs, M.; Puthussery, J.; Gaik, S.; Ihly, R.; Hillhouse, H. W.; Law, M. *Nano Letters* **2010**, *10*, 1960.

(155) Luther, J. M.; Jain, P. K.; Ewers, T.; Alivisatos, A. P. *Nature Materials* **2011**, *10*, 361.

(156) Luther, J. M.; Law, M.; Song, Q.; Perkins, C. L.; Beard, M. C.; Nozik, A. J. *ACS Nano* **2008**, *2*, 271.

(157) Luther, J. M.; Zheng, H. M.; Sadtler, B.; Alivisatos, A. P. *Journal of the American Chemical Society* **2009**, *131*, 16851.

(158) Lyubomirsky, I.; Lyakhovitskaya, V.; Triboulet, R.; Cahen, D. *Journal of Electronic Materials* **1997**, *26*, 97.

(159) Makiura, R.; Yonemura, T.; Yamada, T.; Yamauchi, M.; Ikeda, R.; Kitagawa, H.; Kato, K.; Takata, M. *Nature Materials* **2009**, *8*, 476.

(160) Manzoor, K.; Vadera, S. R.; Kumar, N.; Kutty, T. R. N. *Materials Chemistry and Physics* **2003**, *82*, 718.

(161) McHale, J. M.; Auroux, A.; Perrotta, A. J.; Navrotsky, A. *Science* **1997**, *277*, 788.

(162) Mentzel, T. S.; Porter, V. J.; Geyer, S.; MacLean, K.; Bawendi, M. G.; Kastner, M. A. *Physical Review B* **2008**, *77*, 075316.

(163) Meulenberg, R. W.; van Buuren, T.; Hanif, K. M.; Willey, T. M.; Strouse, G. F.; Terminello, L. J. *Nano Letters* **2004**, *4*, 2277.

(164) Michalet, X.; Pinaud, F. F.; Bentolila, L. A.; Tsay, J. M.; Doose, S.; Li, J. J.; Sundaresan, G.; Wu, A. M.; Gambhir, S. S.; Weiss, S. *Science* **2005**, *307*, 538.

(165) Mie, G. *Annalen Der Physik* **1908**, *25*, 377.

(166) Mikulec, F. V.; Kuno, M.; Bennati, M.; Hall, D. A.; Griffin, R. G.; Bawendi, M. G. *Journal of the American Chemical Society* **2000**, *122*, 2532.

(167) Miller, A.; Abrahams, E. *Physical Review* **1960**, *120*, 745.

(168) Mocatta, D.; Cohen, G.; Schattner, J.; Millo, O.; Rabani, E.; Banin, U. *Science* **2011**, *332*, 77.

(169) Mokari, T.; Aharoni, A.; Popov, I.; Banin, U. *Angewandte Chemie - International Edition* **2006**, *45*, 8001.

(170) Mokari, T.; Rothenberg, E.; Popov, I.; Costi, R.; Banin, U. *Science* **2004**, *304*, 1787.

(171) Moreels, I.; Lambert, K.; De Muynck, D.; Vanhaecke, F.; Poelman, D.; Martins, J. C.; Allan, G.; Hens, Z. *Chemistry of Materials* **2007**, *19*, 6101.

(172) Morgan, N. Y.; Leatherdale, C. A.; Drndic, M.; Jarosz, M. V.; Kastner, M. A.; Bawendi, M. *Physical Review B* **2002**, *66*.

(173) Mott, N. F.; Davis, E. A. *Electronic Processes in Non-Crystalline Materials*; Clarendon Press ; Oxford University Press: Oxford; New York, 1979.

(174) Motte, L.; Billoudet, F.; Lacaze, E.; Douin, J.; Pileni, M. P. *Journal of Physical Chemistry B* **1997**, *101*, 138.

(175) Munro, A. M.; Jen-La Plante, I.; Ng, M. S.; Ginger, D. S. *Journal of Physical Chemistry C* **2007**, *111*, 6220.

(176) Murphy, J. E.; Beard, M. C.; Nozik, A. J. *Journal of Physical Chemistry B* **2006**,

110, 25455.

(177) Murray, C. B.; Kagan, C. R.; Bawendi, M. G. *Annual Review of Material Science* **2000**, *30*, 545.

(178) Murray, C. B.; Norris, D. J.; Bawendi, M. G. *Journal of the American Chemical Society* **1993**, *115*, 8706.

(179) Murray, C. B.; Sun, S. H.; Gaschler, W.; Doyle, H.; Betley, T. A.; Kagan, C. R. *IBM Journal of Research and Development* **2001**, *45*, 47.

(180) Nag, A.; Kovalenko, M. V.; Lee, J. S.; Liu, W. Y.; Spokoyny, B.; Talapin, D. V. *Journal of the American Chemical Society* **2011**, *133*, 10612.

(181) Nalwa, H. S. *Encyclopedia of Nanoscience and Nanotechnology*; American Scientific Publishers: Stevenson Ranch, Calif., 2004.

(182) Nedeoglo, N. D.; Sirkeli, V. P.; Nedeoglo, D. D.; Laiho, R.; Lahderanta, E. *Journal of Physics-Condensed Matter* **2006**, *18*, 8113.

(183) Ng, M. T.; Boothroyd, C.; Vittal, J. J. *Chemical Communications* **2005**, 3820.

(184) Nikolic, M. S.; Krack, M.; Aleksandrovic, V.; Kornowski, A.; Forster, S.; Weller, H. *Angewandte Chemie-International Edition* **2006**, *45*, 6577.

(185) Nikolic, M. S.; Olsson, C.; Salcher, A.; Kornowski, A.; Rank, A.; Schubert, R.; Fromsdorf, A.; Weller, H.; Forster, S. *Angewandte Chemie - International Edition* **2009**, *48*, 2752.

(186) Nirmal, M.; Brus, L. *Accounts of Chemical Research* **1999**, *32*, 407.

(187) Nitsche, R.; Winterer, M.; Hahn, H. *Nanostructured Materials* **1995**, *6*, 679.

(188) Noda, Y.; Orihashi, M.; Nishida, A. I. *Journal of the Japan Institute of Metals* **1997**, *61*, 180.

(189) Norris, D. J.; Bawendi, M. G. *Physical Review B* **1996**, *53*, 16338.

(190) Norris, D. J.; Efros, A. L.; Erwin, S. C. *Science* **2008**, *319*, 1776.

(191) Norris, D. J.; Yao, N.; Charnock, F. T.; Kennedy, T. A. *Nano Letters* **2001**, *1*, 3.

(192) Nozik, A. J. *Physica E - Low-Dimensional Systems & Nanostructures* **2002**, *14*, 115.

(193) Nozik, A. J.; Beard, M. C.; Luther, J. M.; Law, M.; Ellingson, R. J.; Johnson, J. C. *Chemical Reviews* **2010**, *110*, 6873.

(194) Nozik, A. J.; Micic, O. I. *MRS Bulletin* **1998**, *23*, 24.

(195) Okabe, T.; Ura, K. *Journal of Applied Crystallography* **1994**, *27*, 140.

(196) Orihashi, M.; Noda, Y.; Kaibe, T. H.; Nishida, I. A. *Journal of the Japan Institute of Metals* **1997**, *61*, 241.

(197) Orlinskii, S. B.; Schmidt, J.; Baranov, P. G.; Hofmann, D. M.; Donega, C. D.; Meijerink, A. *Physical Review Letters* **2004**, *92*.

(198) Ostwald, W. *Die Welt Der Vernachlässigten Dimensionen*; Steinkopff: Dresden & Leipzig, 1915.

(199) Pankove, J. I. *Optical Processes in Semiconductors*; Prentice-Hall: Englewood Cliffs, N.J., 1971.

(200) Parish, M. M.; Littlewood, P. B. *Nature* **2003**, *426*, 162.

(201) Park, Y. S.; Malko, A. V.; Vela, J.; Chen, Y.; Ghosh, Y.; Garcia-Santamaria, F.; Hollingsworth, J. A.; Klimov, V. I.; Htoon, H. *Physical Review Letters* **2011**, *106*, 187401.

(202) Peng, X. G.; Wickham, J.; Alivisatos, A. P. *Journal of the American Chemical Society* **1998**, *120*, 5343.

(203) Pesavento, P. V.; Chesterfield, R. J.; Newman, C. R.; Frisbie, C. D. *Journal of Applied Physics* **2004**, *96*, 7312.

(204) Petroff, P. M.; MedeirosRibeiro, G. *MRS Bulletin* **1996**, *21*, 50.

(205) Pi, X. D.; Gresback, R.; Liptak, R. W.; Campbell, S. A.; Kortshagen, U. *Applied Physics Letters* **2008**, *92*, 123102.

(206) Pietryga, J. M.; Werder, D. J.; Williams, D. J.; Casson, J. L.; Schaller, R. D.; Klimov, V. I.; Hollingsworth, J. A. *Journal of the American Chemical Society* **2008**, *130*, 4879.

(207) Pradhan, N.; Goorskey, D.; Thessing, J.; Peng, X. G. *Journal of the American Chemical Society* **2005**, *127*, 17586.

(208) Qin, A. M.; Fang, Y. P.; Tao, P. F.; Zhang, J. Y.; Su, C. Y. *Inorganic Chemistry* **2007**, *46*, 7403.

(209) Radovanovic, P. V.; Gamelin, D. R. *Journal of the American Chemical Society* **2001**, *123*, 12207.

(210) Radovanovic, P. V.; Gamelin, D. R. Isocrystalline Core/Shell Synthesis of High Quality II-VI Diluted Magnetic Semiconductor Quantum Dots: Ligand-Field Spectroscopic Studies. In *Physical Chemistry of Interfaces and Nanomaterials*, 2002; Vol. 4807; pp 223.

(211) Rao, C. N. R.; Rao, K. J. *Phase Transitions in Solids*; McGraw-Hill: New York, 1978.

(212) Reinberg, A. R.; Holton, W. C.; Dewit, M.; Watts, R. K. *Physical Review B* **1971**, *3*, 410.

(213) Reiss, P. *New Journal of Chemistry* **2007**, *31*, 1843.

(214) Reiss, P.; Bleuse, J.; Pron, A. *Nano Letters* **2002**, *2*, 781.

(215) Resch-Genger, U.; Grabolle, M.; Cavaliere-Jaricot, S.; Nitschke, R.; Nann, T. *Nature Methods* **2008**, *5*, 763.

(216) Ridley, B. A.; Nivi, B.; Jacobson, J. M. *Science* **1999**, *286*, 746.

(217) Rivest, J. B.; Fong, L. K.; Jain, P. K.; Toney, M. F.; Alivisatos, A. P. *Journal of Physical Chemistry Letters* **2011**, *2*, 2402.

(218) Robinson, A. L.; Bube, R. H. *Journal of Applied Physics* **1971**, *42*, 5280.

(219) Robinson, R. D.; Sadtler, B.; Demchenko, D. O.; Erdonmez, C. K.; Wang, L.-W.; Alivisatos, A. P. *Science* **2007**, *317*, 355.

(220) Roest, A. L.; Kelly, J. J.; Vanmaekelbergh, D.; Meulenkamp, E. A. *Physical Review Letters* **2002**, *89*, 036801.

(221) Rogalski, A. *Infrared Physics & Technology* **2002**, *43*, 187.

(222) Rogalski, A.; Antoszewski, J.; Faraone, L. *Journal of Applied Physics* **2009**, *105*, 091101.

(223) Romero, H. E.; Drndic, M. *Physical Review Letters* **2005**, *95*, 156801.

(224) Rossetti, G. A.; Cline, J. P.; Navrotsky, A. *Journal of Materials Research* **1998**, *13*, 3197.

(225) Roy, S.; Tuinenga, C.; Fungura, F.; Dagtepe, P.; Chikan, V.; Jasinski, J. *Journal of Physical Chemistry C* **2009**, *113*, 13008.

(226) Sadtler, B.; Demchenko, D. O.; Zheng, H.; Hughes, S. M.; Merkle, M. G.; Dahmen, U.; Wang, L. W.; Alivisatos, A. P. *Journal of the American Chemical Society* **2009**,

131, 5285.

(227) Safran, G.; Geszti, O.; Radnoczi, G.; Barna, P. B. *Thin Solid Films* **1998**, *317*, 72.

(228) Sahu, A.; Kang, M. S.; Kompch, A.; Notthoff, C.; Wills, A. W.; Deng, D.; Winterer, M.; Frisbie, C. D.; Norris, D. J. *Nano Letters* **2012**, *12*, 2587.

(229) Sahu, A.; Khare, A.; Deng, D. D.; Norris, D. J. *Chemical Communications* **2012**, *48*, 5458.

(230) Sahu, A.; Qi, L.; Kang, M. S.; Deng, D.; Norris, D. J. *Journal of the American Chemical Society* **2011**, *133*, 6509.

(231) Sato, F.; Kagawa, T.; Yodo, Y.; Iida, T. Ion Microprobe Analysis of Acceptor-Doped II-VI Compounds. In *2003 IEEE Nuclear Science Symposium, Conference Record, Vols 1-5*; IEEE: New York, 2004; pp 3527.

(232) Sato, H.; Kitakami, O.; Sakurai, T.; Shimada, Y.; Otani, Y.; Fukamichi, K. *Journal of Applied Physics* **1997**, *81*, 1858.

(233) Saunders, A. E.; Popov, I.; Banin, U. *Journal of Physical Chemistry B* **2006**, *110*, 25421.

(234) Schlag, S.; Eicke, H. F. *Solid State Communications* **1994**, *91*, 883.

(235) Schoen, D. T.; Xie, C.; Cui, Y. *Journal of the American Chemical Society* **2007**, *129*, 4116.

(236) Shaw, L. B.; Cole, B.; Thielen, P. A.; Sanghera, J. S.; Aggarwal, I. D. *IEEE Journal of Quantum Electronics* **2001**, *37*, 1127.

(237) Shim, M.; Guyot-Sionnest, P. *Nature* **2000**, *407*, 981.

(238) Shim, M.; Guyot-Sionnest, P. *Journal of the American Chemical Society* **2001**, *123*, 11651.

(239) Shim, M.; Wang, C. J.; Guyot-Sionnest, P. *Journal of Physical Chemistry B* **2001**, *105*, 2369.

(240) Shim, M.; Wang, C. J.; Norris, D. J.; Guyot-Sionnest, P. *MRS Bulletin* **2001**, *26*, 1005.

(241) Shklovskii, B. I.; Efros, A. L. *Electronic Properties of Doped Semiconductors*; Springer-Verlag: Berlin; New York, 1984.

(242) Silverstein, R. M.; Bassler, G. C.; Morrill, T. C. *Spectrometric Identification of*

Organic Compounds; Wiley: New York, 1981.

(243) Skandan, G.; Hahn, H.; Roddy, M.; Cannon, W. R. *Journal of the American Ceramic Society* **1994**, *77*, 1706.

(244) Skinner, B.; Chen, T. R.; Shklovskii, B. I. *Physical Review B* **2012**, *85*, 205316.

(245) Smoluchowski, R. *Phase Transformations in Solids*; Wiley: New York, NY, 1951.

(246) Son, D. H.; Hughes, S. M.; Yin, Y.; Paul Alivisatos, A. *Science* **2004**, *306*, 1009.

(247) Son, D. H.; Hughes, S. M.; Yin, Y. D.; Alivisatos, A. P. *Science* **2004**, *306*, 1009.

(248) Sooklal, K.; Cullum, B. S.; Angel, S. M.; Murphy, C. J. *Journal of Physical Chemistry* **1996**, *100*, 4551.

(249) Spinicelli, P.; Buil, S.; Quelin, X.; Mahler, B.; Dubertret, B.; Hermier, J. P. *Physical Review Letters* **2009**, *102*, 136801.

(250) Srivastava, B. B.; Jana, S.; Pradhan, N. *Journal of the American Chemical Society* **2011**, *133*, 1007.

(251) Steckel, J. S.; Yen, B. K. H.; Oertel, D. C.; Bawendi, M. G. *Journal of the American Chemical Society* **2006**, *128*, 13032.

(252) Stegner, A. R.; Pereira, R. N.; Klein, K.; Lechner, R.; Dietmueller, R.; Brandt, M. S.; Stutzmann, M.; Wiggers, H. *Physical Review Letters* **2008**, *100*, 026803.

(253) Stowell, C. A.; Wiacek, R. J.; Saunders, A. E.; Korgel, B. A. *Nano Letters* **2003**, *3*, 1441.

(254) Su, H. L.; Xie, Y.; Li, B.; Qian, Y. T. *Materials Research Bulletin* **2000**, *35*, 465.

(255) Sugano, S.; Kojima, N. *Magneto-Optics*; Springer: Berlin; New York, 2000.

(256) Suresh, A.; Mayo, M. J.; Porter, W. D. *Journal of Materials Research* **2003**, *18*, 2912.

(257) Suyver, J. F.; Wuister, S. F.; Kelly, J. J.; Meijerink, A. *Physical Chemistry Chemical Physics* **2000**, *2*, 5445.

(258) Swaminathan, V.; Greene, L. C. *Journal of Luminescence* **1976**, *14*, 357.

(259) Swihart, M. T. *Current Opinion in Colloid & Interface Science* **2003**, *8*, 127.

(260) Sze, S. M.; Ng, K. K. *Physics of Semiconductor Devices*; Wiley-Interscience: Hoboken, N.J., 2007.

(261) Talapin, D. V.; Lee, J.-S.; Kovalenko, M. V.; Shevchenko, E. V. *Chemical Reviews*

2010, *110*, 389.

(262) Talapin, D. V.; Murray, C. B. *Science* **2005**, *310*, 86.

(263) Tangirala, R.; Baker, J. L.; Alivisatos, A. P.; Milliron, D. J. *Angewandte Chemie - International Edition* **2010**, *49*, 2878.

(264) Terrill, R. H.; Postlethwaite, T. A.; Chen, C. H.; Poon, C. D.; Terzis, A.; Chen, A. D.; Hutchison, J. E.; Clark, M. R.; Wignall, G.; Londono, J. D.; Superfine, R.; Falvo, M.; Johnson, C. S.; Samulski, E. T.; Murray, R. W. *Journal of the American Chemical Society* **1995**, *117*, 12537.

(265) Tessler, N.; Medvedev, V.; Kazes, M.; Kan, S.; Banin, U. *Science* **2002**, *295*, 1506.

(266) Tessler, N.; Medvedev, V.; Kazes, M.; Kan, S. H.; Banin, U. *Science* **2002**, *295*, 1506.

(267) Tisdale, W. A.; Williams, K. J.; Timp, B. A.; Norris, D. J.; Aydil, E. S.; Zhu, X. Y. *Science* **2010**, *328*, 1543.

(268) Tolbert, S. H.; Alivisatos, A. P. *Science* **1994**, *265*, 373.

(269) Tolbert, S. H.; Alivisatos, A. P. *Annual Review of Physical Chemistry* **1995**, *46*, 595.

(270) Turnbull, D. *Journal of Applied Physics* **1950**, *21*, 1022.

(271) Urban, J. J.; Talapin, D. V.; Shevchenko, E. V.; Kagan, C. R.; Murray, C. B. *Nature Materials* **2007**, *6*, 115.

(272) Van de Walle, C. G.; Neugebauer, J. *Nature* **2003**, *423*, 626.

(273) Vanmaekelbergh, D.; Liljeroth, P. *Chemical Society Reviews* **2005**, *34*, 299.

(274) Viswanatha, R.; Brovelli, S.; Pandey, A.; Crooker, S. A.; Klimov, V. I. *Nano Letters* **2012**, *11*, 4753.

(275) Wang, C. J.; Shim, M.; Guyot-Sionnest, P. *Science* **2001**, *291*, 2390.

(276) Wang, C. J.; Wehrenberg, B. L.; Woo, C. Y.; Guyot-Sionnest, P. *Journal of Physical Chemistry B* **2004**, *108*, 9027.

(277) Wang, D.; Xie, T.; Peng, Q.; Li, Y. *Journal of the American Chemical Society* **2008**, *130*, 4016.

(278) Wang, S. B.; Hu, B.; Liu, C. C.; Yu, S. H. *Journal of Colloid and Interface Science* **2008**, *325*, 351.

(279) Wang, W. Z.; Geng, Y.; Qian, Y. T.; Ji, M. R.; Xie, Y. *Materials Research Bulletin* **1999**, *34*, 877.

(280) Wang, X. Y.; Ren, X. F.; Kahen, K.; Hahn, M. A.; Rajeswaran, M.; Maccagnano-Zacher, S.; Silcox, J.; Cragg, G. E.; Efros, A. L.; Krauss, T. D. *Nature* **2009**, *459*, 686.

(281) Wang, Y.; Herron, N.; Moller, K.; Bein, T. *Solid State Communications* **1991**, *77*, 33.

(282) Wang, Y. S.; Thomas, P. J.; O'Brien, P. *Journal of Physical Chemistry B* **2006**, *110*, 4099.

(283) Watts, R. K.; Holton, W. C.; Dewit, M. *Physical Review B* **1971**, *3*, 404.

(284) Wehrenberg, B. L.; Guyot-Sionnest, P. *Journal of the American Chemical Society* **2003**, *125*, 7806.

(285) Wehrenberg, B. L.; Wang, C. J.; Guyot-Sionnest, P. *Journal of Physical Chemistry B* **2002**, *106*, 10634.

(286) Wehrenberg, B. L.; Yu, D.; Ma, J. S.; Guyot-Sionnest, P. *Journal of Physical Chemistry B* **2005**, *109*, 20192.

(287) Wills, A. W.; Kang, M. S.; Wentz, K. M.; Hayes, S. E.; Sahu, A.; Gladfelter, W. L.; Norris, D. J. *Journal of Materials Chemistry* **2012**, *22*, 6335.

(288) Winterer, M.; Nitsche, R.; Redfern, S. A. T.; Schmahl, W. W.; Hahn, H. *Nanostructured Materials* **1995**, *5*, 679.

(289) Wuelfing, W. P.; Green, S. J.; Pietron, J. J.; Cliffel, D. E.; Murray, R. W. *Journal of the American Chemical Society* **2000**, *122*, 11465.

(290) Xi, B. J.; Xiong, S. L.; Xu, D. C.; Li, J. F.; Zhou, H. Y.; Pan, J.; Li, J. Y.; Qian, Y. T. *Chemistry - A European Journal* **2008**, *14*, 9786.

(291) Xia, Y.; Cho, J.; Paulsen, B.; Frisbie, C. D.; Renn, M. J. *Applied Physics Letters* **2009**, *94*, 013304.

(292) Xiao, J.; Xie, Y.; Tang, R.; Luo, W. *Journal of Materials Chemistry* **2002**, *12*, 1148.

(293) Xu, H. Z.; Zhao, E.; Majumdar, A.; Jayasinghe, L.; Shi, Z. *Electronics Letters* **2003**, *39*, 659.

(294) Xu, R.; Husmann, A.; Rosenbaum, T. F.; Saboungi, M. L.; Enderby, J. E.; Littlewood, P. B. *Nature* **1997**, *390*, 57.

(295) Yang, Y.; Chen, O.; Angerhofer, A.; Cao, Y. C. *Journal of the American Chemical Society* **2006**, *128*, 12428.

(296) Yarema, M.; Pichler, S.; Sytnyk, M.; Seyrkammer, R.; Lechner, R. T.; Fritz-Popovski, G.; Jarzab, D.; Szendrei, K.; Resel, R.; Korovyanko, O.; Loi, M. A.; Paris, O.; Hesser, G.; Heiss, W. *ACS Nano* **2011**, *5*, 3758.

(297) Yildiz, A.; Serin, N.; Serin, T.; Kasap, M. *Japanese Journal of Applied Physics* **2009**, *48*, 111203.

(298) Yin, K. B.; Xia, Y. D.; Liu, Z. G.; Yin, J.; Sun, L. T. *Physica Status Solidi A - Applications and Materials Science* **2012**, *209*, 135.

(299) Yoffe, A. D. *Advances in Physics* **2001**, *50*, 1.

(300) Yu, D.; Wang, C. J.; Guyot-Sionnest, P. *Science* **2003**, *300*, 1277.

(301) Yu, D.; Wang, C. J.; Wehrenberg, B. L.; Guyot-Sionnest, P. *Physical Review Letters* **2004**, *92*, 216802.

(302) Yu, D.; Wehrenberg, B. L.; Jha, P.; Ma, J.; Guyot-Sionnest, P. *Journal of Applied Physics* **2006**, *99*, 104315.

(303) Yu, W. W.; Qu, L. H.; Guo, W. Z.; Peng, X. G. *Chemistry of Materials* **2003**, *15*, 2854.

(304) Zeng, J.; Lu, W.; Wang, X.; Wang, B.; Wang, G.; Hou, J. G. *Journal of Colloid and Interface Science* **2006**, *298*, 685.

(305) Zhang, H. Z.; Banfield, J. F. Phase Stability in the Nanocrystalline TiO_2 System. In *Phase Transformations and Systems Driven Far from Equilibrium*; Materials Research Society: Warrendale, 1998; Vol. 481; pp 619.

(306) Zhang, H. Z.; Banfield, J. F. *Journal of Materials Chemistry* **1998**, *8*, 2073.

(307) Zhang, H. Z.; Banfield, J. F. *Journal of Physical Chemistry B* **2000**, *104*, 3481.

(308) Zhao, Y. X.; Pan, H. C.; Lou, Y. B.; Qiu, X. F.; Zhu, J. J.; Burda, C. *Journal of the American Chemical Society* **2009**, *131*, 4253.

(309) Zheng, H.; Rivest, J. B.; Miller, T. A.; Sadtler, B.; Lindenberg, A.; Toney, M. F.; Wang, L.-W.; Kisielowski, C.; Alivisatos, A. P. *Science* **2011**, *333*, 206.